Contents

Plenary Talks

Proceedings of the International School-seminar
"New Physics and Quantum Chromodynamics at External Conditions", pp. 5 – 12,
3-6 May 2011, Dnipropetrovsk, Ukraine

THE SPACE-TIME STRUCTURE OF RELATIVISTIC NUCLEUS-NUCLEUS COLLISIONS

D. V. Anchishkin[a,1], A. O. Muskeyev[b,2], V. Yu. Vovchenko[c,2], S. N. Yezhov[d,2]

[1]Bogolyubov Institute for Theoretical Physics, Kiev, Ukraine
[2]Taras Shevchenko Kiev National University, Kiev, Ukraine

On the bases of the proposed algorithm the space-time structure of the relativistic nucleus-nucleus collisions is studied. The reaction zones and reaction frequencies for different type of reactions are calculated for AGS and SPS energies within the microscopic transport model UrQMD. The reaction density fireball representation is compared to other possible representations. The hypersurfaces which are the reaction zone boundaries are related to the kinetic and chemical freeze-out hypersurfaces. On the basis of performed calculations the characteristic points of the time dependence of fireball evolution are obtained.

1 Introduction

A strongly interacting matter is formed in heavy-ion collisions. A fireball is identified with a space-time region, in which the reactions of particles occur. Hence, reaction zones must reflect the space-time characteristics of a fireball, and its study gives information about evolution of a fireball.

In the study of nucleus-nucleus collisions one can distinguish different stages of fireball evolution. Depending on a model describing the system, we can distinguish the regions of the formation of a fireball, its isotropization and thermalization, the creation of particles, the regions of a chemical freeze-out and a kinetic one, etc. Different models are usually used to describe different stages of heavy-ion collision. In particular, the stages of formation ($\tau \sim 0.1$ fm/c) and thermalization ($\tau \sim 1$ fm/c) are most often described with the use of microscopic models based on the processes of interaction of quarks and gluons [1, 2, 3]. To describe the stage of spreading of a dense medium ($1 \leq \tau \leq 7$ fm/c), the relativistic hydrodynamics is most often in use [4, 5, 6]. The further evolution of a hadron gas and the process of chemical and kinetic freeze-out ($\tau \sim 20 - 25$ fm/c) are covered by kinetic models [7, 8]. The models, which combine hydrodynamic and kinetic description are also applied [9, 10].

As parameters for the determination of the stages of evolution of a system, one can take the particle density, energy density, mean free path, rate of collisions of particles, etc. Depending on the chosen parameter one can get different fireball representations. In the present work, we use the hadron reaction density (number of reactions in a unit volume per unit time) in a given four-dimensional region of the space-time as a parameter of the spatial evolution of the interacting system. Such a quantitative estimate allows one to define the reaction zone, whose study gives a possibility to establish the space-time structure of a fireball from the viewpoint of the interaction intensity at every point of the space-time. The regions of a fireball can be distinguished by the interaction intensity which can be characterized by the number of collisions in a unit volume of the space-time. We use this quantity to determine the boundaries between different reaction zones.

Another important question which can be clarified by the study of the zone of reactions is how the space-time boundary of a fireball is related to the so-called sharp kinetic freeze-out hypersurface. Since the kinetic freeze-out is the process of establishment of a final distribution of particles in the momentum space, the sharp kinetic freeze-out hypersurface is an imaginary hypersurface, outside of which there are no collisions between radiated particles. In that sense the space-time boundary of a reaction zone and the sharp kinetic freeze-out hypersurface can be put in correspondence.

2 Reaction zones

The number of reactions in the given space-time region can be determined, for instance, with the use of the distribution function $f(x,p)$. The probability of a collision of two particles with momenta p_1 and p_2 corresponding to the distribution functions f_1 and f_2, respectively, in the approximation of two-particle reactions $2 \to 2$ is determined at a space-time point x as

$$P(x, \mathbf{p}_1, \mathbf{p}_2) = \int_3 \int_4 W_{12\to 34}\, f(x, p_1)\, f(x, p_2)\,. \tag{1}$$

e-mail: [a]anch@bitp.kiev.ua, [b]anton_muskeyev@bigmir.net, [c]vlvovch@gmail.com, [d]yezhov@univ.kiev.ua

Table 1. Reaction classification by number of participants

1	$1 \to 2' + m,\ m \geq 0$	decay
3	$2 \to 1'$	fusion
4	$2 \to 2$	elastic scattering
5	$2 \to 2' + m,\ m \geq 0$	inelastic reaction

The quantity $W_{12\to34}$ is the transition rate which involves the reaction cross section and the conservation laws, $\int_i \equiv \int \frac{d^3p_i}{E_{p_i}}$, $E_{p_i} = \sqrt{m^2 + \mathbf{p}_i^2}$.

By integrating over the momenta of particles, we obtain the rate or the 4-density of reactions at the point x:

$$\Gamma(x) = \int_1 \int_2 \int_3 \int_4 W_{12\to34}\, f(x, p_1)\, f(x, p_2)\,. \tag{2}$$

Then, the number of reactions in the given space-time region Ω is

$$N_{\rm coll}(\Omega) = \int_\Omega d^4x\, \Gamma(x)\,. \tag{3}$$

It is seen that the number of reactions in the given space-time region depends on the 4-density of reactions $\Gamma(x)$ which can be determined in a certain model approximation, e.g., like that in [11, 12]. In particular, $\Gamma(x)$ can be determined with the use of transport models.

The reaction zone is defined as the space-time region where a certain fraction of all reactions of certain type took place. This space-time region is chosen in a way that it was the most intense with respect to the reaction rate, that is, it has the smallest possible volume. The reaction zones for the given reaction type can be calculated by using the 4-density of reactions (2). Detailed description of the procedure one can find in Ref. [13]. Reaction zone can be calculated for different types of reactions. Reactions can be classified by type and number of particles taking part in these reactions (see Table 1).

To carry out calculations, we use the transport model UrQMD v2.3 [14, 15] which allows one to calculate the four-density of reactions at every point of the space-time region and to select reactions of a given type and for the given species of particles. We take the number of reactions $N_{\rm coll}[\Omega(t, \mathbf{r})]$ in a pixel $\Omega(t, \mathbf{r})$ as a result of the averaging over 1000 events. In the calculations, we took a four-cube of reactions C_R with the size of edges $L_i = 200$ fm, where $i = t,\ x,\ y,\ z$.

In Fig. 1 we show calculation results for conditions at the CERN Super Proton Synchrotron (SPS), Pb+Pb at 158A GeV in the case of central collisions. The figure depicts space-time region where 90% of all hadronic reactions takeconstr place. For this calculations we use coordinates (t, r, z) where $r = \sqrt{x^2 + y^2}$. Also, different projections of the reaction zone are shown at coordinate planes: z-t (yellow), r-t (blue) and z-r (orange). We note that the reaction density (2) does not depend on the azimuthal angle φ because of the symmetry of central collisions.

Henceforth, we will deal with the projection of the reaction zone on the z-t plane. To design this projection we sum first all collisions along the transverse direction at the fixed coordinates $(t,\ z)$. Then, the reaction density in z-t plane takes following form:

$$\widetilde{\Gamma}(t, z) = \int dx\, dy\, \Gamma(t, x, y, z)\,. \tag{4}$$

Then, the number of reactions in the given pixel $\widetilde{\Omega}(t, z)$ on z-t plane is

$$\widetilde{N}_{\rm coll}[\widetilde{\Omega}(t, z)] = \int_{\widetilde{\Omega}(t,z)} dt\, dz\, \widetilde{\Gamma}(t, z)\,. \tag{5}$$

Then, the reaction zone projection can be constructed with the use of above-mentioned algorithm from Ref. [13].

In Figs. 2, 3 and 4, we show the results of calculations for conditions at the BNL Alternating Gradient Synchrotron (AGS), Au+Au, and at the CERN Super Proton Synchrotron (SPS), Pb+Pb, in the case of central collisions. In accordance with our algorithm, the four-volume which contains 99% of all hadronic inelastic reactions, $2 \to 2' + m, m \geq 0$ is determined [depicted as the medium-gray (red) area]. We name this zone as a region of hot fireball. We determine also a four-volume that contains 99% of all possible hadronic reactions which include, of course, the previous zone. We name the region of 99% of all hadronic reactions excluding the zone of the hot fireball as a cold fireball [dark-gray (blue) area]. The additional region [light-gray (cyan) area] is a fireball halo and it contains additional 0.9% of all hadronic reactions. This zone is formed mostly by decays of resonances. That is, the three space-time regions (hot, cold, halo) cover 99.9% of the total number $N_{\rm tot}$ of all hadronic reactions.

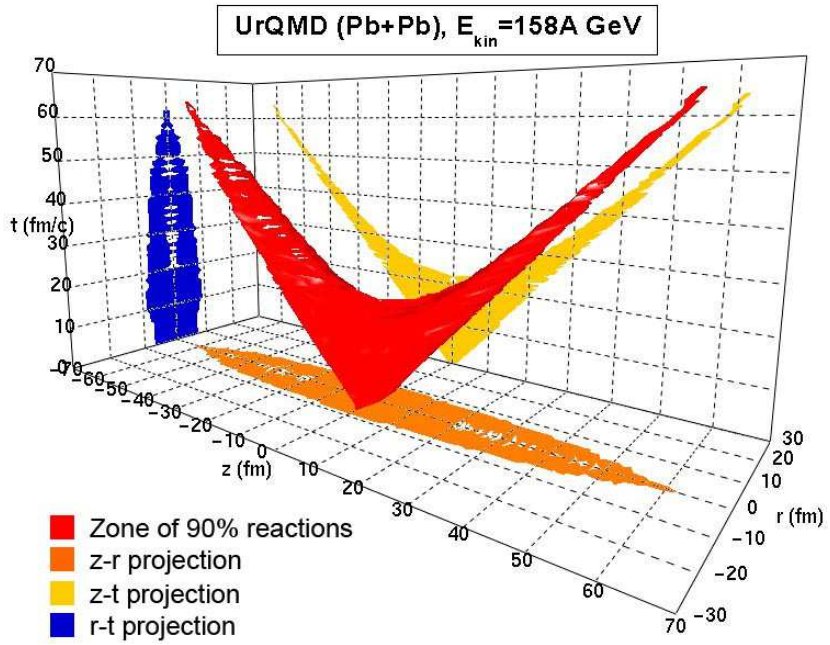

Figure 1. The three-dimensional reaction zone, which determines the space-time region where 90% of all hadronic reactions for SPS conditions ($E_{\rm kin} = 158$A GeV) take place.

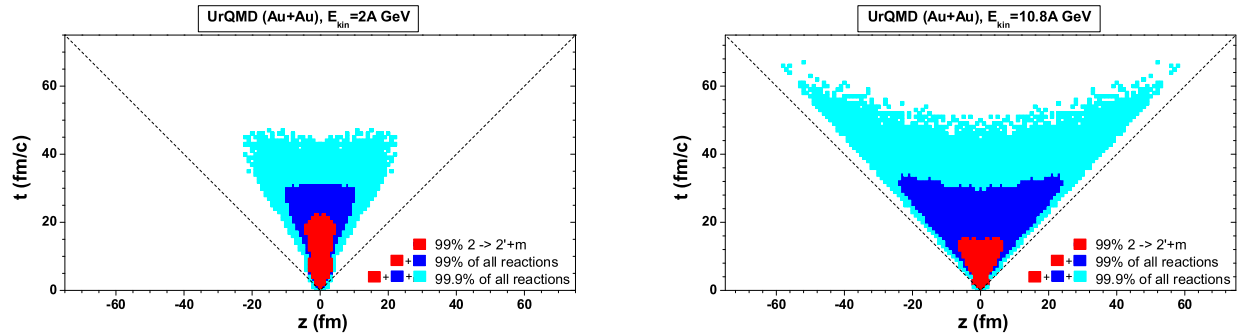

Figure 2. Projection of the reaction zone on the z-t plane under the AGS (Au+Au at 2A GeV and 10.8A GeV) conditions. The medium-gray (red) region contains 99% of all inelastic reactions, $2 \rightarrow 2' + m, m \geq 0$. The medium-gray (red) and the dark-gray (blue) regions together contain 99% of all hadronic reactions. The light-grey (cyan) region contains 0.9% of all hadron reactions only.

It is seen that the interacting system has a comparatively long lifetime: A hot fireball decays completely only in the time intervals of the order of 15–20 fm/c for AGS and low SPS and 20–35 fm/c for SPS. A cold fireball lives for 30–33 fm/c for AGS, 45–60 fm/c for low SPS and 80–100 fm/c for SPS.

The zones of hot and cold fireballs together contain 99% of all reactions by definition. We can compare this reaction zone with the zone which is wrapped by freeze-out hypersurface. Note, following the "classical" definition of the sharp kinetic freeze-out hypersurface it is some boundary that separates the interacting system from the space-time domain where particles do not interact and almost all particles are evaporated (freezed out) from the thin space-time layer determined by this hypersurface. Then, it seems evident that the sharp kinetic freeze-out hypersurface should be inside reaction zone but not out of it. And in addition the sharp chemical freeze-out hypersurface should be inside the hypersurface which separates the region of a hot fireball which contains 99 % of all inelastic reactions.

3 Reaction frequency

Structure of hadronic reactions in the fireball can be analyzed with UrQMD. Reaction density for different types of reactions can be calculated with this model. Reactions can be classified by type and number of participants in this reactions (see Table 1) and the contributions of different types of reactions into the system evolution can be explored. For this purpose we analyze the time dependence of reaction frequency for different types, i,

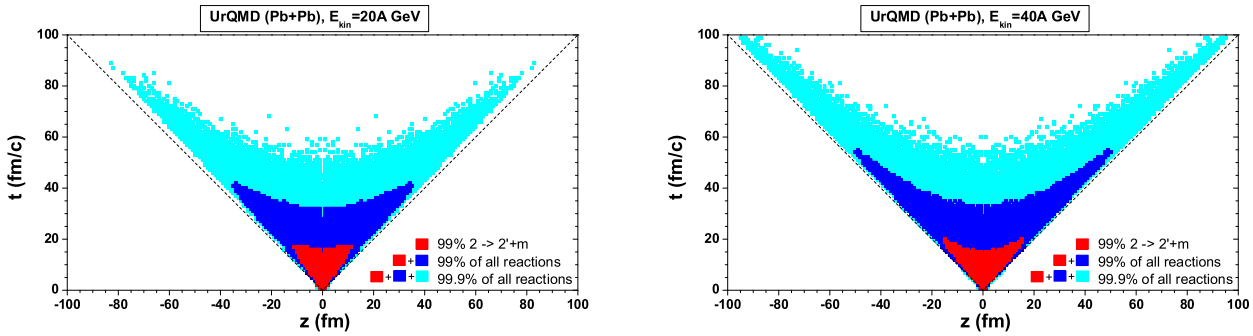

Figure 3. Same as Fig. 2, but for calculations under low SPS conditions (Pb+Pb at 20A GeV and 40A GeV).

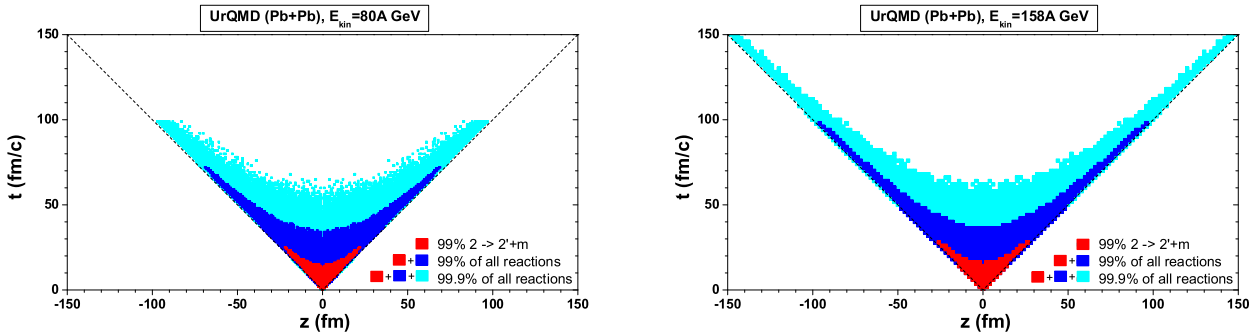

Figure 4. Same as Fig. 2, but for calculations under SPS conditions (Pb+Pb at 80A GeV and 158A GeV).

of reactions:

$$\nu_i(t) = \int_{C_R} dxdydz\, \Gamma_i(t, \mathbf{r}). \tag{6}$$

The results of evaluations of the time dependence of the reaction frequency (6) for AGS and SPS energies are depicted in Figs. 5, 6 and 7. The thick solid line indicates all reaction rates in the fireball, the thin solid line indicates only the elastic scattering of hadrons ($2 \to 2$), the dash-dotted line shows all inelastic reactions ($2 \to 2'+m$, where $m \geq 0$), the dotted line stands for fusion reactions ($2 \to 1'$), and the dashed line distinguishes decays ($1 \to 2' + m, m \geq 0$).

The main feature of the reaction frequency (thick solid lines in Figs. 5-7) is its increase up to $t \simeq 3.9 - 8$ fm/c for AGS energies and $t \simeq 0.84 - 2$ fm/c for SPS energies where it has it's first maximum $t_{\rm m1}$. This can be explained by the increase of the number of nucleons as participants of the reactions, when one nucleus penetrates into another one. The maximum overlap of two nuclei happens when their centers coincide. This time can be estimated as

$$t_c = \frac{R_0}{\gamma}\frac{1}{v}, \tag{7}$$

where R_0 is the nucleus radius, $v = p_{0z}/\sqrt{M_N^2 + p_{0z}^2}$, $\gamma = 1/\sqrt{1 - v^2}$, p_{0z} is the initial nucleon momentum in the c.m. system of two nuclei, and M_N is the nucleon mass. We name t_c as the fireball formation time. The values of t_c (see Table 2) are very close to the time moments which correspond to the first maximum of the reaction frequency (thick solid lines in Figs. 5-7). Slight difference of t_c and the time point of the real maximum can be explained by some decrease of a nucleon velocity which is due to inelastic and elastic reactions (stopping) of nucleons.

For all energies, inelastic and elastic nucleon collisions dominate at the first stage, $t < t_c$, of nucleus-nucleus collision. At later times, the elastic, decay and fusion reactions become more significant. We note that for all energy conditions, the decay processes become the dominant ones after $t \sim 10$ fm/c. After the full overlap of the nuclei, the created system begins to expand in space, which results in the decrease of the reaction rates. At the same time, the number of secondary particles still increases, resulting in an increase of the total reaction integral rate. Hence, the rate of expansion of the system and its ratio to the creation rate of secondary particles will determine the result of the competition of these two tendencies.

The contribution of the secondary particles becomes more significant at the later stage of collision, especially at SPS energies. The number of secondary particles (mainly π mesons) is approximately $\langle n_\pi \rangle \simeq 0.6 - 1.6$ per nucleon for AGS conditions [16] and $\langle n_\pi \rangle \simeq 2 - 6$ for SPS conditions [17, 18]. Such an increase of the number of secondary particles with the collision energy leads to the sufficient change of the reaction frequency's time

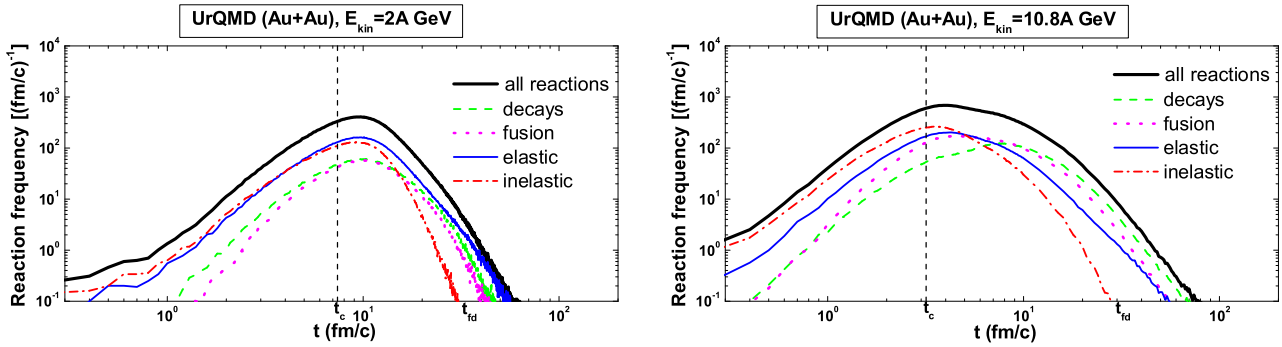

Figure 5. Hadron reaction frequency for AGS conditions (Au+Au at 2 and 10.8A GeV). Different curves correspond to different types of reactions.

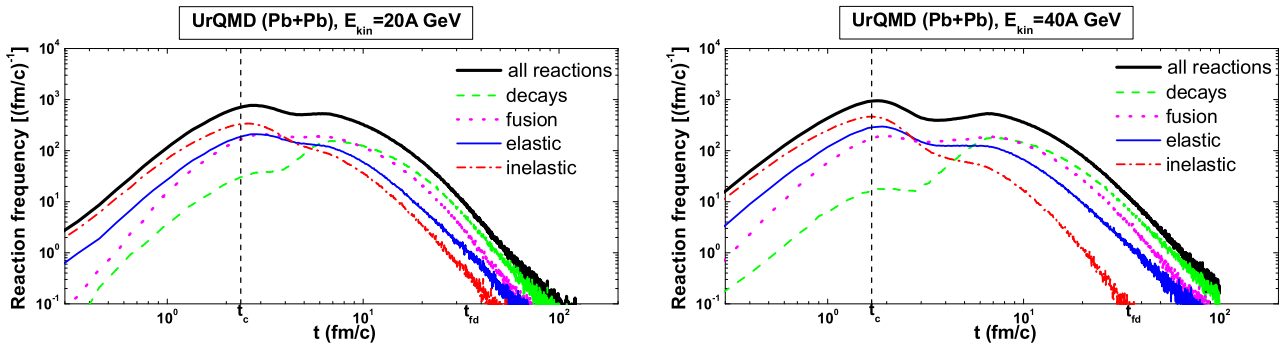

Figure 6. Same as Fig. 5, but for calculations under low SPS conditions (Pb+Pb at 20A GeV and 40A GeV).

dependance. Namely, for AGS conditions after t_c, the the frequency of all reactions goes down. For SPS conditions, one can see the second local maximum of the reaction frequency (see thick solid line in Figs. 6 and 7) at t_{m2} (see Table 2) which is a consequence of a large number of reactions with secondary particles. At later times, the reaction frequency goes down, which results in fireball division into two parts at the time moment $t = t_{\rm fd}$ and the further breakup. The fireball division time is defined as the minimum value of time on the space-like hypersurface, which bounds the region of the cold fireball (blue area) from above, i.e., $t_{\rm fd} \equiv t(z)\big|_{z=0}$ (see Figs. 2-4). This results in an increase of the fireball lifetime:

$$\tau = t_{\rm fd} - t_c\,. \tag{8}$$

We note that the time moment $t_{\rm fd}$ depends very weakly on the collision energy (see Table 2). It is seen that after the time moment $t_{\rm fd}$, the rates of elastic and inelastic reactions vanish. That is, since this moment, the system behavior is determined mainly by the individual properties of particles (basically resonances). That is why, in spite of the sufficient difference of collision energies of the experiments under consideration, the times $t_{\rm fd}$ are approximately the same (see Table 2). If we compare the longitudinal sizes of the fireballs $2R_z$ at the time moment $t = t_{\rm fd}$, we see that they are approximately the same and equal to $R_z = v\,t_{\rm fd}$ [v is defined in Eq. (7), see Figs. 2-4]. This fact can explain the weak dependence of the pion interferometric radius R_L on the beam energy, $R_L \propto R_z$ [19]. It can be claimed that the fireball achieves its maximum longitudinal size at the time moment $t = t_{\rm fd}$, when it is divided into two parts.

4 Discussion and conclusions

Different parameters may be used to analyze the fireball evolution. It can be the energy density, particle density, mean free path etc. In Fig. 8 we show four representations of the fireball which were obtained with making use of the microscopic transport model UrQMD for SPS conditions (Pb-Pb, $E_{\rm kin} = 158$A GeV). First column shows the particle positions of all hadrons at different time moments. In second column the fireball is represented with the help of the energy density. Reaction density at different time moments is shown in third column. One can see that starting from the times $t \approx 25$fm/c the fireball representation given by the reaction density sufficiently differs from the one given by the energy density. For example, it is seen that there are no reactions in the central part of the system at large enough times while energy density there is still high. This situation may occur, e.g., when particles move in the same direction with some collective velocity without collisions. In the fourth column the coordinates of the last reactions of all particles are shown. It is, in fact, a depiction of a continuous kinetic freeze-out. One can see that the fireball representations in the third and fourth columns are qualitatively similar and they differ from one another just in the early stage of a fireball evolution.

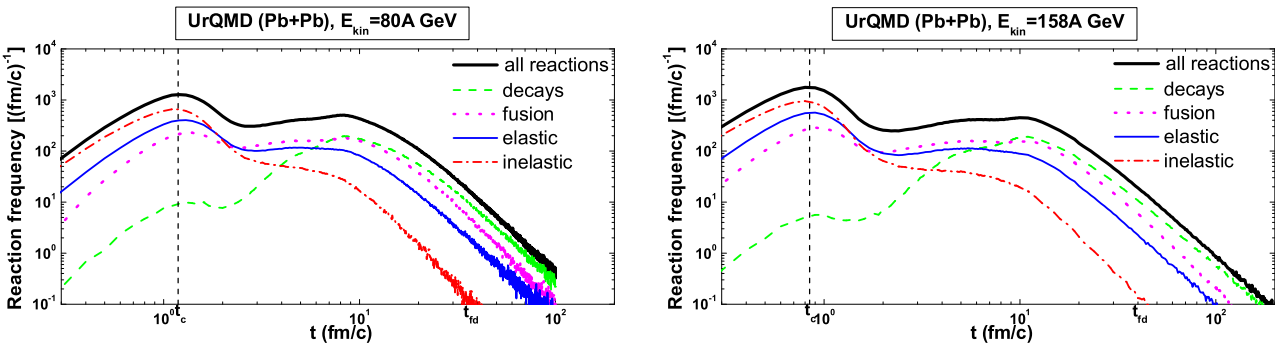

Figure 7. Same as Fig. 5, but for calculations under SPS conditions (Pb+Pb at 80A GeV and 158A GeV).

Table 2. Temporal characteristics of reaction frequency.

$E_{\rm kin}$ (A GeV)	$\sqrt{s_{AA}}$ (A GeV)	$A+A$	t_c (fm/c)	t_{m1} (fm/c)	t_{m2} (fm/c)	t_{fd} (fm/c)
2.0	2.70	$Au+Au$	7.53	9.7		33.0
10.8	4.88		3.21	3.9		30.5
20.0	6.41	$Pb+Pb$	2.38	2.62	6.1	34.0
40.0	8.86		1.68	1.75	6.7	34.5
80.0	12.39		1.19	1.23	8.2	35.0
158.0	17.32		0.85	0.87	10.6	38.5

Our approach allows to investigate the spatial and temporal structures of the hadron system created in relativistic nucleus-nucleus collisions in terms of all hadronic reactions which occur in the system. In other words, the fireball is identified as the system of interacting hadrons. The proposed algorithm gives possibility to separate with a given accuracy the space-time region where the most intensive hadron reactions take place, i.e. we give the method to see a reaction zone in 3D representation (see Fig. 1) and in different projections.

In the present microscopic study, we separate a fireball into the following regions, which characterize its evolution (see Figs. 2-4): (1) a hot fireball region, where 99% of all inelastic hadronic reactions have occurred (medium-gray or red), (2) a cold fireball region (dark-gray or blue), which together with the hot fireball contains 99% of all hadronic reactions $N_{\rm tot}$, and (3) a fireball halo, where 0.9% of all hadronic reactions, i.e., $0.009N_{\rm tot}$, have occurred (light-gray or cyan). Two last regions together are a space-time region containing the hadron-resonance gas, and the reactions in this region are mainly presented by decays of resonances.

The study of hadron reaction zones allows one to analyze the freeze-out process in relativistic nucleus-nucleus collisions. An important question that can be clarified by the study of the reaction zones is how the space-time boundary of a fireball is related to the so-called sharp freeze-out hypersurface. In the literature, the sharp freeze-out hypersurface is usually defined with the help of some parameter $P(t,\mathbf{r})$ which takes the critical value P_c on the hypersurface. That is, the equation of the hypersurface has form $P(t,\mathbf{r})=P_c$. As such a parameter, one may choose the energy density $\epsilon(t,\mathbf{r})$ [5], temperature $T(t,\mathbf{r})$ [20, 21], particle density $n(t,\mathbf{r})$ [22], etc. And the "classical" definition of the sharp kinetic freeze-out assumes the Cooper-Frye picture [23]: a radiation of free particles or a freeze out process takes place within a thin layer determined by the hypersurface. I.e. the initial value problem for the radiation corresponds to a space-like piece of the hypersurface whereas the boundary conditions for the radiative system correspond to a time-like part of the hypersurface. On the other hand, if we determine the reaction zone as that one, which contains, for instance, 99% of all reactions, then we can claim that the sharp kinetic freeze-out hypersurface should be definitely inside the boundary between the zone of a cold fireball and the fireball halo (see Figs. 2-4).

Assuming that the chemical freeze-out occurs when the inelastic reactions are completed (see Ref. [24]), we can also claim that the chemical freeze-out hypersurface should be inside the reaction zone, which contains 99% of all inelastic reactions (red zone).

In the coordinates (t, z), the curve, which is the upper space-like boundary of the "blue" zone, is a hyperbola of the form $t(z)=A\sqrt{\tau_0{}^2+z^2}$, wher $A=0.65$, $\tau_0=46$ fm/c for the AGS energy ($E_{\rm kin}=10.8A$ GeV) and $A=0.95$, $\tau_0=38$ fm/c for the SPS energy ($E_{\rm kin}=158A$ GeV). It is clear that the *fireball division time* is related to the parameters of the hyperbola in the following way $t_{\rm fd}=A\,\tau_0$ and we obtain $t_{\rm fd}\approx 30$ fm/c for AGS ($E_{\rm kin}=10.8A$ GeV) and $t_{\rm fd}\approx 36$ fm/c for SPS ($E_{\rm kin}=158A$ GeV). The lower time-like hypersurface bounding a cold fireball has the form of a straight line $t(z)=t_0+\frac{1}{v}z$, where t_0 is close to zero, and $v=0.8$ for AGS energies and $v=0.98$ for SPS energies. For AGS energies, the time-like boundaries of the reaction zones differ significantly from one another and the light cone (see Fig. 2). However, at higher SPS energies, for example, at $E_{\rm kin}=158A$ GeV, the time-like hypersurfaces bounding all three zones of a fireball practically coincide with

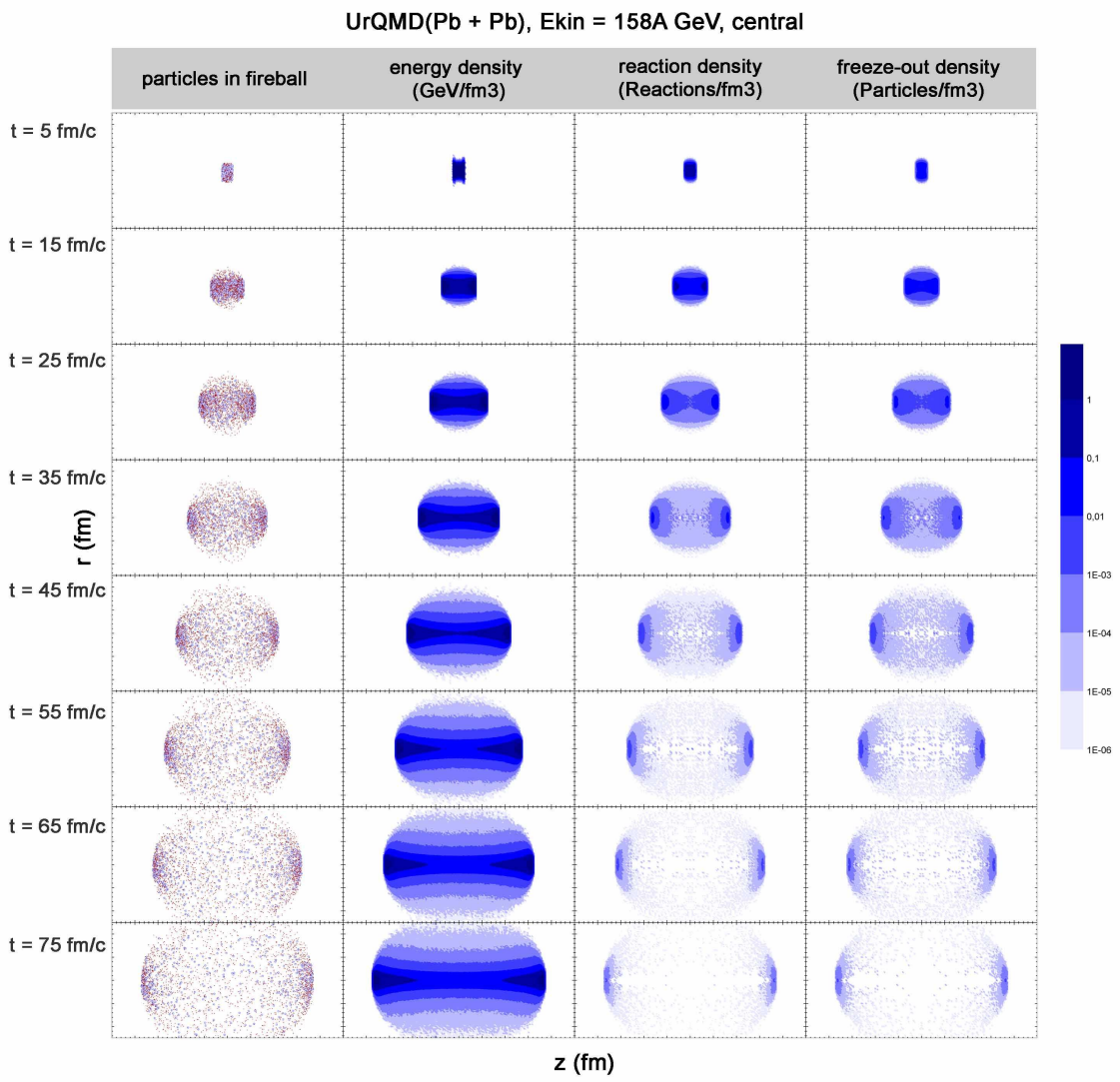

Figure 8. Different fireball representations for SPS conditions, $E_{\rm kin} = 158$A GeV.

one another and are close to the light cone (see Fig. 4). Thus, we can predict that this behavior will result in all time-like hypersurfaces merging on the energies available at the BNL Relativistic Heavy Ion Collider (RHIC) and coinciding with the light cone.

By studying the time dependence of the reaction frequency for different reaction types, we conclude that total reaction rate is dominated by elastic and inelastic hadron collisions at the early stage, whereas individual particles properties (basically resonances) determine system behavior at later stages. We also conclude that there are two specific time points in the evolution of a hadron fireball: the fireball formation time t_c defined as the time of the full overlap of two nuclei [Eq. (7)] and the fireball division time $t_{\rm fd}$, which corresponds to the separation of the fireball into two individual parts and which depends weakly on the collision energy (see last column in Table 2). At SPS energies there is also a second local maximum t_{m2} which is a consequence of a large number of reactions involving secondary particles.

References

[1] R. Baier, A.H. Mueller, *et al.*, Phys. Lett. B **502**, 51 (2001) [hep-ph/0009237].
[2] P. Arnold, J. Lenaghan, G.D.Moore, and L.G.Yaffe, Phys. Rev. Lett. **94**, 072302 (2005) [nucl-th/0409068].
[3] A. Rebhan, P. Romatschke, and M. Strickland, Phys. Rev. Lett. **94**, 102303 (2005) [hep-ph/0412016].
[4] P.F. Kolb, U. Heinz, [nucl-th/0305084].
[5] V.N. Russkikh and Y.B. Ivanov, Phys. Rev. C **76**, 054907 (2007) [nucl-th/0611094].
[6] T. Csorgo, *et al.*, Phys. Lett. B **565**, 107 (2003) [nucl-th/0305059].
[7] D. Molnar and M. Gyulassy, Phys. Rev. C **62**, 054907 (2000) [nucl-th/0005051].
[8] A. Kisiel, W. Florkowski, W. Broniowski, and J. Pluta, Phys. Rev. C **73**, 064902 (2006) [nucl-th/0602039].

[9] S.A. Bass and A. Dumitru, Phys. Rev. C **61**, 064909 (2000) [nucl-th/0001033].
[10] D. Teaney, J. Lauret and E. V. Shuryak, [nucl-th/0110037].
[11] B. Tomasik and U.A. Wiedemann, Phys. Rev. C **68**, 034905 (2003) [nucl-th/0207074].
[12] C.M. Hung and E. Shuryak, Phys. Rev. C **57**, 1891 (1998) [hep-ph/9709264].
[13] D. Anchishkin, A. Muskeyev, and S. Yezhov, Phys. Rev. C **81**, 031902 (2010) [nucl-th/1004.0431].
[14] S.A. Bass *et al.*, Prog. Part. Nucl. Phys. **41**, 225 (1998) [nucl-th/9803035].
[15] M. Bleicher *et al.*, J. Phys. G **25**, 1859 (1999).
[16] J. L. Klay *et al.* (E895 Collaboration), Phys. Rev. C **68**, 054905 (2003).
[17] C. Alt *et al.* (NA49 Collaboration), Phys. Rev. C **77**, 024903 (2008).
[18] S. V. Afanasiev *et al.* (NA49 Collaboration), Phys. Rev. C **66**, 054902 (2002) [nucl-ex/0205002].
[19] J. Chen (for STAR Collaboration), in CPOD2009 *Proceedings*, PoS (CPOD2009)047 (SISSA, Trieste, Italy, 2009) [nucl-ex/0910.0556].
[20] H. von Gersdorff, L. McLerran, M. Kataja, and P.V. Ruuskanen, Phys. Rev. D **34**, 794 (1986).
[21] P. Huovinen, Eur. Phys. J. A **37**, 121 (2008) [0710.4379].
[22] D. Adamova, *et al.* (CERES Collaboration), Phys. Rev. Lett. **90**, 022301 (2003), [nucl-ex/0207008].
[23] F. Cooper and G. Frye, Phys. Rev. D **10** 186 (1974).
[24] U. Heinz, Nucl. Phys. A **661**, 349 (1999); Nucl. Phys. A **685**, 414 (2001).

Proceedings of the International School-seminar
"New Physics and Quantum Chromodynamics at External Conditions", pp. 13 – 20,
3-6 May 2011, Dnipropetrovsk, Ukraine

THERMODYNAMICS OF QUARK-GLUON PLASMA AND LATTICE QCD

V. V. Begun[a,1,2], M. I. Gorenstein[b,1,2], O. A. Mogilevsky[1]

[1]Bogolyubov Institute for Theoretical Physics, Kiev, Ukraine
[2]Frankfurt Institute for Advanced Studies, Frankfurt, Germany

We consider modifications of the bag model that allow to describe the quark-gluon plasma equation of state (EoS) obtained in the lattice QCD calculations. The best fit of the EoS for SU(3) gluon plasma is found in the model with linear in temperature term in the pressure function. The best fit of the full QCD EoS with $2+1$ quarks is found however in the model with quadratic in temperature term in the pressure and energy density. The bag constant is found to be negative in both gluon plasma and quark-gluon plasma.

1 Introduction

A transition to the deconfined phase of quarks and gluons, the quark-gluon plasma (QGP), is expected at high temperature and/or baryonic density (see, e.g., Ref.[1] and references therein). In the present study of the QGP equation of state (EoS) we consider the system with zero values of all conserved charges. This is approximately valid for the QGP created in nucleus-nucleus collisions at the BNL RHIC and even better for future experiments at the CERN LHC. Up to now, the strongly interacting matter EoS could be only calculated from the first principles within the lattice QCD. These calculations are done for zero or very small values of the baryonic chemical potential. The QGP exists at high temperatures $T > T_c$, where the critical temperature T_c corresponds to the 1^{st} order phase transition in the pure SU(3) gluodynamics or to a smooth crossover in the full QCD. The main results for the QCD deconfined matter EoS can be illustrated by the Monte Carlo (MC) lattice results (LR) for the energy density $\varepsilon(T)$ and pressure $p(T)$ in the SU(3) gluodynamics [2]. The qualitative features of the EoS at $T > T_c$ can be summarized as follows (see Figs. 1 and 2):

1. The pressure $p(T)$ is very small at the critical temperature, $p(T_c)/T_c^4 \ll 1$, and rapidly increases at $T > T_c$.
2. At high T the system reaches the ideal massless gas behavior $p \cong \varepsilon/3$, thus, $\varepsilon(T) \cong \sigma T^4$.
3. The constant σ which regulates the high temperature behavior is however about $(10\div20)\%$ smaller than the Stefan-Boltzmann (SB) constant $\sigma_{SB} = 8\pi^2/15$ shown by the dotted horizontal line in Fig. 1.
4. Both ε/T^4 and $3p/T^4$ approach the value σ from below.
5. The interaction measure $(\varepsilon - 3p)/T^4$, called also the trace anomaly, demonstrates a prominent maximum at $T \cong 1.1\ T_c$ as seen in Fig. 2.

Note that these properties of the gluon plasma EoS are also valid in the full QCD [3, 4].

The bag model (BM) [5] was invented to describe the mass spectrum of the hadron states. Soon after that it was suggested [6] to interpret the bag constant B as the non-perturbative energy density term in the deconfined matter EoS. For several decades, the BM EoS has been used to describe the QGP (see, e.g., [7]). In its simplest form, i.e., for non-interacting massless constituents and zero values of all conserved charges, the BM EoS reads:

$$\varepsilon(T) \;=\; \sigma_{SB}\, T^4 \;+\; B\;, \qquad p(T) \;=\; \frac{\sigma_{SB}}{3}\, T^4 \;-\; B\;, \tag{1}$$

where ε and p have a simple dependence on T modified by adding the bag constant B ("vacuum pressure"). The SB constant in Eq. (7) is $\sigma_{SB} = \pi^2/30\ \ (d_B + 7d_F/8)$, where d_B and d_F are the degeneracy factors for the massless bosons (gluons) and fermions (quarks and anti-quarks), respectively.

We study the modifications of the bag model EoS and consider simple analytical parameterizations for the QGP EoS which include a linear and/or quadratic in T terms in the pressure function. This is done to satisfy the qualitative properties listed above. The quantitative comparison with the MC LR in the SU(3) gluodynamics [2] and in the full QCD with dynamical quarks [4] will be done in Sec 2 and Sec 3, respectively. The summary is presented in Sec 4. See also Refs. [8] and [9].

e-mail: [a]viktor.begun@gmail.com, [b]goren@bitp.kiev.ua

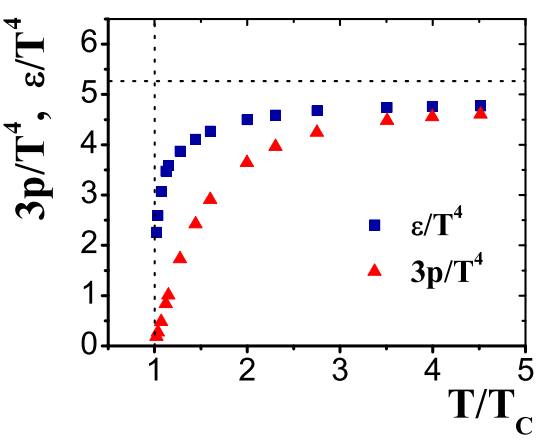

Figure 1. The MC LR [2] in the SU(3) gluodynamics at $T > T_c$ for ε/T^4 and $3p/T^4$ extrapolated to infinite continuous system.

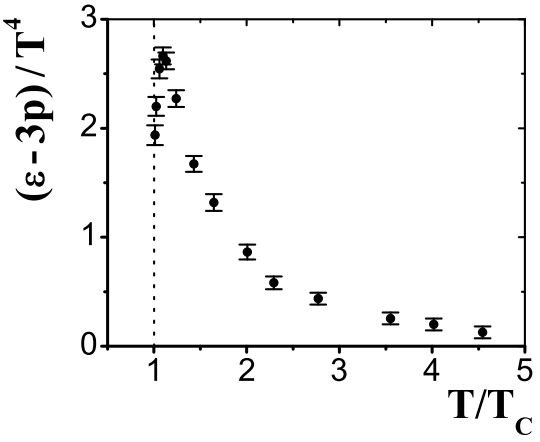

Figure 2. The MC LR [2] in the SU(3) gluodynamics at $T > T_c$ for the interaction measure $(\varepsilon - 3p)/T^4$ for the lattice $32^3 \times 8$.

2 Gluon Plasma Equation of State

In this Section a quantitative comparison of the modified versions of the BM EoS is done with the MC LR [2] in the pure SU(3) gluodynamics. The ε/T^4 and $3p/T^4$ were obtained in [2] by extrapolation to an infinite continuous system. We take the MC values of these extrapolated functions ε/T^4 and $3p/T^4$ at the same T/T_c points where the interaction measure $(\varepsilon - 3p)/T^4$ has been simulated on the finite lattice $32^3 \times 8$. To determine the parameters of different models we minimize the sums of the square deviations at these T/T_c points for $(\varepsilon - \varepsilon_{MC})/T^4$ and/or $3(p - p_{MC})/T^4$, where ε, p are the model functions and ε_{MC}, p_{MC} are the MC LR.

The recent lattice estimate for the pressure at very high temperatures $T/T_c \cong 10^7$ is still about 3% below the SB limit [10]. The lowest order perturbative calculations give $(\sigma_{SB} - \sigma) \propto g^2(T) \propto 1/\ln(T/\Lambda)$. The calculations within the perturbative re-summation scheme [11] are comparable with the LR at $T = (3 \div 4)\, T_c$ and suggest that the dominant effect of interactions is to turn massless quarks and gluons into weakly interacting quasiparticles.

The quasiparticle approach of Ref. [12] (see also recent papers [13] and references therein) treats the system of interacting gluons as a gas of non-interacting quasiparticles with gluon quantum numbers, but with mass $m(T)$ which depends on T. The particle energy ω and momentum k are assumed to be connected as $\omega = \left[k^2 + m^2(T)\right]^{1/2}$. The energy density and pressure take then the following form [12]:

$$\varepsilon(T) \;=\; \frac{d}{2\pi^2} \int_0^\infty k^2 dk \; \frac{\omega}{\exp(\omega/T) \;-\; 1} \;+\; B^*(T) \;\equiv\; \varepsilon_0(T,\omega) \;+\; B^*(T)\;, \tag{2}$$

$$p(T) \;=\; \frac{d}{6\pi^2} \int_0^\infty k^2 dk \; \frac{k^2}{\omega} \; \frac{1}{\exp(\omega/T) \;-\; 1} \;-\; B^*(T) \;\equiv\; p_0(T,\omega) \;-\; B^*(T)\;, \tag{3}$$

where the degeneracy factor $d = 2(N_c^2 - 1)$ equals 16 for the SU(3) gluodynamics. The thermodynamical relation

$$T \frac{dp}{dT} \;-\; p(T) \;=\; \varepsilon(T) \tag{4}$$

leads to the equation for the function $B^*(T)$

$$\frac{dB^*}{dT} \;=\; -\; \frac{\Delta_0(T,\omega)}{m} \; \frac{dm}{dT}\;, \tag{5}$$

where $\Delta_0 \equiv \varepsilon_0 \;-\; 3p_0$, and ε_0, p_0 defined by Eqs. (2,3) are the ideal gas expressions for massive bosons. If the function $m(T)$ is known one can calculate $B^*(T)$ up to an arbitrary integration constant B. The simplest linear mass dependence, $m = aT$, where a is a temperature independent parameter, is the correct assumption at high temperatures $T > 2T_c$. For $m = aT$, the function $B^*(T)$ derived from Eq. (5) equals to [8]:

$$B^*(T) \;=\; B - \; \frac{1}{4}\, \Delta_0(T,\omega)\;. \tag{6}$$

One obtains the energy density (2) and the pressure (3)

$$\varepsilon(T) \;=\; \sigma\, T^4 \;+\; B\;, \qquad p(T) \;=\; \frac{\sigma}{3}\, T^4 \;-\; B\;. \tag{7}$$

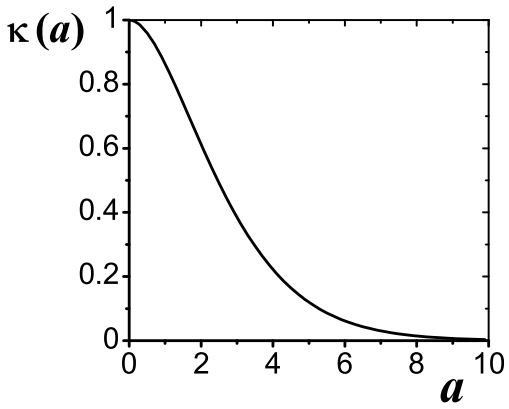

Figure 3. The suppression factor $\kappa(a)$ from Eq. (8) as a function of the parameter a.

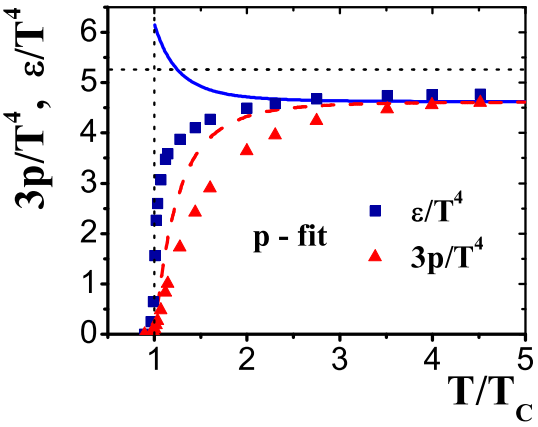

Figure 4. The fit of $3p/T^4$ with the BM EoS (7) gives $\sigma = 4.62$ and $B = 1.56\ T_c^4$.

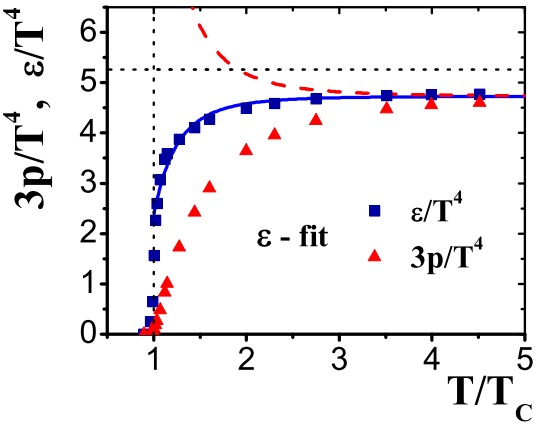

Figure 5. The fit of ε/T^4 with the BM EoS (7) gives $\sigma = 4.73$ and $B = -\ 2.37\ T_c^4$.

Equation (7) has the form of the BM (1) with constant σ equal to

$$\sigma \;=\; \frac{3d}{2\pi^2}\sum_{n=1}^{\infty}\left[\frac{a^2}{n^2}\,K_2(na)\;+\;\frac{a^3}{4n}\,K_1(na)\right] \;\equiv\; \kappa(a)\;\sigma_{SB}\;. \tag{8}$$

The K_1 and K_2 in Eq. (8) are the modified Bessel functions. The constant σ in Eq. (7) includes the suppression factor $\kappa(a)$. For $a \to 0$, it follows $\kappa \to 1$, and Eq. (7) coincides with Eq. (1). The function $\kappa(a)$ decreases monotonously and goes to zero at $a \to \infty$ as presented in Fig. 3. This allows to modify the SB constant and fit the high temperature behavior of $\varepsilon(T)$ and $p(T)$ with $\sigma < \sigma_{SB}$.

Our starting point is the BM EoS (7) with B and σ being free model parameters independent of temperature. The LR [2] cover the temperature range $(0.89 \div 4.5)T_c$. We consider the high temperature phase (gluon plasma) at $T > T_c$, where T_c is a point of the first order phase transition. To be precise, let us note that we use the MC LR [2] for $T > 1.02\ T_c$ to avoid the uncertainties at $T = T_c$ where $\varepsilon(T)$ has a discontinuity in thermodynamical limit. The fit of the MC LR for $3p/T^4$ gives $\sigma = 4.62$ and $B = 1.56\ T_c^4$, and it is shown by the dashed line in Fig. 4. The dotted vertical and horizontal lines correspond to $T/T_c = 1$ and to the Stefan-Boltzmann constant $\sigma_{SB} = 8\pi^2/15$, respectively. The solid shows ε/T^4 for the BM EoS (7). One observes a correct behavior, $3p/T^4 \cong \sigma$, at high T and an abrupt drop near the critical temperature, $3p(T_c)/T_c^4 \approx 0$. These features of $p(T)$ are in a qualitative agreement with the LR. A quantitative agreement is however unsatisfactory. Moreover, the temperature dependence of ε/T^4 calculated by Eq. (7) with $\sigma = 4.62$ and $B = 1.56\ T_c^4$ appears to be in a qualitative contradiction with the MC LR.

One can alternatively start from fitting the MC LR for the energy density function $\varepsilon(T)$ with Eq. (7). Unexpectedly, one obtains a rather good agreement with MC LR for ε/T^4 admitting *negative* values of the bag constant B . The negative bag constant $B = -\ 2.37\ T_c^4$ and $\sigma = 4.73$ needed in Eq. (7) to fit ε/T^4 leads, however, to an incorrect behavior of p/T^4 (see the dashed line in Fig. 5).

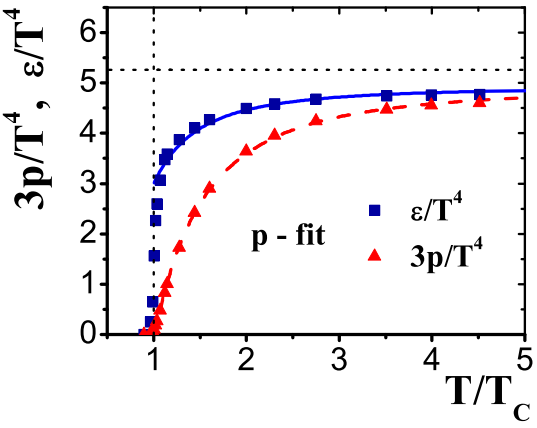

Figure 6. The fit of $3p/T^4$ with the C-BM EoS (9) gives $\sigma = 4.92$, $B = -0.13\ T_c^4$, and $C = 1.8\ T_c^2$.

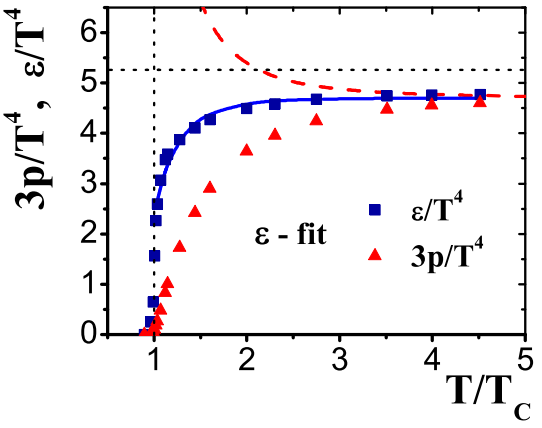

Figure 7. The fit of ε/T^4 with the C-BM EoS (9) gives $\sigma = 4.69$, $B = -2.64\ T_c^4$, and $C = -0.28\ T_c^2$.

A modification of the BM EoS (7) was considered by Pisarski [14]:

$$\varepsilon(T) \ = \ \sigma\, T^4 \ - \ C\, T^2 \ + \ B\ , \quad p(T) \ = \ \frac{\sigma}{3}\, T^4 \ - \ C\, T^2 \ - \ B\ . \tag{9}$$

A presence of the T^2-terms in $p(T)$ and $\varepsilon(T)$ has been further studied in recent papers [15]. For brevity, we will refer to Eq. (9) as the "C-bag model" (C-BM). The fit of the MC LR for p/T^4 with the C-BM EoS (9) is presented in Fig. 6. It gives, $\sigma = 4.92$, $B = -\ 0.13\ T_c^4$, and $C = 1.8\ T_c^2$. One finds an agreement of the C-BM EoS (9) with the LR for $3p/T^4$. In particular, $3p(T_c)/T_c^4 \approx 0$. However, $\varepsilon(T_c)/T_c^4 \approx 3$, which exceeds the LR. Trying to improve the quantitative agreement with the LR, one may start from fitting the ε/T^4 with Eq. (9). One observes indeed a better agreement for ε/T^4 with the parameters $B = -\ 2.64\ T_c^4$ and $C = -\ 0.28\ T_c^2$, being very different from those found in the fitting of $3p/T^4$. These new values of B and C lead, however, to a qualitative disagreement of Eq. (9) with $3p/T^4$ LR, as shown by the dashed line in Fig. 7.

Comparing the BM EoS (7) and C-BM EoS (9) with the MC LR we have faced the serious challenge. Very different values of model parameters, B for Eq. (7), or B and C for Eq. (9), have been found depending on whether we start from fitting $3p/T^4$ or from ε/T^4 . By admitting negative values of the bag constant B in Eq. (7) or Eq. (9), one obtains a good fit of ε/T^4 in the whole temperature interval $T > T_c$, but finds a disagreement with LR for $3p/T^4$, as seen from Fig. 5 and Fig. 7. This finding looks contra-intuitive in view that the functions $\varepsilon(T)$ and $p(T)$ are in the one-to-one correspondence to each other due to the thermodynamical consistency equation (4). In Figs. 8-9 we show the differences between the pressure functions $p(T)$ calculated in the BM EoS (7) or in the C-BM (9), with parameters obtained from the fit of ε/T^4, and the MC LR for pressure $p_{MC}(T)$. The difference of the pressures is divided by T_c^4 . From Figs. 8-9 one clearly observes a linear temperature dependence of $(p - p_{MC})/T_c^4$. The thermodynamical relation (4) does connect the functions $\varepsilon(T)$ and $p(T)$. This connection is, however, not symmetric in the two directions. If the function $p(T)$ is known, one finds $\varepsilon(T)$ from Eq. (4) in a unique way. However, if the function $\varepsilon(T)$ is known, Eq. (4) is the first order differential equation for the function $p(T)$. The general solution of this equation involves an arbitrary integration constant. This results in a linear in temperature term in the function $p(T)$. Thus, for $\varepsilon(T)$ in the form of Eq. (7), a general solution of Eq. (4) for $p(T)$ can be written as follows:

$$\varepsilon(T) \ = \ \sigma\, T^4 \ + \ B\ , \qquad p(T) \ = \ \frac{\sigma}{3}\, T^4 \ - \ B \ - A\, T\ . \tag{10}$$

The term $-A\,T$ with an arbitrary constant A corresponds to a general solution of the homogeneous equation $T dp/dT - p = 0$ as was noticed in Refs. [16, 17]. For brevity we call the EoS (10) the "A-bag model" (A-BM). The A-BM EoS (10), in contrast to the BM EoS (7) and C-BM EoS (9), gives essentially the same values of the model parameters σ, B, and A either one starts from fitting $3p/T^4$ or from ε/T^4. Figures 10-13 demonstrate a good agreement of the A-BM (10) with the MC LR for the thermodynamical functions ε/T^4, $3p/T^4$, and $3s/(4T^3)$ (where $s = (\varepsilon + p)/T$ is the entropy density), interaction measure, $(\varepsilon - 3p)/T^4$, the ratio p/ε, and speed of sound squared, $c_s^2 = dp/d\varepsilon$. For the A-BM EoS (10), $(\varepsilon - 3p)/T^4$ does not depend on the parameter σ whereas the entropy density $s(T)$ does not depend on the bag parameter B.

Let us consider the EoS which includes both $C\,T^2$ and $A\,T$ terms,

$$\varepsilon(T) \ = \ \sigma\, T^4 \ - \ C\, T^2 \ + \ B\ , \qquad p(T) \ = \ \frac{\sigma}{3} T^4 \ - \ C\, T^2 \ - \ A\, T \ - \ B\ , \tag{11}$$

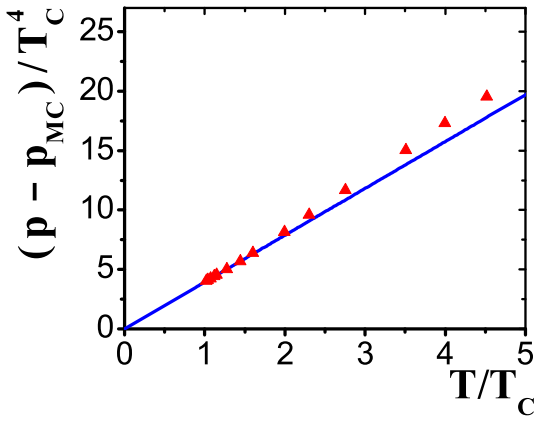

Figure 8. A difference of the model pressure p and the MC LR p_{MC} divided by T_c^4. Pressure p is given by the BM EoS (7) with $\sigma = 4.73$ and $B = -2.37\ T_c^4$. The Solid line presents the linear function $3.94\ T/T_c$.

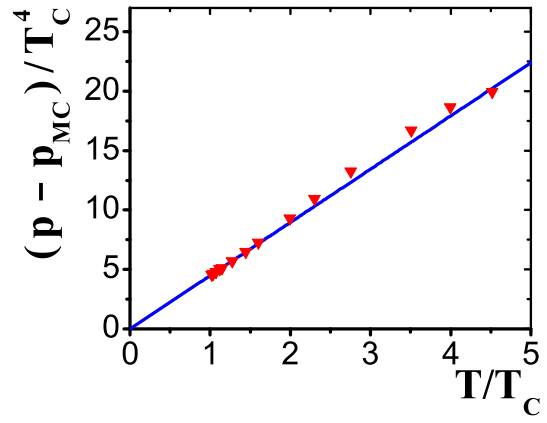

Figure 9. A difference of the model pressure p and the MC LR p_{MC} divided by T_c^4. Pressure p, given by the C-BM EoS (9) with $\sigma = 4.69$, $B = -2.64\ T_c^4$, and $C = -0.28\ T_c^2$. The solid line presents the linear function $4.48\ T/T_c$.

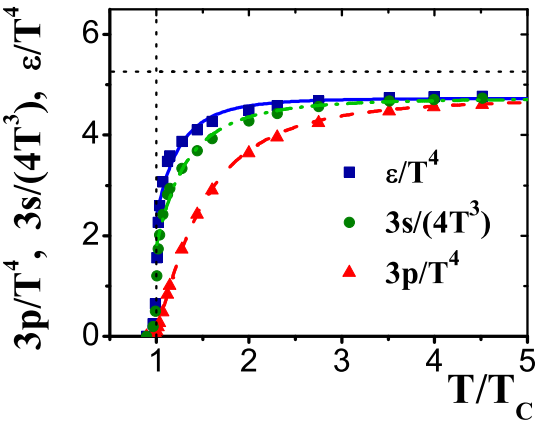

Figure 10. The fit of MC LR in the SU(3) gluodynamics [2] by the A-BM EoS (lines) with $\sigma = 4.73,\ A = 3.94\ T_c^3,\ B = -2.37\ T_c^4$.

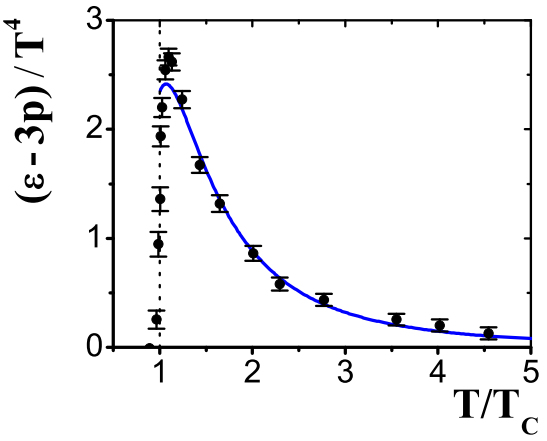

Figure 11. The fit of interaction measure $(\varepsilon - 3p)/T^4$. by the A-BM EoS (lines) with $\sigma = 4.73,\ A = 3.94\ T_c^3,\ B = -2.37\ T_c^4$.

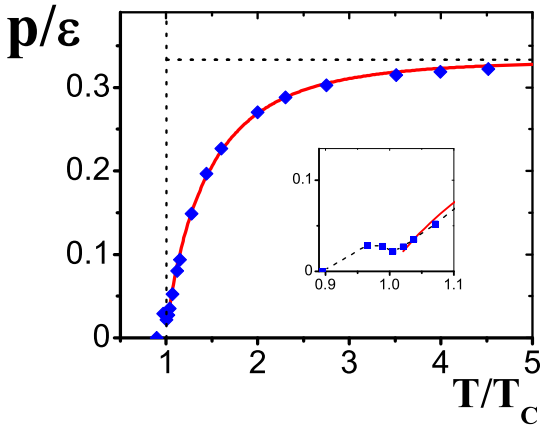

Figure 12. The same fit as in Fig. 10 for the ratio p/ε. The dotted horizontal line corresponds to $p/\varepsilon = 1/3$.

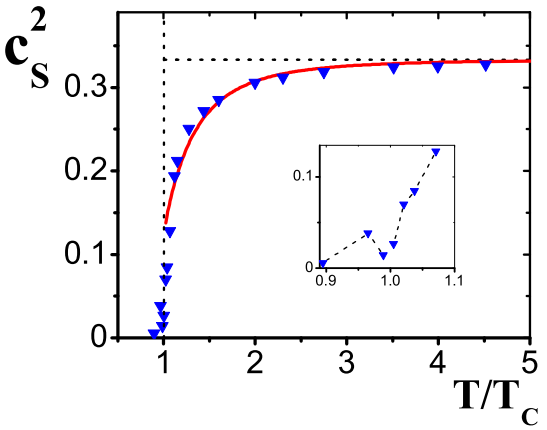

Figure 13. The same fit as in Fig. 10 for the speed of sound squared c_s^2. The dotted horizontal line corresponds to $c_s^2 = 1/3$

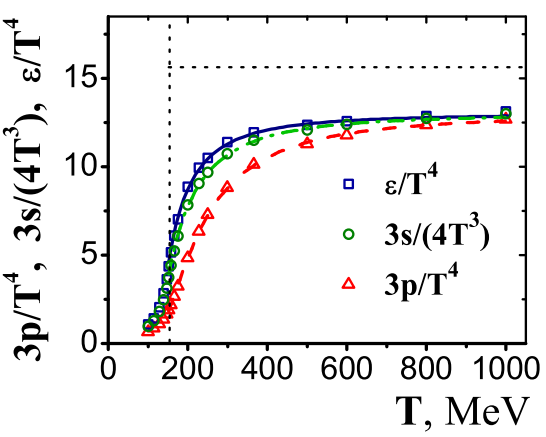

Figure 14. The fit of MC LR for the $2+1$ QCD EoS [4] by the C-BM (9) (lines) with $\sigma = 13.01$, $C = 6.06\ T_i^2$, and $B = -2.34\ T_i^4$.

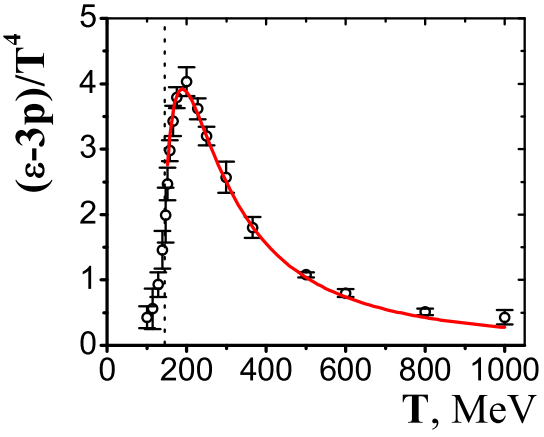

Figure 15. The fit of MC LR for the interaction measure $(\varepsilon - 3p)/T^4$ by the C-BM (9) (lines) with $\sigma = 13.01$, $C = 6.06\ T_i^2$, and $B = -2.34\ T_i^4$.

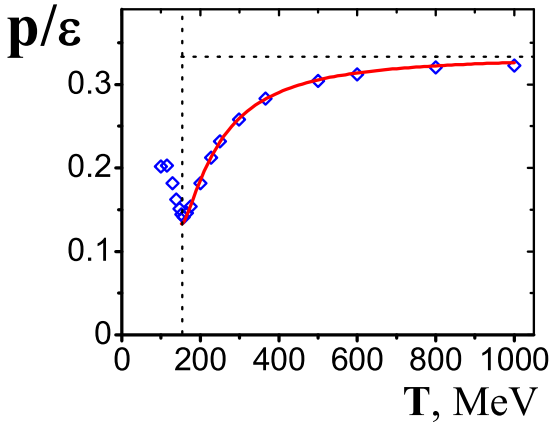

Figure 16. The same fit as in Fig. 14 for the pressure to energy density ratio p/ε. Horizontal line shows $p/\varepsilon = 1/3$.

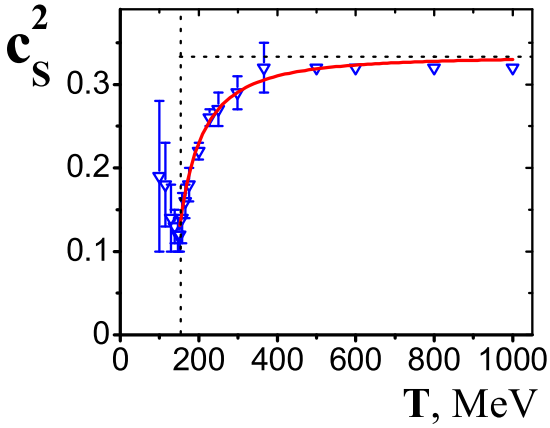

Figure 17. The same fit as in Fig. 14 for the speed of sound squared c_s^2. Horizontal line shows $c_s^2 = 1/3$.

referred to as the AC-BM. The standard BM EoS (7) corresponds to $A = C = 0$, whereas the C-BM EoS (9) and A-BM EoS (10) correspond to $A = 0$ and $C = 0$ in Eq. (11), respectively. A comparison of the AC-BM EoS (11) with the MC LR for the ε/T^4 and $3p/T^4$ in SU(3) gluon plasma leads to $C/T_c^2 \ll 1$. We thus conclude that the AC-BM (11) for the gluon plasma is reduced to the A-BM EoS[1] (10).

A physical origin of the linear in T term requires further studies. In this connection we remind the famous problem of Gribov copies [19] and his suggestion of the modified gluon dispersion relation, $\omega(k) = \sqrt{k^2 + M^4/k^2}$, where M is a QCD mass scale. It was shown in Ref. [20] that at $T \gg M$ this dispersion relation gives the SB limit $\varepsilon/T^4 = 3p/T^4 = \sigma_{SB}$ and power corrections of relative order $1/T^3$ for p/T^4 and $1/T^4$ for ε/T^4 . This also resembles the cut-off K phenomenological model [21] where the low-momentum gluons with $k < K$ are assumed to be suppressed, $\omega(k) = k\ \theta(k - K)$, but high-momentum gluons are effectively free.

3 Quark Gluon Plasma Equation of State

The LR for the equation of state in the QCD with 2+1 flavors (light u-, d- and heavier s-quarks) have been presented by "Wuppertal-Budapest" [3, 4] collaboration. The continuum estimates of the LR results for p/T^4, $(\varepsilon - 3p)$, and c_s^2 in the temperature range 100 MeV$< T <$1000 MeV are presented in Table 5 of Ref. [4]. At the highest available temperatures one observes the ideal gas behavior, $p \cong \varepsilon/3$, but constant $\sigma \cong \varepsilon/T^4$ is about 20% smaller than the SB constant $\sigma_{SB} \cong 15.63$. This behavior is similar to the case of SU(3) gluodynamics. At small temperatures, $T = 100 \div 140$ MeV, the LR are expected to be smoothly connected with the thermodynamical functions of the hadron-resonance gas.

[1]Note that the lattice study of SU(N_c) gluodynamics with $N_c = 3,\ 4,\ 5,\ 6$, and 8 colors performed in Ref. [18] reveals that $3p/T^4$ and ε/T^4 divided by the corresponding SB limits follow essentially the same curves for different N_c .

In contrast to the pure SU(3) gluodynamics with the first order phase transition between glueballs and gluons, the transition from hadrons to quarks and gluons is a crossover. This smooth transition takes place in the narrow temperature range, $T = 150 \div 200$ MeV where the energy density increases strongly. Several characteristic temperature points of the crossover transition are presented in Ref. [4]: T=145(5) MeV at the minimum value of $c_s^2(T)$, $T \equiv T_i$=152(4) MeV at the inflection point of $(\varepsilon - 3p)/T^4$, T=159(5) MeV at the minimum value of p/ε, $T \equiv T_{max}$=191(5) MeV at the maximum of $(\varepsilon - 3p)/T^4$. None of these temperatures is the critical one, and the model fit of the QGP thermodynamical functions does not depend too much on the choice of particular starting point in the range $T = 150 \div 200$. However, the hadron-resonance gas expected at low temperatures gives a concave shape of the interaction measure $(\varepsilon - 3p)/T^4$, while the LR [4] show a convex shape near the maximum at $T \equiv T_{max}$=191 MeV. Thus we use the LR [4] above the inflection temperature $T > T_i$=152 MeV in our model analysis[2]. This temperature will be also used to present the model parameters.

Within the AC-BM (11) we fit the $3p/T^4$ and ε/T^4 LR for the high temperature QGP phase. The best fit corresponds to negligible values of the linear temperature term, $A/T_i^3 \ll 1$. Thus, in contrast to our analysis of the LR in the pure SU(3) gluodynamics, the AC-BM (11) is reduced to the C-BM EoS (9) for QGP LR. The found model parameters are equal to: $\sigma = 13.01$, $C = 6.06\ T_i^2$, and $B = -2.34\ T_i^4$. A comparison of the C-BM (9) with LR [4] at $T > 152$ MeV is shown in Figs. 14-17. In Fig. 14 the vertical dotted line shows $T = T_i$=152 MeV and horizontal line shows the SB constant $\sigma_{SB} = \pi^2/30(16 + 63/2) \simeq 15.63$. It demonstrates a good agreement of the C-BM (9) with the LR for the QGP. In particular, the model leads to the maximum position $T_{max} \cong 189$ MeV and the value of $(\varepsilon - 3p)/T_{max}^4 \cong 4$ which are very close to the LR.

4 Summary

We have considered the modifications of the bag model EoS. They are constructed to satisfy the qualitative features expected for the QGP EoS. We make also the quantitative comparisons with the MC lattice results for the SU(3) gluon plasma [2] and for high temperature equation of state with 2+1 dynamical quarks [4]. Our modification of the bag model equation of state includes the following features: a suppression of the Stephan-Boltzmann constant; linear or quadratic in temperature term in the pressure function; a negative sign of the bag constant. These features are needed to describe the lattice data. The best fit of the LR for thermodynamical functions in SU(3) gluon plasma are found within the A-bag model (10). This model corresponds to: $\varepsilon = \sigma T^4 + B$, $p = \sigma T^4/3 - AT - B$. A linear in T term in the pressure function is admitted by the thermodynamical relation (4) between $\varepsilon(T)$ and $p(T)$. The expression for the energy density looks formally the same as in the standard bag model (7). A principal difference from the standard bag model is a *negative* value of the bag constant B .

The quantitative comparison with the MC lattice results for high temperature equation of state with 2+1 dynamical quarks [4] shows the best fit of the thermodynamical functions for the QGP within the C-bag model (9): $\varepsilon = \sigma T^4 - CT^2 + B$, $p = \sigma T^4/3 - CT^2 - B$. This model also requires $B < 0$ to fit the lattice data. Note that a negative value of B found for the gluon plasma and QGP does not contradict to the bag model hadron spectroscopy [5] which requires $B > 0$ at zero temperature.

Acknowledgements. We thank M. Gaździcki, W. Greiner, V.P. Gusynin, P. Huovinen, L.L. Jenkovszky, O. Linnyk, O. Kaczmarek, E. Megias, L.M. Satarov, H. Satz, and Y. Schröder for fruitful discussions. V.V. Begun thanks the Alexander von Humboldt Foundation for support. This work was in part supported by the Program of Fundamental Research of the Department of Physics and Astronomy of NAS, Ukraine.

References

[1] S. Sarkar, H. Satz, B. Sinha (Editors) *The Physics of the Quark-Gluon Plasma. Introductory Lectures*, Lect. Notes Phys. 785 (Springer, Berlin-Heidelberg, 2010).
[2] G. Boyd *et al.* Phys. Rev. Lett. **75**, 4169 (1995) and Nucl. Phys. B **469**, 419 (1996).
[3] Y. Aoki *et al.* Phys. Lett. B **643**, 46 (2006) [arXiv:0609068[hep-lat]]; Y. Aoki, et al, JHEP **0906**, 088 (2009) [arXiv:0903.4155].
[4] S. Borsanyi *et al.*, [Wuppertal-Budapest Collaboration], JHEP **1009**, 073 (2010) [arXiv:1005.3508]; S. Borsanyi *et al.*, JHEP **1011**, 077 (2010) [arXiv:1007.2580].
[5] A. Chodos *et al.*,Phys. Rev. D **9**, 3471 (1974).
[6] J. Baacke, Acta Phys. Polon. B **8**, 625 (1977).
[7] E.V. Shuryak, Phys. Rep. **61**, 71 (1980); J. Cleymans, R.V. Gavai, and E. Suhonen, *ibid.* **130**, 217 (1986).
[8] V.V. Begun, M.I. Gorenstein, and O.A. Mogilevsky, Ukr. J. Phys. **55**, 1049 (2010) [arXiv:1001.3139];
[9] V.V. Begun, M.I. Gorenstein, and O.A. Mogilevsky, Int. J. Mod. Phys. E **20** (2011) [arXiv:1004.0953v3].
[10] G. Endrodi,*et al.*, PoS **LAT2007**, 228 (2007) [arXiv:0710.4197].

[2] A precise matching of the hadron-resonance gas and LR is beyond the scope of this paper. The discussion of this procedure can be found in Ref. [22].

[11] J. P. Blaizot, E. Iancu and A. Rebhan, Phys. Rev. D **63**, 065003 (2001); Nucl Phys. A **698**, 404 (2002); *Quark gluon plasma*, World Scientific, Editors Hwa R.C. et al., 60-122 (2004) [arXiv:hep-ph/0303185].
[12] M.I. Gorenstein and S.N. Yang. Phys. Rev. D **52**, 5206 (1995).
[13] M. Bluhm and B. Kämpfer, Phys. Rev. D **77** 0344004 (2008), *ibid.* **77**, 114016 (2008); F.G. Gardim and F.M. Steffens, Nucl. Phys. A **825**, 222 (2009) [arXiv:0905.0667]; F. Brau and F. Buisseret, Phys. Rev. D **79**, 114007 (2009) [arXiv:0902.4836].
[14] R.D. Pisarski, Phys. Rev. D **74**, 121703 (2006) [arXiv:hep-ph/0608242]; Prog. Theor. Phys. Suppl. **168**, 276 (2007) [arXiv:hep-ph/0612191].
[15] E. Megias, E.R. Arriola and L.L. Salcedo, Phys. Rev. D **75**, 105019 (2007) [arXiv:hep-ph/0702055]; O. Andreev, Phys. Rev. D **76**, 087702 (2007) [arXiv:0706.3120]; E. Megias, E.R. Arriola and L.L. Salcedo, Phys. Rev. D **80**, 056005 (2009) [arXiv:0903.1060].
[16] C.G. Kallman, Phys. Lett. B **134**, 363 (1984).
[17] M.I. Gorenstein and O.A. Mogilevsky, Z. Phys. C **38**, 161 (1988).
[18] M. Panero, Phys. Rev. Lett. **103**, 232001 (2009).
[19] V.N. Gribov, Nucl. Phys. B **139**, 1 (1978).
[20] D. Zwanziger, Phys. Rev. Lett. **94**, 182301 (2005).
[21] F. Karsch, Z. Phys. C **38**, 147 (1988); D. Rischke *et al.*, M. Gorenstein, A. Schäfer, H. Stöcker, and W. Greiner, Phys. Lett. B **278**, 19 (1992).
[22] P. Huovinen and P. Pétreczky, Nucl. Phys. A **837**, 26 (2010).

Proceedings of the International School-seminar
"New Physics and Quantum Chromodynamics at External Conditions", pp. 21 – 28,
3-6 May 2011, Dnipropetrovsk, Ukraine

THE ROLE OF BAG SURFACE TENSION IN COLOR CONFINEMENT

K. A. Bugaev[a], A. I. Ivanytskyi[b]

Bogolyubov Institute for Theoretical Physics, Kiev, Ukraine

We discuss here the novel view at the color confinement which, on the one hand, allows us to find out the surface tension coefficient of quark gluon bags and, under a plausible assumption, to determine the endpoint temperature of the QCD phase diagram, on the other hand. The present model considers the confining color tube as the cylindrical quark gluon bag with non-zero surface tension. A close inspection of the free energies of elongated cylindrical bag and the confining color tube that connects the static quark-antiquark pair allows us to find out the string tension in terms of the surface tension, thermal pressure and the bag radius. Using the derived relation it is possible to estimate the bag surface tension at zero temperature directly from the lattice QCD data and to estimate the (tri)critical endpoint temperature. In the present analysis the topological free energy of the cylindrical bag is accounted for the first time. The requirement of positive entropy density of such bags leads to negative values of the surface tension coefficient of quark gluon bags at the cross-over region, i.e. at the continuous transition to deconfined quarks and gluons. We argue that the cross-over existence at supercritical temperatures in ordinary liquids is also provided by the negative surface tension coefficient values. It is shown that the confining tube model naturally accounts for an existence of a very pronounced surprising maximum of the tube entropy observed in the lattice QCD simulations, which, as we argue, signals about the fractional surface formation of the confining tube. In addition, using the developed formalism we suggest the gas of free tubes model and demonstrate that it contains two phases.

1 Introduction

A new paradigm of heavy ion phenomenology that the quark gluon plasma (QGP) is a strongly interacting liquid [1] proved to be very successful not only in describing some of its properties measured by lattice quantum chromodynamics (QCD), but also in explaining some experimental observables that cannot be reproduced otherwise. Probably, the two most striking conclusions obtained within the new paradigm are as follows: first, at the cross-over temperature, where the string tension of color tube is almost vanishing, the potential energy of color charge is of the order of a few GeV [2], i.e. it is 10 times larger than its kinetic energy, and, second, the QGP, so far, is the most perfect fluid since its shear viscosity in units of the entropy density is found to be the smallest one [3, 4]. The first of these conclusions tells us that at the cross-over region there is no color charge separation [5], whereas the second one naturally explains the great success of ideal hydrodynamics when applied to relativistic heavy ion collisions.

Here we would like to discuss the recent progress achieved in our understanding of both the confinement phenomenon [6, 7] and the physical origin of the cross-over [8, 9, 10, 11, 12]. As we demonstrate below such a progress was made possible after realizing a principal role played by negative values of the surface tension coefficient of large QGP bags [6, 8]. Also here we argue that the negative values of the surface tension, that are responsible for an existence of the cross-over transition to QGP at low baryonic densities, play the same role in ordinary liquids. Moreover, in this work we would like to draw an attention to the problem of the temperature dependence of surface tension coefficient in liquids by clearly showing that for many liquids the well known Guggenheim relation (see Eq. (10)) is not so well established experimentally as it is usually believed.

The work is organized as follows. Section 2 is devoted to the confining tube model, in which the Fisher topological term of the QGP bag free energy is accounted for. In section 3 we show that at the cross-over region the surface tension of QGP bags is necessarily negative and argue that this is the case for ordinary liquids as well. The maximum of the tube entropy observed in lattice QCD is explained in section 4, where the model of gas of free tubes is also developed. The conclusions are given in the last section.

2 Color confining tube and sQGP

A color confinement, i.e. an absence of free color charges, is usually described by the free energy of heavy (static) quark-antiquark pair $\boldsymbol{F_{q\bar{q}}(T,L) = \sigma_{str} \cdot L}$. In the lattice QCD the functional dependence of $F_{q\bar{q}}(T,L)$ on the temperature T and the separation distance L can be extracted from the Polyakov line correlation in a color singlet channel. Then it is customary to define

e-mail: [a]bugaev@th.physik.uni-frankfurt.de, [b]a_iv_@ukr.net

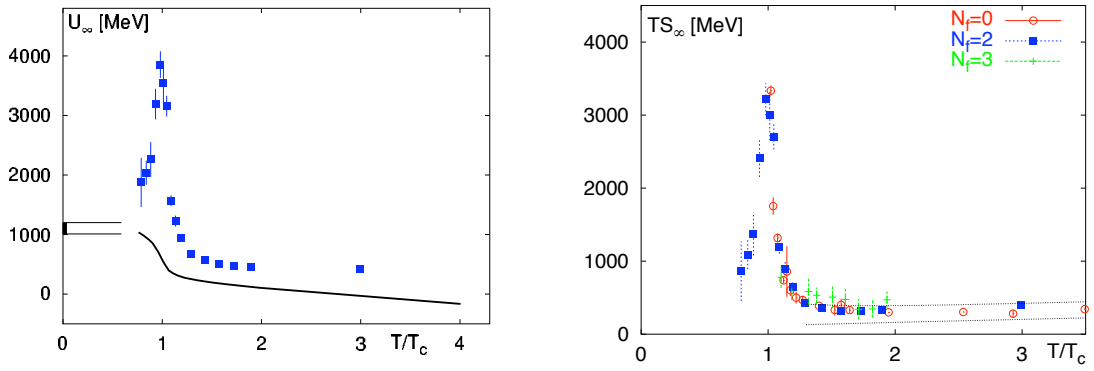

Figure 1. The internal energy U_∞ (left) and entropy S_∞ (right) of confining tube connecting two static color charges found by lattice QCD simulations for infinite separation distance between charges [2]. The internal energy is shown for 2 quark flavors.

- **confinement:** the case of non-zero string tension, i.e. $\boldsymbol{\sigma_{str} > 0}$;
- **deconfinement:** the case of vanishing string tension $\boldsymbol{\sigma_{str} \to 0}$ at $T \to T_{co}$, but one should remember that there is no color charge separation up to $T \geq 1.3\, T_{co}$ values of the cross-over temperature T_{co} [1, 5].

The explanation of the latter is as follows: although at large distances $L \to \infty$ the potential energy of static $q\bar{q}$ pair is finite $U_{q\bar{q}}(T, L) = F_{q\bar{q}} - T\frac{\partial F_{q\bar{q}}}{\partial T} = F_{q\bar{q}} + TS_{q\bar{q}}$ near T_{co}, the values of $U(T, \infty)$ are very large (see Fig. 1). From Fig. 1 one can conclude that near T_{co} region QGP is a strongly interacting plasma (sQGP) which is similar to a liquid, since the ratio of the quark potential energy to its kinetic energy, the so called plasma parameter, $\frac{U(T,\infty)}{3\,T} \in 1 - 10$ has the range of values that is typical for ordinary liquids [1].

The second striking feature of the confining tube can be seen in the right panel of Fig. 1 which clearly demonstrates that at $T = T_{co}$ the entropy of static $q\bar{q}$ pair is very large $S_{q\bar{q}}(T_{co}, \infty) \approx 20$. Such a value signals that really a **huge number of degrees of freedom** $\sim \exp(20)$ is involved, but the origin of large energy $U_{q\bar{q}}(T, \infty)$ and entropy $S_{q\bar{q}}(T, \infty)$ values near T_{co} for awhile remained **mysterious** [1] despite many attempts to explain it.

Another problem of principal importance for phenomenological models of deconfinement phase transition [8, 9, 10, 11, 12, 13, 14, 15] is the value of the surface tension coefficient σ_{surf} of QGP bags. There are several estimates for the surface tension coefficient σ_{surf} of QGP bags [16], but the question is whether can we determine σ_{surf} from lattice QCD? Therefore, in this section we consider an approach that allows us to determine the surface tension coefficient of QGP bags directly from the lattice QCD. As it will be shown in the section 4 such an approach naturally explains an existence of the 'mysterious maximum' [1] of the confining tube entropy.

In order to estimate the surface tension of QGP bags let us consider the static quark-antiquark pair connected by the unbreakable color tube of length L and radius $R \ll L$. In the limit of large L the free energy of the color tube is $F_{str} \to \sigma_{str} L$. Now we consider the same tube as an elongated cylinder of the same radius and length [6]. In this case we neglect the free energy of the regions around the color charges, but for our treatment of large separation distances $L \gg R$ this is sufficient. For the cylinder free energy we use the standard parameterization [8, 9, 10, 11, 12]

$$F_{cyl}(T, L, R) = -p_v(T)\pi R^2 L + \sigma_{surf}(T) 2\pi R L + T\tau \ln\left[\frac{\pi R^2 L}{V_0}\right], \tag{1}$$

where $p_v(T)$ is the bulk pressure inside a bag, $\sigma_{surf}(T)$ is the temperature dependent surface tension coefficient, while the last term on the right hand side above is the Fisher topological term [17] which is proportional to the Fisher exponent $\tau = const > 1$ [8, 9, 10, 11, 12, 15] and $V_0 \approx 1$ fm^3 is a normalization constant. Since we consider the same object then its free energies calculated as the color tube and as the cylindrical bag should be equal to each other. Then for large separating distances $L \gg R$ one finds the following relation

$$\sigma_{str}(T) = \sigma_{surf}(T)\, 2\pi R \; - \; p_v(T)\pi R^2 + \frac{T\tau}{L} \ln\left[\frac{\pi R^2 L}{V_0}\right]. \tag{2}$$

In doing so, in fact, we match an ensemble of all string shapes of fixed L to a mean elongated cylinder, which according to the original Fisher idea [17] and the results of the Hills and Dales Model (HDM) [18, 19] represents a sum of all surface deformations of such a bag. The last equation allows one to determine the T-dependence of bag surface tension as

$$\sigma_{surf}(T) = \frac{\sigma_{str}(T)}{2\pi R} \; + \; \frac{1}{2}\, p_v(T) R \; - \; \frac{T\tau}{2\pi R L} \ln\left[\frac{\pi R^2 L}{V_0}\right], \tag{3}$$

if $R(T)$, $\sigma_{str}(T)$ and $p_v(T)$ are known. This relation opens a principal possibility to determine the bag surface tension directly from the lattice QCD simulations for any T. Also it allows us to estimate the surface tension at $T = 0$. Thus, taking the typical value of the bag model pressure which is used in hadronic spectroscopy $p_v(T = 0) = -(0.25)^4$ GeV^4 and inserting into (3) the lattice QCD values $R = 0.5$ fm and $\sigma_{str}(T = 0) = (0.42)^2$ GeV^2 [20], one finds $\sigma_{surf}(T = 0) = (0.2229 \text{ GeV})^3 + 0.5\, p_v\, R \approx (0.183 \text{ GeV})^3 \approx 157.4$ MeV fm^{-2} [6]. The last term in (3) does not modify our above estimate at $T = 0$, but, in contrast to [6, 7], we keep it in order to demonstrate its importance for the confining tube with free color charges.

The found value of the bag surface tension at zero temperature is very important for the phenomenological equations of state of strongly interacting matter in two respects. Firstly, according to HDM the obtained value defines the temperature at which the bag surface tension coefficient changes the sign [18, 19, 7]

$$T_\sigma = \sigma_{surf}(T = 0)\, V_0^{\frac{2}{3}} \cdot \lambda^{-1} \ \in \ [148.4;\ 157.4] \text{ MeV}\,, \tag{4}$$

where the constant $\lambda = 1$ for the Fisher parameterization of the T-dependent surface tension coefficient [17] or $\lambda \approx 1.06009$, if we use the parameterization derived within the HDM for surface deformations [18, 19, 7]. Secondly, according to one of the most successful models of liquid-gas phase transition, i.e. the Fisher droplet model (FDM) [17] the surface tension coefficient linearly depends on temperature. This conclusion is well supported by HDM and by microscopic models of vapor-liquid interfaces [21]. Therefore, the temperature T_σ in (4), at which the surface tension coefficient vanishes, is also the temperature of the (tri)critical endpoint T_{cep} of the liquid-gas phase diagram. On the basis of these arguments in Ref. [7] we concluded that the value of QCD critical endpoint temperature is $T_{cep} = T_\sigma = 152.9 \pm 4.5$ MeV. Hopefully, the latter can be verified by the lattice QCD simulations using Eq. (3).

Now the question is what is the surface tension coefficient above T_{cep}, i.e. at supercritical temperatures. There are no experimental data on usual liquids in this region. In FDM and in the other well known model of liquid-gas phase transition, the statistical multifragmentation model (SMM) [22, 23, 24], the surface tension at supercritical temperatures is assumed to be zero, while in other models such a question is usually not discussed. The only exceptions known to us are the exactly solvable statistical models of quark gluon bags with surface tension [8, 9], their extension which includes the finite widths of large/heavy QGP bags [10, 11, 12] and recently formulated generalization of the SMM [25]. For all these models it was demonstrated that the negative surface tension is the only physical reason of degeneration of the 1-st order phase transition into cross-over at supercritical temperatures. The question is whether the above suggested formalism can support such a conclusion.

3 Surface tension coefficient at the cross-over temperature

The above results, indeed, allow us to tune the interrelation with the color tube model and to study the bag surface tension near the cross-over to QGP. Consider first the vanishing baryonic densities. The lattice QCD data indicate that at large R the string tension behaves as

$$\sigma_{str} \ = \ \frac{\ln\left(L/L_0\right)}{R^2} g_0\,, \tag{5}$$

where $L_0 > 0$ and $g_0 > 0$ are some positive constants. Assuming the validity of Eq. (5) in the infinite available volume, one finds that for $\sigma_{str}(T) \to +0$ the string radius diverges, i.e. $R \to \infty$.

Using Eqs. (1) and (3) we can write the total pressure p_{tot} of the cylinder as follows

$$\begin{aligned} p_{tot}(L, R, T) \ &= \ p_v(T) - \frac{\sigma_{surf}(T)}{R} - \frac{T\tau}{\pi R^2 L} \equiv \frac{\sigma_{surf}(T)}{R} - \frac{\sigma_{str}}{\pi R^2} + \frac{T\tau}{\pi R^2 L}\left[\ln\left(\frac{\pi R^2 L}{V_0}\right) - 1\right] \\ &= \ \frac{\sigma_{surf}(T)}{R} - \frac{g_0 \ln\left(L/L_0\right)}{\pi R^4} + \frac{T\tau}{\pi R^2 L}\left[\ln\left(\frac{\pi R^2 L}{V_0}\right) - 1\right]. \end{aligned} \tag{6}$$

This equation shows that for fixed separation distance L in the limit $\sigma_{str}(T) \to +0$ the leading term is given by the surface tension contribution, while the next to leading term corresponds to the contribution of the Fisher topological term, whereas the second term on the right hand side of (6) is the smallest one. Therefore, it is evident that for small values of string tension (and large R) the main contribution to the total pressure and to its temperature derivative is given by the first term on the right hand side of (6).

To calculate the total entropy density s_{tot} of the cylinder let us parameterize the string tension as

$$\sigma_{str} = \sigma^0_{str}\, t^\nu \tag{7}$$

where $t \equiv \frac{T_{co} - T}{T_{co}} \to +0$ and $\nu = const > 0$. From (7) it follows $R = \left[\frac{g_0 \ln(L/L_0)}{\sigma^0_{str} t^\nu}\right]^{\frac{1}{2}}$ and then for $t \to 0$ the

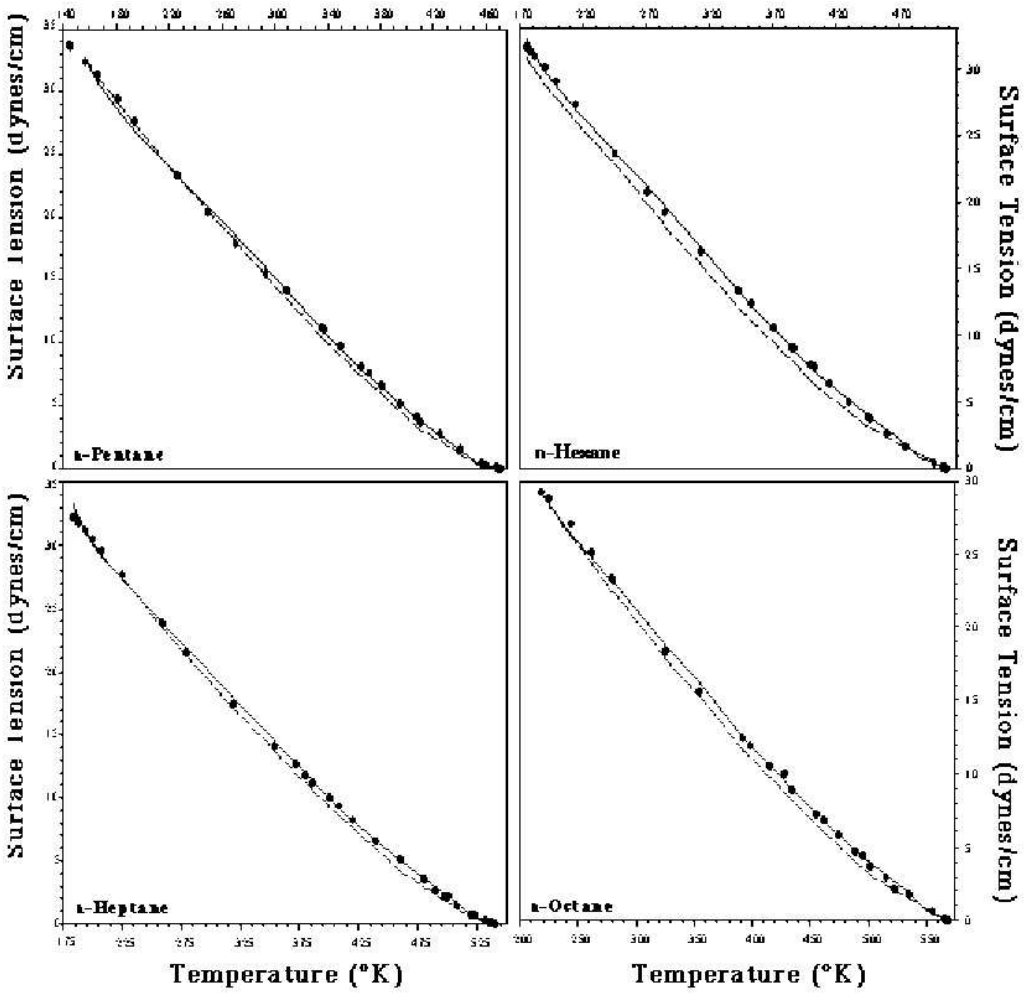

Figure 2. Surface tension of normal paraffins as a function of temperature from the triple point to the critical point. The filled circles indicate the experimental data [30]. The lines are the different theoretical parameterizations [28].

entropy density s_{tot} can be found from (6) and (7) as

$$s_{tot} = \left(\frac{\partial\, p_{tot}}{\partial\, T}\right)_{\mu} \to \underbrace{-\frac{\nu}{2\,R\,T_{co}}\,\frac{\sigma_{surf}}{t}}_{dominant\ \ since\ \ t\to\,0} + \frac{1}{R}\frac{\partial\,\sigma_{surf}}{\partial\,T} \to -\,\frac{\nu}{2\,T_{co}}\left[\frac{\sigma^{0}_{str}}{g_0 \ln\left(L/L_0\right)}\right]^{\frac{1}{2}}\frac{\sigma_{surf}}{t^{1-\nu/2}} \;>\; 0\,. \quad (8)$$

This equation shows that at $T = T_{co}$ the entropy density diverges for $\nu < 2$ and also that at the cross-over region the surface tension coefficient must be negative otherwise the system would be thermodynamically unstable since its entropy density would be negative.

Clearly, the results (1)–(8) are valid for nonzero baryonic chemical potential μ up to the (tri)critical endpoint. The main modification in (1)–(8) is an appearance of μ-dependences of $p_v(T,\mu)$ and $T_{co}(\mu)$ [6]. In the (tri)critical endpoint vicinity the behavior of p_{tot} and s_{tot} is defined by the T-dependence of the surface tension coefficient.

We stress that there is nothing wrong or unphysical with the negative values of surface tension coefficient, since $\sigma_{surf}\,2\pi RL$ in (1) is **the surface free energy** and, hence, as any free energy, it contains the energy part E_{surf} and the entropy part S_{surf} multiplied by temperature T, i.e. $F_{surf} = E_{surf} - TS_{surf}$ [18, 19]. Therefore, at low temperatures the energy part dominates and the surface free energy is positive, whereas at high temperatures the number of configurations of a cylinder with large surface drastically increases and the surface free energy becomes negative since $S_{surf} > \frac{E_{surf}}{T}$. Moreover, the exactly solvable models with phase transition and cross-over [8, 9, 10] have region of negative surface tension coefficient and they clearly show that the only reason why the 1-st order deconfinement phase transition degenerates into a cross-over at low baryonic densities is the negative values of σ_{surf} at this region and the above results independently prove this fact.

We believe that the same is true for many ordinary liquids otherwise one has to search for an alternative explanation for the disappearance of the 1-st order liquid-gas phase transition at the supercritical temperatures.

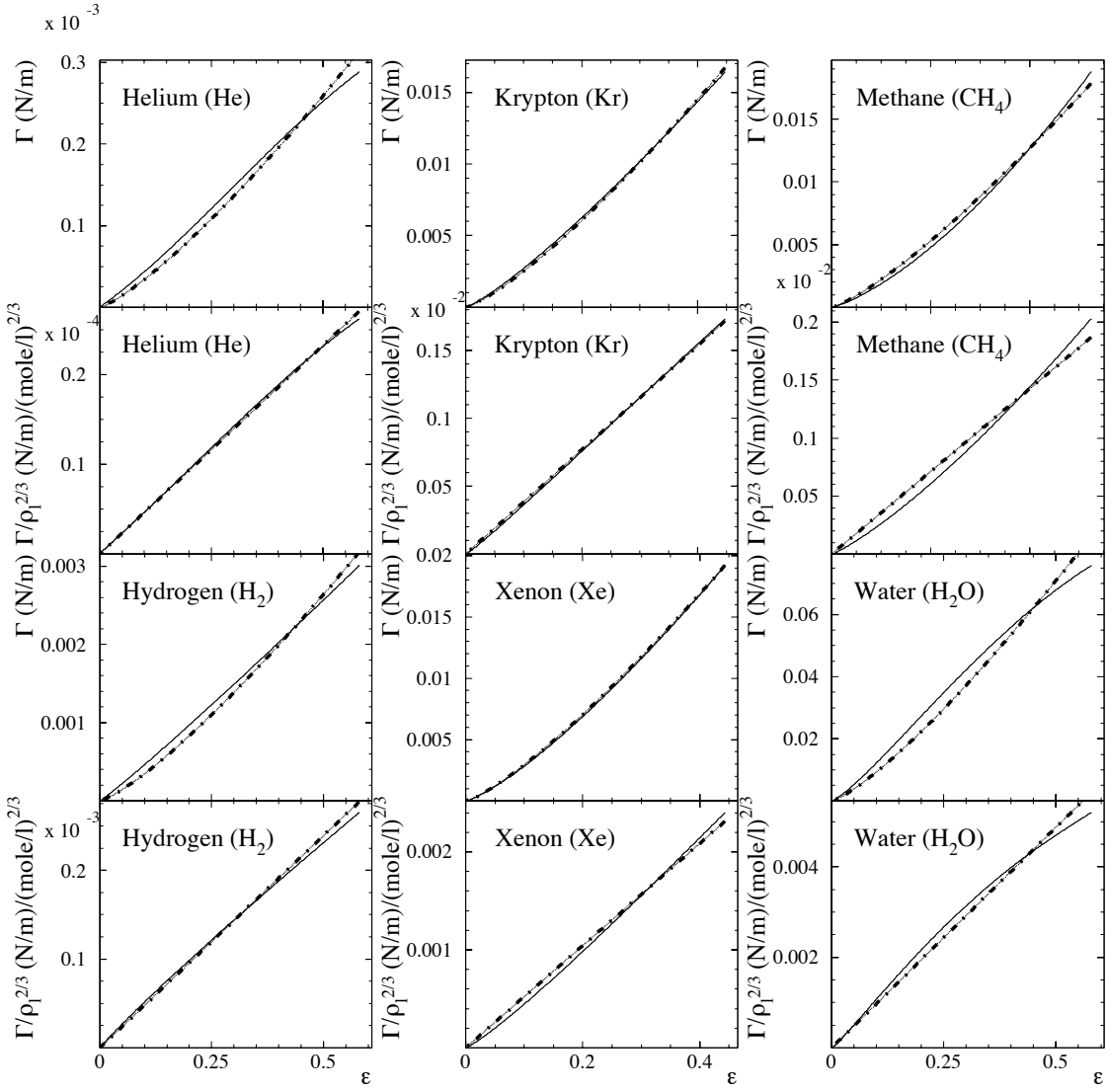

Figure 3. The surface tension Γ (in N/m) in terms of cluster surfaces (first and third rows) and the surface tension $\Gamma/\rho_l^{2/3}$ (in $(N/m)/(mole/l)^{2/3}$) in terms of cluster number (second and fourth rows)) as a function of $\varepsilon = (T_c - T)/T_c$ for: quantum fluids (hydrogen and helium), noble gases (krypton and xenon) and more complex fluids (methane and water). The thin solid lines show data points [33] and the heavy dashed-dotted lines over the thin line show fits to $\Gamma = \Gamma_0\, \rho_l^{2/3} \varepsilon^{2n}$ and $\Gamma/\rho_l^{2/3} = \Gamma_0\, \varepsilon$ according to Eqs. (10) and (9), respectively.

Of course, the experimental data in this region do not exists, but, nevertheless, there is indirect evidence for an existence of negative values of the surface tension coefficient at the supercritical temperatures. To demonstrate the validity of this statement we have to remind that the modern experimental data on the temperature dependence of the surface tension do not allow one to definitely conclude what is T-dependence at the vicinity of critical temperature T_c. In fact there are two alternative prescriptions [26, 27]

$$\text{Eötvös rule}: \quad \frac{\sigma_{surf}}{\rho_l^{\frac{2}{3}}} = a_E (T_c - T)\,, \tag{9}$$

$$\text{Guggenheim rule}: \quad \frac{\sigma_{surf}}{\rho_l^{\frac{2}{3}}} = a_G (T_c - T)^n \quad \text{with} \quad n \approx \frac{11}{9}\,, \tag{10}$$

where ρ_l is the temperature dependent particle density of the liquid phase.

After the Guggenheim work [26] the prescription (10) became a dominant one [28]. Sometimes there appeared even confusions. Thus, in [29] the authors determined the surface tension of water from the triple point to critical point and parametrized it by the polynomial of 9-th power $\sigma_{surf}(T) = \sum_{l=1}^{9} a_l\,(T_c - T)^l$, but then the same authors refitted it to the prescription (10) [30]. Here in Fig. 2 which is taken from [28] we show the temperature

dependence of some paraffins. As one can see for n-Pentane and n-Heptane the data on temperature dependence of surface tension near the critical point, indeed, may show the nonlinear behavior similar to (10), but for the n-Hexane and n-Octane one can see the linear T-dependence of Eq. (9)!

Therefore, in order to clarify this issue a few years ago a thorough analysis [32] of the high quality NIST data [33] was performed. Some of the results are shown in Fig. 3 which is taken from Ref. [32]. As one can see from Fig. 3 for most of the analyzed liquids the linear prescription (9) provides an essentially better fit with the only exceptions of xenon and methane. Therefore, our first conclusion is that for many liquids the rule (9) better describes the data than the rule (10). The second conclusion one can draw from this discussion is that naive extrapolation of the linear T-dependence (9) of the surface tension coefficient σ_{surf} to supercritical temperatures $T > T_c$ would lead to the negative values of the surface tension coefficient. Of course, one may think that $\sigma_{surf} \equiv 0$ for $T > T_c$ like in the FDM [17] and SMM [22, 23, 24], but in this case one has to explain the reason why the T-derivative of σ_{surf} has a discontinuity at $T = T_c$ while the pressure and all its first and second derivatives are continuous functions of it arguments in this region.

4 The mysterious maximum of the lattice entropy and the gas of free tubes

The considered configuration of the unbroken confining tube is only one of many other configurations accounted by the lattice QCD thermodynamics. However, in order to explain a mysterious maximum of the lattice entropy (see Fig 1) it is sufficient to assume that the probability of the unbroken confining tube among other configurations measured by lattice QCD is $W(L) \sim [L\, g_0 \ln(L/L_0)]^{-1}$, i.e. in the limit $L \to \infty$ it is negligible for any $\nu \neq 0$. Then the contribution of the unbroken confining tube into the lattice free energy is small, since $W(L)F_{str}(L) \sim R^{-2}$ for $t \to +0$ and $R \to R_{lat} - 0$ (R_{lat} denotes the lattice size), but its contribution to the tube entropy

$$W(L)S_{str} = -W\frac{dF_{str}}{dT} = WL\frac{\sigma^0_{str}\nu}{T_{co}}t^{\nu-1} \to WL\frac{\nu}{T_{co}}\left[\frac{\sigma^0_{str}}{[g_0\ln(L/L_0)]^{1-\nu}}\right]^{\frac{1}{\nu}} R^{\frac{2(1-\nu)}{\nu}} \sim R^{\frac{2(1-\nu)}{\nu}} \qquad (11)$$

is an increasing function of the tube radius R for $\nu < 1$. Clearly, if the available size of the lattice R_{lat} would be infinite then the contribution of the unbroken tube would diverge, but for finite lattice size one should observe a fast increase at $T \to T_{co}$.

The physical origin of a singular behavior of the tube entropy (11) encoded in $\nu < 1$ is rooted in the formation of fractal surfaces of the confining tube in the cross-over temperature vicinity [6]. This can be clearly seen from the power $\frac{2(1-\nu)}{\nu}$ of R on the right hand side of (11) which is fractal for any $\nu \neq \frac{2}{2+n}$ where $n = 1, 2, 3, ...$ Moreover, the appearance of fractal structures at $T = T_{co}$ can be easily understood within our model, if one recalls that only at this temperature the fractal surfaces can emerge at almost no energy costs due to almost zero total pressure (7). An explanation of the tube entropy decrease for $t < 0$ is similar [6, 7]. It means that the fractal surfaces gradually disappear since for $T > T_{co}$ the tube gradually occupies the whole available lattice volume.

Here we also would like to consider a toy model based on the total pressure (6) of the confining tube, but for the non-static (or free) quark-antiquark pair. In this case the parameter L should be considered as a free parameter which has to be determined from the maximum of the total pressure (6). Finding from this condition the radius dependent separation distance $L_w(R)$ which corresponds to the most probable and the stable state of the free confining tube one has to substitute it into expression for the pressure (6) and find the corresponding radius of the tube from the equation $p = p_{tot}(L_w(R), R, T)$ for the set of given external pressure p and temperature T. Clearly the determination of an extremum of the total pressure (6) with respect to R with subsequent finding of the separation distance L should give the same result, but the first way is technically easier.

Instead of the quantitative analysis of the resulting pressure $p_{tot}(L_w(R), R, T)$ which requires the knowledge of values of all constants, i.e. L_0, g_0, τ e.t.c., we prefer to discuss some qualitative properties of the model and show that it has two phases. Also we have to stress that such a model cannot be applied to high pressures (or high densities) directly because in this case the pressure of the system should account for the short range repulsion between the tubes. Therefore in what follows it is assumed that the gas of tubes has some low particle density ρ and, hence, one can consider this gas as an ideal gas with the pressure $p = T\rho$.

To determine the density ρ one has to maximize the pressure p_{tot} first. From the vanishing derivative condition

$$\frac{\delta\, p_{tot}(L, R, T)}{\delta\, L} = -\frac{g_0}{\pi R^4 L} - \frac{T\tau}{\pi R^2 L^2}\left[\ln\left(\frac{\pi R^2 L}{V_0}\right) - 1\right] + \frac{T\tau}{\pi R^2 L^2} = 0 \qquad (12)$$

one can find the following equation for $L_w(R)$

$$L_w = \frac{T\tau R^2}{g_0}\left[2 - \ln\left(\frac{\pi R^2 L_w}{V_0}\right)\right] \qquad (13)$$

and show that it corresponds to a maximum of pressure. From Eq. (12) it is clearly seen that, in contrast to previous findings [6, 7], the role of the Fisher topological term is a decisive one for an establishing Eq. (13).

Consider a few limiting cases of Eq. (13). In the limit $T \to 0$ and finite R one gets

$$L_w^0 \;\approx\; -\frac{T\tau R^2}{g_0}\ln\left(\frac{\pi R^4 \tau T}{V_0\, g_0\, e^2}\right) \to\; 0\,, \tag{14}$$

which can be interpreted as a confinement of color charges. The same solution is true for the case of $R \to 0$ and finite T. In the other extreme $T \to \infty$ (or $R \to \infty$) one obtains a different solution of Eq. (13)

$$L_w^\infty \;\approx\; \frac{V_0 e^2}{\pi R^2}\,, \tag{15}$$

which again shows that for large R values the separation distance is small. This situation resembles what is observed in lattice QCD for the non-static color charges: the long tubes that connect such charges simply break up at some separation distances [1].

From Eq. (13) one can show that the solution L_w is a monotonically increasing function of T, while for $T \neq 0$ it always has a maximum as the function of R. Searching for the maximum of $L_w(R)$ (13) one can find the corresponding value of the radius R_{max} and $L_w(R_{max})$

$$R_{max} \;=\; \left[\frac{g_0\, V_0\, e}{\pi\,\tau\, T}\right]^{\frac{1}{4}}\,, \tag{16}$$

$$L_w(R_{max}) \;=\; \left[\frac{V_0\, e\,\tau\, T}{\pi\, g_0}\right]^{\frac{1}{2}}\,, \tag{17}$$

which, evidently, obey the condition $\pi R_{max}^2 L_w(R_{max}) = V_0\, e$. The presence of the maximum of function $L_w(R)$ leads to an existence of two different radii for the same value of separation distance L, or in other words, there are two solutions of the equation $L = L_w(R)$. Clearly, the parameters of the maximum R_{max} and $L_w(R_{max})$ given, respectively, by Eqs. (16) and (17), separate the regions of these solutions. Evidently, the latter correspond to two phases of the gas of tubes which have different tube radius for the same separation distance L. The analysis of these solutions shows that there are many possibilities which strongly depend on the values of the involved constants L_0, g_0, τ and V_0, whereas for low but non-vanishing temperatures one can show that the higher pressure corresponds to the phase of the tubes with smaller radius. This is clear because in case of low temperatures the leading contribution to the total pressure (6) is given by the surface tension term $\frac{\sigma_{surf}}{R}$.

5 Conclusions

In this work we discuss the most general relation between the tension of the color tube connecting the static quark-antiquark pair and the surface tension of the corresponding cylindrical bag. Such a relation allows us to determine the surface tension of the QGP bags at zero temperature and, under the plausible assumptions that are typical for ordinary liquids, to estimate the temperature of vanishing surface tension coefficient of QGP bags at zero baryonic charge density as $T_\sigma = 152.9 \pm 4.5$ MeV. Using the Fisher conjecture [17] and the exact results found for the temperature dependence of surface tension coefficient from the partition of surface deformations [18, 19, 7], we conclude that the same temperature range corresponds to the value of QCD (tri)critical endpoint temperature, i.e. $T_{cep} = T_\sigma = 152.9 \pm 4.5$ MeV. Then requiring the positive values for the confining tube entropy density we demonstrate that at the cross-over region the surface tension coefficient of the QGP bags is unavoidably negative. Furthermore, analyzing the data on the temperature dependence of the surface tension coefficient of some ordinary liquids in the vicinity of the critical endpoint we conclude that the negative values of the surface tension coefficient of QGP bags are not unique, but they also should exist at the supercritical temperatures of usual liquids. We believe such a conclusion is worth to verify experimentally for ordinary liquids.

Also we demonstrate that the long unbroken tube taken with a vanishing probability which generates a finite contribution into the lattice free energy may, under certain assumptions, provide a very fast increase of the lattice entropy of such configurations and, thus, it may explain the maximum of the tube entropy observed by lattice QCD. Additionally, we considered the non-static (free) tube and used the developed formalism to work out the model of the gas of free tubes. The performed analysis of such a model showed that there are two phases in this model which correspond to different radii of the tube for the same separation length L. Since this toy model resembles some important features of the confining tubes observed in the lattice QCD, we believe it is important for QCD phenomenology and can be used to build up more elaborate statistical model which accounts for a realistic interaction between tubes.

Acknowledgements. The research made in this work was supported in part by the Program "Fundamental Properties of Physical Systems under Extreme Conditions" of the Bureau of the Section of Physics and Astronomy of the National Academy of Sciences of Ukraine.

References

[1] E. V. Shuryak, Prog. Part. Nucl. Phys. **62**, 48 (2009).
[2] see, for instance, O. Kaczmarek and F. Zantow, PoS LAT2005, 192 (2006) [arXiv:hep-lat/0510094].
[3] P. Romatschke and U. Romatschke, Phys. Rev. Lett. **99**, 172301 (2007).
[4] K. Dusling and D. Teaney, Phys. Rev. C 77, 034905 (2008).
[5] E. Shuryak, Nucl. Phys. A **774**, 387 (2006).
[6] K. A. Bugaev and G. M. Zinovjev, Nucl. Phys. A **848**, 443 (2010).
[7] K. A. Bugaev, arXiv:1101.2831 [nucl-th]; K. A. Bugaev et al., arXiv:1101.4549 [hep-ph].
[8] K. A. Bugaev, Phys. Rev. **C 76**, 014903 (2007); Phys. Atom. Nucl. **71**, 1585 (2008); arXiv:0711.3169.
[9] K. A. Bugaev, V. K. Petrov and G. M. Zinovjev, arXiv:0904.4420 [hep-ph].
[10] K. A. Bugaev, V. K. Petrov and G. M. Zinovjev, Europhys. Lett. **85**, 22002 (2009); arXiv:0801.4869.
[11] K. A. Bugaev, V. K. Petrov and G. M. Zinovjev, Phys. Rev. **C 79**, 054913 (2009); K. A. Bugaev arXiv:0809.1023 [nucl-th].
[12] K. A. Bugaev, arXiv:0909.0731 [nucl-th]; A. I. Ivanytskyi, arXiv:1104.1900 [hep-ph].
[13] C. Greiner *et al.*, J. Phys. **G 31**, S725 (2005); C. Greiner, P. Koch-Steinheimer, F. M. Liu, I. A. Shovkovy and H. Stöcker, arXiv:nucl-th/0703079.
[14] I. Zakout, C. Greiner, J. Schaffner-Bielich, Nucl. Phys. **A 781**, 150 (2007).
[15] K. A. Bugaev, Phys. Part. Nucl. **38**, (2007) 447; Acta Phys. Pol. **B 36**, 3083 (2005).
[16] M. G. Alford, K. Rajagopal, S. Reddy and A. W. Steiner, Phys. Rev. D **73** (2006) 114016 and references therein.
[17] M. E. Fisher, Physics **3**, 255 (1967).
[18] K. A. Bugaev, L. Phair and J. B. Elliott, Phys. Rev. **E 72**, 047106 (2005).
[19] K. A. Bugaev and J. B. Elliott, Ukr. J. Phys. **52** (2007) 301.
[20] A. Mocsy and P. Petreczky, PoS LAT2007 **216** (2007).
[21] J. Gross, J. Chem. Phys. **131**, 204705 (2009) and references therein.
[22] J. P. Bondorf *et al.*, Phys. Rep. **257**, 131 (1995).
[23] K. A. Bugaev, M. I. Gorenstein, I. N. Mishustin and W. Greiner, Phys. Rev. **C 62**, 044320 (2000); nucl-th/0007062; Phys. Lett. **B 498**, 144 (2001); nucl-th/0103075 and references therein.
[24] P. T. Reuter and K. A. Bugaev, Phys. Lett. **B 517**, 233 (2001); and Ukr. J. Phys. **52**, (2007) 489.
[25] K. A. Bugaev, A. I. Ivanytskyi, E. G. Nikonov, A. S. Sorin and G. M. Zinovjev, arXiv:1106.5939 [nucl-th].
[26] E. A. Guggenheim, J. Chem. Phys. **13**, 253 (1945).
[27] G. R. Somayajulu, Int. J. Thermophys. **9**, 559 (1988).
[28] see a discussion in J. Escobedo and G. Ali Mansoori, AIChE Journal **42**, 1425 (1996) and references therein.
[29] N. B. Vargaftik, L. D. Voljak, and B. N. Volkov, Proc. 8th Int. Conf. Prop. Steam Water (Giens, France, 1974), Vol. II, p. 1075.
[30] N. B. Vargaftik, B. N. Volkov, and L. D. Voljak, J. Phys. Chem. Ref. Data **12**, 817 (1983).
[31] B. A. Grigoryev, B. V. Nemzer, D. S. Kurumov and J. V. Sengers, Int. J. Thermophys. **13**, 453 (1992).
[32] J. B. Elliott, K. A. Bugaev, L. G. Moretto and L. Phair, arXiv:nucl-ex/0608022.
[33] E. W. Lemmon, M. O. McLinden and D. G. Friend, "Thermophysical Properties of Fluid Systems" in NIST Chemistry WebBook, NIST Standard Reference Database Number 69, Eds. P. J. Linstrom and W .G. Mallard, June 2005, National Institute of Standards and Technology, Gaithersburg MD, 20899 (http://webbook.nist.gov).

Proceedings of the International School-seminar
"New Physics and Quantum Chromodynamics at External Conditions", pp. 29 – 33,
3-6 May 2011, Dnipropetrovsk, Ukraine

SU(3) GLUODYNAMICS ON GRAPHICS PROCESSING UNITS

V. I. Demchik

Dnipropetrovsk National University, Dnipropetrovsk, Ukraine

SU(3) gluodynamics is implemented on graphics processing units (GPU) with the open cross-platform computational language OpenCL. The architecture of the first open computer cluster for high performance computing on graphics processing units (HGPU) with peak performance over 12 TFlops is described.

1 Introduction

Most of the modern achievements in science and technology are closely related to the use of high performance computing. The ever-increasing performance requirements of computing systems cause high rates of their development. Every year the computing power, which completely covers the overall performance of all existing high-end systems reached before is introduced according to popular TOP-500 list of the most powerful (non-distributed) computer systems in the world [1]. Obvious desire to reduce the cost of acquisition and maintenance of computer systems simultaneously, along with the growing demands on their performance shift the supercomputing architecture in the direction of heterogeneous systems. These kind of architecture also contains special computational accelerators in addition to traditional central processing units (CPU).

One of such accelerators becomes graphics processing units (GPU), which are traditionally designed and used primarily for narrow tasks visualization of 2D and 3D scenes in games and applications. The peak performance of modern high-end GPUs (AMD Radeon HD 6970, AMD Radeon HD 5870, nVidia GeForce GTX 580) is about 20 times faster than the peak performance of comparable CPUs (see Fig. 1). For last five years the GPU performance has been increasing twice per year. Thanks to a substantially lower cost (per Flops[1]), as well as high rates of productivity growth compared to CPUs, the graphics accelerators have become a very attractive platform for high performance computing.

Current overall performance of all computer systems ranked in the last TOP-500 list is about 85 PFlops [1]. The number of computer systems for different countries is: USA - 255 computers (51.0%), China - 61 (12.2%), Germany - 30 (6.0%), UK - 27 (5.4%), Japan - 26 (5.2%), France - 25 (5.0%), Russia - 12 (2.4%). Some of these supercomputer systems, equipped with graphics accelerators are shown in Table 1 (peak performance of corresponding system measured in GFlops is shown in the last column).

According to Flynn's taxonomy [2], which describes four classes in both a serial and parallel context, GPUs are based on so-called SIMD architecture. SIMD (*Single Instruction stream - Multiple Data stream*) is an architecture, in which each processing unit executes the same instruction stream as the others on its own set of data. In other words, a set of processors share the same control unit, and their execution differs only by the different data elements each processor operates on. Due to a large number of processing units in GPU and SIMD architecture it is reasonable to implement the lattice simulations on GPU.

The technique of using GPU, which typically handles computations only for computer graphics, to perform computation in applications traditionally handled by the CPU is called general-purpose computing on graphics processing units (GPGPU). There are different approaches for GPU utilization. One of the novel languages for programming heterogeneous systems is an open computational language OpenCL [3]. It is maintained by the group of industry vendors, Khronos Group, that have interest in promoting a general way to target different computational devices. In spite of some performance inefficiency, OpenCL possesses a very important feature for high performance computation – portability. So, we choose OpenCL as programming environment for our task.

The technical details of lattice simulations on computers are well-known [4, 5, 6, 7]. We implemented the standard lattice simulation scheme on the GPU with the OpenCL language. The scheme is described in the next Section. The details of GPU implementation is shown in Section 3.

[1] Flops (*floating point operations per second*) – is a measure of computer's performance

e-mail: vadimdi@yahoo.com

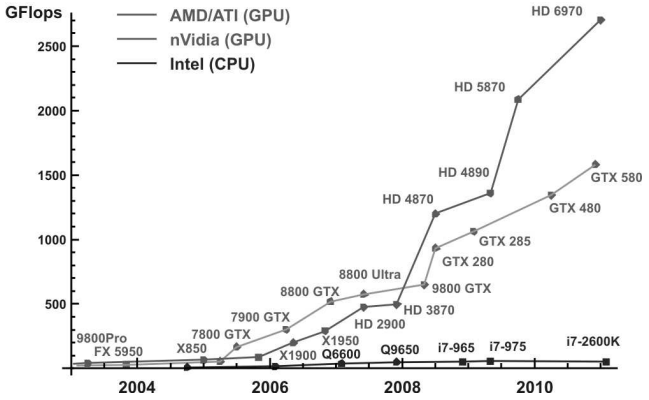

Figure 1. GPU and CPU performance growth.

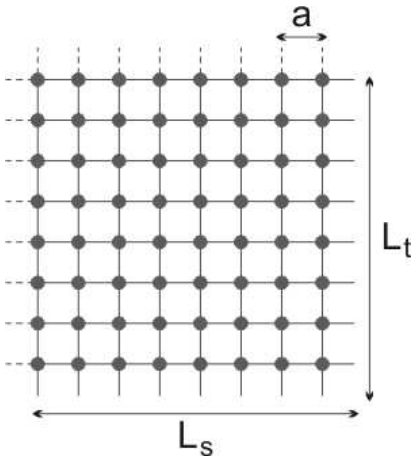

Figure 2. Checkerboard decomposition of the lattice.

2 Lattice formulation

We used hypercubic lattice $L_t \times L_s^3$ ($L_t < L_s$) with hypertorus geometry; L_t and L_s are the temporal and the spatial sizes of the lattice, respectively. Evidently, the total number of lattice sites is $N_{sites} = L_1 \times L_2 \times L_3 \times L_t$. In order to parallelize the simulation algorithm we have implemented so-called *checkerboard scheme* (see Fig. 2) – the whole lattice is divided into 2 parts – odd (red) and even (green) sites. The number of odd sites is $N_{vect} = N_{sites}/2$, as well as the number of even ones. The lattice may be initialized by cold or hot configuration.

Standard Wilson one-plaquette action of $SU(3)$ lattice gauge theory is used,

$$S_W = \beta \sum_x \sum_{\mu<\nu} \left[1 - \frac{1}{3} \text{ Tr } \mathbf{U}_{\mu\nu}(x) \right]; \tag{1}$$

$$\mathbf{U}_{\mu\nu}(x) = \mathbf{U}_\mu(x)\mathbf{U}_\nu(x + a\hat{\mu})\mathbf{U}_\mu^\dagger(x + a\hat{\nu})\mathbf{U}_\nu^\dagger(x), \tag{2}$$

where $\beta = 6/g^2$ is the lattice coupling constant, g is the bare coupling, $\mathbf{U}_\mu(x)$ is the link variable located on the link leaving the lattice site x in the direction μ, $\mathbf{U}_{\mu\nu}(x)$ is the ordered product of the link variables (here and below we omit the group indices).

The defining representations of the gauge field variables are the complex 3×3 matrices for $SU(3)$. Due to the unitarity of the $SU(3)$ group the minimal number of parameters is 8. There are different possible representations of $SU(3)$ matrices in computer memory [4]. In order to speed up the practical calculations it is more convenient to use a redundant representation. The $SU(3)$ group elements may be represented either by the complete complex matrix, or by the first two rows, corresponding to the complex 3-vectors $\mathbf{u}$ and $\mathbf{v}$. Due to the group properties of $SU(3)$ matrices, the third row of the matrix can be reconstructed from vectors $\mathbf{u}$ and $\mathbf{v}$:

$$\mathbf{U}_\mu(x) = \begin{pmatrix} \mathbf{u} \\ \mathbf{v} \\ \mathbf{u}^* \times \mathbf{v}^* \end{pmatrix}. \tag{3}$$

So, $SU(3)$ lattice variable could be presented as a set of 6 complex numbers (12 real numbers).

No	Computer	Country	Year	Cores	R_{max}
1	K computer	Japan	2011	548352	8162000
2	NUDT TH MPP, **Tesla C2050 GPU**	China	2010	186368	2566000
3	Cray XT5-HE	USA	2009	224162	1759000
4	Dawning TC3600 Blade, **Tesla C2050 GPU**	China	2010	120640	1271000
5	HP ProLiant SL390s, **Tesla C2050 GPU**	Japan	2010	73278	1192000
13	T-Platforms T-Blade2/1.1, **Tesla C2070 GPU**	Russia	2011	33072	674105
22	Supermicro Cluster, **ATI Radeon GPU**	Germany	2011	16368	299300
499	Cluster Platform 3000 BL2x220	Germany	2010	4800	40217
500	BladeCenter HS22 Cluster	China	2010	7104	40187

Table 1. Some computer systems in TOP-500 list of World's Supercomputers [1]

To avoid the accumulation of rounding errors in the multiplications of the group elements, all the matrices have to be projected to unitarity regularly. It is well-know Gram-Schmidt method for building orthonormal basis elements in vector spaces,

$$\begin{aligned} \mathbf{u_{new}} &= \mathbf{u}/|\mathbf{u}|, \\ \mathbf{v_{new}} &= \mathbf{v}'/|\mathbf{v}'|, \quad \mathbf{v}' = \mathbf{v} - \mathbf{u_{new}}(\mathbf{v} \cdot \mathbf{u}^*_{\mathbf{new}}). \end{aligned} \tag{4}$$

To generate a candidate matrix for the updating algorithm we used Cabibbo-Marinari scheme [14]. $SU(3)$ random matrices are constructed from three 2×2 $SU(2)$ random matrices (R, S and T):

$$\bar{\mathbf{U}}^a_\mu(x) = \begin{pmatrix} r_{11} & r_{12} & 0 \\ r_{21} & r_{22} & 0 \\ 0 & 0 & 1 \end{pmatrix} \begin{pmatrix} s_{11} & 0 & s_{12} \\ 0 & 1 & 0 \\ s_{21} & 0 & s_{22} \end{pmatrix} \begin{pmatrix} 1 & 0 & 0 \\ 0 & t_{11} & t_{12} \\ 0 & t_{21} & t_{22} \end{pmatrix} \tag{5}$$

To update the lattice, heat-bath algorithm with overrelaxation was used [8, 15]. At every MC iteration we successively replaced each lattice link

$$\mathbf{U}_\mu(x) \rightarrow \bar{\mathbf{U}}_\mu(x) = w\mathbf{W}_\mu(x), \tag{6}$$

$$\mathbf{W}_\mu(x) = \sum_{\nu \ (\mu<\nu)} \Big[\mathbf{U}_\nu(x)\mathbf{U}_\mu(x+a\hat{\nu})\mathbf{U}^\dagger_\nu(x+a\hat{\mu}) + \mathbf{U}^\dagger_\nu(x-a\hat{\nu})\mathbf{U}_\mu(x-a\hat{\nu})\mathbf{U}_\nu(x+a(\hat{\mu}-\hat{\nu}))\Big], \tag{7}$$

w is a normalization constant such that

$$\bar{\mathbf{U}}_\mu(x) \in SU(3). \tag{8}$$

The central part of the lattice simulation program is the updating subroutine. We have to systematically update all lattice links for given configuration by suggesting new variables and accepting them. One time visiting all links is called a *lattice sweep*. Sufficiently many updates have to be done, until the subsequently generated configurations represent the equilibrium distribution. This procedure is known as *thermalization*. After the thermalization, one can start to compute the observables (e.g. energy) on the Monte Carlo configurations. The configurations used for measuring are separated by several intermediate updates.

There are several software packages for Monte Carlo simulations on a lattice:

- **FermiQCD**: an open C++ library for development of parallel Lattice Quantum Field Theory computations [9, 10].
- **MILC**: an open code of high performance research software written in C for doing $SU(3)$ lattice gauge theory simulations on several different (MIMD) parallel computers [11].
- **SZIN**: the open-source software system supports data-parallel programming constructs for lattice field theory and in particular lattice QCD [12].
- **QUDA**: a library for performing calculations in lattice QCD on graphics processing units [13].

First three mentioned packages are central processing unit (CPU)-based, while the later one is intended for using nVidia GPUs only.

In the next Section we will show how the described simulation algorithm can be implemented both on AMD/ATI, and nVidia GPUs.

3 GPU implementation

To design the GPU-applications the following key features of GPU hardware architecture must be taken in consideration: each general-purpose register (GPR), as well as memory cells, has four 32-bit components that are called *GPR slots* and usually designated as $.x$, $.y$, $.z$ and $.w$; memory operations are the bottleneck of GPU; floating point operations are more productive on GPU than integer operations (in compare with CPUs); double precision floating point operations are the slowest on GPU.

First of all, we introduce GPU-memory representation of $SU(3)$-link variable. As it was mentioned in the previous section, $SU(3)$ matrices could be presented in the form (3). So, we need 12 real single precision numbers to store one $SU(3)$ matrix. These 12 numbers could be placed into three GPU-memory cells **r1**, **r2** and **r3**:

	.x	**.y**	**.z**	**.w**
r1	Re $[u_1]$	Re $[u_2]$	Re $[u_3]$	Re $[v_3]$
r2	Im $[u_1]$	Im $[u_2]$	Im $[u_3]$	Im $[v_3]$
r3	Re $[v_1]$	Re $[v_2]$	Im $[v_1]$	Im $[v_2]$

(9)

It should be noted that as opposite to the $SU(3)$ case one $SU(2)$ matrix could be placed in one GPR only.

All necessary data for simulations are stored in global GPU memory. GPU carries out intermediate actions and returns the results to host program for final data handling and output. We avoid any data transfer during run-time between host program and GPU to speed-up the execution process. Intermediate configurations could be saved, but it slows-up the execution and is turned off by default.

Lattice is stored in GPU memory as single precision data. It allows significantly reduce the memory requirements for the simulation, as well as increase the performance of the program. All measuring and averaging kernels work with double precision and output results as 64-bit values to avoid error accumulation.

Usual amount of memory of modern GPU is 2GB. So, lattices up to 16×48^3 could be simulated on single GPU device without incorporation of host memory. Due to the memory limitations the bigger lattices could be simulated on GPU only with the CPU-GPU runtime data transfer. It sufficiently slows down the program, but allows to investigate very large lattices.

The next step is the implementation of pseudo-random number generator on GPU. As it was researched in [16], the best GPU-oriented generators are **XOR128** and **RANLUX**. We have implemented both of the generators on OpenCL. We use **XOR128** generator (as a very fast generator) for a rough definition of parameter space in the investigation and the **RANLUX** generator to perform all key measurements. The generator could be easily chosen by initial parameter.

The lattice may be initialized by cold or hot configuration. There are two possibilities for hot initialization to fill lattice with the pseudo-random $SU(3)$ matrices: constant series (by predefined seeds) or random series (by system timer-dependent random seeds) of pseudo-random numbers. In the first case every startup process would reproduce the same results for every execution (it is convenient for debugging purposes).

At the moment the stable-working simulation program is the single GPU-device program, so we can use the trivial parallelization scheme only for the computational cluster with multiple GPU-devices: each GPU-device performs the simulation with own initial parameters. After each run the simulation program writes all the measurements in file on the disk. Such scheme allows to use different machines for one investigation simultaneously.

It should be noted that the use of OpenCL language allows to run the simulation program not only on GPUs, but on CPUs also.

4 HGPU cluster

In order to increase the performance of computational system we have joined several GPU into one **HGPU** (*High performance computing on Graphics Processing Units*) cluster (see Fig. 3). The HGPU cluster consists of almost all ATI/AMD product line – ATI Radeon HD 4850, ATI Radeon HD 4870, ATI Radeon HD 5850, ATI Radeon HD 5870 and ATI Radeon HD 6970. In addition nVidia GeForce 560Ti is included into the HGPU cluster.

The HGPU cluster has a mixed structure – it contains dedicated and non-dedicated resources. Current overall peak performance of whole HGPU cluster is about 12 TFlops. Current overall peak performance of dedicated servers of HGPU cluster is about 7 TFlops.

For Monte Carlo simulations on GPU-cluster we imply the trivial parallelization scheme – each node simulates the lattice with own lattice parameters, which are defined by host through the ini-file. Cluster task scheduler is running on one of the cluster node, which plays a host role. After execution node outputs results in text file with unique filename (which contains node prefix and system time to avoid files overwriting) and writes *finish.txt* file in working directory to start a new task. Host investigates the working directories of nodes with some delay and waits for the file *finish.txt*. Node waits with delay for the deletion of *finish.txt* file in working directory to start a new task. Host creates ini-file for node and deletes *finish.txt* file, so node may start a new task.

The main features of HGPU-cluster is the following:

- cluster may be totally heterogeneous(different nodes may have different GPUs or different OSs and so on);
- host and node softwares take a small amount of computer resources, so it could be run on a very poor PC with modern GPUs;
- host software may be run on one of the nodes;
- several nodes may be on one PC (two-core GPU hardware, several cards, and so on);
- host parses the task file, where cluster parameters and tasks are specified (for example, we may use only part of cluster);
- only parameters, which have to be changed for particular run, are presented between the tasks in task file.

Figure 3. Dedicated servers of HGPU cluster.

5 hgpu.org

There are several Internet resources devoted to GPGPU [17, 18]. We have created the site **http://hgpu.org/** to provide a technical information for people who seek the possibility to accelerate their scientific computations by means of graphics processing units [19]. The site contains links to reviews, tutorials, research papers, program packages concerning various aspects of graphics and non-graphics (general purpose computing) using of GPU and related parallel architectures (FPGA, Cell processors etc.). The site also collects and catalogizes information about programming tools and modern hardware for development of GPU applications. The *Events* page provides links to related conferences, seminars and meetings. We are continuously updating links, papers and other information in our effort push the envelope of GPU computations. Now the site contains over 4000 research papers and over 300 GPU program packages. Registered users can place their own information on **http://hgpu.org/**. The dedicated servers of HGPU cluster are available through the *Dashboard* free of charge for registered users.

6 Conclusions

In this paper we introduce a developed OpenCL package for $SU(3)$ simulations on GPU. The package gives a possibility to study gauge field dynamics on lattices up to 16×48^3 in single-GPU mode. The framework of the package gives a possibility to modify the gauge group $SU(3)$ to any $SU(N)$ group easily. Currently we continue to work on incorporating the MPI technology in order to develop the full multi-GPU package. In order to increase the overall performance of our computational system we have built small GPU-cluster with peak performance about 12 TFlops. The trivial architecture of the cluster allows to increase compute performance with adding new nodes in GPU-cluster additively. The dedicated servers of the cluster is free of charge and available for researchers through the first open GPU-hardware Internet resource **hgpu.org**.

References

[1] The Top-500 list, http://www.top500.org/ (Last access: oct.2011)
[2] M. Flynn, IEEE Trans. Comput. **C-21**, 948 (1972).
[3] OpenCL – The open standard for parallel programming of heterogeneous systems, Khronos Group http://www.khronos.org/opencl/ (Last access: oct.2011)
[4] C. Gattringer, C. B. Lang, Lect. Notes Phys. **788**, 1-211 (2010).
[5] T. DeGrand, C. E. Detar, New Jersey, USA: World Scientific (2006) 345 p.
[6] H. J. Rothe, World Sci. Lect. Notes Phys. **74**, 1-605 (2005).
[7] I. Montvay, G. Munster, Cambridge, UK: Univ. Pr. (1994) 491 p. (Cambridge monographs on mathematical physics).
[8] M. Creutz, Phys. Rev. **D36**, 515 (1987).
[9] M. Di Pierro and J. M. Flynn, *"Lattice QFT with FermiQCD"*, PoS **LAT2005**, 104 (2006) [arXiv:hep-lat/0509058].
[10] FermiQCD, http://web2py.com/fermiqcd/ (Last access: oct.2011)
[11] MILC Collaboration, http://www.physics.utah.edu/∼detar/milc/ (Last access: oct.2011)
[12] SZIN Software System, http://www.jlab.org/∼edwards/szin/ (Last access: oct.2011)
[13] QUDA: A library for QCD on GPUs, http://lattice.github.com/quda/ (Last access: oct.2011)
[14] N. Cabibbo, E. Marinari, Phys. Lett. **B119**, 387-390 (1982).
[15] A. D. Kennedy, B. J. Pendleton, Phys. Lett. **B156**, 393-399 (1985).
[16] V. Demchik, Comput. Phys. Commun. **182**, 692-705 (2011). [arXiv:1003.1898 [hep-lat]].
[17] General-Purpose Computation on Graphics Hardware, http://gpgpu.org/ (Last access: oct.2011)
[18] GPUcomputing, http://gpucomputing.net/ (Last access: oct.2011)
[19] High performance computing on graphics processing units, http://hgpu.org/ (Last access: oct.2011)

Proceedings of the International School-seminar
"New Physics and Quantum Chromodynamics at External Conditions", pp. 34 – 40,
3-6 May 2011, Dnipropetrovsk, Ukraine

PERSPECTIVES OF MODEL-INDEPENDENT SEARCHING FOR Z' BOSON AT MODERN HADRON COLLIDERS

A. V. Gulov[a], A. A. Kozhushko[b]

Dnipropetrovsk National University, Dnipropetrovsk, Ukraine

The model-independent constraints on the Abelian Z' couplings from the LEP data are applied to estimate the Z' production in experiments at hadron colliders. The Z' total and partial decay widths are analyzed. The results are compared with model-dependent predictions and present experimental data from the Tevatron. If we assume the 1-2σ hints from the LEP data to be a signal of the Abelian Z' boson, then the Tevatron data constrain the Z' mass between 400 GeV and 1.2 TeV.

1 Introduction

A new heavy neutral vector boson (Z' boson) is probably the most perspective intermediate state in scattering processes of quarks and leptons which could be discovered in experiments at modern hadron colliders. At the parton level it can appear in the annihilation channel carrying a large part of energy of the colliding particles, its mass is allowed to be of order 1 TeV by current experimental constraints, and it is a necessary component of popular grand unification theories and other models with extended gauge sector (see [1, 2, 3] for review).

Searching for Z' boson is an essential part of the reports of the Tevatron and LHC collaborations. The particle could be discovered through deviations of observed quantities from the predicted SM background. However, observables in experiments at hadron colliders can be calculated with significant theoretical uncertainties coming mainly from the parton distribution functions of initial states and complicated structure of hadronic final states. In this situation one can only hope to discover the most prominent signals in the most clear processes. This is the reason to pay attention to searching for resonances of new heavy particles decaying into lepton pairs.

The most accurate description of resonances requires to calculate scattering amplitudes with intermediate virtual states. But if the resonance is a narrow one, then it can be described by the production cross-section of the on-shell particle and by the decay widths (total and partial). These parameters can be easily constrained from previous experiments giving a possibility to estimate the perspectives of the current experiments.

The Tevatron and LHC collaborations usually perform the model-dependent fits trying to discover Z' boson hints. Of course, effects of Z' boson can be calculated in details for each specific model beyond the SM. Such estimates are widely presented in the literature [4, 5, 6]. Some set of popular E_6 based models and left-right models is usually considered in this approach. However, probing the set we can still miss the actual Z' model. In this regard, it is useful to complement model-dependent Z' searching by some kind of model-independent analysis, i.e. the analysis covering a lot of models.

Almost all of the usually considered models belong to the models with so-called Abelian Z' boson. In Ref. [8, 9] we found the relations which hold in any model containing the Abelian Z' boson and satisfying the following conditions: 1) only one neutral vector boson exists at the energy scale about 1-10 TeV, 2) the Z' boson can be phenomenologically described by the effective Lagrangian [1, 2, 3] at low energies, 3) the Z' boson and other possible heavy particles are decoupled at considered energies, and the theory beyond the Z' decoupling scale is either one- or two-Higgs-doublet standard model (THDM), 4) the SM gauge group is a subgroup of a possible extended gauge group of the underlying theory. So, the only origin of possible tree-level Z' interactions to the SM vector bosons is the Z–Z' mixing.

The mentioned relations cover almost all of the usually considered set of models (see [10, 11] for details). They require the same Z' couplings to the left-handed fermion currents within any SM doublet and the universal absolute value of the Z' couplings to the axial-vector currents for all the massive SM fermions. The relations reduce significantly the number of unknown Z' parameters. This allows to constrain the parameters by existing experiments as well as to predict the quantities used in the analysis of the Tevatron and LHC experiments.

Recently we summarized the information about Z' couplings to leptons and quarks which can be extracted from the LEP experiments [10, 11]. The Z' coupling to axial-vector currents was constrained by both LEP I and LEP II $\mu^+\mu^-, \tau^+\tau^-$ data. In different processes it shows hints at about 1σ confidence level (CL) with approximately the same maximum-likelihood value. This value can be used in estimates of observables in the Tevatron and LHC experiments. As for the couplings to vector currents, the Z' coupling constant to electron

e-mail: [a]alexey.gulov@gmail.com, [b]a.kozhushko@yandex.ru

can be constrained by the LEP II e^+e^- data only. Although the backward scattering shows a signal at the 2σ CL, the maximum-likelihood value is outside of the 95% CL interval calculated by the complete set of bins. In this situation we refrain from using that maximum-likelihood value in our estimates. Nevertheless, the vector coupling is constrained at the 95% CL. The upper bound on the electron vector coupling agrees closely with the corresponding upper bound on the axial-vector coupling. This fact allows us to suppose the rest of vector couplings to be constrained by the same value, since no evident signals were discovered in other scattering processes measured by the LEP collaborations. It is worth to note that all the conclusions derived from the LEP data are also valid if one considers the THDM as the low-energy theory instead of the usual minimal SM.

Our main goal is to obtain estimates for the Z' parameters used in searching for the narrow resonance by applying the LEP constraints on the Z' couplings. Both the minimal SM and the THDM will be considered as the low-energy theory. Also we compare these results to the Tevatron experimental data and model-dependent predictions for the Tevatron.

2 Theoretical and experimental constraints on the Z' couplings

In this paper we discuss mainly the Z' couplings to the vector and axial-vector fermion currents described by the Lagrangian

$$\begin{aligned}\mathcal{L}_{Z\bar{f}f} &= \frac{1}{2}Z_\mu \bar{f}\gamma^\mu \left[(v_{fZ}^{\mathrm{SM}} + \gamma^5 a_{fZ}^{\mathrm{SM}})\cos\theta_0 + (v_f + \gamma^5 a_f)\sin\theta_0\right] f,\\ \mathcal{L}_{Z'\bar{f}f} &= \frac{1}{2}Z'_\mu \bar{f}\gamma^\mu \left[(v_f + \gamma^5 a_f)\cos\theta_0 - (v_{fZ}^{\mathrm{SM}} + \gamma^5 a_{fZ}^{\mathrm{SM}})\sin\theta_0\right] f,\end{aligned} \tag{1}$$

where f is an arbitrary SM fermion state; a_f and v_f are the Z' couplings to the axial-vector and vector fermion currents; θ_0 is the Z–Z' mixing angle; v_{fZ}^{SM}, a_{fZ}^{SM} are the SM couplings of the Z-boson. Such a parametrization is suggested by a number of natural conditions. First of all, the Z' interactions of renormalizable types are to be dominant at low energies $\sim m_W$. The non-renormalizable interactions generated at high energies due to radiation corrections are suppressed by the inverse heavy mass $1/m_{Z'}$ (or by other heavier scales $1/\Lambda_i \ll 1/m_{Z'}$) and therefore at low energies can be neglected. It is also assumed that the Z' is the only neutral vector boson with the mass $\sim m_{Z'}$.

It is obvious that the Lagrangian (1) requires the Z' boson to enter the theory as a gauge field through covariant derivatives with a corresponding charge. This idea allows also to introduce Z' couplings to SM scalar and vector fields. Although the latter couplings are inessential in the analysis of the Z' production cross-section in fermion collisions, they contribute to the Z' width. We assume that the $\mathrm{SU}(2)_L \times \mathrm{U}(1)_Y$ gauge group of the SM is a subgroup of the GUT group. In this case, a product of generators associated with the SM subgroup is a linear combination of these generators. As a consequence, all the structure constants connecting two SM gauge bosons with Z' have to be zero. Hence, the Z' interactions to the SM gauge fields at the tree level are possible due to the Z–Z' mixing only.

We will consider both the SM and the THDM as the low-energy theory. The explicit Lagrangian describing Z' couplings to the SM fields can be found in [7].

The parameters a_f, v_f, and θ_0 must be fitted in experiments. In a particular model, one has some specific values for them. In case when the model is unknown, these parameters remain potentially arbitrary numbers. In most investigations they are usually considered as independent ones. However, this is not the case if one assumes that the underlying extended model is a renormalizable one. In Refs. [8, 9] it was shown that these parameters are correlated as

$$v_f - a_f = v_{f^*} - a_{f^*}, \qquad a_f = T_{3f}\tilde{g}\tilde{Y}_\phi, \tag{2}$$

where f and f^* are the partners of the $SU(2)_L$ fermion doublet ($l^* = \nu_l, \nu^* = l, q_u^* = q_d$ and $q_d^* = q_u$), T_{3f} is the third component of the weak isospin, and $\tilde{g}\tilde{Y}_\phi$ determines the Z' interactions to the SM scalar fields (see [10] for details). The parameter $\tilde{g}\tilde{Y}_\phi$ defines also the Z–Z' mixing angle in (1).

As it was discussed in [10, 11], the relations (2) cover a popular class of models based on the E_6 group (the so called LR, χ-ψ models) and other models, such as the Sequential SM [12]. Thus, they describe correlations between Z' couplings for a wide set of models beyond the SM. That is the reason to call the relations model-independent ones.

The couplings of the Abelian Z' to the axial-vector fermion current have a universal absolute value. The value is proportional to the Z' coupling to scalar fields. Then, the Z–Z' mixing angle θ_0 can be also determined by the axial-vector coupling.

At low energies the Z' couplings enter the cross-section together with the inverse Z' mass, so it is convenient to introduce the dimensionless couplings

$$\bar{a}_f = \frac{m_Z}{\sqrt{4\pi}m_{Z'}}a_f, \quad \bar{v}_f = \frac{m_Z}{\sqrt{4\pi}m_{Z'}}v_f, \tag{3}$$

which are constrained by experiments. Since the axial-vector coupling is universal, we will use the notation

$$\bar{a} = \bar{a}_d = \bar{a}_{e^-} = -\bar{a}_u = -\bar{a}_\nu. \tag{4}$$

Then the Z–Z' mixing is

$$\theta_0 \approx -2\bar{a}\frac{\sin\theta_W \cos\theta_W}{\sqrt{\alpha_{\rm em}}}\frac{m_Z}{m_{Z'}}. \tag{5}$$

It also follows from (2) that for each fermion doublet only one vector coupling is independent:

$$\bar{v}_{f_d} = \bar{v}_{f_u} + 2\bar{a}. \tag{6}$$

As a result, Z' couplings can be parameterized by seven independent constants $\bar{a}$, $\bar{v}_u$, $\bar{v}_c$, $\bar{v}_t$, $\bar{v}_e$, $\bar{v}_\mu$, $\bar{v}_\tau$.

Recently we obtained limits on Z' couplings from the LEP I and LEP II data [10, 11]. We found some hints of Z' boson at 1-2σ CL. Namely, the constants $\bar{a}$ and $\bar{v}_e$ show non-zero maximum-likelihood (ML) values. The axial-vector coupling $\bar{a}$ can be constrained by the LEP I data (through the mixing angle) and by the LEP II $e^+e^- \to \mu^+\mu^-, \tau^+\tau^-$ data. The corresponding ML values are very close to each other. This value

$$\bar{a}^2 = 1.3 \times 10^{-5} \tag{7}$$

will be used in our estimates. The 95% CL interval was also obtained by the experimental data:

$$0 < \bar{a}^2 < 3.61 \times 10^{-4}. \tag{8}$$

The electron vector coupling $\bar{v}_e$ can be constrained by the LEP II $e^+e^- \to e^+e^-$ data. An evident non-zero ML value occurred in fits taking into account the backward scattering bins only. Those fits showed 2σ signal of the Z' boson. On the other hand, that ML value was excluded at 95% CL by fits including all the bins. This instability is the reason to refrain from using the ML value of $\bar{v}_e$ in our estimates. The 95% CL interval on $\bar{v}_e$ will be taken into account only:

$$4 \times 10^{-5} < \bar{v}_e^2 < 1.69 \times 10^{-4}. \tag{9}$$

Other Z' coupling constants cannot be severely constrained by existing data. Among them $\bar{v}_u$, $\bar{v}_c$, and $\bar{v}_\mu$ play an important role in the process $q\bar{q} \to Z' \to \mu^+\mu^-$ which is most perspective to discover the Z' resonance. Taking into account that no evident signals of new physics were found by the LEP collaborations in the processes involving quarks, muons and tau-leptons, we constrain the values of $\bar{v}_u$, $\bar{v}_c$, $\bar{v}_t$, $\bar{v}_\mu$, and $\bar{v}_\tau$ by the widest interval from the 95% CL intervals for $\bar{a}$ and $\bar{v}_e$:

$$0 < \bar{v}^2_{\text{other } f} < 4 \times 10^{-4}. \tag{10}$$

Due to the existence of the ML value for the axial-vector coupling we perform two different estimates for the production cross-section and decay widths:

- *95% CL estimate.* In this scheme both the couplings $\bar{a}$ and $\bar{v}_u$ are varied in their 95% CL intervals (8), (10). Then the Z' production cross-section in the Drell-Yan process lies inside of the interval between zero and some maximal value. The maximal value is reached when both the couplings $\bar{a}$ and $\bar{v}_u$ are of the same sign and take their maximal values: $\bar{a} = \sqrt{3.61} \times 10^{-2}$, $\bar{v}_u = 0.02$. The uncertainty from the parton distribution functions should be also added. The minimal value of the width is calculated at $\bar{a} = \bar{v}_u = \bar{v}_{\mu,\tau} = 0$, $\bar{v}_e = \pm\sqrt{0.4} \times 10^{-2}$. The maximal value is realized when all the couplings are at their maximal absolute values, $\bar{a}$ and $\bar{v}_{u,c,t}$ are of the same sign, while $\bar{v}_{e,\mu,\tau}$ have the opposite sign with respect to $\bar{a}$: $\bar{a} = \pm\sqrt{3.61} \times 10^{-2}$, $\bar{v}_{u,c,t} = \pm 0.02$, $\bar{v}_{\mu,\tau} = \mp 0.02$, $\bar{v}_e = \mp\sqrt{1.69} \times 10^{-2}$. This estimate scheme leads to the widest intervals of possible values of the production cross-section and Z' decay widths.

- *Maximum-likelihood estimate.* In this approach the axial-vector coupling is substituted by its ML value $\bar{a} = \sqrt{1.3 \times 10^{-5}}$. The vector coupling $\bar{v}_u$ is varied in its 95% CL interval. If one chooses the positive value of the axial-vector coupling, then the minimal value of the cross-section corresponds to $\bar{v}_u \simeq -0.02$ whereas the maximal value is reached at $\bar{v}_u \simeq 0.02$. The obtained interval should be also enlarged by $\Delta\sigma^{\rm pdf}$. The minimum value of the width corresponds to $\bar{v}_e = \sqrt{0.4} \times 10^{-2}$ and $\bar{v}_f = -\bar{a}_f\tilde{\Gamma}_{\bar{a}_f\bar{v}_f}/2\tilde{\Gamma}_{\bar{v}_f^2}$ ($f = \mu, \tau, u, c, t$). The maximum value is reached at $\bar{v}_{u,c,t} = 0.02$, $\bar{v}_{\mu,\tau} = -0.02$, $\bar{v}_e = -\sqrt{1.69} \times 10^{-2}$. This estimate scheme gives a more narrow interval for the production cross-section and the Z' decay widths which can be considered as an 'optimistic' scenario to discover the Z' boson.

The knowledge of possible values of the Z' couplings allows to estimate the Z' production cross-section at the LHC and Tevatron and the Z' decay width without specifying the model beyond the SM.

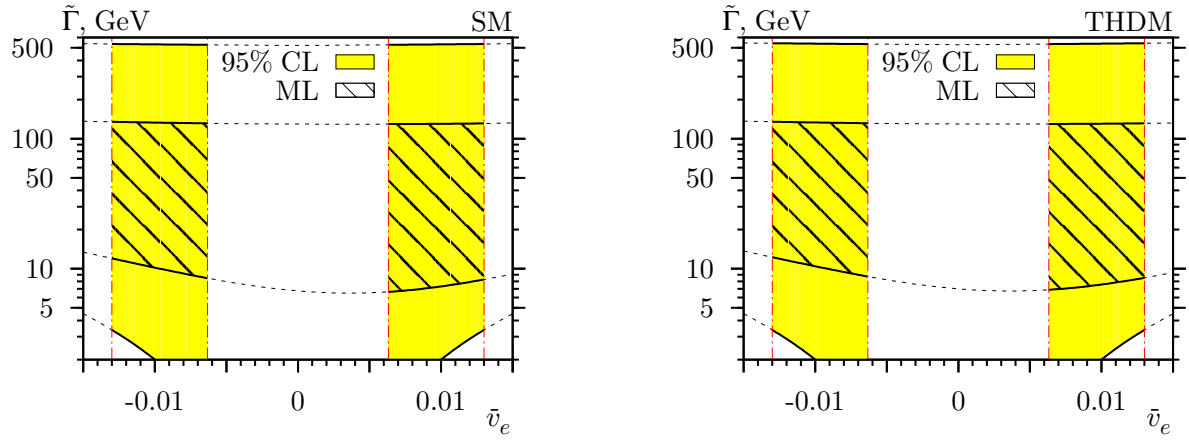

Figure 1. The Z' width (13) versus $\bar{v}_e$ for the SM and THDM cases. The filled areas represent the 95% CL estimate, whereas the hatched areas represent the ML estimate. The minimum and maximum values of the 95% CL interval for $\bar{v}_e$ are plotted as the vertical dot-dashed lines.

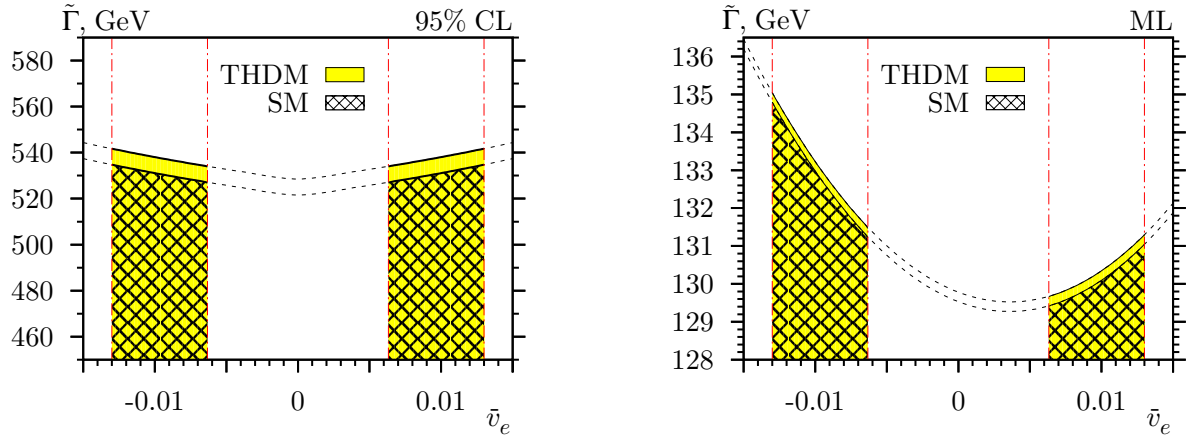

Figure 2. The $\tilde{\Gamma}$ estimates versus $\bar{v}_e$ for the SM and THDM cases. The filled areas represent the estimate for the THDM case, and the hatched areas represent the estimate for the SM case. The minimum and maximum values of the 95% CL interval for $\bar{v}_e$ are plotted as the vertical dot-dashed lines.

3 Z' production cross-section and width

In modern experiments Z' bosons are expected to be produced in proton-antiproton collisions $p\bar{p} \to Z'$ (Tevatron) or proton-proton collisions $pp \to Z'$ (LHC). At the parton level both the processes are described by the annihilation of a quark-antiquark pair, $q\bar{q} \to Z'$. The Z' production cross-section is the result of usual integration of the partonic cross-section $\sigma_{q\bar{q}\to Z'}$ with the parton distribution functions. We use the parton distribution functions provided by the MSTW PDF package [13] taking into account the 90% CL uncertainties of the parton distribution functions provided by the package.

The Z' decay width $\Gamma_{Z'}$ can be calculated by using the optical theorem:

$$\Gamma_{Z'} = -\frac{\operatorname{Im} G(m^2_{Z'})}{m_{Z'}}, \tag{11}$$

where $G(p^2)$ is the two-point one-particle-irreducible Green's function. We compute $\Gamma_{Z'}$ at the one-loop level with the help of the FeynArts, FormCalc and LoopTools software [14, 15]. The Feynman diagrams with internal Z' lines as well as the Passarino-Veltman integrals of type A give no contribution to the result, since they are real. The rest of diagrams correspond to different channels of Z' decay. As a result, we obtain also all the partial widths corresponding to Z' decays into two SM particles.

All the Z' couplings to the SM scalar and vector bosons can be determined by the universal axial-vector constant a_f and can be constrained. Then the partial widths corresponding to Z' decays into scalar and vector bosons are proportional to a_f^2. As for the fermionic decays, the width can be written in the form

$$\Gamma_{Z'\to\bar{f}f} = a_f^2\Gamma_{a_f^2} + a_f v_f \Gamma_{a_f v_f} + v_f^2 \Gamma_{v_f^2}. \tag{12}$$

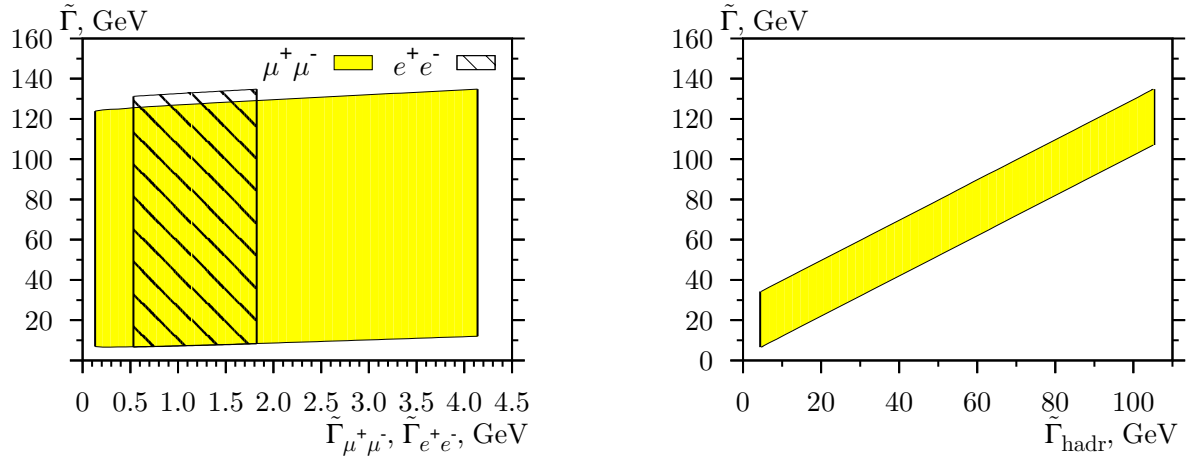

Figure 3. (a) The ML estimates on the $\tilde{\Gamma}$ versus $\tilde{\Gamma}_{e^+e^-}$ and $\tilde{\Gamma}_{\mu^+\mu^-}$ plane. The filled area is for dimuon channel, and the hatched area represents the dielectron channel. (b) The ML domain on the and $\tilde{\Gamma}$ versus $\tilde{\Gamma}_{\mathrm{hadr}}$ plane.

The factors $\Gamma_{a_f^2}$, $\Gamma_{a_f v_f}$ and $\Gamma_{v_f^2}$ are proportional to $m_{Z'}$. Expressing eq. (12) through the constants (3) one can see that the width is proportional to $m_{Z'}^3$ and quadratic combinations of couplings $\bar{a}$, $\bar{v}_f$. Thus it is convenient to introduce quantity

$$\tilde{\Gamma} = \Gamma_{Z'} \times \left(\frac{1\ \mathrm{TeV}}{m_{Z'}}\right)^3, \tag{13}$$

which is independent of $m_{Z'}$ in our estimates.

To calculate $\tilde{\Gamma}$ numerically one has to choose values of the unknown masses of the SM scalar particles. If the minimal SM is considered as the low-energy theory, the only unknown mass is the Higgs boson mass m_h. The modern constraints on its value indicate that it is quite heavy, $m_h \geq 114$ GeV. The contribution to the decay width from the scalar sector appears to be two or three orders of magnitude lower than the leading contribution from the fermionic decay channel. So the decay widths calculated at different values of m_h are practically indistinguishable. In this regard, we present the results obtained for $m_h = 125$ GeV.

When the THDM is considered, the scalar sector has six free parameters that can be expressed in terms of the masses m_h, m_H, m_{A_0}, $m_{H^\pm}$ and the mixing angles $\tan\alpha$, $\tan\beta$ (see [7] for details). Because of the large number of physical scalar fields the estimates for the Z' width within the THDM can deviate from the results obtained in the case of the minimal SM. In order to obtain the most significant difference, we choose $H^\pm$ and A_0 to be as light as it is allowed by the LEP constraints [16], namely $m_{H^\pm} = 81$ GeV, $m_{A_0} = 92$ GeV. The h and H masses are set to $m_h = m_H = 125$ GeV just like in the SM case. The dependence of $\tilde{\Gamma}$ on the mixing angles is negligibly weak. We take $\tan\beta = 2$, which respects the LEP constraints. The $\tan\alpha$ value is set to 0.75.

The Z' width (13) is plotted in Fig. 1 as the function of $\bar{v}_e$. The minimal SM and the THDM lead to slightly different bounds depicted in Fig. 2.

Since we chose the positive ML value of the axial-vector coupling $\bar{a}$, we obtain asymmetric domain in the parameter space within the ML estimate as it is seen in Figs. 1 and 2. This asymmetry arises from the term $\bar{a}\bar{v}_e\Gamma_{\bar{a}\bar{v}_e}$ in (12). Of course, the sign of $\bar{a}$ is not constrained by the experimental data, so the sign of the vector coupling should be considered as the relative sign with respect to the axial-vector coupling. For the electron vector coupling the 2σ hint was observed [11]. This allows to exclude the area near $\bar{v}_e = 0$ shown in the figures.

Consider an example of usage of the obtained estimates. Let us assume that the Z' mass is of order 1–2 TeV, for instance $m_{Z'} = 1.5$ TeV, so that the Z' production rate in the LHC and Tevatron processes is non-negligible and the direct searches are possible. The ML value $\tilde{\Gamma} \approx 50$ GeV leads to the total decay width $\Gamma_{Z'} = 169$ GeV. Thus we can expect the Z' resonance compatible with the narrow width approximation (NWA), $\Gamma_{Z'}^2/m_{Z'}^2 = 0.013 \ll 1$. However, one has to keep in mind that $\Gamma_{Z'} \approx m_{Z'}$ is not excluded at the 95% CL. The extremely narrow resonances with $\Gamma_{Z'} \approx 1$ GeV are also not excluded.

It is also useful to estimate the partial decay widths of the Z' boson. In this analysis we take the ML value of the axial-vector coupling $\bar{a} = \sqrt{0.13} \times 10^{-2}$ and vary other couplings in their 95% CL intervals. The results are presented as the plots in which a partial width is depicted versus the total width. In this way the branching ratios can be easily obtained.

The partial decay widths for the electron-positron, muon-antimuon, and quark-antiquark channels are shown in Fig. 3. On these plots, the difference between the SM and the THDM case is negligible. As it is seen, the

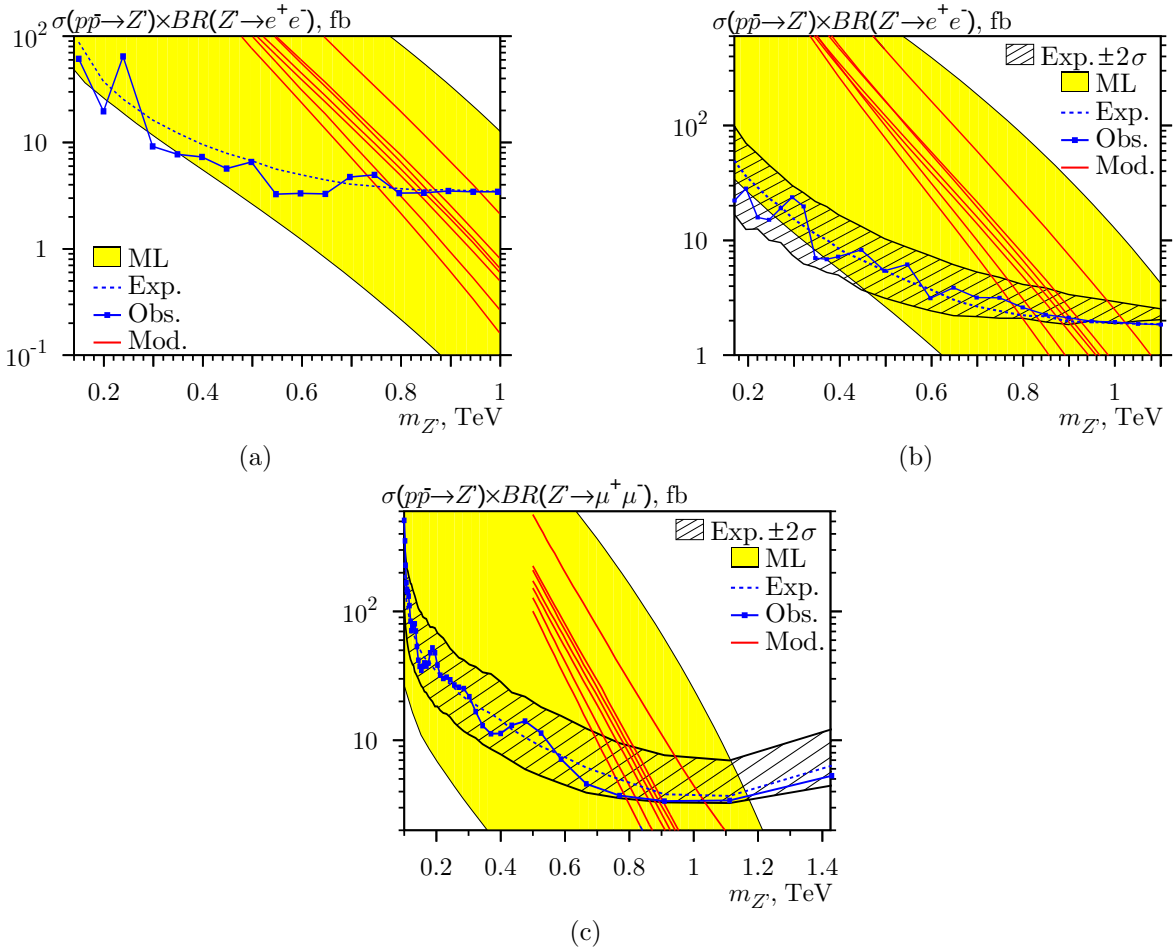

Figure 4. The ML domains for $\sigma(p\bar{p} \to Z') \times BR(Z' \to e^+e^-)$ and $\sigma(p\bar{p} \to Z') \times BR(Z' \to \mu^+\mu^-)$ at $\sqrt{S} = 1.96$ TeV together with the experimentally obtained upper limits on these contributions and E_6-model-based predictions. In all plots the filled areas represent the ML estimates; the E_6-model predictions are plotted in solid lines. The models are (corresponding to the plotted lines from left to right): $Z'_{\rm I}$, $Z'_{\rm sec}$, $Z'_{\rm N}$, Z'_{ψ}, Z'_{χ}, Z'_{η} and SSM Z'. The expected and observed 95% CL upper limits on the Z' contribution are shown as the dashed lines and line charts, respectively, and the hatched areas are the 2σ standard deviation bands for the expected values. The estimates for the dielectron channel compared to the data from CDF [17] and D0 [19] are presented in Figs. (a) and (b). In Fig. (c) the dimuon channel estimate and the CDF results [18] are shown.

branching ratio for the electron-positron decay channel can be expected in the wide interval

$$0.004 \leq BR(Z' \to e^+e^-) \leq 0.21. \tag{14}$$

Here, the minimal value corresponds to $\bar{v}_e = 0$, whereas the maximal value is reached at $\bar{v}_e = -\sqrt{1.69} \times 10^{-2}$. The significant difference between the estimates for $\tilde{\Gamma}_{e^+e^-}$ and $\tilde{\Gamma}_{\mu^+\mu^-}$ is caused by the fact that the Z' vector coupling to electron is much better constrained by the LEP II data that the muon one. The decay into quark-antiquark pairs can be the dominant decay channel. The corresponding probability can amount to 98%.

Considering the Z' partial widths, one can find a significant distinction between the SM and THDM in the scalar sector. Since $\bar{a}$ is the only Z' coupling entering the scalar and vector contributions to $\Gamma_{Z'}$, there is the ML value of the partial decay width into two SM bosons (vectors or scalars). In the SM case, $\tilde{\Gamma}_{\rm bosons} = 0.27$ GeV. In the THDM case, $\tilde{\Gamma}_{\rm bosons} = 0.53$ GeV. The corresponding branching ratios are less than 2.5%.

4 Constraints on the Z' mass from Tevatron data

The recent experiments at the LEP gave some hints of the Abelian Z' boson. Although these hints correspond to 68-95% CL, they can be used as a beacon showing the most optimistic scenario to find Z' boson with a mass near 1 TeV. It is interesting to speculate about the question how can those hints look like at Tevatron and LHC experiments. Taking the LEP ML value of the axial-vector coupling we can give predictions under the assumption that a signal of the Abelian Z' boson has been probably observed in the LEP data. This estimate, called maximum-likelihood scheme, represents the most bold expectations concerning the Abelian Z' boson. Of course, such predictions do not exclude Z' boson with weaker axial-vector couplings.

On the other hand the 95% CL bounds on possible Z' couplings to the SM particles are left behind the LEP experiments. Taking these bounds for all the Z' couplings we can exclude some values of the observables at hadron colliders. In this scheme the values outside of the predicted intervals are forbidden for the Abelian Z' boson. Being measured in experiments, such values have to be interpreted as a signal of new physics which is something else than the Z' boson. For example, considering the Z' width, we can expect $\Gamma_{Z'} \times (1\ \text{TeV}/m_{Z'})^3 \simeq 10 - 150$ GeV from the ML estimate, and we can think about the NWA for $m_{Z'} \leq 2$ TeV. On the other hand, only extremely narrow resonances, $\Gamma_{Z'} \times (1\ \text{TeV}/m_{Z'})^3 < 1$ GeV, and extremely wide resonances, $\Gamma_{Z'} \times (1\ \text{TeV}/m_{Z'})^3 > 500$ GeV, can be surely excluded at the 95% CL. Thus, waiting for a narrow Z' resonance at hadron colliders we have to keep in mind that a more rich Z' phenomenology is still allowed by existing data.

Now let us present the ML estimate for the Drell-Yan cross-section for the Tevatron experiments. As it was mentioned, in this case the NWA can be applied and the Z' contribution to the cross-section of the $pp\,(p\bar{p}) \to l\bar{l}$ process reads $\sigma(pp\,(p\bar{p}) \to Z') \times BR(Z' \to l\bar{l})$ where the branching ratio can be extracted from the total and partial Z' decay widths. The experimental bounds on the Z' contribution to the Drell-Yan process at the Tevatron are available in [17, 18, 19] together with the predictions from popular Z' models. The comparison between those results and our ML estimate for $\sigma(p\bar{p} \to Z' \to e^+e^-,\ \mu^+\mu^-)$ is presented in Figs. 4. We can conclude from both the D0 and CDF limits that the Z' hints from the LEP data can be the Abelian Z' boson with the mass between 400 GeV and 1.2 TeV. Our model-independent results cover all the popular Z' models. We can also conclude that the model-independent lower bound on the Z' mass is still about 400 GeV whereas the popular models give the lower bound of order $800 - 900$ GeV.

5 Conclusion

The model-independent relations for the Z' couplings give a good possibility to reduce the number of unknown Z' parameters. As a consequence, the Z' width and the production cross-sections of the processes at modern hadron colliders can be estimated using the constraints on the Z' couplings obtained from previous experiments at LEP. A combined analysis of the LEP, Tevatron and LHC data seems to be possible.

Our new model-independent results are complementary to the usual model-dependent schemes. The predictions of all the popular Z' models agree with our model-independent bounds.

Finally the Z' hints observed in the LEP data can be still hidden as the resonance in the Tevatron experiments. We can expect this Z' boson with the mass between 400 GeV and 1.2 TeV.

References

[1] A. Leike, Phys. Rep. **317**, 143 (1999).
[2] P. Langacker, Rev. Mod. Phys. **81**, 1199-1228 (2008) e-print arXiv:0801.1345 [hep-ph].
[3] T. Rizzo, e-print hep-ph/0610104.
[4] J. Erler, P. Langacker, S. Munir and E. R. Pena, JHEP **08**, 017 (2009).
[5] F. del Aguila, J. de Blas and M. Perez-Victoria, e-print arXiv:1005.3998.
[6] J. Erler, P. Langacker, S. Munir, E. Rojas, e-print arXiv:1010.3097v1 [hep-ph].
[7] A. V. Gulov and A. A. Kozhushko, Int. J. Mod. Phys. A **26**, 4083-4100 (2011) e-print arXiv:1105.3025v1.
[8] A. V. Gulov and V. V. Skalozub, Eur. Phys. J. C **17**, 685 (2000).
[9] A. V. Gulov and V. V. Skalozub, Phys. Rev. D **61**, 055007 (2000).
[10] A. V. Gulov and V. V. Skalozub, e-print arXiv:0905.2596v2 [hep-ph].
[11] A. V. Gulov and V. V. Skalozub, Int. J. Mod. Phys. A **25**, 5787-5815 (2010).
[12] G. Altarelli et al., Z. Phys. C **45**, 109 (1989); erratum Z. Phys. C **47**, 676 (1990).
[13] A.D. Martin, W.J. Stirling, R.S. Thorne and G. Watt, Eur. Phys. J. C **63**, 189 (2009); *ibid.* **64**, 653 (2009); *ibid.* **70**, 51 (2010); e-print arXiv:0901.0002v3 [hep-ph]; e-print arXiv:0905.3531v2 [hep-ph]; e-print arXiv:1007.2624v2 [hep-ph]; http://projects.hepforge.org/mstwpdf/.
[14] T. Hahn, Comput. Phys. Commun. **140**, 418 (2001) e-print arXiv:hep-ph/0012260v2; http://www.feynarts.de/.
[15] T. Hahn and M. Perez-Victoria, Comput. Phys. Commun. **118**, 153 (1999) e-print arXiv:hep-ph/9807565v1; http://www.feynarts.de/formcalc/, http://www.feynarts.de/looptools/.
[16] K. Nakamura et al. (Particle Data Group), J. Phys. G **37**, 2010 (075021).
[17] CDF Collaboration, T. Aaltonen et al., Phys. Rev. Lett. **102**, 031801 (2009) e-print arXiv:0810.2059.
[18] CDF Collaboration, T. Aaltonen et al., Phys. Rev. Lett. **102**, 091805 (2009) e-print arXiv:0811.0053.
[19] D0 Collaboration, V. Abazov, et al., Phys. Lett. B **695**, 88 (2011) e-print arXiv:1008.2023.

Proceedings of the International School-seminar
"New Physics and Quantum Chromodynamics at External Conditions", pp. 41 – 48,
3-6 May 2011, Dnipropetrovsk, Ukraine

RARE DECAY OF $\bar{B}^0$ MESON TO $\bar{K}^{*0}$ AND LEPTON PAIR

A. Yu. Korchin[a], V. A. Kovalchuk[b], D. O. Lazarenko[c]

Akhiezer Institute for Theoretical Physics, NSC "Kharkov Institute of Physics and Technology", Kharkov 61108, Ukraine

Branching ratio and other observables for the rare flavour-changing neutral current decay $\bar{B}^0_d \to \bar{K}^{*0}(\to K^-\pi^+)\, e^+ e^-$ are studied below $\bar{c}c$ threshold. The total amplitude for this decay includes the term coming from the Standard Model effective Hamiltonian and the term generated by the processes $\bar{B}^0_d \to \bar{K}^{*0}(\to K^-\pi^+)\, V$ with intermediate low-lying vector resonances $V = \rho(770)$, $\omega(782)$, $\phi(1020)$ decaying into the e^+e^- pair. Influence of the resonances in the region of electron-positron invariant mass up to 2.5 GeV is studied in view of measurements on LHCb.

1 Introduction

The investigation of rare B decays induced by the flavour-changing neutral current (FCNC) transitions $b \to s$ and $b \to d$ represents an important test of the Standard Model (SM) or its extensions (see [1] for a review). Among the rare decays, the radiative decay $b \to s\gamma$ has probably been the most popular FCNC transition ever since its experimental observation as $B \to K^*\gamma$ at CLEO in 1993 [2]. This decay proceeds through a loop (penguin) diagram, to which high-mass particles introduced in extensions to the SM may contribute with a sizeable amplitude. The size of the decay rate itself, however, provides only a mild constraint on such extensions, because the SM predictions for exclusive rates suffer from large and model dependent form factor uncertainties [3, 4]. Further reduction in the theory errors appears rather difficult. Therefore it is advantageous to use in addition to the rates other observables that can reveal New Physics (NP).

In particular, in framework of the SM, the photons emitted in $b \to s\gamma$ decays are predominantly left-handed, while those emitted in $\bar{b}$ decay are predominantly right-handed. The amplitude for emission of wrong-helicity photons is suppressed by a factor $\propto m_s/m_b$ [5], but this suppression can easily be alleviated in a large number of NP scenarios where the helicity flip occurs on an internal line.

Measurement of the photon helicity is therefore of interest. Several different methods of measuring the photon polarization have been suggested, however it appears that the photon polarization is difficult to measure, and one has to use rather the process $b \to s\gamma^* \to s\ell^+\ell^-$, where the photon is converted to the lepton pair. In this decay the angular distributions and lepton polarizations can probe the chiral structure of the matrix element [6, 7, 8, 9, 10, 11, 12] and thereby the NP effects.

In order to measure effects of NP in the process $b \to s\ell^+\ell^-$ one needs to calculate the SM predictions with a rather good accuracy. The SM amplitude consists of the short-distance (SD) contribution and the long-distance (LD) ones. The former is expressed in terms of the Wilson coefficients C_i calculated in perturbative QCD; they carry information on processes at energy scale $\sim m_W,\ m_t$. These coefficients are then evolved using the renormalization group methods to the energies related to the bottom quark mass m_b.

The LD terms include factorizable and non-factorizable effects from virtual photon via the semi-leptonic operators $\mathcal{O}_{9V,\,10A}$ and electromagnetic dipole penguin operator $\mathcal{O}_{7\gamma}$ in effective Hamiltonian. The radiative corrections coming from operators $\mathcal{O}_{1-6}$ and gluon penguin operator $\mathcal{O}_{8g}$ are also accounted for [13].

The LD effects describing the hadronization process are expressed in terms of matrix elements of the $b \to s$ operators between the initial B and the K^* final state. These matrix elements are parameterized in terms of form factors [8] that are calculated with the help of light-cone sum rules (LCSR) [14] or in soft-collinear effective theory (SCET) [15]. The form factors have large theoretical uncertainties that are presently the dominant uncertainties in the SM predictions for exclusive decays.

The presence of additional LD effects originating from intermediate vector resonances $\rho(770)$, $\omega(782)$, $\phi(1020)$, $J/\psi(1S)$, $\psi(2S)$,... complicates the description. These resonances show up in the region of relatively small dilepton invariant mass $m_{ee} \equiv \sqrt{q^2}$, where $q^2 = (q_+ + q_-)^2$. In order to suppress the charmonia contribution, often the region of large dilepton mass ($q^2 \gg 4m_c^2 \approx 6.5$ GeV^2) is selected, for example, BaBar and Belle Collaborations apply the corresponding experimental cuts [16, 17].

The region of small dilepton invariant mass, $m_{ee} < 1$ GeV, has also high potential of searching effects of the NP [6]. At small $m_{ee} \sim M_R$ the low-lying vector resonances modify the amplitude, and thus may induce in certain observables the right-handed photon polarization, which is still small but not negligible. The presence of

e-mail: [a]korchin@kipt.kharkov.ua, [b]koval@kipt.kharkov.ua, [c]denis.lazarenko@gmail.com

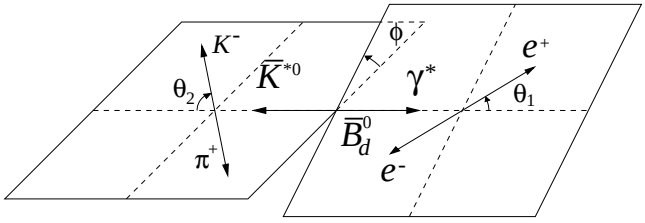

Figure 1. Definition of helicity angles θ_1, θ_2, and ϕ, for the decay $\bar{B}^0_d \to \bar{K}^{*0}\, e^+\, e^-$.

the photon propagator $1/q^2$ enhances the resonance contribution. Recently the authors of [18] analyzed angular distribution in the rare decay $\bar{B}^0 \to \bar{K}^{*0} e^+ e^-$ in the small-q^2 region in order to test possibility to measure this distribution at LHCb.

We study the $\bar{B}^0 \to \bar{K}^{*0} e^+ e^-$ decay at dilepton invariant mass $m_{ee} < 2.5$ GeV. Both the SD and LD effects in the amplitude are evaluated. The effective Hamiltonian with the Wilson coefficients in next-to-next-to-leading order (NNLO) approximation is used. The LD effects mediated by the resonances, *i.e.* $\bar{B}^0 \to \bar{K}^{*0} V \to \bar{K}^{*0}\gamma^* \to \bar{K}^{*0} e^+ e^-$ with $V = \rho(770),\ \omega(782),\ \phi(1020)$, are included explicitly in terms of amplitudes of the decays $\bar{B}^0 \to \bar{K}^{*0} V$.

Sensitivity of the observables to the choice of form factors of the transition $B \to K^*$ is also investigated. Various models are chosen in our calculation.

Among all observables we calculate, in particular, the coefficient $A_{\rm T}^{(2)}$ which determines $\cos(2\phi)$ dependence in the angular distribution of the leptons (ϕ is the angle between the plane spanned by $e^+,\ e^-$ and the plane spanned by the decay products $K^-,\ \pi^+$ of the $\bar{K}^{*0}$ meson) and fraction of longitudinal polarization of $\bar{K}^{*0}$ meson.

2 Angular distributions and amplitudes for the $\bar{B}^0_d \to \bar{K}^{*0}\, e^+\, e^-$ decay

The decay $\bar{B}^0_d \to \bar{K}^{*0}\, e^+\, e^-$ with $\bar{K}^{*0} \to K^-\pi^+$ on the mass shell is completely described by four independent kinematic variables, the electron-positron pair invariant mass squared, q^2, and the three angles θ_1, θ_2, ϕ. In the helicity frame (Fig. 1), the angle θ_1 (θ_2) is defined as the angle between the directions of motion of e^+ (K^-) in the γ^* ($\bar{K}^{*0}$) rest frame and the γ^* ($\bar{K}^{*0}$) in the $\bar{B}^0_d$ rest frame. The azimuthal angle ϕ is defined as the angle between the decay planes of $\gamma^* \to e^+\, e^-$ and $\bar{K}^{*0} \to K^-\pi^+$ in the $\bar{B}^0_d$ rest frame.

The differential decay rate in these coordinates is specified and discusses in Ref. [19]. Having rich multi-dimensional structure, this decay rate is sensitive to various effects modifying the SM, such as CP violation beyond the CKM and/or right-handed currents. Given sufficient data, all bilinear combinations of amplitudes can in principle be completely measured from the full angular distribution in all three angles θ_1, θ_2 and ϕ.

Here we concentrate on the two-dimensional differential decay rate in q^2 and azimuthal angle ϕ. After integration of fully differential decay rate over the polar angles $\cos\theta_1$ and $\cos\theta_2$, we obtain:

$$\frac{d^2\,\Gamma}{d\hat{q}^2 d\phi} = \frac{1}{2\pi}\frac{d\,\Gamma}{d\hat{q}^2}\left(1 + \frac{1}{2}(1-f_0)A_{\rm T}^{(2)}\cos 2\phi - A_{\rm Im}\sin 2\phi\right)\,, \tag{1}$$

where the electron-positron pairs invariant mass spectrum is

$$\frac{d\,\Gamma}{d\hat{q}^2} = m_B\left(|A_0|^2 + |A_\parallel|^2 + |A_\perp|^2\right)\,, \tag{2}$$

and coefficients determining angular dependence in (1) are

$$A_{\rm T}^{(2)} \equiv \frac{f_\perp - f_\parallel}{f_\perp + f_\parallel}\,, \qquad\qquad A_{\rm Im} \equiv \frac{{\rm Im}(A_\parallel A_\perp^*)}{\sum_k |A_k|^2}\,, \tag{3}$$

where the fractions of K^* meson polarization are defined as

$$f_i = \frac{|A_i|^2}{\sum_k |A_k|^2}\,, \qquad\qquad f_0 + f_\parallel + f_\perp = 1 \tag{4}$$

with $i,k = (0,\parallel,\perp)$. Further, m_B is the mass of the B^0_d meson, $\hat{q}^2 \equiv q^2/m_B^2$, and $A_i A_j^* \equiv A_{iL}(q^2)A_{jL}^*(q^2) + A_{iR}(q^2)A_{jR}^*(q^2)$, where $A_{0L(R)}$, $A_{\parallel L(R)}$ and $A_{\perp L(R)}$ are the complex decay amplitudes of the three helicity states in the transversity basis (see details in [19]).

At present the decay rate (1) is experimentally studied at LHCb [18].

3 Formalism of the $\bar{B}^0_d \to \bar{K}^{*0}\, e^+\, e^-$ decay

Within the SM, neglecting contributions proportional to the small CKM factor $V^*_{us}V_{ub}$, the effective Hamiltonian for the quark-level transition $b \to s\, e^+ e^-$ is

$$\mathcal{H}_{\rm eff} = -\frac{4G_F}{\sqrt{2}}\, V^*_{ts}V_{tb} \Big\{ \sum_{i=1}^{6} C_i \mathcal{O}_i + C_{7\gamma}\mathcal{O}_{7\gamma} \ + C_{8g}\mathcal{O}_{8g} + C_{9V}\mathcal{O}_{9V} + C_{10A}\mathcal{O}_{10A} \Big\}, \tag{5}$$

where V_{ij} are the CKM matrix elements [20] and G_F is the Fermi coupling constant. We use the operator basis introduced in [21] for the operators $\mathcal{O}_i$, $i = 1, \ldots, 6$, while the remaining ones are given by

$$\mathcal{O}_{7\gamma} = \frac{e}{16\pi^2}\, \bar{s}\, \sigma^{\mu\nu} (\overline{m}_b(\mu) P_R + \overline{m}_s(\mu) P_L)\, b\, F_{\mu\nu}\,, \tag{6}$$

$$\mathcal{O}_{8g} = \frac{g_s}{16\pi^2}\, \bar{s}\, \sigma^{\mu\nu} (\overline{m}_b(\mu) P_R + \overline{m}_s(\mu) P_L)\, T^a\, b\, G^a_{\mu\nu}, \tag{7}$$

$$\mathcal{O}_{9V} = \frac{\alpha_{\rm em}}{4\pi}\, (\bar{s}\gamma_\mu P_L b)\, \bar{e}\gamma^\mu e\,, \qquad \mathcal{O}_{10A} = \frac{\alpha_{\rm em}}{4\pi}\, (\bar{s}\,\gamma_\mu P_L b)\, \bar{e}\,\gamma^\mu\gamma_5 e\,, \tag{8}$$

where $\alpha_{\rm em} = e^2/(4\pi) = 1/137$ is the electromagnetic fine-structure constant, g_s is the QCD coupling constant and $P_{L,R} = (1 \mp \gamma_5)/2$ denote chiral projectors. $\overline{m}_b(\mu)$ ($\overline{m}_s(\mu)$) is the running bottom (strange) quark mass in the $\overline{\rm MS}$ scheme at the scale μ. T^a ($a = 1, \ldots, 8$) are the generators of $SU(3)$ color group. Here $F_{\mu\nu}$ and $G^a_{\mu\nu}$ denote the electromagnetic and chromomagnetic field strength tensor, respectively. The Wilson coefficients C_i in Eq. (5) are calculated at the scale $\mu = m_W$, in a perturbative expansion in powers of $\alpha_s(m_W)$ ($\alpha_s(\mu) \equiv g_s^2/(4\pi)$ is the effective QCD coupling constant), and are then evolved down to scales $\mu \sim m_b$ using the renormalization group equations. The $\overline{\rm MS}$ mass $\overline{m}_b(\mu)$ can be related with the pole mass m_b at the scale $\mu = m_b$ through [22, 23]:

$$\overline{m}_b(m_b) = m_b \Big(1 - \frac{4}{3}\frac{\alpha_s(m_b)}{\pi} - 10.167 \Big(\frac{\alpha_s(m_b)}{\pi}\Big)^2 + \mathcal{O}\Big(\Big(\frac{\alpha_s(m_b)}{\pi}\Big)^3\Big)\Big)\,. \tag{9}$$

The up to date value of the strange quark mass is $\overline{m}_s(2\,{\rm GeV}) = 95 \pm 25\,{\rm MeV}$. Note that this running mass is evaluated at $\mu_0 = 2\,{\rm GeV}$ with three active quark flavours. The evolution of the $\overline{m}_s(\mu)$ is governed by the renormalization group equation. It has the solution [24]

$$\frac{\overline{m}_s(\mu)}{\overline{m}_s(\mu_0)} = \frac{f(\alpha_s(\mu)/\pi)}{f(\alpha_s(\mu_0)/\pi)}\,, \qquad \text{with} \quad f(x) = x^{\frac{4}{9}}(1 + 0.895062\, x + 1.37143\, x^2) + \mathcal{O}(x^4)\,.$$

The matrix element of the effective Hamiltonian Eq. (5) for the non-resonance (NR) decay $\bar{B}^0_d(p) \to \bar{K}^{*0}(k,\epsilon)\, e^+(q_+)\, e^-(q_-)$ can be written, in the so-called naïve factorization [25], as

$$\begin{aligned} \mathcal{M}_{\rm NR} = \frac{G_F\alpha_{\rm em}}{\sqrt{2}\pi}\, V^*_{ts}V_{tb} \Big(& \langle \overline{K^{*0}}(k,\epsilon)|\bar{s}\gamma_\mu P_L b|\overline{B^0_d}(p)\rangle \big(C^{\rm eff}_{9V}\, \bar{u}(q_-)\gamma^\mu v(q_+) + C_{10A}\, \bar{u}(q_-)\gamma^\mu\gamma_5 v(q_+)\big) \\ & - \frac{2}{q^2} C^{\rm eff}_{7\gamma} \langle \overline{K^{*0}}(k,\epsilon)|\bar{s}\, i\, \sigma_{\mu\nu} q^\nu (\overline{m}_b(\mu) P_R + \overline{m}_s(\mu) P_L)\, b|\overline{B^0_d}(p)\rangle\, \bar{u}(q_-)\gamma^\mu v(q_+)\Big)\,. \end{aligned} \tag{10}$$

Here, $\sigma_{\mu\nu} = \frac{i}{2}[\gamma_\mu, \gamma_\nu]$, $q_\mu = (q_+ + q_-)_\mu$, $C^{\rm eff}_{7\gamma} = C_{7\gamma} - (4\bar{C}_3 - \bar{C}_5)/9 - (4\bar{C}_4 - \bar{C}_6)/3$, $C^{\rm eff}_{9V} = C_{9V} + Y(q^2)$, and the function $Y(q^2)$ is given by [26]

$$\begin{aligned} Y(q^2) = {} & h(q^2, m_c)(3\,\bar{C}_1 + \bar{C}_2 + 3\,\bar{C}_3 + \bar{C}_4 + 3\,\bar{C}_5 + \bar{C}_6) - \frac{1}{2}h(q^2, m_b)(4\,\bar{C}_3 + 4\,\bar{C}_4 + 3\,\bar{C}_5 + \bar{C}_6) \\ & - \frac{1}{2}h(q^2, 0)(\bar{C}_3 + 3\,\bar{C}_4) + \frac{2}{9}\,(\frac{2}{3}\,\bar{C}_3 + 2\,\bar{C}_4 + \frac{16}{3}\,\bar{C}_5)\,, \end{aligned} \tag{11}$$

where the "barred" coefficients $\bar{C}_i$ (for $i = 1, \ldots, 6$) are defined as certain linear combinations of the C_i, such that the $\bar{C}_i$ coincide at leading logarithmic order with the Wilson coefficients in the standard basis [13]. m_c denotes the pole mass of charm quark. The function

$$h(q^2, m_q) = -\frac{4}{9}\left(\ln\frac{m_q^2}{\mu^2} - \frac{2}{3} - z\right) - \frac{4}{9}\,(2+z)\,\sqrt{|z-1|} \begin{cases} \arctan\dfrac{1}{\sqrt{z-1}} & z > 1\,, \\ \ln\dfrac{1+\sqrt{1-z}}{\sqrt{z}} - \dfrac{i\pi}{2} & z \le 1\,, \end{cases} \tag{12}$$

$$h(q^2, 0) = -\frac{4}{9}\ln\frac{q^2}{\mu^2} + \frac{8}{27} + i\frac{4\pi}{9}\,, \tag{13}$$

Figure 2. Non-resonant and resonant contributions to the decay amplitude.

with $z = 4m_q^2/q^2$, is related to the basic fermion loop.

The hadronic part of the matrix element in Eq. (10) describing the $B \to K^* e^+ e^-$ transition can be parameterized in terms of $B \to K^*$ vector, axial-vector and tensor form factors. The models for the form factors are discussed in [19].

Based on the matrix element in Eq. (10), the non-resonant amplitudes can be written in terms of the vector $V(q^2)$, axial-vector $A_{1,2}(q^2)$ and tensor $T_{1,2,3}(q^2)$ form factors as

$$A^{\rm NR}_{0L,R} = -\frac{N\hat{\lambda}^{1/4}}{2\hat{m}_{K^*}}\Bigg((C^{\rm eff}_{9V} \mp C_{10A}) \left((1-\hat{q}^2-\hat{m}^2_{K^*})(1+\hat{m}_{K^*})\, A_1(q^2) - \hat{\lambda}\frac{A_2(q^2)}{1+\hat{m}_{K^*}} \right)$$

$$+2(\hat{m}_b-\hat{m}_s)\, C^{\rm eff}_{7\gamma} \left((1-\hat{q}^2+3\hat{m}^2_{K^*})\, T_2(q^2) - \frac{\hat{\lambda}}{1-\hat{m}^2_{K^*}} T_3(q^2) \right) \Bigg), \qquad (14)$$

$$A^{\rm NR}_{\parallel L,R} = N(1-\hat{m}^2_{K^*})\sqrt{2\hat{q}^2}\,\hat{\lambda}^{1/4} \Big((C^{\rm eff}_{9V} \mp C_{10A}) \frac{A_1(q^2)}{1-\hat{m}_{K^*}} + 2\frac{\hat{m}_b-\hat{m}_s}{\hat{q}^2}\, C^{\rm eff}_{7\gamma}\, T_2(q^2) \Big), \qquad (15)$$

$$A^{\rm NR}_{\perp L,R} = -N\sqrt{2\hat{q}^2}\,\hat{\lambda}^{3/4} \Big((C^{\rm eff}_{9V} \mp C_{10A}) \frac{V(q^2)}{1+\hat{m}_{K^*}} + 2\frac{\hat{m}_b+\hat{m}_s}{\hat{q}^2}\, C^{\rm eff}_{7\gamma}\, T_1(q^2) \Big). \qquad (16)$$

In the above formulas the definition $\hat{m}_{K^*} \equiv m_{K^*}/m_B$, $\hat{\lambda} \equiv \lambda(1,\hat{q}^2,\hat{m}^2_{K^*}) = (1-\hat{q}^2)^2 - 2(1+\hat{q}^2)\hat{m}^2_{K^*} + \hat{m}^4_{K^*}$, $\hat{m}_b \equiv \overline{m}_b(\mu)/m_B$, $\hat{m}_s \equiv \overline{m}_s(\mu)/m_B$ is used, where m_{K^*} is the mass of the K^{*0} meson, and $N = |V_{tb}V^*_{ts}|\, G_F m_B^2 \alpha_{\rm em}/(32\,\pi^2\sqrt{3\,\pi})$.

The transversity amplitudes in (14)–(16) take a particularly simple form in the heavy-quark and large-energy limit. This limit is analyzed in Ref. [19]. It follows from this analysis that in the region of very small invariant masses, $q^2 \ll m^2_{K^*} = 0.803$ GeV^2, the asymmetry $A^{(2)}_{\rm T}$ in Eq. (3) takes the simple form

$$A^{(2)}_{\rm T} \approx \frac{2m_s}{m_b}\,. \qquad (17)$$

This result is in agreement with well-known fact, that in the SM for $m_s = 0$ in naïve factorization, $A^{(2)}_{\rm T} = 0$ [9].

In some extensions of the SM, such as left-right model and unconstrained supersymmetric SM, there are right-handed currents in the matrix element, with the magnitude determined by the coupling $C'^{\rm eff}_{7\gamma}$ (see, e.g. Ref. [9]). In this case the asymmetry $A^{(2)}_{\rm T}$ is written as

$$A^{(2)}_{\rm T} \;\approx\; \frac{2\, C'^{\rm eff}_{7\gamma}\, C^{\rm eff}_{7\gamma}}{(C^{\rm eff}_{7\gamma})^2 \,+\, (C'^{\rm eff}_{7\gamma})^2}. \qquad (18)$$

3.1 Resonant contribution

Next, we implement the effects of LD contributions from the decays $\bar{B}^0_d \to \bar{K}^{*0}\, V$ where $V = \rho^0\,, \omega\,, \phi$ mesons, followed by $V \to e^+\, e^-$ in the decay $\bar{B}^0_d \to \bar{K}^{*0}\, e^+\, e^-$ (see Fig. 2):

We apply vector-meson dominance (VMD) approach. In general, the $\gamma - V$ transition can be included into consideration using various versions of VMD model. In the "standard" version (see, e.g. [27], chapter 6), the $\gamma - V$ transition vertex can be written as

$$\langle \gamma(\mu)|V(\nu)\,\rangle = -e f_V Q_V m_V\, g^{\mu\nu}\,, \qquad (19)$$

where $g^{\mu\nu}$ is the metric tensor, Q_V is the effective electric charge of the quarks in the vector meson: $Q_\rho = \frac{1}{\sqrt{2}}\,, \quad Q_\omega = \frac{1}{3\sqrt{2}}\,, \quad Q_\phi = -\frac{1}{3}$.

The constants f_V can be found from the vector-meson decay width to lepton pair

$$\Gamma(V \to l^+ l^-) = \frac{4\pi\alpha^2_{em}}{3}\frac{f_V^2 Q_V^2}{m_V}\left(1+\frac{2m_l^2}{m_V^2}\right)\sqrt{1-\frac{4m_l^2}{m_V^2}}\,. \qquad (20)$$

Table 1. Mass, total width, leptonic decay width and coupling f_V of vector mesons [32] (experimental uncertainties are not shown).

V	m_V , MeV	Γ_V , MeV	$\Gamma(V \to e^+ e^-)$, keV	f_V , MeV
ρ^0	775.49	149.1	7.04	221.3
ω	782.65	8.49	0.60	194.7
ϕ	1019.455	4.26	1.27	228.6

This version of VMD model will be called VMD1. The vertex (19) comes from the transition Lagrangian

$$\mathcal{L}_{\gamma V} = -eA^\mu \sum_V f_V Q_V m_V V_\mu \,. \tag{21}$$

A more elaborate model (called hereafter VMD2) originates from Lagrangian

$$\mathcal{L}_{\gamma V} = -\frac{e}{2} F^{\mu\nu} \sum_V \frac{f_V Q_V}{m_V} V_{\mu\nu} \,, \tag{22}$$

where $V_{\mu\nu} \equiv \partial_\mu V_\nu - \partial_\nu V_\mu$ and $F^{\mu\nu} \equiv \partial^\mu A^\nu - \partial^\nu A^\mu$ is the electromagnetic field tensor.

Lagrangian (22) is explicitly gauge invariant, unlike Eq. (21), and gives rise to to the $\gamma - V$ vertex

$$\langle\, \gamma(\mu) | V(\nu) \,\rangle = -\frac{e f_V Q_V}{m_V} \left(q^2 g^{\mu\nu} - q^\mu q^\nu\right), \tag{23}$$

where q is the virtual photon (vector meson) four-momentum. This transition vertex is suppressed at small invariant masses, $q^2 \ll m_V^2$, i.e. in the region far from the vector-meson mass shell [1].

Note that these two versions of the VMD model have been discussed in Refs. [28, 29]. The VMD2 version naturally follows from the Resonance Chiral Theory [30]; in this context VMD2 coupling has been applied in [31] for studying electron-positron annihilation into $\pi^0\pi^0\gamma$ and $\pi^0\eta\gamma$ final states.

Parameters of vector resonances are presented in Table 1.

3.2 Amplitudes for $\bar{B}_d^0 \to \bar{K}^{*0} V$ decay

An important ingredient of the resonant contribution is amplitude of the decay of B meson into two vector mesons, $B(p) \to V_1(q, \lambda_1) + V_2(k, \lambda_2)$, with on-mass-shell meson V_2 ($k^2 = m_2^2$) and off-mass-shell meson V_1 ($q^2 \neq m_1^2$).

For the case of two on-mass-shell final mesons one can write the amplitude in the form

$$\mathcal{M} = \Gamma_{\mu\nu} \epsilon_1^{\mu *}(q) \epsilon_2^{\nu *}(k) \,, \qquad \Gamma_{\mu\nu} = a\, g_{\mu\nu} + b\, p_\mu p_\nu - ic\, \epsilon_{\mu\nu\alpha\beta} q^\alpha k^\beta \tag{24}$$

in terms of Lorentz scalars a, b, c, $\epsilon_{0123} = +1$, and the four-momenta in the B-meson rest frame are $p^\mu = (m_B, \overrightarrow{0})$, $q^\mu = (E_1, 0, 0, |\overrightarrow{q}^*|)$, $k^\mu = (E_2, 0, 0, -|\overrightarrow{q}^*|)$. We will use the notation $\hat{m}_{1(2)} \equiv m_{1(2)}/m_B$ and put $p^2 = m_B^2$. Conservation of angular momentum requires for the vector-meson helicities $\lambda_1 = \lambda_2 \equiv \lambda$.

Define $H_\lambda \equiv H_{\lambda_1 \lambda_2} = \Gamma_{\mu\nu} \epsilon_1^{\mu *}(\lambda) \epsilon_2^{\nu *}(\lambda)$ and find the relations:

$$H_0 = -\frac{1}{2\hat{m}_1 \hat{m}_2} \left[(1 - \hat{m}_1^2 - \hat{m}_2^2)\, a + \frac{m_B^2}{2} \lambda(1, \hat{m}_1^2, \hat{m}_2^2)\, b \right], \qquad H_\pm = a \pm \frac{m_B^2}{2} \sqrt{\lambda(1, \hat{m}_1^2, \hat{m}_2^2)}\, c \,, \tag{25}$$

with $\lambda(1, \hat{m}_1^2, \hat{m}_2^2) \equiv (1 - \hat{m}_1^2)^2 - 2\hat{m}_2^2(1 + \hat{m}_1^2) + \hat{m}_2^4$.

One can also introduce another set of amplitudes

$$A_\parallel = \frac{1}{\sqrt{2}}(H_+ + H_-) \,, \qquad A_\perp = \frac{1}{\sqrt{2}}(H_+ - H_-) \,, \qquad A_0 = H_0 \,, \tag{26}$$

$$A_\parallel = \sqrt{2}\, a \,, \quad A_\perp = m_B^2 \sqrt{\frac{\lambda(1, \hat{m}_1^2, \hat{m}_2^2)}{2}}\, c \,, \quad A_0 = -\frac{1}{2\hat{m}_1 \hat{m}_2} \left[(1 - \hat{m}_1^2 - \hat{m}_2^2)\, a + \frac{m_B^2}{2} \lambda(1, \hat{m}_1^2, \hat{m}_2^2)\, b \right]. \tag{27}$$

The decay width is expresses as follows:

$$\Gamma(B \to V_1 V_2) = \frac{m_B}{2} \sqrt{\lambda(1, \hat{m}_1^2, \hat{m}_2^2)} \frac{1}{8\pi m_B^2} \left(|H_0|^2 + |H_+|^2 + |H_-|^2 \right) = \frac{\sqrt{\lambda(1, \hat{m}_1^2, \hat{m}_2^2)}}{16\pi m_B} \sum_\lambda |A_\lambda|^2 \,. \tag{28}$$

[1] The term $\propto q^\mu q^\nu / q^2$ in (23) does not contribute when contracted with the leptonic current

Table 2. Branching ratio [33], and decay amplitudes for $B_d^0 \to K^{*0}\rho^0$ [34], $B_d^0 \to K^{*0}\omega$ [34] and $B_d^0 \to K^{*0}\phi$ [33].

Mode	$K^{*0}\rho^0$	$K^{*0}\omega$	$K^{*0}\phi$
$\mathrm{Br}(B_d^0 \to K^{*0}V)$	3.4×10^{-6}	2.0×10^{-6}	9.8×10^{-6}
$\lvert h_0^V\rvert^2$	0.70	0.75	0.480
$\lvert h_\perp^V\rvert^2$	0.14	0.12	0.24
$\arg(h_\parallel^V/h_0^V)$ (rad)	1.17	1.79	2.40
$\arg(h_\perp^V/h_0^V)$ (rad)	1.17	1.82	2.39

Table 3. The numerical input used in our analysis. Quark and meson masses are given in GeV.

$\lvert V_{tb}V_{ts}^*\rvert$	G_F, GeV^{-2}	$\mu = m_b$	m_c	$\overline{m}_b(\mu)$	$\overline{m}_s(\mu)$	m_B	m_{K^*}	τ_B, ps
0.0407	1.16637×10^{-5}	4.8	1.4	4.14	0.079	5.2795	0.896	1.525

Next, we define the normalized amplitudes:

$$h_\lambda \equiv \frac{A_\lambda}{\sqrt{\sum_{\lambda'}|A_{\lambda'}|^2}}\,, \qquad \sum_\lambda |h_\lambda|^2 = 1 \qquad (\lambda,\lambda' = 0,\parallel,\perp)\,. \tag{29}$$

By putting $m_1 = m_V$, $m_2 = m_{K^*}$ and using (28), (29) we obtain the relation between the amplitudes h_λ and A_λ of the process under study $\bar{B}_d^0 \to \bar{K}^{*0}V$ for any vector meson $V = \rho(770),\ \omega(782),\ \phi(1020)$:

$$h_\lambda^V = \frac{1}{4}\lambda^{1/4}(1,\hat{m}_V^2,\hat{m}_{K^*}^2)\sqrt{\frac{\tau_B}{\pi\, m_B\,\mathrm{Br}(\bar{B}_d^0 \to \bar{K}^{*0}V)}}A_\lambda^V\,, \tag{30}$$

where $\mathrm{Br}(\ldots)$ is the branching ratio of $\bar{B}_d^0 \to \bar{K}^{*0}V$ decay and τ_B is the lifetime of a B meson.

Solving Eqs. (27) we find the scalars a, b and c, and then extend the helicity amplitudes A_λ^V off the mass shell of the meson V, i.e. for $q^2 \neq m_V^2$. We introduce the phases $\delta_\lambda^V \equiv \arg(h_\lambda^V) = \arg(A_\lambda^V)$, and will count the phases of the off-shell amplitudes relative to the phase of h_0^V. Then we have

$$\begin{aligned}
A_\parallel^V(q^2) &= |A_\parallel^V|\, e^{i(\delta_\parallel^V - \delta_0^V)}\,, \qquad A_\perp^V(q^2) = \sqrt{\frac{\lambda(1,\hat{q}^2,\hat{m}_{K^*}^2)}{\lambda(1,\hat{m_V}^2,\hat{m}_{K^*}^2)}}\,|A_\perp^V|\, e^{i(\delta_\perp^V - \delta_0^V)}\,,\\
A_0^V(q^2) &= -\frac{1}{4\sqrt{\hat{q}^2}\hat{m}_{K^*}}\left[\sqrt{2}(1-\hat{q}^2-\hat{m}_{K^*}^2)|A_\parallel^V|\, e^{i(\delta_\parallel^V-\delta_0^V)} + \lambda(1,\hat{q}^2,\hat{m}_{K^*}^2)|\hat{b}^V|\, e^{i(\Phi_b-\delta_0^V)}\right],\\
|\hat{b}^V| &\equiv m_B^2|b^V| = \frac{\sqrt{2}}{\lambda(1,\hat{m}_V^2,\hat{m}_{K^*}^2)}\Big[8\hat{m}_{K^*}^2\hat{m}_V^2|A_0^V|^2 + \left(1-\hat{m}_V^2-\hat{m}_{K^*}^2\right)^2|A_\parallel^V|^2\\
&+ 4\sqrt{2}\hat{m}_{K^*}\hat{m}_V(1-\hat{m}_V^2-\hat{m}_{K^*}^2)|A_0^V||A_\parallel^V|\cos((\delta_\parallel^V-\delta_0^V))\Big]^{1/2},\\
\sin(\Phi_b^V-\delta_0^V) &= -\frac{1}{|\hat{b}^V|}\frac{\sqrt{2}}{\lambda(1,\hat{m}_V^2,\hat{m}_{K^*}^2)}(1-\hat{m}_V^2-\hat{m}_{K^*}^2)|A_\parallel^V|\sin((\delta_\parallel^V-\delta_0^V))\,,\\
\cos(\Phi_b^V-\delta_0^V) &= -\frac{1}{|\hat{b}^V|}\frac{\sqrt{2}}{\lambda(1,\hat{m}_V^2,\hat{m}_{K^*}^2)}\left[2\sqrt{2}\hat{m}_V\hat{m}_{K^*}|A_0^V| + (1-\hat{m}_V^2-\hat{m}_{K^*}^2)|A_\parallel^V|\cos((\delta_\parallel^V-\delta_0^V)\right].
\end{aligned} \tag{31}$$

Finally, we obtain the total amplitude including non-resonant and resonant parts

$$A_{\lambda L,R} = A_{\lambda L,R}^{NR} + \frac{\alpha_{em}\lambda^{1/4}(1,\hat{q}^2,\hat{m}_{K^*}^2)}{\sqrt{24\pi}}\sum_V \frac{Q_V f_V}{D_V(q^2)}\,C_{\gamma V}\,e^{i\delta_0^V}\,A_\lambda^V(q^2)\,, \tag{32}$$

where $\lambda = (0,\parallel,\perp)$, $C_{\gamma V} = \frac{m_V}{\sqrt{q^2}}\left(\frac{\sqrt{q^2}}{m_V}\right)$ for the VMD1 (VMD2) version, and $D_V(q^2) = q^2 - m_V^2 + im_V\Gamma_V(q^2)$ is the Breit-Wigner function for the V meson resonance shape with the energy-dependent width $\Gamma_V(q^2)$. For details regarding energy-dependent widths see [19].

At present only the amplitudes h_λ^V for $B_d^0 \to K^{*0}\phi$ decay are known from experiment [33], therefore we use the amplitudes of $B_d^0 \to K^{*0}\rho$ and $B_d^0 \to K^{*0}\omega$ decays from theoretical prediction [34]. The absolute values and phases of h_λ^V are shown in Table 2. Other parameters of the model are indicated in Table 3, and the SM Wilson coefficients at the scale $\mu = 4.8$ GeV to NNLO accuracy [11] are shown in Table 4.

Table 4. The SM Wilson coefficients at the scale $\mu = 4.8\,\mathrm{GeV}$, to NNLO accuracy. Input: $\alpha_s(m_W) = 0.120$, $\alpha_s(\mu) = 0.214$, obtained from $\alpha_s(m_Z) = 0.1176$ using three-loop evolution, $\overline{m}_t(\overline{m}_t) = 162.3\,\mathrm{GeV}$, $m_W = 80.4\,\mathrm{GeV}$ and $\sin^2\theta_W = 0.23$.

$\bar{C}_1(\mu)$	$\bar{C}_2(\mu)$	$\bar{C}_3(\mu)$	$\bar{C}_4(\mu)$	$\bar{C}_5(\mu)$	$\bar{C}_6(\mu)$	$C_{7\gamma}^{\mathrm{eff}}(\mu)$	$C_{8g}^{\mathrm{eff}}(\mu)$	$C_{9\mathrm{V}}(\mu)$	$C_{10\mathrm{A}}(\mu)$
-0.128	1.052	0.011	-0.032	0.009	-0.037	-0.304	-0.167	4.211	-4.103

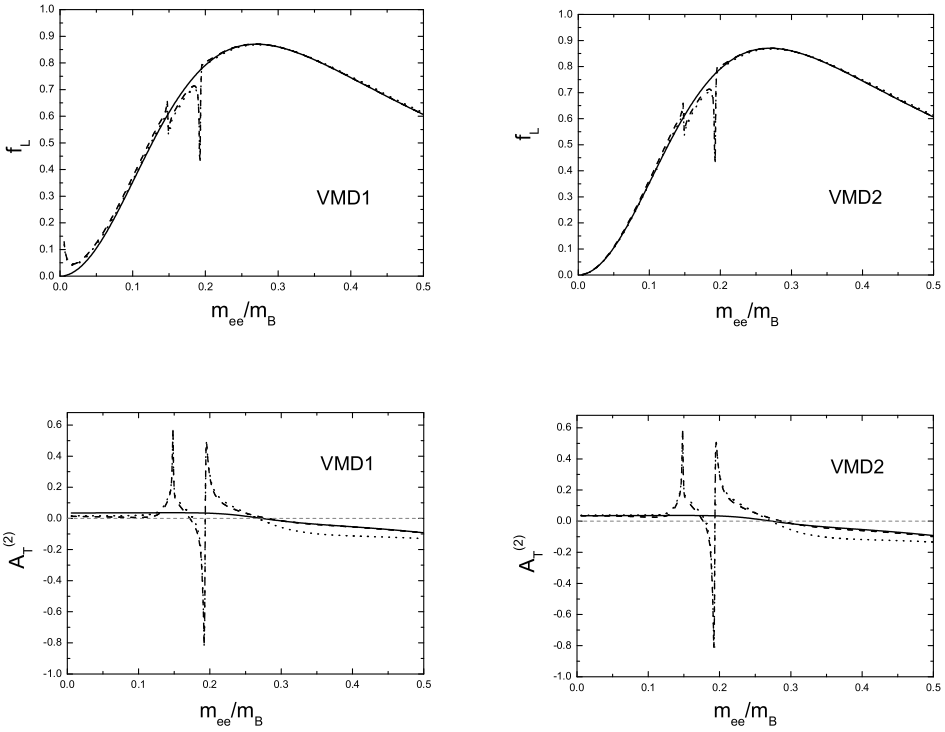

Figure 3. Longitudinal polarization fraction of K^* meson $f_L \equiv f_0$ (upper panels) and transverse asymmetry $A_{\mathrm{T}}^{(2)}$ (lower panels) as functions of m_{ee}/m_B. Left (right) panel corresponds to calculation within VMD1 (VMD2) version of the VMD model. Solid line corresponds to calculation without resonances in the transition form factor model [14]. Dashed and dotted lines are calculations including resonances in the form factor model from [14] and [19] (Eqs. (A7)-(A9) and (A17) there), respectively. The horizontal dashed line indicates zero.

4 Results of calculation for the $\bar{B}_d^0 \to \bar{K}^{*0}\, e^+\, e^-$ decay and discussion

On Fig. 3 we present results for the invariant mass dependence of a few observables for the $\bar{B}_d^0 \to \bar{K}^{*0}\, e^+\, e^-$ decay. The upper limit of the invariant mass region, 2.5 GeV, is taken to exclude the contribution from $J/\psi(1S)$ and higher resonances. Of course the presented results may depend on the phase δ_0^V in Eq. (32); for definiteness, we choose $\delta_0^V = 0$ for all resonances ρ, ω and ϕ.

In general, the resonances ρ, ω and ϕ show up as irregularities on the smooth non-resonant background. There is practically no dependence of longitudinal polarization fraction f_L on the choice of form factors. At very small m_{ee} this observable shows a sensitivity to the version of the VMD model.

The asymmetry coefficient $A_{\mathrm{T}}^{(2)}$ in Eq. (7) is more sensitive to the form factor model. Addition of the resonances change considerably this observable. The resonant contribution depends on the version of the VMD model, in particular, at invariant mass below 0.5 GeV (where $q^2 \ll m_{K^*}^2$), in the VMD2 version, $A_{\mathrm{T}}^{(2)}$ is about 0.04 which is in agreement with Eq. (17). While in the VMD1 version, the resonances influence $A_{\mathrm{T}}^{(2)}$ even at small m_{ee}.

Note, that the dependence of $A_{\mathrm{T}}^{(2)}$ on the mass of the strange quark has been studied in [19], and it appeared to be important. Indeed, comparison of $A_{\mathrm{T}}^{(2)}$ for $m_s = 0$ and $m_s \neq 0$ demonstrates effect of the "wrong" helicity transition $b_L \to s_R + \gamma_R$. In the SM this effect is proportional to $2m_s/m_b$ (see Eq. (17)), while in some extensions of the SM it can reach bigger values depending on the coefficient $C_{7\gamma}^{\prime\,\mathrm{eff}}$ in Eq. (18).

5 Conclusions

The rare FCNC decay $\bar{B}_d^0 \to \bar{K}^{*0}\,(\to K^-\,\pi^+)\,e^+\,e^-$ has been studied in the region of electron-positron invariant mass below $\bar{c}c$ threshold. Main emphasis has been put on an accurate account of the mechanism $\bar{B}_d^0 \to \bar{K}^{*0}\,(\to K^-\,\pi^+)\,V$ with low lying vector resonances $V = \rho(770)$, $\omega(782)$, $\phi(1020)$ decaying into the e^+e^- pair.

The invariant mass dependence of the coefficient $A_{\rm T}^{(2)}$ in the azimuthal angle distribution of the lepton pair has been calculated and studied.

In view of the current experiments on LHCb, in which the integrated over invariant mass observables will be measured [18], we have also calculated the corresponding quantities [19]. Two integration regions have been selected which are particularly suitable for the planned future measurements on LHCb [18]. The predictions for integrated observables are given in framework of the SM with account of low lying vector resonances.

Acknowledgements. A.Yu. K. is grateful to the Organizers of NPQCD-2011 School-Seminar for invitation and kind hospitality in Dniepropetrovsk.

References

[1] M. Antonelli, D.M. Asner, D. Bauer, et al., Phys. Rept. **494** 197 (2010) [arXiv:0907.5386v1 [hep-ph]].
[2] R. Ammar *et al.*, [CLEO Collaboration], Phys. Rev. Lett. **71**, 674 (1993).
[3] A. Ali and A.Ya. Parkhomenko, Eur. Phys. J. C **23**, 89 (2002).
[4] S.W. Bosch and G. Buchalla, Nucl. Phys. B **621**, 459 (2002).
[5] D. Atwood, M. Gronau, and A. Soni, Phys. Rev. Lett. **79**, 185 (1997); B. Grinstein, Y. Grossman, Z. Ligeti, and D. Pirjol, Phys. Rev. D **71**, 011504 (2005); D. Atwood, T. Gershon, M. Hazumi, and A. Soni, Phys. Rev. D **71**, 076003 (2005).
[6] Y. Grossman and D. Pirjol, JHEP **06**, 029 (2000).
[7] D. Melikhov, N. Nikitin, and S. Simula, Phys. Lett. B **442**, 381 (1998); F. Krüger, L.M. Seghal, N. Sinha, and R. Sinha, Phys. Rev. D **61**, 114028 (2000); Phys. Rev. D **63**, 019901(E) (2001); C.S. Kim, Y.G. Kim, C.-D. Lu, and T. Morozumi, Phys. Rev. D **62**, 034013 (2000).
[8] A. Ali, P. Ball, L.T. Handoko, and G. Hiller, Phys. Rev. D **61**, 074024 (2000); A. Ali, E. Lunghi, C. Greub, and G. Hiller, *ibid.* D **66**, 034002 (2002).
[9] F. Krüger and J. Matias, Phys. Rev. D **71**, 094009 (2005).
[10] C. Bobeth, G. Hiller, and G. Piranishvili, JHEP **07**, 106 (2008); U. Egede, T. Hurth, J. Matias, M. Ramon, and W. Reece, *ibid.* **11**, 032 (2008).
[11] W. Altmannshofer, P. Ball, A. Bharucha, A.J. Buras, D.M. Straub, and M. Wick, JHEP **01**, 019 (2009).
[12] U. Egede, T. Hurth, J. Matias, M. Ramon, and W. Reece, arXiv:1005.0571v1.
[13] G. Buchalla, A.J. Buras, and M.E. Lautenbacher, Rev. Mod. Phys. **68**, 1125 (1996).
[14] P. Ball and R. Zwicky, Phys. Rev. D **71**, 014029 (2005).
[15] F. De Fazio, T. Feldmann, and T. Hurth, Nucl. Phys. B **733**, 1 (2006); Erratum-*ibid.* B **800**, 405 (2008); JHEP **0802**, 031 (2008).
[16] B. Aubert *et al.*, (The BABAR Collaboration), Phys. Rev. Lett. **102**, 091803 (2009).
[17] J.-T. Wei *et al.*, (The Belle Collaboration), Phys. Rev. Lett. **103**, 171801 (2009).
[18] J. Lefrancois and M.H. Schune, LHCb-PUB-2009-008, 2009.
[19] A.Yu. Korchin and V.A. Kovalchuk, Phys. Rev. D **82**, 034013 (2010) [arXiv:1004.3647 [hep-ph]].
[20] N. Cabibbo, Phys. Rev. Lett. **10**, 531 (1963); M. Kobayashi and T. Maskawa, Prog. Theor. Phys. **49**, 652 (1973).
[21] K. Chetyrkin, M. Misiak, and M. Münz, Phys. Lett. B **400**, 206 (1997); E: B **425**, 414 (1998).
[22] N. Gray, D.J. Broadhurst, W. Grafe, and K. Schilcher, Z. Phys. C **48**, 673 (1990).
[23] K.G. Chetyrkin and M. Steinhauser, Phys. Rev. Lett. **83**, 4001 (1999); K. Melnikov and T. van Ritbergen, Phys. Lett. B **482**, 99 (2000).
[24] K.G. Chetyrkin, Phys. Lett. B **404**, 161 (1997); J.A.M. Vermaseren, S.A. Larin, and T. van Ritbergen, Phys. Lett. B **405**, 327 (1997).
[25] T. Hurth, Int. J. Mod. Phys. A **22**, 1781 (2007).
[26] M. Beneke, Th. Feldmann, and D. Seidel, Nucl. Phys. B **612**, 25 (2001).
[27] R.P. Feynman, *Photon-hadron interactions*, W.A. Benjamin, Inc. Reading, Massachusets, 1972.
[28] F. Klingl, N. Kaiser, and W. Weise, Z. Phys. A **356**, 193 (1996) [arXiv:hep-ph/9607431].
[29] H.B. O'Connell, B.C. Pearce, A.W. Thomas, and A.G. Williams, Prog. Nucl. Part. Phys. **39** (1997) 201.
[30] G. Ecker, J. Gasser, A. Pich, and E. de Rafael, Nucl. Phys. B **321** (1989) 311.
[31] S. Eidelman, S. Ivashyn, A. Korchin, G. Pancheri, and O. Shekhovtsova, Eur. Phys. J. C **69**, 103 (2010).
[32] K. Nakamura et al. (Particle Data Group), J. Phys. G **37**, 075021 (2010).
[33] Heavy Flavor Averaging Group (HFAG), http://www.slac.stanford.edu/xorg/hfag/rare/.
[34] C.H. Chen, arXiv:hep-ph/0601019v2.

Proceedings of the International School-seminar
"New Physics and Quantum Chromodynamics at External Conditions", pp. 49 – 56,
3-6 May 2011, Dnipropetrovsk, Ukraine

TOWARDS THERMODYNAMICS OF THE QUARK QUASI-PARTICLES

S. V. Molodtsov[1,2,a], G. M. Zinovjev[3,b]

[1]Joint Institute for Nuclear Research, Dubna, Moscow region, RUSSIA
[2]Institute of Theoretical and Experimental Physics, Moscow, RUSSIA
[3]Bogolyubov Institute for Theoretical Physics, National Academy of Sciences of Ukraine, Kiev, UKRAINE

Some features of hot and dense gas of quarks which are considered as the quasi-particles of the model Hamiltonian with four-fermion interaction are studied. Being adapted to the Nambu-Jona-Lasinio model this approach allows us to accommodate a phase transition similar to the nuclear liquid-gas one at the proper scale and to argue an existence of the mixed phase of vacuum and normal baryonic matter as a plausible scenario of chiral symmetry (partial) restoration. Analyzing the transition layer between two phases we estimate the surface tension coefficient and discuss the possibility of quark droplet formation.

Understanding in full and describing dependably the critical phenomena (chiral and deconfinement phase transitions) in QCD is still elusive because of a necessity to have the corresponding efficient non-perturbative methods for strongly coupled regime. For the time being such studies are pursued by invoking diverse effective models. The Nambu-Jona-Lasinio(NJL)-type models are certainly playing the most advanced role in this analysis [1]. This approach deals with the multi-fermion interactions in lieu of a gluon field QCD dynamics and does not incorporate the property of confinement. At the same time it is quite successful in realizing the spontaneous breakdown of chiral symmetry and its restoration at nonzero temperatures or quark densities.

These and some related items are discussed in this paper inspired by well known and fruitful idea about the specific role of surface degrees of freedom in the finite fermi-liquid systems and in considerable extent by our previous works [2] and [3] in which the quarks were treated as the quasi-particles of the model Hamiltonian and the problem of filling up the Fermi sphere was studied in detail. Under such a treatment an unexpected singularity (discontinuity) of the mean energy functional as a function of the current quark mass was found. In the particular case of the NJL model the existence of new solution branches of the equation for dynamical quark mass as a function of chemical potential have been demonstrated and the appearance of state filled up with quarks which is almost degenerate with the vacuum state both in the quasi-particle chemical potential and in the ensemble pressure has been discovered.

Here we are going to study the quark ensemble features at finite temperature and fixed baryonic chemical potential and to analyse the first order phase transition which takes place in such a system of free quasi-particles. Analysis is performed within the framework of two approaches which are supplementary, in a sense, albeit giving the identical results. One of those approaches, based on the Bogolyubov transformations, is especially informative to study the process of filling the Fermi sphere up because at this point the density of quark ensemble develops a continuous dependence on the Fermi momentum. It allows us to reveal an additional structure in the solution of gap equation for dynamical quark mass just in the proper interval of parameters characteristic for phase transition and to trace its evolution. The result is that a quark ensemble might be found in two aggregate states, gas and liquid, and the chiral condensate is partially restored in a liquid phase. In order to make these conclusions easily perceptible we deal with the simplest version of the NJL model (with one flavor and one of the standard parameter sets) and, actually, do not aim to adjust the result obtained with well-known nuclear liquid-gas phase transition. Besides, it seems our approach might be treated as a sort of microscopic ground of the conventional bag model and those states filled up with quarks are conceivable as a natural 'construction material' for baryons.

Now as an input to start with we remind the key elements of approach developed. The corresponding Hamiltonian includes the interaction term taken in the form of a product of two coloured currents located in the spatial points $\mathbf{x}$ and $\mathbf{y}$ which are connected by a form-factor and its density reads as

$$\mathcal{H} = -\bar{q}(i\gamma\nabla + im)q - \bar{q}t^a\gamma_\mu q \int d\mathbf{y}\bar{q}'t^b\gamma_\nu q'\langle A^a_\mu A'^b_\nu\rangle, \tag{1}$$

where $q = q(\mathbf{x})$, $\bar{q} = \bar{q}(\mathbf{x})$, $q' = q(\mathbf{y})$, $\bar{q}' = \bar{q}(\mathbf{y})$ are the quark and anti-quark operators,

$$q_{\alpha i}(\mathbf{x}) = \int \frac{d\mathbf{p}}{(2\pi)^3}\frac{1}{(2|p_4|)^{1/2}}\left[a(\mathbf{p},s,c)u_{\alpha i}(\mathbf{p},s,c)e^{i\mathbf{px}} + b^+(\mathbf{p},s,c)v_{\alpha i}(\mathbf{p},s,c)e^{-i\mathbf{px}}\right], \tag{2}$$

e-mail: [a]molodtsov@itep.ru, [b]Gennady.Zinovjev@cern.ch

$p_4^2 = -\mathbf{p}^2 - m^2$, i–is the colour index, α is the spinor index in the coordinate space, a^+, a and b^+, b are the creation and annihilation operators of quarks and anti-quarks, $a|0\rangle = 0$, $b|0\rangle = 0$, $|0\rangle$ is the vacuum state of free Hamiltonian and m is a current quark mass. The summation over indices s and c is meant everywhere, the index s describes two spin polarizations of quark and the index c plays the similar role for a colour. $t^a = \lambda^a/2$ are the generators of $SU(N_c)$ colour gauge group, the Hamiltonian density is considered in the Euclidean space and γ_μ denote the Hermitian Dirac matrices, $\mu, \nu = 1, 2, 3, 4$. $\langle A^a_\mu A'^b_\nu \rangle$ stands for the form-factor of the following form $\langle A^a_\mu A'^b_\nu \rangle = \delta^{ab} \frac{2}{N_c^2-1} \widetilde{G} \left[I(\mathbf{x}-\mathbf{y})\delta_{\mu\nu} - J_{\mu\nu}(\mathbf{x}-\mathbf{y}) \right]$, where the second term is spanned by the relative distance vector and the gluon field primed denotes that in the spatial point $\mathbf{y}$. The effective Hamiltonian density (1) results from averaging the ensemble of quarks influenced by intensive stochastic gluon field A^a_μ, see Ref. [2]. For the sake of simplicity in what follows we neglect the contribution of the second term of Eq.(1). The ground state of the system is searched as the Bogolyubov trial function composed of the quark-anti-quark pairs with opposite momenta and with vacuum quantum numbers, i.e.

$$|\sigma\rangle = \mathcal{T}\ |0\rangle\ , \quad \mathcal{T} = \Pi_{p,s} \exp\{\varphi\ [a^+(\mathbf{p},s)b^+(-\mathbf{p},s) + a(\mathbf{p},s)b(-\mathbf{p},s)]\}. \tag{3}$$

In this formula and below, in order to simplify the notations we refer to one compound index only which means both the spin and colour polarizations. The parameter $\varphi(\mathbf{p})$ which describes the pairing strength is determined by the minimum of mean energy $E = \langle\sigma|H|\sigma\rangle$. By introducing the 'dressing transformation' we define the creation and annihilation operators of quasi-particles as $A = \mathcal{T}a\mathcal{T}^{-1}$, $B^+ = \mathcal{T}b^+\mathcal{T}^{-1}$ and for fermions $\mathcal{T}^{-1} = \mathcal{T}^\dagger$. Then the quark field operators are presented as

$$q(\mathbf{x}) = \int \frac{d\mathbf{p}}{(2\pi)^3} \frac{1}{(2|p_4|)^{1/2}}\ \left[\ A(\mathbf{p},s)\ U(\mathbf{p},s)\ e^{i\mathbf{px}} + B^+(\mathbf{p},s)\ V(\mathbf{p},s)\ e^{-i\mathbf{px}}\right]\ ,$$
$$\bar{q}(\mathbf{x}) = \int \frac{d\mathbf{p}}{(2\pi)^3} \frac{1}{(2|p_4|)^{1/2}}\ \left[\ A^+(\mathbf{p},s)\ \overline{U}(\mathbf{p},s)\ e^{-i\mathbf{px}} + B(\mathbf{p},s)\ \overline{V}(\mathbf{p},s)\ e^{i\mathbf{px}}\right]\ ,$$

and the transformed spinors U and V are given by the following forms $U(\mathbf{p},s) = \cos(\varphi)u(\mathbf{p},s) - \sin(\varphi)v(-\mathbf{p},s)$, $V(\mathbf{p},s) = \sin(\varphi)u(-\mathbf{p},s) + \cos(\varphi)v(\mathbf{p},s)$ where $\overline{U}(\mathbf{p},s) = U^+(\mathbf{p},s)\gamma_4$, $\overline{V}(\mathbf{p},s) = V^+(\mathbf{p},s)\gamma_4$ are the Dirac conjugated spinors.

In Ref. [3] the process of filling in the Fermi sphere with the quasi-particles of quarks was studied by constructing the state of the Sletter determinant type $|N\rangle = \prod_{|\mathbf{P}|<P_F;S} A^+(\mathbf{P};S)|\sigma\rangle$ which possesses the minimal mean energy over the state $|N\rangle$. The polarization indices run through all permissible values here and the quark momenta are bounded by the limiting Fermi momentum P_F. The momenta and polarizations of states forming the quasi-particle gas are marked by the capital letters similar to above formula and the small letters are used in all other cases.

As it is known the ensemble state at finite temperature T is described by the equilibrium statistical operator ρ. Here we use the Bogolyubov-Hartree-Fock approximation in which the corresponding statistical operator is presented by the following form

$$\rho = \frac{e^{-\beta\ \hat{H}_{\rm app}}}{Z_0}\ , \quad Z_0 = {\rm Tr}\ \{e^{-\beta\ \hat{H}_{\rm app}}\}\ , \tag{4}$$

where an approximating effective Hamiltonian $H_{\rm app}$ is quadratic in the creation and annihilation operators of quark and anti-quark quasi-particles A^+, A, B^+, B and is defined in the corresponding Fock space with the vacuum state $|\sigma\rangle$ and $\beta = T^{-1}$. There is no need to know the exact form of this operator henceforth because all the quantities of our interest in the Bogolyubov-Hartree-Fock approximation are expressed by the corresponding averages (a density matrix) $n(P) = {\rm Tr}\{\rho\ A^+(\mathbf{P};S)A(\mathbf{P};S)\}$, $\bar{n}(Q) = {\rm Tr}\{\rho\ B^+(\mathbf{Q};T)B(\mathbf{Q};T)\}$, which are found by solving the following variational problem. The statistical operator ρ is determined in such a form in order to have at the fixed mean charge

$$\bar{Q}_4 = {\rm Tr}\{\rho\ Q_4\} = V\ 2N_c \int \frac{d\mathbf{p}}{(2\pi)^3}\ [n(p) - \bar{n}(p)]\ , \tag{5}$$

where $Q_4 = \int \frac{d\mathbf{p}}{(2\pi)^3} \frac{-ip_4}{|p_4|} [A^+(p)A(p) + B(p)B^+(p)]$ (for the diagonal component of our interest here, $Q_4 = -\int d\mathbf{x}\bar{q}i\gamma_4 q$) and fixed mean entropy

$$\begin{aligned} &\bar{S} = -{\rm Tr}\{\rho \ln\rho\} = \\ &= -V2N_c \int \frac{d\mathbf{p}}{(2\pi)^3} \left[n(p)\ln n(p) + (1-n(p))\ln(1-n(p)) + \bar{n}(p)\ln\bar{n}(p) + (1-\bar{n}(p))\ln(1-\bar{n}(p))\right], \end{aligned} \tag{6}$$

$(S = -\ln\rho)$ the minimal value of mean energy of quark ensemble $E = {\rm Tr}\{\rho H\}$. The definition of mean charge is given here up to the unessential (infinite) constant coming from permuting the operators BB^+ in the charge

operator Q_4. It is reasonable to remind that the mean charge should be treated in some statistical sense because it characterizes quark ensemble density and has no colour indices.

Calculating the corresponding matrix elements leads to the following result for mean energy density per one quark degree of freedom (the details can be found in [4]) $w = \mathcal{E}/2N_c$, $\mathcal{E} = E/V$ where E is a total ensemble energy

$$\begin{aligned} w &= \int \frac{d\mathbf{p}}{(2\pi)^3}|p_4| + \int \frac{d\mathbf{p}}{(2\pi)^3}|p_4|\cos\theta[n(p)+\bar{n}(p)-1] - \\ &- G\int \frac{d\mathbf{p}}{(2\pi)^3}\sin(\theta-\theta_m)\,[n(p)+\bar{n}(p)-1]\int \frac{d\mathbf{q}}{(2\pi)^3}\sin(\theta'-\theta'_m)\,[n(q)+\bar{n}(q)-1]\; I\;. \end{aligned} \tag{7}$$

(up to the constant unessential for our consideration here). Here the following denotes are used $p = |\mathbf{p}|$, $q = |\mathbf{q}|$, $\theta = 2\varphi$, $\theta' = \theta(q)$, $I = I(\mathbf{p}+\mathbf{q})$ and the angle $\theta_m(p)$ is determined by $\sin\theta_m = m/|p_4|$. It was quite practical to single out the colour factor in the four-fermion coupling constant as $G = 2\widetilde{G}/N_c$. It is of important to notice that the existence of such an angle stipulates the discontinuity of mean energy functional mentioned above and found out in [2]

We are interested in minimizing the following functional $\Omega = E - \mu\ \bar{Q}_4 - T\ \bar{S}$ where μ and T are the Lagrange factors for the chemical potential and temperature respectively. The approximating Hamiltonian $\hat{H}_{\rm app}$ is constructed simply by using the information on $E - \mu\ \bar{Q}_4$ of presented functional (see, also below). For the specific contribution per one quark degree of freedom $f = F/2N_c$, $F = \Omega/V$ we receive

$$\begin{aligned} f = &\int \frac{d\mathbf{p}}{(2\pi)^3}\left[|p_4|\cos\theta(n+\bar{n}-1) - \mu(n-\bar{n})\right] + \int \frac{d\mathbf{p}}{(2\pi)^3}|p_4| - G\int \frac{d\mathbf{p}}{(2\pi)^3}\sin(\theta-\theta_m)\,(n+\bar{n}-1)\times \\ &\times\int \frac{d\mathbf{q}}{(2\pi)^3}\sin(\theta'-\theta'_m)\,(n'+\bar{n}'-1)I + T\int \frac{d\mathbf{p}}{(2\pi)^3}\left[n\ln n + (1-n)\ln(1-n) + \bar{n}\ln\bar{n} + (1-\bar{n})\ln(1-\bar{n})\right]. \end{aligned} \tag{8}$$

Here the primed variables correspond to the momentum q. The optimal values of parameters are determined by solving the following system of equations ($df/d\theta = 0$, $df/dn = 0$, $df/d\bar{n} = 0$)

$$\begin{aligned} &|p_4|\ \sin\theta - M\cos(\theta-\theta_m) = 0\ , \\ &|p_4|\ \cos\theta - \mu + M\ \sin(\theta-\theta_m) - T\ \ln\left(n^{-1}-1\right) = 0\ , \\ &|p_4|\ \cos\theta + \mu + M\ \sin(\theta-\theta_m) - T\ \ln\left(\bar{n}^{-1}-1\right) = 0 \end{aligned} \tag{9}$$

where we denoted the induced quark mass as

$$M(\mathbf{p}) = 2G\int \frac{d\mathbf{q}}{(2\pi)^3}(1-n'-\bar{n}')\sin(\theta'-\theta'_m)\,I(\mathbf{p}+\mathbf{q}). \tag{10}$$

Turning to the presentation of obtained results in the form customary for mean field approximation we introduce a dynamical quark mass M_q parameterized as $\sin(\theta-\theta_m) = \frac{M_q}{|P_4|}$, $|P_4| = (\mathbf{p}^2 + M_q^2(\mathbf{p}))^{1/2}$ and ascertain the interrelation between induced and dynamical quark masses. From the first equation of system (9) we fix the pairing angle as $\sin\theta = pM/(|p_4||P_4|)$ and making use of the identity

$$(|p_4|^2 - M\ m)^2 + M^2p^2 = [p^2 + (M-m)^2]\ |p_4|^2$$

find out that $\cos\theta = \pm\frac{|p_4|^2 - m\ M}{|p_4||P_4|}$. For clarity we choose the upper sign 'plus'. Then, as an analysis of the NJL model teaches, the branch of equation solution for negative dynamical quark mass is the most stable one. Let us remember here that we are dealing with the Euclidean metrics (though it is not a principal point) and a quark mass appears in the corresponding expressions as an imaginary quantity. Now substituting the calculated expressions for the pairing angle into the trigonometrical factor expression $\sin(\theta-\theta_m) = \sin\theta\frac{p}{|p_4|} - \cos\theta\frac{m}{|p_4|}$ and performing some algebraic transformations of both parts of equation we define $M_q(\mathbf{p}) = M(\mathbf{p}) - m$. And then the equation for dynamical quark mass (10) is getting the form characteristic for the mean field approximation

$$M = 2G\int \frac{d\mathbf{q}}{(2\pi)^3}(1-n'-\bar{n}')\ \frac{M'_q}{|P'_4|}\ I(\mathbf{p}+\mathbf{q})\ .$$

The second and third equations of system (9) allow us to find for the equilibrium densities of quarks and anti-quarks as $n = [e^{\beta\ (|P_4|-\mu)} + 1]^{-1}$, $\bar{n} = [e^{\beta\ (|P_4|+\mu)} + 1]^{-1}$ and, hence, the thermodynamic properties of our system as well and, in particular, the pressure of quark ensemble $P = -dE/dV$. By definition we should calculate this derivative at constant mean entropy $d\bar{S}/dV = 0$. This condition allows us, for example, to calculate the derivative $d\mu/dV$. However, this way is not reliable because then the mean charge $\bar{Q}_4$ might

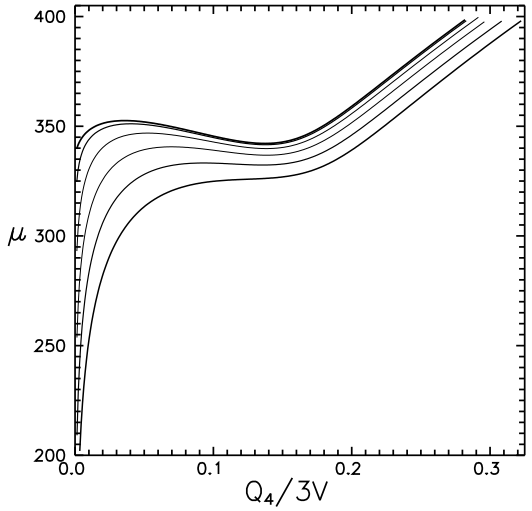

Figure 1. The chemical potential μ (MeV) as a function of charge density $\mathcal{Q}_4 = Q_4/(3V)$ (in the units of charge/fm^3). The factor 3 relates the densities of quark and baryon matter. The top curve corresponds to the zero temperature. The curves following down correspond to the temperature values $T = 10$ MeV, ... , $T = 50$ MeV with spacing $T = 10$ MeV.

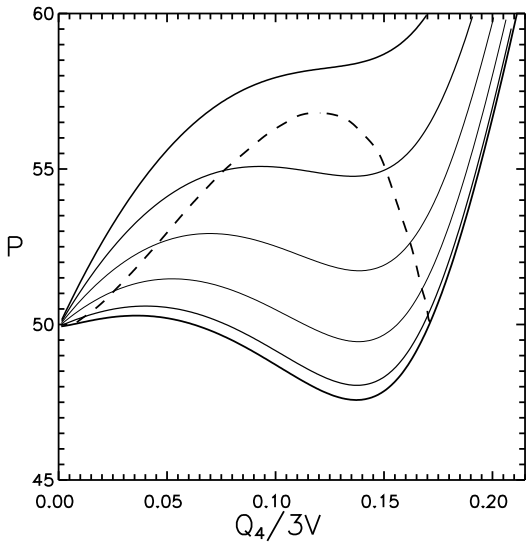

Figure 2. The ensemble pressure P (MeV/fm^3) as a function of charge density $\mathcal{Q}_4$ at temperatures $T = 0$ MeV, ... , $T = 50$ MeV with spacing $T = 10$ MeV. The lowest curve corresponds to zero temperature. The dashed curve shows the boundary of phase transition liquid–gas, see the text.

change, and it is more practical to introduce two independent chemical potentials — for quarks μ and for anti-quarks $\bar{\mu}$ (following formula for $\bar{n}$ with an opposite sign). In fact, it is the only possibility to obey both conditions simultaneously. It leads to the following definitions of corresponding densities $n = [e^{\beta\,(|P_4|-\mu)}+1]^{-1}$, $\bar{n} = [e^{\beta\,(|P_4|+\bar{\mu})}+1]^{-1}$. On this way of description we are able even to treat some non-equilibrium states of quark ensemble (albeit with losing a covariance similar to the situation which takes place in electrodynamics while one deals with electron-positron gas). But here we are interested in the particular case of $\bar{\mu} = \mu$. Then the corresponding derivative of specific energy dw/dV might be presented as

$$\frac{dw}{dV} = \int \frac{d\mathbf{p}}{(2\pi)^3}\left(\frac{dn}{d\mu}\frac{d\mu}{dV} + \frac{d\bar{n}}{d\bar{\mu}}\frac{d\bar{\mu}}{dV}\right)\left[|p_4|\cos\theta - 2G\sin(\theta-\theta_m)\int\frac{d\mathbf{q}}{(2\pi)^3}\sin(\theta'-\theta'_m)\,(n'+\bar{n}'-1)I\right]. \quad (11)$$

Now expressing the trigonometric factors via dynamical quark mass and exploiting Eq.(10) we obtain the ensemble pressure as $P = -\frac{E}{V} - V2N_c\int\frac{d\mathbf{p}}{(2\pi)^3}\left(\frac{dn}{d\mu}\frac{d\mu}{dV} + \frac{d\bar{n}}{d\bar{\mu}}\frac{d\bar{\mu}}{dV}\right)|P_4|$. The requirement for mean charge conservation $\frac{d\bar{Q}_4}{dV} = \frac{\bar{Q}_4}{V} + V2N_c\int\frac{d\mathbf{p}}{(2\pi)^3}\left(\frac{dn}{d\mu}\frac{d\mu}{dV} - \frac{d\bar{n}}{d\bar{\mu}}\frac{d\bar{\mu}}{dV}\right) = 0$ provides us with an equation which interrelates the derivatives $d\mu/dV$, $d\bar{\mu}/dV$. Apparently, the regularized expressions for mean charge of quarks and anti-quarks are meant here. Dealing in a similar way with the requirement of mean entropy conservation, $d\bar{S}/dV = 0$, we receive another equation as $\frac{\bar{S}}{2N_c\,V^2} = -\int\frac{d\mathbf{p}}{(2\pi)^3}\ln(n^{-1}-1)\,\frac{dn}{d\mu}\frac{d\mu}{dV} + \int\frac{d\mathbf{p}}{(2\pi)^3}\ln(\bar{n}^{-1}-1)\,\frac{d\bar{n}}{d\bar{\mu}}\frac{d\bar{\mu}}{dV}$. Substituting here $T\ln(n^{-1}-1) = -\mu + |P_4|$ and $T\ln(\bar{n}^{-1}-1) = \bar{\mu} + |P_4|$ after simple calculations (keeping in mind that $\bar{\mu} = \mu$ and the charge conservation) we have that $\int\frac{d\mathbf{p}}{(2\pi)^3}\left(\frac{dn}{d\mu}\frac{d\mu}{dV} + \frac{d\bar{n}}{d\bar{\mu}}\frac{d\bar{\mu}}{dV}\right)|P_4| = -\frac{\bar{S}T}{2N_cV^2} - \frac{\bar{Q}_4\mu}{2N_cV^2}$. Finally it leads for the pressure to the following expression $P = -\frac{E}{V} + \frac{\bar{S}\;T}{V} + \frac{\bar{Q}_4\;\mu}{V}$ (of course, the thermodynamic potential is $\Omega = -PV$). At small temperatures the anti-quark contribution is negligible and thermodynamic description can be grounded on utilizing one chemical potential μ only. If the anti-quark contribution is getting intrinsic the thermodynamic picture becomes complicated due to the presence of chemical potential $\bar{\mu}$ with the condition $\bar{\mu} = \mu$ imposed. In particular, at zero temperature the anti-quark contribution is absent and we might receive $P = -\mathcal{E} + \mu\;\rho_q$ where $\mu = [P_F^2 + M_q^2(P_F)]^{1/2}$, P_F is the Fermi momentum and $\rho_q = N/V$ is the quark ensemble density.

For clarity, we consider the NJL model in this paper, i.e. the correlation function behaves as the δ-function in coordinate space. It is a well known fact that in order to have an intelligent result in this model one needs to use a regularization cutting of momentum integration in Eq. (8). We adjust the standard set of parameters [5] here with $|\mathbf{p}| < \Lambda$, $\Lambda = 631$ MeV, $m = 5.5$ MeV and $G\Lambda^2/(2\pi^2) = 1.3$. This set of parameters at $n = 0$, $\bar{n} = 0$, $T = 0$ gives for the dynamical quark mass $M_q = 335$ MeV. Besides, it may be shown that the following form of

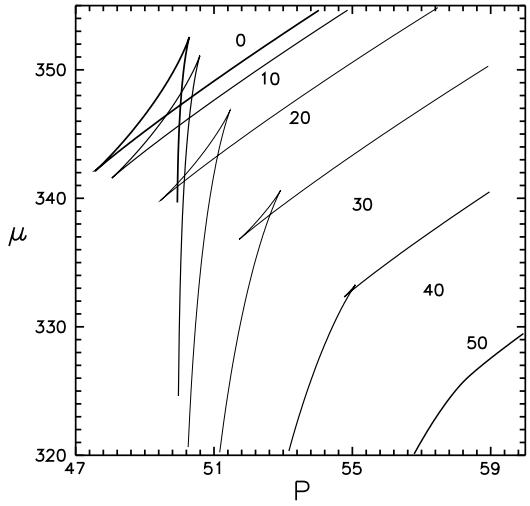

Figure 3. The fragments of isotherms in Fig. 1, see text. Chemical potential μ (MeV) as a function of pressure P (MeV/fm^3). The top curve corresponds to the zero isotherm and following down with spacing 10 MeV till the isotherm 50 MeV (the lowest curve).

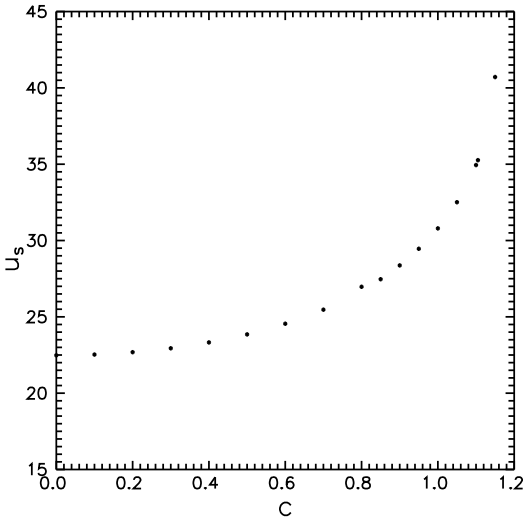

Figure 4. The surface tension coefficient u_s in MeV as a function of parameter c ($\zeta = c\,\eta$) for the curve of stable kinks (with $\eta \leq 1.2$).

ensemble energy is valid at the extremals of functional (8)

$$E = E_{vac} + 2N_cV\int^{\Lambda}\frac{d\mathbf{p}}{(2\pi)^3}|P_4|(n+\bar{n})\ ,\quad E_{vac} = 2N_cV\int^{\Lambda}\frac{d\mathbf{p}}{(2\pi)^3}(|p_4|-|P_4|) + 2N_cV\frac{M^2}{4G}\ .$$

It is easy to understand that this expression with the vacuum contribution subtracted looks like an energy of a gas of relativistic particles and anti-particles with the mass M_q and coincides identically with that calculated in the mean field approximation.

Thus, we determine the density of quark n and anti-quark $\bar{n}$ quasi- particles at given parameters μ and T from the second and third equations of system (9). From the first equation we receive the angle of quark and anti-quark pairing θ as a function of dynamical quark mass M_q which is handled as a parameter. The evolution of chemical potential as a function of charge density $\mathcal{Q}_4 = Q_4/(3V)$ (in the units of charge/fm^3) with the temperature increasing is depicted in Fig. 1 (factor 3 connects the quark and baryon matter densities). The top curve corresponds to the zero temperature. The other curves following down have been calculated for the temperatures $T = 10$ MeV, ... , $T = 50$ MeV with spacing $T = 10$ MeV. As it was found in Ref. [3] the chemical potential at zero temperature increases first with the charge density increasing, reaches its maximal value, then decreases and at the densities of order of normal nuclear matter density[1], $\rho_q \sim 0.16/fm^3$, becomes almost equal to its vacuum value. Such a behaviour of chemical potential results from the fast decrease of dynamical quark mass with the Fermi momentum increasing. It is clear from Fig. 1 that the charge density is still a multivalued function of chemical potential at the temperature slightly below 50 MeV. Fig. 2 shows the ensemble pressure P (MeV/fm^3) as the function of charge density $\mathcal{Q}_4$ at several temperatures. The lowest curve corresponds to the zero temperature. The other curves following up correspond to the temperatures $T = 10$ MeV, ... , $T = 50$ MeV (the top curve) with spacing $T = 10$ MeV. It is interesting to remember now that in Ref. [3] the vacuum pressure estimate for the NJL model was received as 40—50 MeV/fm^3 which is entirely compatible with the results of the conventional bag model. Besides, some hints at instability presence (rooted in the anomalous behavior of pressure $dP/dn < 0$) in an interval of Fermi momenta has been found. Fig. 3 shows the fragments of isotherms of Fig. 1, 2 but in the different coordinates (chemical potential — ensemble pressure). The top curve is calculated at the zero temperature, the other isotherms following down correspond to the temperatures increasing with spacing 10 MeV. The lowest curve is calculated at the temperature 50 MeV. The Fig. 3 obviously demonstrates a presence of the states on isotherm which are thermodynamically equilibrated and have equal pressure and chemical potential (see the characteristic Van der Waals triangle with the crossing curves). The calculated equilibrium points are shown in Fig. 2 by the dashed curve. The intersection points of dashed curve with an isotherm are fixing the boundary of gas —liquid phase transition. The corresponding straight line $P = \text{const}$ which obeys the Maxwell rule separates the non-equilibrium and unstable fragments of isotherm and describes a mixed phase and appropriate critical temperature for the parameter we are using in

[1] At the Fermi momenta of dynamical quark mass order.

this paper turns out to be $T_c \sim 45.7$ MeV with the critical charge density as $\bar{Q}_4 \sim 0.12$ charge/fm^3. Usually the thermodynamic description is grounded on the mean energy functional which is the homogeneous function of particle number like $E = N\ f(S/N, V/N)$ (without vacuum contribution). It is clear that such a description requires the corresponding subtractions to be introduced, however, this operation does not change the final results considerably. It was argued in Ref. [3] that the states filled up with quarks and separated from the instability region look like 'natural construction material' to compose the baryons and to understand the existing fact of equilibrium between vacuum and octet of stable (in strong interaction) baryons[2].

Apparently, our study of the quark ensemble thermodynamics produces quite reasonable arguments to propound the hypothesis that the phase transition of chiral symmetry (partial) restoration has already been realized as the mixed phase of physical vacuum and baryonic matter[3]. However, it is clear our quantitative estimates should not be taken as ones to be compared with, for example, the critical temperature of nuclear matter which has been experimentally measured and equals to 15 – 20 MeV. Besides, the gas component (at $T = 0$) has nonzero density (as 0.01 of the normal nuclear density) but in reality this branch should correspond to the physical vacuum, i.e. zero baryonic density[4]. In principle, an idea of global equilibrium of gas and liquid phases makes it possible to formulate the adequate boundary conditions at describing the transitional layer arising between the vacuum and filled state and to calculate the surface tension effects.

The idea advanced would obtain substantial confirmation if it becomes possible to claim an evidence of existing the transition layer at which the ensemble transformation from one aggregate state to another takes place. As it was argued above the practical parameter for describing an uniform phase (at a given temperature) is the mean charge (density) of ensemble. Thus, one can reconstruct all other characteristics, for example, a chiral condensate, dynamical quark mass, etc. Analyzing the transition layer at zero temperature we assume the parameters in the gas phase are approximately the same as at zero charge $\rho_g = 0$, i.e. as in the vacuum (ignoring the negligible distinctions in the pressure, chemical potential and quark condensate). Then dynamical quark mass obtained has maximal value and for the parameter choice of the NJL model it is $M = 335$ MeV. From the Van der Waals diagram one may draw out that the second (liquid) phase being in equilibrium with the gas phase develops the density $\rho_l = 3 \times 0.185$ ch/fm^3. The detached factor 3 here relates the magnitudes of quark and baryon densities. The quark mass in this phase is approximately $\overset{*}{M} \approx 70$ MeV (we are dealing further with the simple one-dimensional picture).

Usually an adequate description of heterogeneous states can be developed basing on the mean field approximation [7], specifically for our case, by dealing with the corresponding effective quark-meson Lagrangian (a sort of the Ginzburg-Landau functional)

$$\mathcal{L} = -\bar{q}\ (\hat{\partial} + M)\ q - \frac{1}{2}\ (\partial_\mu \sigma)^2 - U(\sigma) - \frac{1}{4}\ F_{\mu\nu}F_{\mu\nu} - \frac{m_v^2}{2}\ V_\mu V_\mu - g_\sigma\ \bar{q}q\ \sigma + i g_v\ \bar{q}\ \gamma_\mu\ q\ V_\mu\ , \qquad (12)$$

where $F_{\mu\nu} = \partial_\mu V_\nu - \partial_\nu V_\mu$, $U(\sigma) = \frac{m_\sigma^2}{2}\sigma^2 + \frac{b}{3}\sigma^3 + \frac{c}{4}\sigma^4$, σ is the scalar field, V_μ is the field of vector mesons, m_σ, m_v are the masses of scalar and vector mesons and g_σ, g_v are the coupling constants of quark-meson interaction. The $U(\sigma)$ potential includes the nonlinear terms of sigma-field interactions up to the fourth order, for example. For the sake of simplicity we do not include the contribution coming from the pseudoscalar and axial-vector mesons.

We are not going beyond well elaborated (and quite reliable) one loop approximation (12), although recently the considerable progress was reached in scrutinizing the non uniform quark condensates by utilizing the powerful methods of exact integration [8]. We believe it is more practical to adjust phenomenologically the parameters of effective Lagrangian being guided also by transparent physical picture. It is easy to see that handling one loop approximation actually we have the Walecka model [9] but applied for the quarks. In what follows we are working with the notations of that model hoping it does not lead to the misunderstandings. In the context of our deliberation Eq. (12) can be interpreted in the following way. Each phase, in some extent, might be considered as an excited state as to its relation with another phase which requires an additional (besides a charge density) set of parameters just as the meson fields for describing and those fields characterize the measure of deviation from the equilibrium state. Then the key question becomes whether it is possible to adjust the effective Lagrangian parameters of (12) in order to obtain the solutions in which the quark field interpolates between the quasi-particles in the gas (vacuum) phase and in the quasi-particles of the filled up state. The density of ensemble of the filled up states should asymptotically approach an equilibrium value of ρ_l and turn to zero value in the gas phase (vacuum).

Taking the parameterization of the potential $U(\sigma)$ as $b_\sigma = 1.5\ m_\sigma^2\ (g_\sigma/M)$, $c_\sigma = 0.5\ m_\sigma^2\ (g_\sigma/M)^2$ we come to the sigma model and the choice $b = 0$, $c = 0$ results in the Walecka model. As to the application for nuclear

[2]The chiral quark condensate for the filled up state discussed develops the quantity about (100 MeV)^3 (at $T = 0$), see [3], that demonstrates the obvious tendency of restoring a chiral symmetry.

[3]Indirect confirmation of this hypothesis one could see, for example, in the existing degeneracy of excited baryon states Ref. [6].

[4]Similar uncertainty is present in the other predictions of chiral symmetry restoration scenarios, for example, it stretches from 2 to 6 units of normal nuclear density.

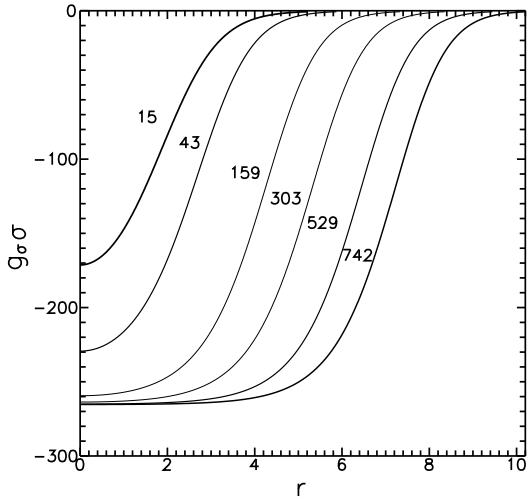

Figure 5. σ-field (MeV) as a function of the distance r (fm) for several solutions of the equation system (13) which are characterized by the net quark number N_q written to the left of each curve.

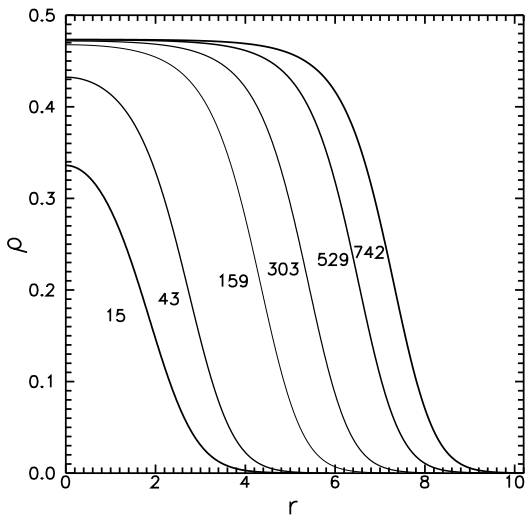

Figure 6. Distribution of the quark density ρ (ch/fm^3) for the corresponding solutions presented in the Fig. 5.

matter the parameters b and c demonstrate essentially the model dependent character and are different from the parameter values of the sigma model. They are phenomenologically adjusted with requiring an accurate description of the saturation property. On the contrary, for the quark Lagrangian (12) we could intuitively anticipate some resemblance with the sigma model and, hence, introduce two dimensionless parameters η, ζ as $b = \eta\ b_\sigma$, $c = \zeta^2\ c_\sigma$ which characterize some fluctuations of the effective potential. Then the scalar field potential is presented by the following form $U(\sigma) = \frac{m_\sigma^2}{8}\frac{g_\sigma^2}{M^2}\left(4\frac{M^2}{g_\sigma^2} + 4\frac{M}{g_\sigma}\eta\sigma + \zeta^2\sigma^2\right)\sigma^2$. The meson and quark fields are defined by the following system of the stationary equations

$$\begin{aligned} &\Delta\ \sigma - m_\sigma^2\ \sigma = b\ \sigma^2 + c\ \sigma^3 + g_\sigma\ \rho_s\ , \\ &\Delta\ V - m_v^2\ V = -g_v\ \rho\ , \\ &(\hat{\nabla} + \overset{*}{M})\ q = (E - g_v\ V)\ q \end{aligned} \tag{13}$$

where $\overset{*}{M} = M + g_\sigma\sigma$ is the running value of dynamical quark mass, E stands for the quark energy and $V = -iV_4$. The density matrix describing the quark ensemble at $T = 0$ has the form $\xi(x) = \int^{P_F} \frac{d\mathbf{p}}{(2\pi)^3} q_{\mathbf{p}}(x)\bar{q}_{\mathbf{p}}(x)$ where $\mathbf{p}$ is the quasi-particle momentum and the Fermi momentum P_F is defined by the ensemble chemical potential. The densities ρ_s, ρ in the right hand sides of equations (13) equal (by definition) to $\rho_s(x) = Tr\,\{\xi(x), 1\}$, $\rho(x) = Tr\,\{\xi(x), \gamma_4\}$. Here we confine ourselves to the Thomas–Fermi approximation while describing the quark ensemble. Then the densities in which we are interested in are given with some local Fermi momentum $P_F(x)$ as $\rho = \gamma\int^{P_F}\frac{d\mathbf{p}}{(2\pi)^3} = \frac{\gamma}{6\pi^2}P_F^3$ $\rho_s = \gamma\int^{P_F}\frac{d\mathbf{p}}{(2\pi)^3}\frac{\overset{*}{M}}{E}$ where γ is the quark gamma factor ($\gamma = 2N_cN_f$, N_c is the number of colours, N_f number of flavours), $E = (\mathbf{p}^2 + \overset{*}{M}^2)^{1/2}$. By definition the ensemble chemical potential does not change and it leads to the situation in which the local value of Fermi momentum is defined by the running value of dynamical quark mass and vector field as $\mu = M = g_v\ V + (P_F^2 + \overset{*}{M}^2)^{1/2}$. The details of tuning the Lagrangian parameters (12) can be found in [10]. The point of our attraction here is the surface tension coefficient [11] $u_s = 4\pi\ r_o^2\ \int_{-\infty}^{\infty} dx\ \left[\mathcal{E}(x) - \frac{\mathcal{E}_l}{\rho_l}\ \rho(x)\right]$, here $\mathcal{E}_l$ is the energy density in the liquid phase. The parameter r_o is discussed below. In the Thomas–Fermi approximation $\mathcal{E}(x) = \gamma\int^{P_F(x)}\frac{d\mathbf{p}}{(2\pi)^3}[\mathbf{p}^2 + \overset{*}{M}(x)]^{1/2} + \frac{1}{2}g_v\rho(x)V(x) - \frac{1}{2}g_\sigma\rho_s(x)\sigma(x)$. The surface tension coefficient u_s in MeV for the curve of stable kinks (see the details in Ref. [10]) with parameter $\eta \leq 1.2$ as the function of another parameter c ($\zeta = c\ \eta$) is depicted in Fig. 4.

Above results lead us to put the challenging question about the properties of finite quark systems or droplets of quark liquid which are in equilibrium with the vacuum state. As a droplet here we imply the spherically-symmetric solution of the equation system (13) for $\sigma(r)$ and $V(r)$ with the obvious boundary conditions $\sigma'(0) = 0$ and $V'(0) = 0$ in the origin (the primed variables denote the first derivatives over r) and rapidly decreasing at the large distances $\sigma \to 0$, $V \to 0$ when $r \to \infty$. Fig. 5 shows the set of solutions (σ-field (MeV)) of the equation system (13) at number of flavors $N_f = 1$. Fig. 6 presents the corresponding distributions of ensemble

Table 1. Results of fitting by the Fermi distribution ($N_f = 1$).

N_q	$\widetilde{\rho}_0$ (ch/fm^3)	R_0 (fm)	b (fm^{-1})	t (fm)	r_0 (fm)	m_σ (MeV)	η
15	0.34	1.84	0.51	2.24	0.74	351	0.65
43	0.43	2.19	0.52	2.28	0.75	384	0.73
159	0.46	4.19	0.52	2.29	0.77	409	0.78
303	0.47	5.23	0.52	2.29	0.78	417	0.795
529	0.47	6.37	0.52	2.27	0.79	423	0.805
742	0.47	7.15	0.52	2.27	0.79	426	0.81

density ρ (ch/fm^3). The Table 1 exhibits the results of fitting the density $\rho(r)$ with the Fermi distribution $\rho_F(r) = \frac{\widetilde{\rho}_0}{1+e^{(R_0-r)/b}}$ where $\widetilde{\rho}_0$ is the density at the origin, R_0 is the mean size of the droplet and the parameter b determines the thickness of surface layer $t = 4\ln(3)b$. Besides, the coefficient r_0 which is included in the definition of surface tension coefficient, $R_0 = r_0 N_q^{1/3}$ is also presented together with the characteristic values of the σ-meson mass and the coefficient η at which all this values were obtained. The curves plotted in the Fig. 5 and results of Table 1 allows us to conclude that the density distributions at $N_q \geq 50$ correspond quite well to the data typical for the nuclear medium. The thicknesses of transition layers are also similar. The coefficient r_0 with the factor $3^{1/3}$ included is in full correspondence with nuclear one. The values of the σ-meson mass turn out to be quite reasonable as well. Although at small quark numbers in the droplet the corresponding behaviors become essentially different. We know experimentally that in the nuclear matter one can observe some increase of the ensemble density which is quite considerable for the Helium and is much higher than the normal nuclear matter density for the Hydrogen. One may criticize us in this point because working within the Thomas–Fermi approximations becomes hardly justified at the small number of quarks and it is necessary to handle the solution of equation system (13). However, fortunately, the exploration we are interested in has been performed in the chiral soliton model of nucleon [12]. It has been demonstrated there that adding the contributions of pseudo-scalar and axial-vector fields to the Lagrangian (12) leads to reasonably good description of nucleon and Δ. The interesting remark here is that the soliton solutions obtained in [12] could be interpreted as a confluence of two kinks. Each of those kinks develops the restoration of chiral symmetry in a sense that the scalar field is approaching its zero value at the distance ~ 0.5 fm from the kink center. Actually, one branch corresponds to the solution with the positive value of the dynamical quark mass and another branch presents the solution with negative dynamical quark mass (in three-dimensional picture the pseudo-scalar fields appears just as a phase of chiral rotation from positive to negative value of quark mass).

Acknowledgements. We are grateful to the meeting organizers and personally Professor V. Skalozub for a hospitality and excellent conditions for efficient work.

References

[1] Y. Nambu and G. Jona-Lasinio, Phys. Rev. **122**, 345 (1961);
M. Buballa, Phys. Rep. **407**, 205 (2005).
[2] S. V. Molodtsov and G. M. Zinovjev, Teor. Mat. Fiz. **160**, 244 (2009); Phys. Rev. D **80**, 076001 (2009).
[3] S. V. Molodtsov, A. N. Sissakian and G. M. Zinovjev, Europhys. Lett. **87**, 61001 (2009);
Phys. of Atomic Nucl. **73** 1245 (2010).
[4] S. V. Molodtsov and G. M. Zinovjev, arXiv:1008.2319 [hep-ph].
[5] T. Hatsuda and T. Kunihiro, Phys. Rep. **247**, 221 (1994).
[6] L. Ya. Glozman, Phys. Rep. **444**, 1 (2007).
[7] A. I. Larkin and Yu. N. Ovchinnikov, JETF, **47**, 1136 (1964).
[8] T. Kunihiro, Y. Minami and Z. Zhang, arXiv:1009.4534 [nucl-th];
S. Carignano, D. Nickel and M. Buballa, arXiv:1007.1397 [hep-ph];
D. Nickel, Phys. Rev. Lett. **103**, 072301 (2009);
G. Basar and G. V. Dunne, Phys. Rev. Lett. **100**, 200404 (2008).
[9] J. D. Walecka, Annals of Phys. **83**, 491 (1974).
[10] S. V. Molodtsov and G. M. Zinovjev, arXiv:1103.3351 [hep-ph].
[11] J. Boguta and A. Bodmer, Nucl. Phys. A **292**, 413 (1977).
[12] W. Broniowski and M. K. Banerjee, Phys. Lett. B **158**, 335 (1978).

Proceedings of the International School-seminar
"New Physics and Quantum Chromodynamics at External Conditions", pp. 57 – 64,
3-6 May 2011, Dnipropetrovsk, Ukraine

FEMTOSCOPIC AND NON-FEMTOSCOPIC TWO-PION CORRELATIONS IN THE LIGHT OF RECENT ALICE LHC RESULTS

Yu. M. Sinyukov[a], S. V. Akkelin[b], Iu. A. Karpenko[c], V. M. Shapoval[d]

Bogolyubov Institute for Theoretical Physics, Metrolohichna str. 14b, 03680 Kiev, Ukraine

The hydrokinetic predictions for the HBT radii in heavy ion collisions at the LHC energies are compared with the recent results of the ALICE Collaboration. The role of non-equilibrium and non-hydrodynamic stage of the matter evolution in formation of the femtoscopy scales at the LHC energies is analyzed. Non-femtoscopic two-pion correlations in proton-proton collisions at the LHC energies are analyzed and a simple model that takes into account correlations induced by the conservation laws and minijets is proposed. It gives reasonable description of the non-femtoscopic correlations of like-sign and unlike-sign pion pairs in proton-proton collision events reported by the ALICE Collaboration.

1 Introduction

The two-particle femtoscopy of identical particles allows one to analyze the space-time structure of the particle emission from the systems created in heavy ion, hadron and lepton collisions (for recent reviews see, e.g., Ref. [1]). It was established that specific transverse momentum dependence of femtoscopy scales - interferometry, or HBT radii - in heavy ion collisions at RHIC energies is caused by the followings: a relatively hard equation of state because of crossover transition (instead of the 1st order one) between quark-gluon and hadron phases and due to nonequilibrium composition of hadronic matter, presence of prethermal transverse flows and their anisotropy developed to thermalization time, an "additional portion" of the transverse flows owing to the shear viscosity effect and fluctuation of initial conditions. An account of these factors gives the possibility to describe properly the pion and kaon momentum spectra together with the femtoscopy data of RHIC within realistic freeze-out picture with a gradual decay of nonequilibrium fluid into observed particles [2]. As for elementary particle collisions, like $p+p$, there is no unambiguous interpretation of p_T-dependence of the HBT radii. It is known that the transverse momentum behavior of the femtoscopy scales in $p+p$ collisions depends on the non-femtoscopic correlations, and it was established that these correlations can appear because of energy and momentum conservation laws (see e.g. [3]). Note that the collective (hydrodynamic) behavior of the matter in $p+p$ collisions is still open to quest.

Now, when the first LHC results of the femtoscopy analysis in $p+p$ and $Pb+Pb$ collisions have been published by the ALICE Collaboration [4, 5, 6], the main question is whether an understanding of the physics responsible for the space-time matter evolution in proton and heavy ion collisions at lower energies can be extrapolated to the LHC energies. Our aim here is twofold. First, we present the quantitative predictions given for LHC within hydrokinetic model (HKM) earlier [2], compare them with the recent ALICE LHC results and make the corresponding inference based on the first results of new hybrid hydrokinetic model (hHKM). Second, we analyze two-pion non-femtoscopic correlations in proton-proton collision events reported by the ALICE Collaboration [4] and show that simple analytical model with minijets and momentum conservation induced correlations can fit non-femtoscopic correlations of unlike-sign as well as like-sign pion pairs.

2 Hydrokinetic approach to A+A collisions and femtoscopic scales at LHC energies

The detailed description of the hydrokinetic model (HKM) is done in Refs. [7, 8]. It incorporates hydrodynamical expansion of the systems formed in $A+A$ collisions and their dynamical continuous decoupling described by the escape probabilities. The HKM also is the correct basis [9] to switch over a hydrodynamic evolution of continuous medium to an evolution of particles within cascade model like UrQMD. The model which matches the hydrokinetic model and UrQMD we call hybrid HKM (hHKM).

Our results are all related to the central rapidity slice where we use the boost-invariant Bjorken-like initial condition. We suppose the proper time of thermalization of quark-gluon matter to be $\tau_0 = 1$ fm/c. The initial energy density in the transverse plane is supposed to be Glauber-like [10] with zero impact parameter. The maximal initial energy density, $\epsilon(r=0) = \epsilon_0$, is the fitting parameter. From the analysis of particle multiplicities we choose it for the top RHIC energy to be $\epsilon_0 = 15$ GeV/fm^3. For the LHC energy $\sqrt{s} = 2.76$

e-mail: [a]sinyukov@bitp.kiev.ua, [b]akkelin@bitp.kiev.ua, [c]yu.karpenko@gmail.com, [d]shapoval@bitp.kiev.ua

TeV the corresponding value is $\epsilon_0 = 40$ GeV/fm^3 that in hydrokinetic model corresponds to multiplicity of charged particles $dN_{ch}/d\eta \approx 1500$. The pre-thermal transverse flow which the system already has at $\tau_0 = 1$ fm/c [11] is supposed to be linear in radius r_T: $y_T = \alpha r_T/R_T$ where α is the second fitting parameter and $R_T = \sqrt{< r_T^2 >}$. From the best fit of the pion transverse spectra at the RHIC energy we take $\alpha = 0.28$ in HKM and $\alpha = 0.18$ for hHKM and the same value we keep for the LHC energy. Note that the fitting parameter α absorbs also a positive correction for underestimated resulting transverse flow especially in HKM where we do not account for the viscosity effects [12] (in hHKM these effects are effectively included at the hadronic stage, therefore α is essentially less than in HKM).

Following to Ref. [8] we use at high temperatures the EoS [13] adjusted to the QCD lattice data. We suppose the chemical freeze-out for the hadron gas at $T_{ch} = 165$ MeV [14]. Below T_{ch} a composition of the hadron gas is changed only due to resonance decays into expanding fluid. We include 359 hadron states made of u, d, s quarks with masses up to 2.6 GeV. The EoS in this non chemically equilibrated system depends on particle number densities n_i of all the 359 particle species i: $p = p(\epsilon, \{n_i\})$. Since the energy densities in expanding system do not directly correlate with resonance decays, all the variables in the EoS depend on space-time points and so an evaluation of the EoS is incorporated in the hydrodynamic code. We calculate the EoS below T_{ch} in the Boltzmann approximation of ideal multi-component hadron gas.

At the temperatures higher than T_{ch} the hydrodynamic evolution is related to the quark-gluon and hadron phases which are in chemical equilibrium with zero baryonic chemical potential. The evolution is described by the conservation law for the energy-momentum tensor of perfect fluid:

$$\partial_\nu T^{\mu\nu}(x) = 0. \tag{1}$$

At $T < T_{ch}$=165 MeV the system evolves as non chemically equilibrated hadronic gas. The concept of the chemical freeze-out implies that afterwards only elastic collisions and resonance decays take place because of relatively small densities allied with a fast rate of expansion at the last stage. Thus, in addition to (1), the equations accounting for the particle number conservation and resonance decays are added. If one neglects the thermal motion of heavy resonances the equations for particle densities $n_i(x)$ take the form:

$$\partial_\mu (n_i(x) u^\mu(x)) = -\Gamma_i n_i(x) + \sum_j b_{ij} \Gamma_j n_j(x), \tag{2}$$

where $b_{ij} = B_{ij} N_{ij}$ denote the average number of i-th particles coming from arbitrary decay of j-th resonance, $B_{ij} = \Gamma_{ij}/\Gamma_{j,tot}$ is branching ratio, N_{ij} is a number of i-th particles produced in $j \to i$ decay channel. We also can account for recombination in the processes of resonance decays into expanding medium just by utilizing the effective decay width $\Gamma_{i,eff} = \gamma \Gamma_i$. We use $\gamma = 0.75$ supposing thus that near 30% of resonances are recombining during the evolution. All the equations (1) and 359 equations (2) are solving simultaneously with calculation of the EoS, $p(x) = p(\epsilon(x), \{n_i(x)\})$, at each point x.

During the matter evolution, in fact, at $T \leq T_{ch}$, hadrons continuously leave the system. Such a process is described by means of the emission function $S(x,p)$ which is expressed for pions through the *gain* term, $G_\pi(x,p)$, in Boltzmann equations and the escape probabilities $\mathcal{P}_\pi(x,p) = \exp(-\int_t^\infty ds R_{\pi+h}(s, \mathbf{r} + \frac{\mathbf{p}}{p^0}(s-t), p))$: $S_\pi(x,p) = G_\pi(x,p)\mathcal{P}_\pi(x,p)$ [7, 8]. For pion emission in relaxation time approximation $G_\pi \approx f_\pi R_{\pi+h} + G_{H\to\pi}$ where $f_\pi(x,p)$ is the pion Bose-Einstein phase-space distribution, $R_{\pi+h}(x,p)$ is the total collision rate of the pion, carrying momentum p, with all the hadrons h in the system in a vicinity of point x, the term $G_{H\to\pi}$ describes an inflow of the pions into phase-space point (x,p) due to the resonance decays. It is calculated according to the kinematics of decays with simplification that the spectral function of the resonance H is $\delta(p^2 - \langle m_H \rangle^2)$. The cross-sections in the hadronic gas, that determine via the collision rate $R_{\pi+h}$ the escape probabilities $\mathcal{P}(x,p)$ and emission function $S(x,p)$, are calculated in accordance with the UrQMD method [15]. The spectra and correlation functions are found from the emission function S in the standard way (see, e.g., [7]).

In the case of hHKM we provide a switch to UrQMD at the hypersurface $\tau(r) = \tau_{sw} = const$ where τ_{sw} is defined from the condition: temperature $T(\tau = \tau_{sw}, r_T = 0) = 165$ MeV. Then the non-equilibrium distribution functions in hadron resonance gas calculated in HKM are the input distribution functions for UrQMD at $\tau = \tau_{sw}$.

The pion emission functions per unit (central) rapidity, integrated over azimuthal angular and transverse momenta, are presented in Fig. 1 for the top RHIC and LHC $\sqrt{s} = 2.76$ TeV energies as a function of transverse radius r and proper time τ. As one can see the duration of particle emission in the cental part of the fireball is half of its lifetime. At a periphery a surface emission is significant, it lasts a total lifetime of the fireballs. The hypersurface of the surface emission approaches the light cone when collision energy grows. The latter fact is correlated with a non trivial result on the energy behavior of the R_{out}/R_{side} ratio. It slowly drops when energy grows and apparently is saturated at fairly high energies at the value close to unity (Fig. 1). In rough approximation $R_{out}/R_{side} \approx 1 + const/\epsilon_0$ [2]. This effect is caused by a strengthening of positive correlations

between space and time positions of pions emitted at the radial periphery of the system as one can see in Fig. 1, top (see theoretical details in Ref. [2]). This central prediction of [2] as for the energy dependence of the femtoscopy scales with energy growth is completely conformed by the ALICE results, see Fig. 1.

The transverse femtoscopy scales, predicted for LHC are quite close (but slightly less) to the corresponding experimental data. As for the longitudinal HBT radius, R_{long}, it is underestimated in HKM by around 20%. As the result, HKM gives smaller interferometry volume than is observed at LHC, see Fig. 1, bottom. The reason could be that HKM describes a gradual decay of the system which evolves hydrodynamically until fairly large times. It is known [16] that at the isentropic and chemically frozen hydrodynamic evolution the interferometry volume increases quite moderate with initial energy density growth in collisions of the same/similar nucleus. The RHIC results support such a theoretical view (see experimental and HKM results for SPS and RHIC, Fig. 1, bottom), while the ALICE Collaboration observes a significant increase of the interferometry volume at LHC. An essential growth of the interferometry volume in $Pb+Pb$ collisions at the LHC energy is conditioned by a dominance of very non-equilibrium and non-hydrodynamic stage of the matter evolution at LHC. We demonstrate it within the hHKM that contains such a stage, see Fig. 1. Then the results obtained in [16] for isentropic and chemically frozen evolution are violated. Most significant effect is observed for the LHC energy. It is worthy noting that linear fit cannot be done to describe simultaneously $V_{int}(dN/d\eta)$-dependence for both heavy (Pb, Au) ion and proton collisions, see for the latter the data discovered by the ALICE Collaboration [5] (Fig. 1, bottom). This experimental observation supports the theoretical result that the interferometry volume depends not only on multiplicity but also on initial size of colliding systems [16]. So, qualitatively, we see no new "LHC HBT puzzle" in the newest HBT results obtained at LHC in $Pb+Pb$ and $p+p$ collisions.

3 Simple analytical model of non-femtoscopic correlations in $p+p$ collisions at LHC energies

Recently the ALICE Collaboration utilized some event generators for an estimate of the correlation baseline (i.e., non-femtoscopic correlation function of identical pions) under the Bose-Einstein peak [4, 5]. It was motivated by the reasonable agreement of the corresponding event generator simulations with the experimental data for the correlation functions of oppositely charged pions in proton-proton collision at LHC energies. Based on the physical background of such generators, one can conjecture that the corresponding non-femtoscopic correlations can be caused by the jet-like and energy-momentum conservation induced correlations. Here, to describe the non-femtoscopic pion correlations in a simple analytical model, we assume that that N pions are produced with momenta $\mathbf{p}_1, ..., \mathbf{p}_N$ in $(N+X)$ multiparticle production events, and consider pions as distinguishable, yet equivalent particles with symmetrical probability density functions. A distinguishably of equivalent particles means that there is no quantum interference between possibilities that correspond to all $N!$ permutations of the particle momenta p_i. Then single-particle probability, $P_N(p_1)$, and the two-particle probability, $P_N(p_1, p_2)$, can be written as

$$P_N(p_1) = \frac{1}{N}\sum_{i=1}^{N}\int d\Omega_{p^*} E_i^* \delta^{(3)}(\mathbf{p}_1 - \mathbf{p}_i^*)\widehat{P}_N(p_1^*, ..., p_N^*), \tag{3}$$

$$P_N(p_1, p_2) = \frac{1}{N(N-1)}\sum_{i\neq j=1}^{N}\int d\Omega_{p^*} E_i^* \delta^{(3)}(\mathbf{p}_1 - \mathbf{p}_i^*) E_j^* \delta^{(3)}(\mathbf{p}_2 - \mathbf{p}_j^*)\widehat{P}_N(p_1^*, ..., p_N^*). \tag{4}$$

where $d\Omega_p = \frac{d^3p_1}{E_1}...\frac{d^3p_N}{E_N}$. The non-symmetrized N-pion probability density in such events reads

$$\widehat{P}_N(p_1, ..., p_N) = \frac{1}{K}\sum_X \int d\Omega_k \delta^{(4)}(p_a + p_b - \sum_{i=1}^{N} p_i - \sum_{j=1}^{X} k_j)|M_{N+X}(p_1, ..., k_X)|^2, \tag{5}$$

where $M_{N+X}(p_1, ..., k_X)$ is non-symmetrized $(N+X)$-particle production amplitude, p_a and p_b are 4-momenta of colliding particles (protons), and K is the normalization factor,

$$K = \sum_X \int d\Omega_k d\Omega_p \delta^{(4)}(p_a + p_b - \sum_{i=1}^{N} p_i - \sum_{j=1}^{X} k_j)|M_{N+X}(p_1, ..., k_X)|^2. \tag{6}$$

Expression (5) for $\widehat{P}_N(p_1, ..., p_N)$ is rather complicated because, in particular, it depends on X particles that are produced in addition to N pions. The latter means also that one can hardly expect that total energy or momentum of the pion subsystem are constants in the system's center of mass, instead, one can expect that they fluctuate in event-by-event basis. Here we assume that the total transverse momentum of N pions is equal to zero in the system's center of mass (keeping, however, in mind that this constraint is, in fact, too strong and can be weakened if necessary), and neglect the constrains conditioned by the conservation of energy and longitudinal momentum supposing that the system under consideration is barely N-pion subsystem in a small

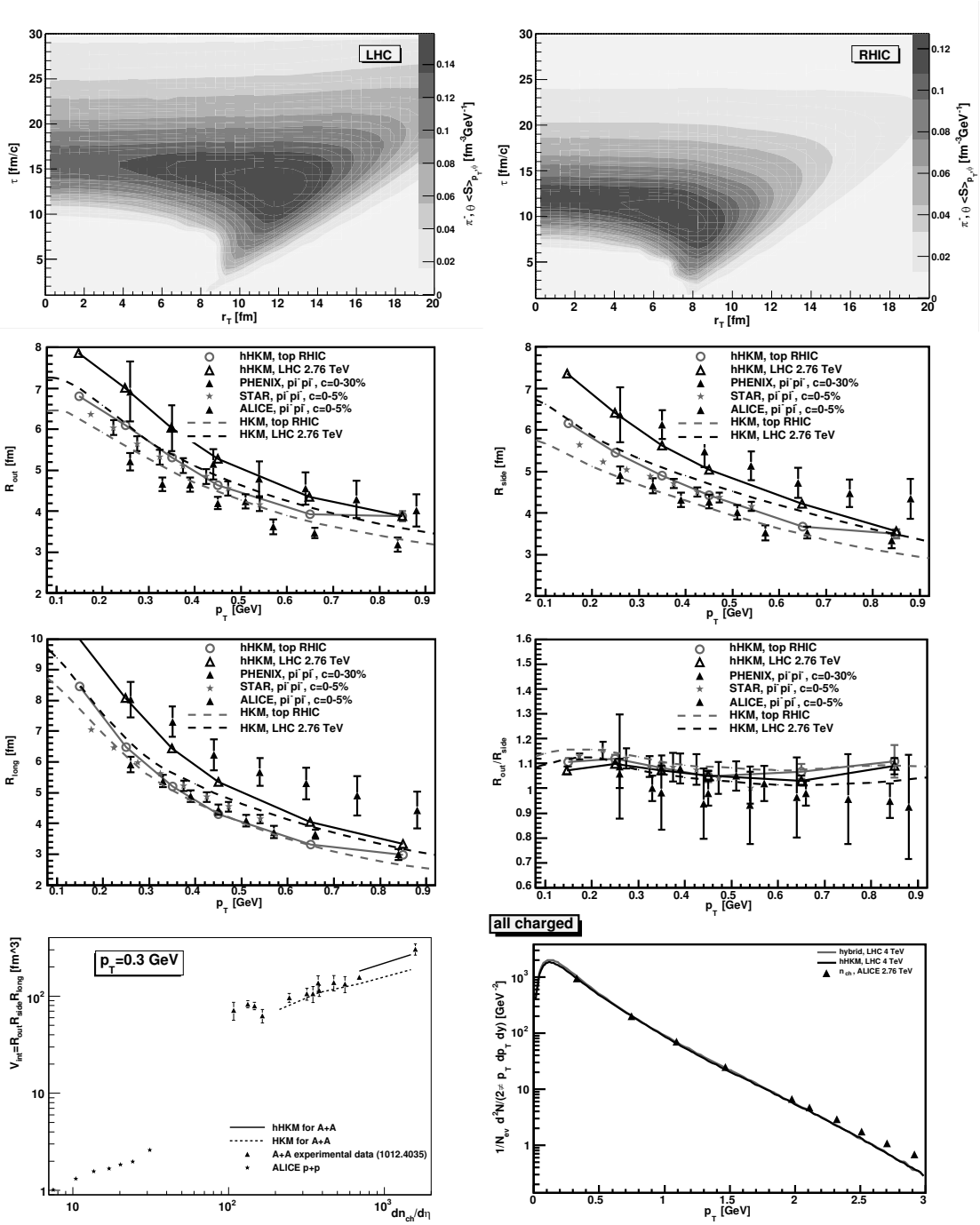

Figure 1. The p_T-integrated emission functions of negative pions for the top RHIC and LHC energies in HKM(top); the interferometry radii and R_{out}/R_{side} ratio (middle); the transverse momentum spectra of all charged pions at the LHC energy 2.76 TeV in hHKM model, and multiplicity dependence of the pion interferometry volume for central heavy ion collisions at AGS, SPS, RHIC and LHC energies in comparison with the results in p+p collisions (bottom). The solid lines connect the points obtained within HKM and hHKM. The experimental data for A+A collisions are taken from [6, 17, 18, 19, 20, 21, 22, 23]. For $p + p$ collisions at LHC the points for $p_T = 0.3$ GeV are interpolated from the results of Ref. [5].

midrapidity region of the total system. Then, motivated by Eq. (5), we assume that a non-symmetrized N-pion probability density can be written as

$$\widehat{P}_N(p_1,...,p_N) = \frac{1}{K}\delta(p_1,...,p_N)F_N(p_1,...,p_N), \tag{7}$$

where $F_N(p_1,...,p_N)$ is a non-symmetrized function of pionic momenta, $\delta(p_1,...,p_N)$ denotes average constraints on the N-pion states that appear due to energy and momentum conservations in multiparticle production events, and we assume that

$$\delta(p_1,...,p_N) = \delta^{(2)}(\mathbf{p}_{T1} + \mathbf{p}_{T2} + ... + \mathbf{p}_{TN}), \tag{8}$$

where $\mathbf{p}_{T1}, \mathbf{p}_{T2}, ...\mathbf{p}_{TN}$ are transverse components of the momenta of the N particles. Then the normalization factor is

$$K = \int d\Omega_p \delta(p_1,...,p_N)F_N(p_1,...,p_N). \tag{9}$$

Now, to describe the non-femtoscopic pion correlations in a simple analytical model, we assume that there are no other correlations in the production of N-pion states except the correlations induced by transverse momentum conservation and cluster (minijet) structures in momentum space. For the sake of simplicity we assume here that the only two-particle clusters appear. Then one can write for fairly large $N \gg 1$

$$F_N(p_1,...,p_N) = f(p_1)...f(p_N)Q(p_1,p_2)...Q(p_{N-1},p_N), \tag{10}$$

where $Q(p_i,p_j)$ denotes the jet-like correlations between momenta $\mathbf{p}_i$ and $\mathbf{p}_j$; existence of such correlations means that F_N cannot be expressed as a product of one-particle distributions. Then, utilizing the integral representation of the δ-function by means of the Fourier transformation, $\delta^{(2)}(\mathbf{p}_T) = (2\pi)^{-2}\int d^2r_T \exp(i\mathbf{r}_T\mathbf{p}_T)$, and accounting for Eqs. (3), (7), (8), (10), the single-particle probability reads

$$P_N(p_1) = \frac{1}{(2\pi)^2 K}\int d^2r_T G_N(\mathbf{p}_1,\mathbf{r}_T), \tag{11}$$

where

$$G_N(\mathbf{p}_1,\mathbf{r}_T) = \int d\Omega_{p^*} E_1^* \delta^{(3)}(\mathbf{p}_1 - \mathbf{p}_1^*)e^{i\mathbf{r}_T(\mathbf{p}_{T1}^* + ... + \mathbf{p}_{TN}^*)}F_N(p_1^*,...,p_N^*). \tag{12}$$

A possibility of different cluster configurations of particles means, in particular, that registered particles with momenta $\mathbf{p}_1$ and $\mathbf{p}_2$ can belong either to different minijets or to the same minijet. Then, taking into account Eqs. (4), (7), (8), (10), we get

$$P_N(p_1,p_2) = \frac{N}{N(N-1)}P_N^{1jet}(p_1,p_2) + \frac{N(N-1)-N}{N(N-1)}P_N^{2jet}(p_1,p_2), \tag{13}$$

where

$$P_N^{1jet}(p_1,p_2) = \frac{1}{(2\pi)^2 K}\int d^2r_T G_N^{1jet}(\mathbf{p}_1,\mathbf{p}_2,\mathbf{r}_T), \tag{14}$$

$$P_N^{2jet}(p_1,p_2) = \frac{1}{(2\pi)^2 K}\int d^2r_T G_N^{2jet}(\mathbf{p}_1,\mathbf{p}_2,\mathbf{r}_T), \tag{15}$$

and

$$G_N^{1jet}(\mathbf{p}_1,\mathbf{p}_2,\mathbf{r}_T) = \int d\Omega_{p^*} E_i^* \delta^{(3)}(\mathbf{p}_1 - \mathbf{p}_1^*)E_j^* \delta^{(3)}(\mathbf{p}_2 - \mathbf{p}_2^*)e^{i\mathbf{r}_T(\mathbf{p}_{T1}^* + ... + \mathbf{p}_{TN}^*)}F_N, \tag{16}$$

$$G_N^{2jet}(\mathbf{p}_1,\mathbf{p}_2,\mathbf{r}_T) = \int d\Omega_{p^*} E_i^* \delta^{(3)}(\mathbf{p}_1 - \mathbf{p}_1^*)E_j^* \delta^{(3)}(\mathbf{p}_2 - \mathbf{p}_3^*)e^{i\mathbf{r}_T(\mathbf{p}_{T1}^* + ... + \mathbf{p}_{TN}^*)}F_N, \tag{17}$$

here $F_N \equiv F_N(p_1^*,...,p_N^*)$. The first term in the right hand side of Eq. (13) is associated with events where the two registered particles appear from the different minijets, and second term corresponds to events when the particles belong to the same minijet. Evidently, the latter happens relatively rare, however notice that the second term can be significant for small systems with not very large N.

Now let us check whether this model can reproduce with reasonable parameters the non-femtoscopic correlation functions of unlike-sign pions measured by the ALICE Collaboration [4] and like-sign pions that are generated in PHOJET simulations and utilized as the correlation baseline by the ALICE Collaboration [4].

Calculations within the model will be deliberately as simple as possible just to demonstrate its viability. We do not use here the approximate methods like the saddle point approach, instead we utilize appropriate analytical parameterizations of the functions in interest, namely,

$$f(p_i) = E_i \exp\left(-\frac{\mathbf{p}_{i,T}^2}{T_T^2}\right) \exp\left(-\frac{\mathbf{p}_{i,L}^2}{T_L^2}\right), \tag{18}$$

and

$$Q(p_i, p_j) = \exp\left(-\frac{(\mathbf{p}_i - \mathbf{p}_j)^2}{\alpha^2}\right), \tag{19}$$

where T_T, T_L and α are some parameters, and in what follows we assume that $T_L \gg T_T$. In accordance with ALICE baseline obtained from the PHOJET event generator simulations, we assume that only q_{inv} is measured for each $\mathbf{p}_T$ bin. Assuming that longitudinal components of the registered particles are equal to zero, $p_{1L} = p_{2L} = 0$, we approximate q_{inv}^2 as

$$q_{inv}^2 \approx \mathbf{q}_T^2 \left(\frac{m^2 + \mathbf{p}_T^2 \sin^2\phi}{m^2 + \mathbf{p}_T^2}\right), \tag{20}$$

where ϕ denotes unregistered angle between $\mathbf{p}_T$ and $\mathbf{q}_T$, $\mathbf{p}_T\mathbf{q}_T = |\mathbf{p}_T||\mathbf{q}_T|\cos\phi$. Then

$$C_{NF}(|\mathbf{p}_T|, q_{inv}) = \frac{\int_0^{2\pi} d\phi P_N(p_1, p_2)}{\int_0^{2\pi} d\phi P_N(p_1) P_N(p_2)} \tag{21}$$

and, taking into account Eq. (13), we get

$$C_{NF}(|\mathbf{p}_T|, q_{inv}) = \frac{N-2}{N-1}\left(C_N^{2jet}(|\mathbf{p}_T|, q_{inv}) + \frac{1}{N-2} C_N^{1jet}(|\mathbf{p}_T|, q_{inv})\right), \tag{22}$$

where

$$C_N^{2jet}(|\mathbf{p}_T|, q_{inv}) = \frac{\int_0^{2\pi} d\phi P_N^{2jet}(p_1, p_2)}{\int_0^{2\pi} d\phi P_N(p_1) P_N(p_2)}, \tag{23}$$

$$C_N^{1jet}(|\mathbf{p}_T|, q_{inv}) = \frac{\int_0^{2\pi} d\phi P_N^{1jet}(p_1, p_2)}{\int_0^{2\pi} d\phi P_N(p_1) P_N(p_2)}. \tag{24}$$

It is well known, see e.g. Ref. [3], that influence of exact conservation laws on single-particle and two-particle momentum probability densities at the N-particle production process depends on a value of N and disappears at $N \to \infty$. Since one considers a subsystem of N pions but not total system, to weaken influence of total transverse momentum conservation on pions we shall consider C_M^{1jet} and C_M^{2jet} with $M > N$ instead of C_N^{1jet} and C_N^{2jet} in Eq. (22). It is the simplest way to account for a weakened conservation law in our model. At the same time the factor $1/(N-2)$ in (22) is associated with combinatorics of distribution of particles between clusters in momentum space ("minijets"), which happens no matter if one weakens or not the total momentum conservation law. Also, for more exact fitting of the data points in each average transverse momentum bin, we utilize the auxiliary factors, Λ, when compared results of our calculations with ALICE two-pion correlation and simulation data, these proportionality factors differ slightly from unit in our calculations (nearly 0.9). Then Eq. (22) gets the form

$$C_{NF}(|\mathbf{p}_T|, q_{inv}) = \Lambda(\mathbf{p}_T)(C_M^{2jet}(|\mathbf{p}_T|, q_{inv}) + \frac{1}{N-2} C_M^{1jet}(|\mathbf{p}_T|, q_{inv})). \tag{25}$$

The results of our calculations of the non-femtoscopic correlation functions C_{NF} are shown in Figs. 2, 3 in comparison with the non-femtoscopic correlation functions reported by the ALICE Collaboration [4] for different transverse momentum of pion pairs (actually, we performed calculations for the mean value in each bin). The data for unlike-sign pion correlations as well as for PHOJET simulations of identical two-pion non-femtoscopic correlation functions at midrapidity for total charged multiplicity $N_{ch} \geq 12$ bin in $p + p$ collisions at $\sqrt{s} = 900$ GeV are taken from Refs. [4, 24]. Our results are obtained for $M = 50$, $T_T = \alpha = 0.65$ GeV (to minimize the number of fit parameters, we fixed $T_T = \alpha$ for all calculations, note that with these parameter values the mean transverse momentum, $\langle p_T \rangle$, is about 0.58 GeV), and the fitted values of N are different for like-sign and unlike-sign pion pairs, namely, $N^{\pm\pm} = 20$ for the former and $N^{+-} = 11$ for the latter. The relatively high value of M can be interpreted as residual effect to pion subsystem of total energy-momentum

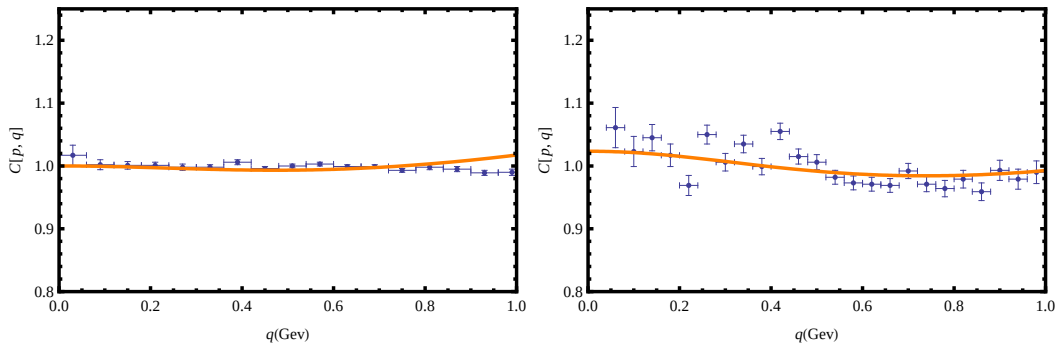

Figure 2. The non-femtoscopic correlation functions of like-sign (left) and unlike-sign (right) pions in $0.1 < p_T < 0.25$ GeV bin from Refs. [4, 24] (full dots) and that calculated from the analytical model (full line).

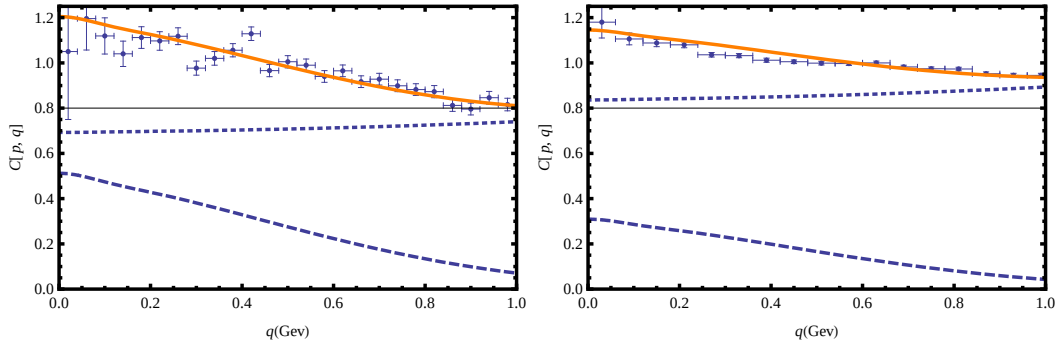

Figure 3. Above thin horizontal line: the non-femtoscopic correlation functions of like-sign (left) and unlike-sign (right) pions in $0.7 < p_T < 1.0$ GeV bin from Refs. [4, 24] (full dots) and that calculated from the analytical model (full line). Below thin horizontal line: relative contribution to non-femtoscopic correlation function by first (dotted line) and second (dashed line) terms of Eq. (25).

conservation in multiparticle production process. The relation, $N^{+-} < N^{\pm\pm}$, between fitted N values means that the magnitude of minijet induced correlations for unlike-sign pion pairs is higher than for like-sign ones. It is natural for minijet induced two-pion correlations because there is no local charge conservation constraint for production of oppositely-charged pion pair and, therefore, one can expect less identically-charged pion pairs from the fragmenting minijets than oppositely-charged ones. It is worth to note that such a difference in the strength of the two-pion correlations cannot be attributed to resonances: although it is easier to produce an oppositely-charged pion pair from a resonance than an identically-charged one because, again, of the charge conservation constraint, a resonance decay results, typically, in back-to-back correlations of the produced particles according to local energy-momentum conservation laws. It is unlike to one-side correlations from the minijet fragmentation. One can see from the figures that the behavior of the non-femtoscopic correlation functions of pions, C_{NF}, are reproduced well despite a simplicity of our model. This is a result of the competition of the two trends: an increase of the correlation function with q_{inv} because of the momentum conservation and a decrease of it due to the fragmentation of one minijet into the registered pion pair. Figure 3 demonstrates also the relative contribution of the first and second terms in Eq. (25) to the non-femtoscopic correlation functions.

4 Summary

We conclude that the behavior of femtoscopy scales in heavy ion collisions at LHC energy can be understood with the same hydrokinetic basis as was used for RHIC [2, 9] supplemented by hadronic cascade model at the latest stage of the evolution: HKM → hHKM. In this approach the following factors are important: a presence of prethermal transverse flow, a crossover transition between quark-gluon and hadron matters, non-hydrodynamic behavior of the hadron gas at the latest stage, and correct matching between hydrodynamic and non-hydrodynamic stages. Then the particle spectra together with the femtoscopy data at RHIC and LHC energies can be well described.

We also conclude that noticeable non-femtoscopic two-pion correlations can appear for small systems such as created in $p+p$ collisions as a result of the cluster (minijet) structures in final momentum space of produced particles, and as a result of the global energy-momentum conservation constraints. The latter typically results in an increase with q_{inv} for fairly high q_{inv} of the non-femtoscopic two-pion correlation functions of small systems, whereas the former mostly determines a decrease of the ones at relatively low q_{inv}. We presented here the simple

analytical model that takes into account correlations induced by the total transverse momentum conservation as well as minijets, and show that the model gives reasonable description of the two-pion non-femtoscopic correlations of identical and non-identical pions in proton-proton collision events at $\sqrt{s} = 900$ GeV reported by the ALICE Collaboration [4] (for more details see [25]).

Acknowledgements. The research was carried out within the scope of the EUREA: European Ultra Relativistic Energies Agreement (European Research Group: "Heavy ions at ultrarelativistic energies"), and is supported by the National Academy of Sciences of Ukraine (Agreement No. F8-2011) and by the State fund for fundamental researches of Ukraine (Project No. F33.2/001).

References

[1] M. Lisa, S. Pratt, R. Soltz, U. Wiedemann, Ann. Rev. Nucl. Part. Sci. **55**, 357 (2005); M. Lisa, S. Pratt, arXiv:0811.1352 [nucl-ex]; Z. Chajęcki, Acta Phys. Polon. B **40**, 1119 (2009).
[2] Iu.A. Karpenko, Yu.M. Sinyukov, Phys. Rev. C **81**, 054903 (2010).
[3] Z. Chajęcki, M. Lisa, Phys. Rev. C **78**, 064903 (2008); Phys. Rev. C **79**, 034908 (2009).
[4] K. Aamodt, *et al.* (ALICE Collaboration), Phys. Rev. D **82**, 052001 (2010).
[5] K. Aamodt, *et al.* (ALICE Collaboration), arXiv:1101.3665 [hep-ex].
[6] K. Aamodt, *et al.*(ALICE Collaboration), Phys. Lett. B **696**, 328 (2011).
[7] Yu.M. Sinyukov, S.V. Akkelin, Y. Hama, Phys. Rev. Lett. **89**, 052301 (2002).
[8] S.V. Akkelin, Y. Hama, Iu.A. Karpenko, Yu.M. Sinyukov, Phys. Rev. C **78**, 034906 (2008).
[9] Iu.A. Karpenko, Yu.M. Sinyukov. Phys. Rev. C **81**, 50 (2010).
[10] P.F. Kolb, J. Sollfrank, U. Heinz. Phys. Lett. B **459**, 667 (1999); Phys. Rev. C **62**, 054909 (2000).
[11] Yu.M. Sinyukov, Acta Phys. Polon. B **37**, 3343 (2006); M. Gyulassy, Iu.A. Karpenko, A.V. Nazarenko, Yu.M. Sinyukov, Braz. J. Phys. **37**, 1031 (2007).
[12] D. Teaney, Phys. Rev. C **68**, 034913 (2003).
[13] M. Laine, Y. Schröder, Phys. Rev. D **73**, 085009 (2006).
[14] F. Becattini, J. Manninen, J. Phys. G: Nucl. Part. Phys. **35**, 104013 (2008); A. Andronic, P. Braun-Munzinger, J. Stachel, Phys. Lett. B **673**, 142 (2009) [Erratum-ibid: Phys. Lett. B **678**, 516 (2009)]; Acta Phys. Polon. B **40**, 1005 (2009).
[15] M. Bleicher, *et al.*, J. Phys. G: Nucl. Part. Phys. **25**, 1859 (1999).
[16] S.V. Akkelin, Yu.M. Sinyukov, Phys. Rev. C **70**, 064901 (2004); Phys. Rev. C **73**, 034908 (2006).
[17] D. Antończyk, Acta Phys. Polon. B **40**, 1137 (2009).
[18] S.V. Afanasiev, *et al.* (NA49 Collaboration), Phys. Rev. C **66**, 054902 (2002).
[19] C. Alt, *et al.* (NA49 Collaboration), Phys. Rev. C **77**, 064908 (2008).
[20] J. Adams, *et al.* (STAR Collaboration), Phys. Rev. Lett. **92**, 112301 (2004).
[21] J. Adams, *et al.* (STAR Collaboration), Phys. Rev. C **71**, 044906 (2004).
[22] S.S. Adler, *et al.* (PHENIX Collaboration), Phys. Rev. C **69**, 034909 (2004).
[23] S.S. Adler, *et al.* (PHENIX Collaboration), Phys. Rev. Lett. **93**, 152302 (2004).
[24] The Durham HepData Project, http://hepdata.cedar.ac.uk/.
[25] S.V. Akkelin, Yu.M. Sinyukov, arXiv:1106.5120 [hep-ph].

Proceedings of the International School-seminar
"New Physics and Quantum Chromodynamics at External Conditions", pp. 65 – 72,
3-6 May 2011, Dnipropetrovsk, Ukraine

THE BJORKEN SUM RULE: HOW FAR CAN PERTURBATIVE THEORY PENETRATE TO NONPERTURBATIVE REGION?

O. P. Solovtsova[1, a], O. V. Teryaev[2, b], V. L. Khandramai[1, c]

[1] International Center for Advanced Studies, Gomel State Technical University, Gomel 246746, Belarus
[2] Bogoliubov Laboratory of Theoretical Physics, Joint Institute for Nuclear Research, Dubna, 141980 Russia

We study the polarized Bjorken sum rule, $\Gamma_1^{p-n}(Q^2)$, using recent experimental data of the Jefferson Lab on this sum rule at low momentum transfers in the range $0.05 < Q^2 < 3\,\mathrm{GeV}^2$ and the four-loop expression for the coefficient function $C_{\mathrm{Bj}}(\alpha_s)$ available now both in the framework of the standard QCD perturbation theory (PT) and the singularity-free analytic perturbation theory (APT). The analysis of the standard perturbative series for $C_{\mathrm{Bj}}(\alpha_s)$ up to N^{3}LO level exposes its asymptotic character in the region of low $Q \leq 1$ GeV, and the precision of the theoretical PT predictions can not be reached to better than 10%. Our analysis shows that the usage of APT allows to describe the precise low energy JLab data down to $Q \sim 300$ MeV and gives a possibility for reliable extraction of the higher twist coefficients.

1 Introduction

The spin-dependent structure function g_1 for the deep-inelastic lepton-nucleon scattering is one of the main sources of information about the nucleon structure. The g_1 structure function depends both on the Bjorken variable x, the fractional momentum carried by a parton, and the four-momentum squared of the exchanged virtual photon, Q^2. A fundamental sum rule originally derived from the current algebra by J.D. Bjorken in Ref. [1] predicts that the integral of the difference of the proton and neutron structure functions over all possible values of x (or its first moment),

$$\Gamma_1^{p-n}(Q^2) \,=\, \int_0^1 \,\left[g_1^p(x,Q^2) - g_1^n(x,Q^2)\right] dx\,, \tag{1}$$

in the limit $Q^2 \to \infty$ is equal to $g_A/6$, where $g_A = 1.267 \pm 0.004$ [2] is the nucleon axial charge defined from the neutron β-decay data.

Among the moments of the nucleon structure functions, the Bjorken sum rule (BjSR) is one of the convenient tests of the perturbative QCD (pQCD), especially, at low momentum transfers Q. Since this sum rule relates the difference of the proton and neutron first moments, only flavor non-singlet quark operators appear in the operator product expansion (OPE), which is the basis for the theoretical QCD analysis.

The Q^2-evolution of the BjSR is given by a double series in powers of $1/Q^2$ (OPE higher twists corrections) and in powers of the QCD running coupling $\alpha_s(Q^2)$ (pQCD radiative corrections). Until very recently, the pQCD contribution to BjSR has been known up to a third order in perturbative α_s expansion [3]. So far, the corresponding expression have been used in many studies aimed, in particular, to extraction of the α_s values at low momentum scales (see, e.g. [4, 5, 6, 7]).

New high precision data on the BjSR at low Q^2 in the wide range $0.05 < Q^2 < 3$ GeV^2 was obtained recently at Jefferson Lab (JLab) [8]. Using this data, in our previous works [9, 10] we have shown that the satisfactory description of the data down to $Q_{min} \sim \Lambda_{QCD}$ can be achieved by using the ghost-free Analytic Perturbation Theory (APT) [11].

The APT approach is based on the causality principle implemented as the analyticity imperative in the complex Q^2-plane for the QCD coupling $\alpha_s(Q^2)$ in the form of the Källen-Lehmann spectral representation (for a review on APT concepts, see e.g. Ref. [12]). It is important to notice that in the framework of APT, the theoretical ambiguity associated with pQCD higher-loop corrections is diminished (see Ref. [13]). This allows to increase stability of the pQCD results at low Q^2 and reliability of the information about the non-perturbative corrections extracted from the data.

A comparison of the theoretical description with experimental data on the Bjorken integral (1) supplies us with the important information both on the pQCD contributions and the higher twists (HT) effects. One of the important theoretical questions is the interplay between the higher twists and higher order pQCD corrections at low Q^2, which has previously been investigated in Refs. [9, 10]. The question we now rise in the current

e-mail: [a]olsol07@mail.ru, [b]teryaev@theor.jinr.ru, [c]khandramai.gstu.by

work is what the best theoretical uncertainty inherent to pQCD series could be reached at low energies by taking into account the higher order QCD and higher OPE corrections. Answer to this question is very critical for understanding the limitations of the pQCD description. The most precise ever experimental data from the Jefferson lab on $\Gamma_1^{p-n}(Q^2)$ is the challenge to the accuracy of the pQCD expansions, such that we approach and might even be able to see how the asymptotic character of the perturbative series imposes constraints on pQCD capabilities at low energies.

The four-loop expression for the pQCD contribution to the BjSR, which became recently available in Ref. [14], gives us a reasonable motivation for a new extended QCD analysis of the precise low energy combined data on $\Gamma_1^{p-n}(Q^2)$ [8, 15, 16] accounting for up to α_s^4-order of the Perturbation Theory in both the standard PT and APT approaches. The goal of the present work is to reveal features of the four-loop PT and APT expansions in the analysis of the BjSR.

2 The perturbative QCD contribution

It is convenient to write down the Bjorken integral (1) as a sum of the perturbative part and the higher twist contributions

$$\Gamma_1^{p-n}(Q^2) = \frac{g_A}{6}\left[1 - \Delta_{\rm Bj}(Q^2)\right] + \sum_{i=2}^{\infty} \frac{\mu_{2i}}{Q^{2i-2}}\,. \tag{2}$$

The contribution $\Delta_{\rm Bj}(Q^2)$ is defined by the coefficient function $C_{\rm Bj}(\alpha_s)$,

$$\Delta_{\rm Bj}(Q^2) \equiv 1 - C_{\rm Bj}(\alpha_s),$$

which is proportional to the flavor-nonsinglet axial vector current in the corresponding correction of the short distance Wilson expansion. In the framework of the standard pQCD, the approximation for $\Delta_{\rm Bj}(Q^2)$ has a form of the power series in the running coupling α_s. At the up-to-date four-loop ($\rm N^3LO$) level in the massless case, the standard PT expansion reads

$$\Delta_{\rm Bj}^{\rm PT}(Q^2) = c_1\, a(Q^2) + c_2\, a^2(Q^2) + c_3\, a^3(Q^2) + \, c_4\, a^4(Q^2)\,, \quad a(Q^2) \equiv \alpha_{\rm PT}(Q^2)/\pi\,, \tag{3}$$

where the expansion coefficients c_i in the modified minimal subtraction scheme, $\overline{\rm MS}$, for three active flavors are $c_1 = 1$, $c_2 = 3.5833$ [17], $c_3 = 20.2153$ [3] and $c_4 = 175.7$ [14].

The evolution of the pQCD running coupling can be obtained by integration of the renormalization group equation

$$\mu^2 \frac{\partial\, a}{\partial\, \mu^2} = -\beta_0\, a^2\, (1 + b_1\, a + b_2\, a^2 + b_3\, a^3 + \ldots)\,, \tag{4}$$

where $b_i = \beta_i/\beta_0$ are related to the coefficients of the β-function. For the four-loop $\overline{\rm MS}$-coupling normalized at the scale $\mu = Q$ the equation can be rewritten as

$$\beta_0 \ln\left(\frac{Q^2}{\Lambda^2_{\overline{\rm MS}}}\right) = \frac{1}{a} + b_1 \ln\frac{\beta_0\, a}{1 + b_1 a} + b_2 \int_0^a dx \frac{b_2 + b_3 x}{(1 + b_1 x)(1 + b_1 x + b_2 x^2 + b_3 x^3)}\,, \tag{5}$$

where $\beta_0 = 9/4 = 2.25$, $b_1 = 1.778$, $b_2 = 4.471$ [18], $b_3 = 20.990$ [19] [1] (see Ref. [20] for details).

The moments of the structure functions are analytic functions of Q^2 in the complex Q^2-plane with a cut along the negative part of the real axis (see Refs. [21, 22, 23]). The perturbative representation (3) violates these analytic properties due to the unphysical singularities of the PT running coupling for $Q^2 > 0$. To avoid this problem we apply the APT method [11, 12], which gives the possibility for combining the renormalization group resummation with correct analytical properties of the QCD correction to the BjSR. In the framework of the APT, the correct analytic properties of the perturbative expansions are preserved at any fixed PT order including the four-loop one where expression for $\Delta_{\rm Bj}(Q^2)$ is given by

$$\Delta_{\rm Bj}^{\rm APT}(Q^2) = c_1\, \mathcal{A}_1(Q^2) + c_2\, \mathcal{A}_2(Q^2) + c_3\, \mathcal{A}_3(Q^2) + c_4\, \mathcal{A}_4(Q^2)\,. \tag{6}$$

Here coefficients c_1, c_2, c_3 c_4 are the same as in Eq. (3), and functions $\mathcal{A}_{k)}(Q^2)$ can be expressed through the spectral functions $\varrho_k(\sigma) \equiv {\rm Im}\left[a^k(-\sigma - i\epsilon)\right]$ by the Källen-Lehman representation as

$$\mathcal{A}_k(Q^2) = \frac{1}{\pi}\int\limits_0^\infty d\sigma\, \frac{\varrho_k(\sigma)}{\sigma + Q^2}\,.$$

[1] All numerical coefficients are given here for three flavors that is adequate for the low energy scale.

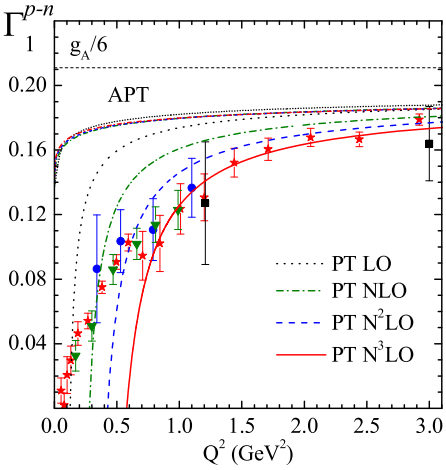

Figure 1. Perturbative part of the BjSR in different orders in the standard PT.

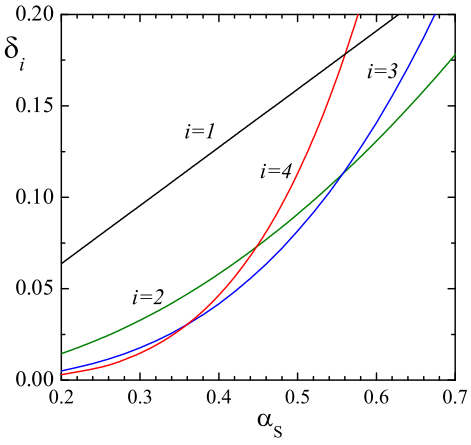

Figure 2. Contributions to the pQCD correction $\Delta_{\rm Bj}$ vs the PT running coupling α_s.

Note, the first function in Eq. (6), i.e. $\mathcal{A}_1(Q^2)$, is related with the analytic coupling: $\alpha_{\rm APT}(Q^2) = \pi\mathcal{A}_1(Q^2)$. Relation (6) shows that in the framework of the APT the pQCD contribution is expressed not in terms of the expansion in power series of the strong coupling, as it is done in the standard PT, but as an expansion in analytic functions $\mathcal{A}_k(Q^2)$. At large momentum transfers, these functions become proportional to k-th power of the usual perturbative coupling, $a^k(Q^2)$, and the expansion reduces to the power series. However, at small Q^2 the properties of the non-power expansion (6) become considerably different from the PT power series (3). More details about applications of the APT method can be found in Refs. [10, 12, 24, 25].

2.1 The Q^2-dependence

Now we analyze the Q^2-dependence of the BjSR in the framework of both PT and APT approaches in different orders (LO, NLO, N^{2}LO and N^{3}LO) of the perturbative expansions (3) and (6), respectively. As a normalization point, we use the most accurate α_s-value at $Q = M_Z$, $\alpha_s(M_Z) = 0.1184 \pm 0.0007$ [2, 7]. In order to take into account flavor thresholds, we apply the matching conditions for the values of α_s which are rather nontrivial in higher PT orders (see Refs. [20, 26, 27]). Following to analysis in Ref. [28], our matched calculation for the four-loop $\overline{\rm MS}$-coupling gives $\Lambda^{(n_f=3)} = 340 \pm 10$ MeV. Note, we obtain practically the same results, but with larger errors, if we choose the pseudo-observable value $R(M_Z^2) = 1.03904 \pm 0.00087$ as a normalization point [29], which leads to the four-loop running coupling equal to $\alpha_s(M_Z) = 0.1190 \pm 0.0026$.

In Fig. 1, we illustrate the behavior of the perturbative part of the BjSR in different orders in α_s in both PT and APT approaches. For completeness, we also show here the combined SLAC and JLab data on $\Gamma_1^{p-n}(Q^2)$ which are used in our analysis. The SLAC data points [15] are denoted by squares, the JLab CLAS Hall A 2002 data – by downward pointing triangles, the JLab CLAS Hall B 2003 data – by circles [16], and the most recent JLab data [8] – by stars.

As it follows from this figures, in the framework of the standard PT, the low energy behavior of $\Gamma_1^{p-n}(Q^2)$ is strongly dependent on the order of the initial expansion, and the lower border of satisfactory description of the JLab data shifts towards the larger Q^2 values when increasing the number of loops in the pQCD expansion (3). At the same time, in the framework of the APT, we observe the higher-loop stability given the fact that curves corresponding to different PT orders in APT are very close to each other (see Fig. 1). The reason for such infrared stability is absence of the unphysical singularities in APT expansions and, additionally, the analytic coupling in all orders has stable infrared-finite value, $\alpha_{\rm APT}(0) = \pi/\beta_0$.

2.2 Convergence of the PT and APT expansions

At low Q^2 a value of the strong coupling is quite large, questioning the convergence of pQCD series. We first illustrate the problem of convergence of the PT power series truncated after four-loop order (c.f. Eq. (3))

$$\Delta_{\rm Bj}^{\rm PT}(\alpha_s) = 0.3183\,\alpha_s \,+\, 0.3631\,\alpha_s^2 \,+ 0.6520\,\alpha_s^3 + \,1.804\,\alpha_s^4 = \sum_{i=1}^{4} \delta_i(\alpha_s),$$

by drawing δ_i (i-th term series) vs. α_s in Fig. 2. This figure demonstrates that at $\alpha_s \sim 0.36$ forth term becomes larger than the third one, at $\alpha_s \sim 0.45$ — than the second one, and at $\alpha_s \sim 0.56$ it is even bigger the first one.

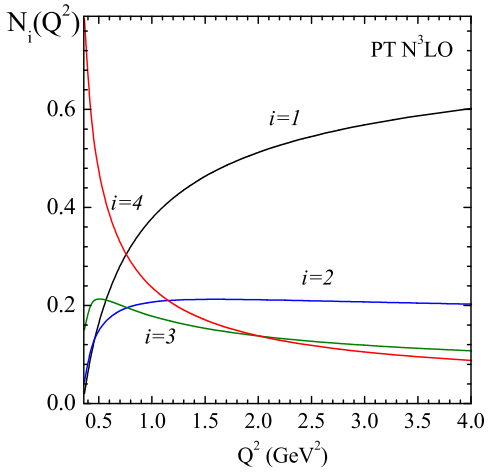

Figure 3. The Q^2-dependence of the relative contributions of the perturbative expansion terms in Eq. (3) at the four-loop level (N^3LO) in the standard PT.

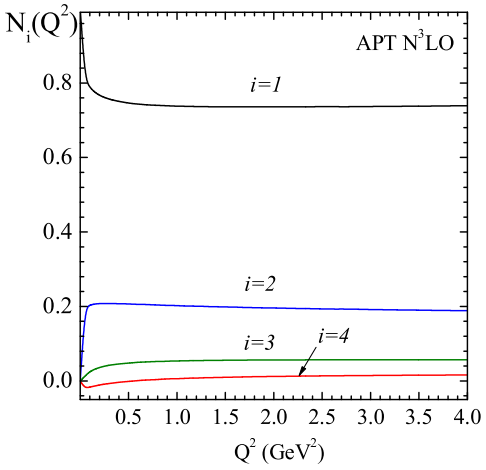

Figure 4. The Q^2-dependence of the relative contributions of the perturbative expansion terms in Eq. (3) at the four-loop level (N^3LO) in the APT.

Similar behavior can be seen from Fig. 3, where we present the relative contributions: $N_i(Q^2) = \delta_i(Q^2)/\Delta_{Bj}(Q^2)$. As it is seen from this figure, in the region of small momentum transfers $Q^2 < 1$ GeV^2 the dominant contribution comes from the four-loop term. Moreover, when decreasing Q^2 its relative contribution increases. In the region $Q^2 > 2$ GeV^2 the situation changes – the major contribution comes from one- and two-loop orders there. So, the fourth order PT correction does not improve the convergence that is presumably due to an asymptotic character of the PT series.

Analogical investigation for the APT series (6) is presented at Fig. 3. This figure demonstrates that there is an essential difference between PT and APT cases. The APT expansion obeys much better convergence than the PT one. In the APT case, the higher order contributions are stable at all Q^2, and one-loop contribution gives about 70 %, two-loop – 20 %, three-loop – not exceeds 5%, and four-loop – up to 1 %.

2.3 The μ-scale dependence

As it is known, any observable obtained to all orders in pQCD expansion should be independent of the renormalisation scale μ, but in any truncated-order perturbative series the cancelation is not perfect, such that the pQCD predictions depend on the choice of the μ-scale (for a review see, e.g., Ref. [7]).

Now let us estimate the ambiguity in choosing the renormalization scale, μ for the coefficient function $C_{Bj}(\alpha_s)$. The corresponding four-loop expression [14] can be rewritten as

$$C_{Bj}\left(\frac{\mu^2}{Q^2},\alpha_s\right) = 1 - 0.31831\,\alpha_s(\mu^2) + \left[-0.36307 - 0.22797\ln\left(\frac{\mu^2}{Q^2}\right)\right]\alpha_s^2(\mu^2) \qquad (7)$$
$$+ \left[-0.65197 - 0.64906\ln\left(\frac{\mu^2}{Q^2}\right) - 0.16327\ln^2\left(\frac{\mu^2}{Q^2}\right)\right]\alpha_s^3(\mu^2)$$
$$+ \left[-1.8042 - 1.7984\ln\left(\frac{\mu^2}{Q^2}\right) - 0.78968\ln^2\left(\frac{\mu^2}{Q^2}\right) - 0.11694\ln^3\left(\frac{\mu^2}{Q^2}\right)\right]\alpha_s^4(\mu^2)\,.$$

Next, we introduce the dimensionless parameter x_μ ($\mu^2 = x_\mu Q^2$), which is changed within the interval $x_\mu = 0.5 \div 2$ (see, for example, the analysis in Ref. [29]), and compare the μ-scale ambiguities between the two-, three- and four-loop PT and APT series at low Q^2.

We present our results in Fig. 5, where the perturbative part of the BjSR is plotted as a function of Q^2. This figure demonstrates that in the considered region of Q^2 there is an essential difference between μ-dependence of PT and APT expansions. The APT result is practically μ-scale independent even at small momentum transfers. The standard PT results are rather sensitive to μ-scale variations indicating quite significant theoretical uncertainties of the corresponding PT expansions.

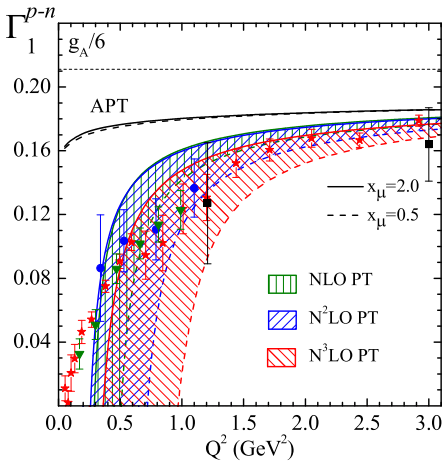

Figure 5. The μ-scale ambiguities for the perturbative part of the BjSR vs. Q^2 for two-, three- and four-loop orders of PT and APT series corresponding to x_μ in the interval $0.5 \div 2$.

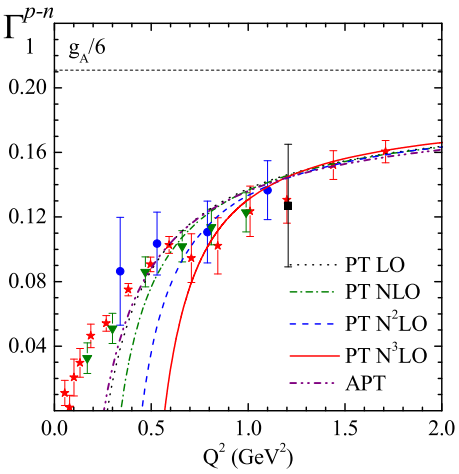

Figure 6. The μ_4-fits of the BjSR JLab data in various orders of PT and APT.

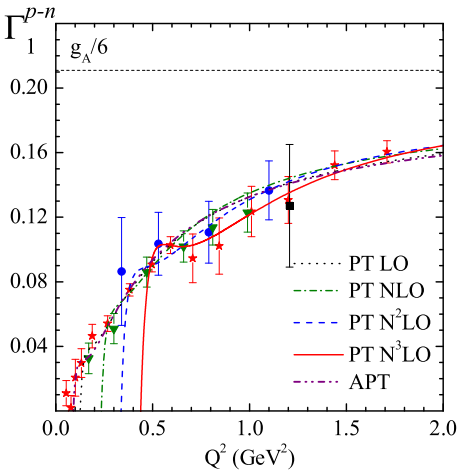

Figure 7. The $\mu_{4,6,8}$-fits of the BjSR JLab data in various orders of PT and APT.

3 Higher twists contribution

3.1 The results of the QCD fit

Previously, a detailed higher-twist analysis of the two- and three-loop expansions in powers of α_s was performed in Refs. [9]. Now, we extend the analysis up to an order $\sim \alpha_s^4$. Using the expression (2) being fitted to above mentioned experimental data [8, 16], we extract coefficients μ_{2i} of the higher twist OPE corrections. The minimal borders of fitting domains in Q^2 are settled from the *ad hoc* restriction $\chi^2 < 1$ and monotonous behavior of the resulting fitted curves.

In Figs. 6 and 7 we present the results of 1- and 3-parametric fits in various orders of PT and APT. Corresponding fit results for HT terms, extracted in different orders of PT and APT, are given in Tables 1 and 2 (all numerical results are normalized to corresponding powers of the nucleon mass M). It should be stressed that the APT result is practically coincides in various orders, therefore for it we draws one curve.

From these figures and tables we see that APT allows to move down to lower Q^2 in description of the experimental data. At the same time, in the framework of standard PT the lower border shifts up to higher Q^2 scales when increasing the order of PT expansion. This is caused by extra unphysical singularities in the higher-loop strong coupling. Note that in Figs. 6 and 7 the LO PT and APT curves are close to each other. This is explained by the fact that unphysical Landau pole in the one-loop PT α_s ($\Lambda = 285$ MeV) is located out of the fit domain, $Q_{min} \ll \Lambda$. So, the pole does not affect the results of the higher twists extraction in contrast to much stronger singularities in the higher PT orders.

Table 1. Results of higher twists extraction from the JLab data on BjSR in various orders of the PT.

PT	Q^2_{min},	μ_4/M^2	μ_6/M^4	μ_8/M^6
The best μ_4-fit results				
NLO	0.5	$-0.028(5)$	–	–
N^2LO	0.66	$-0.014(7)$	–	–
N^3LO	0.707	0.006(9)	–	–
The best $\mu_{4,6,8}$-fit results				
NLO	0.268	$-0.03(1)$	$-0.01(1)$	0.008(4)
N^2LO	0.34	0.01(2)	$-0.06(4)$	0.04(2)
N^3LO	0.47	0.05(4)	$-0.2(1)$	0.12(6)

Table 2. Results of higher twists extraction from the JLab data on BjSR in various orders of the APT.

APT	Q^2_{min}, GeV^2	μ_4/M^2	μ_6/M^4	μ_8/M^6
The best μ_4-fit results				
NLO	0.47	$-0.049(3)$	–	–
N^2LO	0.47	$-0.049(3)$	–	–
N^3LO	0.47	$-0.050(3)$	–	–
The best $\mu_{4,6,8}$-fit results				
NLO	0.078	$-0.061(4)$	0.009(1)	$-0.0004(1)$
N^2LO	0.078	$-0.061(4)$	0.009(1)	$-0.0004(1)$
N^3LO	0.078	$-0.061(4)$	0.009(1)	$-0.0004(1)$

3.2 Sensitivity of the higher twists to Λ_{QCD} variations

In the above analysis, we normalized the strong coupling $\alpha_s(Q^2)$ at the Z-boson mass, and then fixed the value of the Λ parameter separately in each order in α_s expansion (it was enough for understanding the role of the fourth order in the PT/APT perturbative series). However, corresponding values of the Λ parameter extracted in this way may be different from ones obtained in the direct QCD analysis of the experimental data on the moments of the structure functions (cf., e.g., Refs. [30, 31, 32]). Having this in mind, we investigate additionally the sensitivity of the extracted values of the higher twist coefficient μ_4 to the QCD scale parameter Λ in various orders of PT and APT. Note, the coefficient μ_4 corresponds of the $1/Q^2$ twist-4 term, which contains an information on quark-gluon correlations in nucleons. Different theoretical estimates for the μ_4 term can be found in our previous paper [10].

In figures 8 and 9, we show values of the coefficient μ_4 extracted from the JLab data using one-, two-, three- and four-loop PT and APT expansions vs. parameter Λ at $Q^2_{min} = 0.66$ GeV^2. From figures 8 and 9 it follows that results obtained in the framework of APT approach demonstrate a weak sensitivity of the extracted value of μ_4 to the QCD scale parameter Λ variations. This fact points out to the stability of extracted higher twist parameters. Analogous effect was also noticed above in the APT analysis of the perturbative part of the Bjorken integral.

The standard PT approach does not lead to a stable result for extracted μ_4 value with respect to Λ variations. Higher twist μ_4 contribution in PT rather strongly changes between different orders of the PT expansion and it happens both in absolute value and in sign, namely, at $\Lambda > 320$ MeV at four-loop level the higher twist coefficient becomes positive.

4 Conclusion

In this work, we performed the QCD analysis of the precise low energy JLab data on the BjSR and extracted the OPE higher twist terms using the four-loop expression for the QCD correction to the Bjorken integral $\Delta_{\rm Bj}$ published recently in Ref. [14].

Our analysis has demonstrated that in the low region $Q^2 < 2$ GeV^2, the four-loop PT order, as well as the three-loop one, contributes more than 10 % to the QCD correction $\Delta_{\rm Bj}$. It means that inclusion of the N^3LO correction to the PT series for $\Delta_{\rm Bj}$ does not improve the precision of the theoretical description of the BjSR preserving it at the level of N^2LO approximation. Additionally, in standard PT analysis the N^3LO correction induces extra unphysical singularities in the PT series, which shift the lower border of the pQCD applicability range Q_{min} to higher values compared to ones in the lower PT orders.

In the case of APT analysis, the N^3LO correction is sufficiently smaller than the N^2LO one and provides the percentage precision of the theoretical predictions. Since APT series obey the analytic properties at any

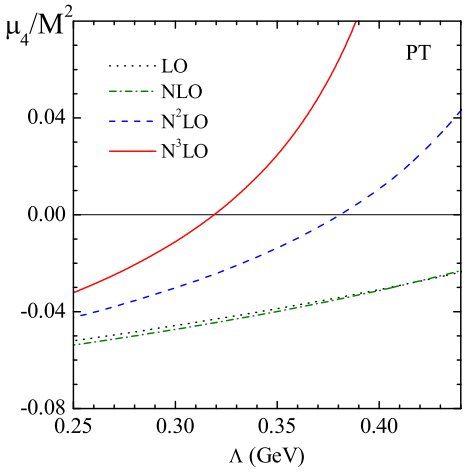

Figure 8. Value of the higher twist coefficient μ_4 extracted from the JLab data using the standard PT at different orders at $Q^2_{min} = 0.66$ GeV^2.

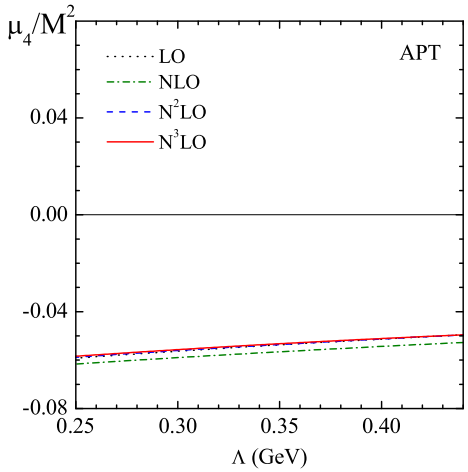

Figure 9. Value of the coefficient μ_4 extracted from the JLab data using the APT at different orders at $Q^2_{min} = 0.66$ GeV^2.

Q^2 (i.e. free of unphysical singularities), then APT allows to describe the precise low energy JLab data down to the scales $Q \sim \Lambda$ and give a possibility for reliable extraction of the higher twist coefficients.

Performing the higher-twist analysis of the JLab data on BjSR at low Q^2 in the framework of PT and APT approaches, we have shown that

- values of the higher twist coefficients extracted from the data in the standard PT approach in different PT orders are different, i.e. they are not stable with respect to higher loop corrections. The value of μ_4 coefficient at two- and three-loop levels is negative, whereas at the four-loop level it becomes positive.

- since APT exhibits the higher loop stability then the values of μ_4 extracted in the NLO, N^{2}LO and N^{3}LO APT coincide within the data fits uncertainty.

Therefore, the analysis of the standard N^{3}LO PT series for $\Delta_{\rm Bj}$ using precise JLab data on the Bjorken integral Γ^{p-n} demonstrates an asymptotic character of the standard PT expansions in the region of low $Q^2 < 2$ GeV^2, and account the four-loop corrections does not improve precision of the theoretical predictions. In addition, extra unphysical singularities emerging at the four-loop level do not allow to move deeper to the low-energy domain and to obtain stable values of the higher twist coefficients. Using the APT one can move the lower border of the pQCD JLab data description down to scales $Q \sim \Lambda \sim 300$ MeV. Extracted value of the higher twist coefficient μ_4 is universal due to its very little sensitivity to the higher loop APT corrections and $\Lambda_{\rm QCD}$ variations. So, the remarkable properties of the APT in the low-energy domain create a basis for preferring the application of this technique.

Acknowledgements. We are grateful to D.V. Shirkov, K.G. Chetyrkin, S.V. Mikhailov, R.S. Pasechnik and V.V Skalazub for interest in this work and helpful discussions. This work was partly supported by the BelRFFR-JINR grant F10D-001 and the RFBR grants 09-02-00732, 09-02-01149, 11-01-00182.

References

[1] J.D. Bjorken, Phys. Rev. **148**, 1467 (1966); Phys. Rev. D **1**, 376 (1970).
[2] K. Nakamura et al. (Particle Data Group), J. Phys. G **37**, 075021 (2010).
[3] S.A. Larin, J.A.M. Vermaseren, Phys. Lett. B **259**, 345 (1991).
[4] J. Ellis, M. Karliner, Phys. Lett. B **34**, 397 (1995).
[5] K.A. Milton, I.L. Solovtsov, O.P. Solovtsova, Phys. Lett. B **415**, 104 (1997).
[6] A. Deur *et al.*, Phys. Lett. B **665**, 349 (2008); Phys. Rev. D **78**, 032001 (2008).
[7] S. Bethke, Eur. Phys. J. C **64**, 689 (2009).
[8] K.V. Dharmawardane et al., Phys. Lett. B **641**, 11 (2006);
P.E. Bosted et al., Phys. Rev. C **75**, 035203 (2007);
Y. Prok et al., Phys. Lett. B **672**, 12 (2009).
[9] R.S. Pasechnik, D.V. Shirkov, O.V. Teryaev, Phys. Rev. D **78**, 071902 (2008).

[10] R.S. Pasechnik, D.V. Shirkov, O.V. Teryaev, O.P. Solovtsova, V.L. Khandramai, Phys. Rev. D **81**, 016010 (2010).
[11] D.V. Shirkov, I.L. Solovtsov, JINR Rapid Comm. No.**2**[76-96], 5 (1996); Phys. Rev. Lett. **79**, 1209 (1997); K.A. Milton, I.L. Solovtsov, Phys. Rev. D **55**, 5295 (1997).
[12] D.V. Shirkov, I.L. Solovtsov, Theor. Math. Phys. **150**, 132 (2007).
[13] D.V. Shirkov, Eur. Phys. J. C **22**, 331 (2001).
[14] P.A. Baikov, K.G. Chetyrkin, J.H. Kühn, Phys. Rev. Lett. **104**, 132004 (2010).
[15] K. Abe et al., Phys. Rev. Lett. **79**, 26 (1997);
P.L. Anthony et al., Phys. Lett. B **493**, 19 (2000).
[16] M. Amarian et al., Phys. Rev. Lett. **89**, 242301 (2002);
R. Fatemi et al., Phys. Rev. Lett. **91**, 222002 (2003);
M. Amarian et al., Phys. Rev. Lett. **92**, 022301 (2004);
A. Deur et al., Phys. Rev. Lett. **93**, 212001 (2004).
[17] S.G. Gorishny, S.A. Larin, Phys. Lett. B **172**, 109 (1986).
[18] O.V. Tarasov, A.A. Vladimirov, A.Yu. Zharkov, Phys. Lett. B **93**, 429 (1980);
S.A. Larin, J.A.M. Vermaseren, Phys. Lett. B **303**, 334 (1993).
[19] T. van Ritbergen, J.A.M. Vermaseren, S.A. Larin, Phys. Lett. B **400**, 379 (1997).
[20] K.G. Chetyrkin, B.A. Kniehl, M. Steinhauser, Phys. Rev. Lett **79**, 2184 (1997).
[21] W. Wetzel, Nucl. Phys. B **139**, 170 (1978).
[22] B. Geyer, D. Robaschik, E. Wieczorek, Fortschr. Phys. **27**, 75 (1979).
[23] I.L. Solovtsov, Part. Nucl. Lett. **4** [101], 10 (2000).
[24] K.A. Milton, I.L. Solovtsov, O.P. Solovtsova, Phys. Lett. B **439** (1998) 421.
[25] K.A. Milton, I.L. Solovtsov, O.P. Solovtsova, Phys. Rev. D **60**, 016001 (1999).
[26] Y. Schröder, M. Steinhauser, JHEP **0601**, 051 (2006).
[27] B.A. Kniehl, A.V. Kotikov, A.I. Onishchenko, O.L. Veretin, Phys. Rev. Lett. **97**, 042001 (2006).
[28] K.G. Chetyrkin, J.H. Kuhn, M. Steinhauser, Comput. Phys. Commun. **133**, 43 (2000).
[29] P.A. Baikov, K.G. Chetyrkin, J.H. Kuhn, Phys. Rev. Lett. **101**, 012002 (2008).
[30] J. Blümlein, H. Böttcher, A. Guffanti, Nucl. Phys. B **774**, 182 (2007).
[31] S. Alekhin, J. Blümlein, S. Klein, S. Moch, Phys. Rev. D **81**, 014032 (2009).
[32] V. Mateu, R. Abbate, M. Fickinger, A. Hoang, I.W. Stewart, PoS D **IS2010**, 124 (2010).

Section Talks

Proceedings of the International School-seminar
"New Physics and Quantum Chromodynamics at External Conditions", pp. 74 – 76,
3-6 May 2011, Dnipropetrovsk, Ukraine

BOUNDS ON THE MASS AND MIXING OF Z'-BOSONS FROM LEP2 EXPERIMENTAL DATA

V. V. Andreev[a,1], A. A. Pankov[b,2]

[1]Gomel State University, Gomel, Belarus

[2]Abdus Salam ICTP Affiliated Centre at Gomel State Technical University, Gomel, Belarus

Analysis of effects induced by Z'-bosons based on LEP2 experimental data (OPAL, DELPHI, ALEPH, L3) on differential cross sections of the $W^{\pm}$-pair production process was performed. Constraints on Z'-boson mass $M_{Z'}$ and $Z - Z'$ mixing angle ϕ were obtained for some specific extended gauge models.

1 Introduction

With the advent of the LHC, particle physics has entered a new exciting era. Within a few years of data accumulation, the LHC should be able to test and constrain many types of new physics beyond the standard model (SM). In particular, the discovery reach for extra neutral gauge bosons, the existence of which is predicted by extended gauge models, such as left-right (LR) models, E_6-models and others, is exceptional. Searches for a high invariant dilepton mass peak in about 100 fb^{-1} of accumulated data will find or exclude Z'-bosons up to about 5 TeV, and a luminosity upgraded LHC (by roughly a factor of 10) can extend the reach by another TeV. However, the hadronic LHC environment will make it difficult to specify the Z' properties completely or with satisfactory precision. Investigation of Z' properties in other processes will therefore play an important complementary role in this context [1, 2, 3].

The process

$$e^+ + e^- \to W^+ + W^- \tag{1}$$

should be quite sensitive to indirect new physics effects, in particular, at high energies $\sqrt{s} \gg 2M_W$, which can destroy the SM gauge cancellation among the different contributions to the cross section, and hence cause deviations of the cross section from the SM prediction, which can increase with the CM energy [4]. In this regard, it is very interesting to analyze the data on $W^{\pm}$-pair boson production collected at OPAL, L3, DELPHI and ALEPH experiments at LEP2 [5, 6, 7, 8] in order to extract information on Z'-bosons. In particular, accumulated data on the angular distributions of charged gauge $W^{\pm}$-bosons allow to obtain constraints on the parameters of Z'-boson ($Z - Z'$ mixing angle ϕ and Z'-boson mass $M_{Z'}$).

2 Extended gauge models

The most popular models that predict the existence of Z'-bosons are the following:

E_6-models. E_6-models are based on the ideas of Grand Unification. They comprise $SU(5)$ and $SO(10)$ subgroups and are free of anomalies.

E_6-models break into SM in the following way: $E_6 \to SU(3)_C \times SU(2)_L \times U(1)_Y \times U(1)_{Y'}$. We consider the class of models, in which the linear combination

$$U(1)' = \cos\beta\, U(1)_\chi + \sin\beta\, U(1)_\psi$$

keeps safe up to the energies associated with electroweak processes.

The angle β satisfies the condition $-1 \le \cos\beta \le 1$. Depending on the values of β one can distinguish several E_6-based models:

$$\chi\text{-model: } \beta = 0^\circ \Longrightarrow U(1)' = U(1)_\chi\ ,$$

$$\psi\text{-model: } \beta = 90^\circ \Longrightarrow U(1)' = U(1)_\psi\ ,$$

$$\eta\text{-model: } \beta = -\arctan\sqrt{5/3} \simeq -52,2^\circ \Longrightarrow U(1)' = \sqrt{3/8}\, U(1)_\chi - \sqrt{5/8}\, U(1)_\psi\ ,$$

$$I\text{-model: } \beta = \arctan\sqrt{3/5} \simeq 37,8^\circ \Longrightarrow U(1)' = \sqrt{5/8}\, U(1)_\chi + \sqrt{3/8}\, U(1)_\psi\ .$$

e-mail: [a]quarks@gsu.by, [b]pankov@ictp.it

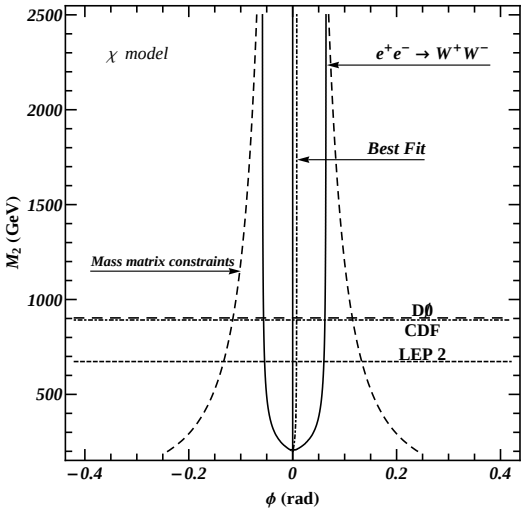

Figure 1. Constraints on ϕ and M_2 (95% $C.L.$) for χ-model

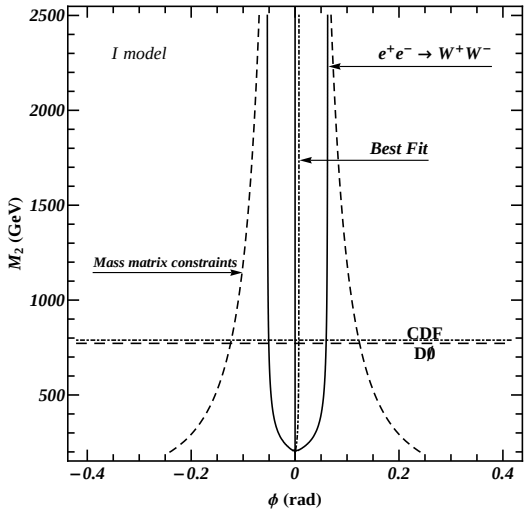

Figure 2. Constraints on ϕ and M_2 (95% $C.L.$) for I-model

LR-models. LR-models are based on the gauge group $SU(2)_L \times SU(2)_R \times U(1)_{B-L}$. Depending on the values of model parameter α_{LR} one can introduce a set of LR-models. In the general case parameter α_{LR} lies within the interval

$$1/\sqrt{2} \leq \alpha_{LR} \leq 1.53\ .$$

Sequential Standard Model. In addition to the above-mentioned models that are based on the extended gauge groups we will consider the so-called "sequential standard model" (SSM). The main feature of this model is that Z'-boson gauge couplings and standard Z-boson couplings are equal in this model. It's a good benchmark model, therefore the analysis of Z'-boson effects in the framework of SSM is quite interesting.

3 Differential distribution of $W^{\pm}$-pair production

In the SM the process (1) in born approximation consists of two s-channel diagrams with γ and Z-boson exchange and a t-channel diagram with neutrino ν exchange. Extended gauge models generate a different set of diagrams, that consists of the same t-channel diagram with neutrino ν and s-channel diagrams with γ, Z_1- and Z_2-bosons (mass eigenstates that correspond to Z- and Z'-bosons) exchange:

$$\begin{pmatrix} Z_1 \\ Z_2 \end{pmatrix} = \begin{pmatrix} \cos\phi & \sin\phi \\ -\sin\phi & \cos\phi \end{pmatrix} \begin{pmatrix} Z \\ Z' \end{pmatrix}, \tag{2}$$

where $Z,\ Z'$ are weak-eigenstates, $Z_1,\ Z_2$ are mass-eigenstates and ϕ is the $Z - Z'$ mixing angle. Taking Eq. (2) into account, the electron neutral current couplings to Z_1 and Z_2 are, respectively:

$$g^f_{1a} = g^f_a \cos\phi + g'^f_a \sin\phi\,; \qquad g^f_{2a} = -g^f_a \sin\phi + g'^f_a \cos\phi. \tag{3}$$

Finally, trilinear gauge boson couplings can be written as: $g_{WWZ_1} = \cot\theta_W \cos\phi$ and $g_{WWZ_2} = -\cot\theta_W \sin\phi$. Obviously, the SM case is reobtained when all (fermion and gauge boson) mixing angles are put equal to zero.

The unpolarized cross section of process (1) can be expressed in general as

$$\frac{d\sigma}{d\cos\theta} = \frac{1}{4}\left[\frac{d\sigma^{RL}}{d\cos\theta} + \frac{d\sigma^{LR}}{d\cos\theta} + \frac{d\sigma^{RR}}{d\cos\theta} + \frac{d\sigma^{LL}}{d\cos\theta}\right]. \tag{4}$$

The relevant polarized differential cross sections for $e^-_a e^+_b \to W^-_\alpha W^+_\beta$ can be written as

$$\frac{d\sigma^{ab}_{\alpha\beta}}{d\cos\theta} = C \cdot \sum_{k=0}^{k=2} F^{ab}_k\, \mathcal{O}_{k\,\alpha\beta}. \tag{5}$$

Here $C = \pi\alpha^2_{e.m.}\beta_W/2s$, with $\beta_W = (1 - 4M^2_W/s)^{1/2}$ to be the W velocity in the CM frame, the helicities of the initial e^+e^- and final W^+W^- states are labeled as $ab = (RL,\ LR,\ LL,\ RR)$ and $\alpha\beta = (LL,\ TT,\ TL)$, respectively. The $\mathcal{O}_k$ are functions of the kinematical variables, which characterize the various possibilities for the final W^+W^- polarizations (TT, LL, TL+LT or the sum over all W^+W^- polarization states for unpolarized W's). The F_k are combinations of coupling constants including the two kinds of mixings [4].

Table 1. Constraints on $Z - Z'$ mixing angle ϕ for different extended gauge models at M_2= 1 TeV obtained from LEP2 data for $W^{\pm}$-pair production.

Model	ϕ_{min}	ϕ_{max}	ϕ_{best}
χ-model	-0.05	0.06	0.01
ψ-model	-0.15	0.13	0.02
η-model	-0.50	0.15	0.03
I-model	-0.05	0.06	0.01
LR-model	-0.09	0.11	0.01
SSM	-0.07	0.05	-0.01

4 Numerical results

In order to obtain constraints on parameters ϕ ($Z - Z'$ mixing angle) and M_2 (Z_2-boson mass) a χ^2 method was used [9]. We construct the function

$$\chi^2\left(\mathbf{\Omega}\right) = \sum_{j}^{energy} \sum_{i=1}^{bins} \left[\frac{\Delta\sigma_i(exp) - \Delta\sigma_i\left(theory\right)}{\delta\sigma_i^2} \right]^2 , \tag{6}$$

where $\mathbf{\Omega} = \{\phi, M_2\}$, $\Delta\sigma_i(exp)$ – experimental values of differential cross sections of the process (1) in i-th bin, $\Delta\sigma_i\left(theory\right)$ – theoretical values of differential cross sections in i-th bin defined as $\Delta\sigma_i = \int_{bin}(d\sigma_i/\cos\theta)\, d\cos\theta$. Here we take into account both theoretical and experimental uncertainties as

$$\delta\sigma_i = \sqrt{\delta\sigma_i^2(exp) + \delta\sigma_i^2(theory)} \, .$$

Constraints on parameters that appear in $\mathbf{\Omega}$ can be obtained on the basis of the following inequality:

$$\chi^2\left(\mathbf{\Omega}\right) \leq \chi^2_{min} + \Delta\chi^2_{C.L.} \, . \tag{7}$$

Using inequality (7) one can obtain constraints on parameters ϕ and M_2 shown for some specific extended models in Fig. 1 and Fig. 2. Horizontal lines correspond to the lower bounds on Z'-boson mass obtained from D0 [10] and CDF [11] experiments at Tevatron. Also, constrains on Z'-boson mass obtained from LEP2 experiments [12] with four-fermion processes above Z peak are displayed in the figures. Finally, figures also contain the mass matrix constraints obtained by using the properties of mass matrix (2). As can be seen from the Fig. 1 and Fig. 2, the typical scale of constraints on the mixing angle for the mass of $M_2 \sim$1 TeV is as large as $\phi \sim 5 \cdot 10^{-2}$. The constraints for other extended gauge models are summarized in Tab. 1.

Acknowledgements. This research has been partially supported by funds of the University of Trieste, the Abdus Salam ICTP under the TRIL and STEP programmes and by the Belarusian Republican Foundation for Fundamental Research.

References

[1] A. Leike, Phys. Rept. **317**, 143 (1999).
[2] T. G. Rizzo, hep-ph/0610104, 537 (2006).
[3] P. Langacker, Rev. Mod. Phys. **81**, 1199 (2009).
[4] A. A. Babich, A. A. Pankov, and N. Paver, Phys. Lett. B **299**, 351 (1993).
[5] G. Abbiendy *et al.*, Eur. Phys. J. C **52**, 767 (2007).
[6] P. Achard *et al.*, Phys. Lett. B **600**, 22 (2004).
[7] J. Abdallah *et al.*, Eur. Phys. J. C **34**, 127 (2004).
[8] S. Schael *et al.*, Phys. Lett. B **614**, 7 (2005).
[9] K. Nakamura (Particle Data Group), J. Phys. G **37**, 075021 (2010).
[10] V. Abazov *et al.*, Phys. Lett. B **695**, 88 (2011).
[11] T. Aaltonen *et al.*, Phys. Rev. Lett. **102**, 091805 (2009).
[12] R. Barate *et al.*, Phys. Lett. B **565**, 61 (2003).

Proceedings of the International School-seminar
"New Physics and Quantum Chromodynamics at External Conditions", pp. 77 – 80,
3-6 May 2011, Dnipropetrovsk, Ukraine

MEASUREMENT OF THE GLUON MAGNETIC MASS IN EXTERNAL ABELIAN MAGNETIC FIELD

S. S. Antropov[a], V. I. Demchik[b], V. V. Skalozub[c]

Dnipropetrovsk National University, Dnipropetrovsk, Ukraine

The magnetic mass of neutral gluons in Abelian chromomagnetic field at high temperature is calculated in $SU(2)$ gluodynamics. It is noted that such type fields are spontaneously generated at high temperature. The mass is computed in Monte-Carlo simulations on a lattice. An average magnetic flux penetrating a plaquette is measured for a number of lattices. Calculations result in zero magnetic mass. Some applications of the results obtained are discussed.

1 Introduction

Investigation of deconfinement phase of QCD is a topic of actual interest in modern high energy physics. For instance, it is related to confinement models involving monopole condensation in the dual superconductor scenario. Further it is discussed as lowering the phase transition temperature [1]. It is also of interest for the QCD phase diagram, for quark-gluon plasma and related topics like the state of the early universe.

As it was discovered recently, in the non-Abelian gauge theories at high temperature a spontaneous vacuum magnetization happens. This has been determined either by analytic quantum field theory methods [2], [3], [5], [4] or in lattice simulations [6]. This phenomenon is analogous to the spontaneous creation of Abelian chromomagnetic field $B = const$ discovered at zero temperature $T = 0$ by Savvidy [7].

As it is occurred, the situation changes at finite temperature $T \neq 0$ and the spectrum stabilization happens due to either a gluon magnetic mass [4] or so-called A_0-condensate which is proportional to the Polyakov loop [8]. These are the extensions of the Savvidy model to the finite temperature case. Further investigations of quarks and gluons at this background are of interest if the generated classical fields are long range ones.

The most essential field characteristics at finite temperature are the electric (Debye) and magnetic masses responsible for screening of long range color electric and magnetic fields, respectively. As concerns the magnetic mass, it requires an additional consideration that is the topic of the present investigation. The point is that in the field presence it is natural to divide gluons in two types - the charged and the neutral gluons, - which have different magnetic masses at high temperatures. For the former fields, the nonzero magnetic mass has been determined in one-loop order [4]. The zero value has been obtained in one-loop approximation in Refs. [9], [10]. In next section the magnetic mass of Abelian chromomagnetic field is computed by using Monte-Carlo simulations. The discussion and possible applications are given in section 3.

2 Magnetic mass on a lattice

To solve the problem, we calculate the magnetic mass of the Abelian chromomagnetic field by using Monte-Carlo (MC) simulations on a lattice. For this purpose we, following Ref.[14], investigate the behavior of the average magnetic flux penetrating a lattice plaquette oriented perpendicular to the magnetic field direction. To introduce the classical magnetic field on a lattice we apply the twisted boundary conditions discussed below.

In the MC simulations, we use the hypercubic lattice $L_t \times L_s^3$ with hypertorus geometry. The standard Wilson action of the $SU(2)$ lattice gauge theory is

$$S_W = \beta \sum_x \sum_{\mu<\nu} \left[1 - \frac{1}{2} \mathrm{Tr} \left[\mathbf{U}_\mu(x) \mathbf{U}_\nu(x + a\hat{\mu}) \mathbf{U}_\mu^\dagger(x + a\hat{\nu}) \mathbf{U}_\nu^\dagger(x) \right] \right], \tag{1}$$

where $\beta = 4/g^2$ is the lattice coupling constant, g is a bare gauge coupling, $\mathbf{U}_\mu(x)$ is the link variable located on the link leaving the lattice site x in the μ-th direction. The link variables $\mathbf{U}_\mu(x)$ are $SU(2)$ matrices decomposed in terms of the unity, I, and Pauli σ_j, matrices in color space,

$$U_\mu(x) = IU_\mu^0(x) + i\sigma_j U_\mu^j(x) = \begin{pmatrix} U_\mu^0(x) + iU_\mu^3(x) & U_\mu^2(x) + iU_\mu^1(x) \\ -U_\mu^2(x) + iU_\mu^1(x) & U_\mu^0(x) - iU_\mu^3(x) \end{pmatrix}. \tag{2}$$

e-mail: [a]santrop_2@yahoo.com, [b]vadimdi@yahoo.com, [c]skalozubv@daad-alumni.de

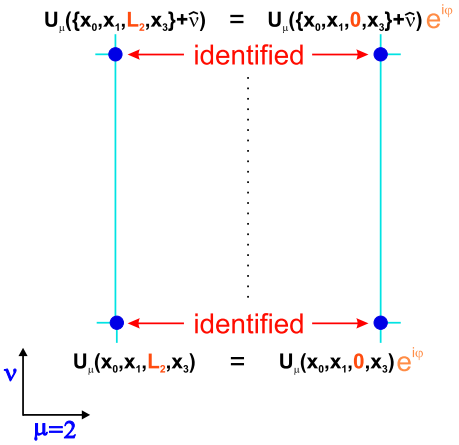

Figure 1. The plaquette presentation of the twisted boundary conditions.

Next let us incorporate the external Abelian magnetic field into this formalism. As in Refs.[6], [13] we represent the field in terms of external fluxes φ. The constant homogeneous external flux φ in the third spatial direction can be introduced by applying the following twisted boundary conditions (t.b.c.) [13]:

$$\begin{aligned} U_\mu(L_t, x_1, x_2, x_3) &= U_\mu(0, x_1, x_2, x_3), \\ U_\mu(x_0, L_s, x_2, x_3) &= U_\mu(x_0, 0, x_2, x_3), \\ U_\mu(x_0, x_1, L_s, x_3) &= e^{i\varphi} U_\mu(x_0, x_1, 0, x_3), \\ U_\mu(x_0, x_1, x_2, L_s) &= U_\mu(x_0, x_1, x_2, 0). \end{aligned} \tag{3}$$

These give

$$U^0_\mu(x) = \begin{cases} U^0_\mu(x)\cos(\varphi) - U^3_\mu(x)\sin(\varphi) & \text{for } x = (x_0, x_1, L_s, x_3) \text{ and } \mu = 2 \\ U^0_\mu(x) & \text{for other links} \end{cases},$$

$$U^3_\mu(x) = \begin{cases} U^0_\mu(x)\sin(\varphi) + U^3_\mu(x)\cos(\varphi) & \text{for } x = (x_0, x_1, L_s, x_3) \text{ and } \mu = 2 \\ U^0_\mu(x) & \text{for other links} \end{cases}.$$

The edge links in all directions are identified as usual periodic boundary conditions except for the links in the second spatial direction for which the additional phase φ is added (Fig. 1). In the continuum limit, such t.b.c. settle the magnetic field with the potential $\bar{A}_\mu = (0, 0, Bx^1, 0)$. The magnetic flux φ is measured in angular units and can take continuous values from 0 to 2π.

The magnetic mass of the field of interest is measured by investigating the average plaquette values for the twisted and untwisted lattices. The main object of investigations is the difference (magnetic flux through a lattice plaquette perpendicular to the OZ axis):

$$\langle U_{untwisted} \rangle - \langle U_{twisted} \rangle = f(m, L_s), \tag{4}$$

which is fitted for each lattice geometry $L_t \times L_s^3$ by different functions $f(m, L_s)$. The temperature is introduced in a standard way through a lattice asymmetry in the temporal direction ($L_t < L_s$). The measurements were fulfilled for the value of $\beta = 2.6$ in the perturbation regime for the deconfinement phase. Lattices with $L_t = 4$ and L_s up to 32 were used. To update the lattice, heat-bath algorithm with overrelaxation was used [15]. To thermalize the system, up to 6000 MC iterations were used. The plaquette average is calculated by averaging up to 10000 working iterations.

To estimate the behavior of magnetic fields a large amount of simulation data must be prepared. Unfortunately, traditional computational resources are lack to perform the detailed analysis. In our case, we use the General Purpose computation on Graphics Processing Units (GPGPU) technology allowing to study large lattices on personal computers. GPU programming model implemented here and some technical details on MC simulations on ATI graphics processing units (GPU) are given in Ref. [11].

To generate the pseudo-random numbers for MC procedure, three different pseudo-random number generators are used: RANMAR, RANLUX and XOR128 [12]. The last one allows to obtain the maximal performance but is not widely used in MC simulations. So, all the results were checked with the slower generators RANMAR and RANLUX.

Performance analysis indicates that the GPU-based MC simulation program shows better speed-up factors for big lattices in comparing with the CPU-based one. For the majority lattice geometries the GPU vs. CPU

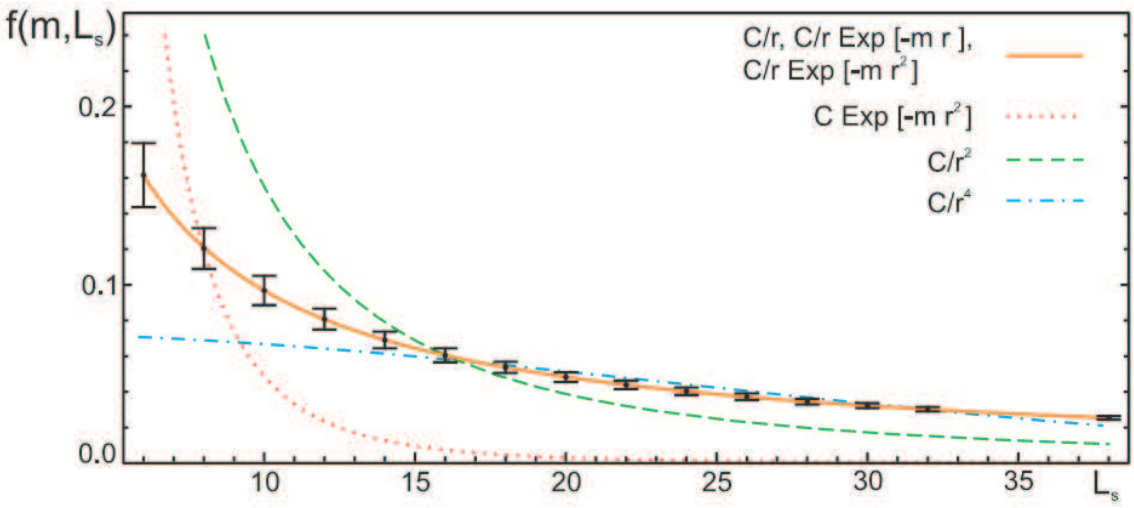

Figure 2. $f(m, L_s)$ versus L_s and fitting curves ($L_t = 4$, $\beta = 2.6$).

(single-thread CPU execution) speed-up factor is above 50x and for some lattice sizes could overcome the factor 100x.

Thus, GPU-based MC program allows to calculate the difference (4) for a wide interval of lattice geometries. Also, up to 1000 independent runs for each lattice size were performed in order to decrease the dispersion of the obtained values $f(m, L_s)$. The whole set of simulation data for different lattice geometries was fitted with the several functions which correspond to the different behavior of magnetic flux.

The flux value $f(m, L_s)$ is determined by (4) and shown in Table 1 and Figure 2. The whole set of the data obtained in MC simulations is divided into 15 bins. The mean values are presented as the black points and the corresponding 2σ confidential level intervals are depicted by the vertical lines. The plotted data refer to $L_t = 4$ and $\beta = 2.6$. The relative errors decrease from 11.1% to 4.1% with increasing L_s, as it should be.

In order to investigate different hypothesis for the behavior of the magnetic flux we try to fit the MC data with some set of functions by means of the χ^2-method. The first test function C/r^2 corresponds to the magnetic flux tube formation. Here r is the lattice size L_s in the X and Y directions, C is an unknown parameter. The total magnetic flux through the lattice is conserved in this case. Next function C/r^4 describes the Coulomb-like behavior and the function $C/r^2 \exp(-m^2 r^2)$ is signaling the generation of the magnetic mass m [14]. The last functions $C/r \exp(-mr)$ and C/r can be related to increasing of the field strength with a temperature growth. This is because the total magnetic flux through the lattice is growing faster than in the case of the magnetic flux tube formation.

The fitted curves are shown in Fig. 2. These are: a) the visually coinciding solid curves – C/r, $C/r \exp(-mr)$, $C/r \exp(-mr^2)$; b) the dot curve – $C \exp(-mr^2)$; c) the dash curve – C/r^2; d) the dash-dot curve – C/r^4.

The numerical results of fitting procedure are collected in Table 2. The table contains the test functions, the values of the χ^2-function corresponding to the 95% confidence level, the obtained magnetic masses m and parameters C.

As it follows from Table 2, the best fit function is $C/r \exp(-mr)$ with a small value of the magnetic mass $m = 1.25 \times 10^{-6}$. The value of χ^2 function in this case is very close to the $m = 0$ situation and statistically these cases are indistinguishable. Really, the statistical errors are larger than the fitted value of m. Thus, from the performed analysis we can conclude that the neutral component of the gluon field is not screened at high temperature like usual magnetic field.

3 Discussion

We performed calculation of the magnetic mass for neutral gluons in the Abelian chromomagnetic field at high temperature. Such type fields have to be spontaneously generated in deconfinement phase. They are stable due to a large value of the charged gluon magnetic mass [4], [13]. The obtained results indicate the zero mass value is determined with the accuracy proper to the method used. Hence, we conclude that such magnetic fields are long range ones. This, in particular, means that Abelian magnetic fields, being the solutions to the non-Abelian gauge field equations without sources, are spontaneously created at high temperature and exist till the confinement phase transition happens.

Interesting additional arguments in favor of spontaneous vacuum magnetization at high temperature were obtained in sect. 3. In the measurements fulfilled, we observed that for the fitting function $f(m, L_s) = C/r^2$ corresponding to the magnetic flux tube formation the χ^2 value is very large and entirely inconsistent with the data. But in the geometry of measurements it describes the conservation of the magnetic flux introduced

Table 1. Monte-Carlo data.

$f(m, L_S)$	L_S
0.161 ± 0.018	6
0.12 ± 0.011	8
0.097 ± 0.008	10
0.081 ± 0.006	12
0.069 ± 0.005	14
0.06 ± 0.004	16
0.054 ± 0.003	18
0.048 ± 0.003	20
0.044 ± 0.002	22
0.04 ± 0.002	24
0.037 ± 0.002	26
0.0345 ± 0.0016	28
0.0322 ± 0.0014	30
0.0302 ± 0.0013	32
0.025 ± 0.001	38

Table 2. Fit results for magnetic mass of Abelian magnetic field.

	Abelian field		
Fit function	χ^2	C	m
$C\exp(-mr)$	901.8	0.063	$m = (2.44^{+0.06}_{-0.06}) \times 10^{-2}$
$C\exp(-m^2r^2)$	1924.4	0.035	$m = (1.57^{+0.02}_{-0.02}) \times 10^{-2}$
C/r	7.090	0.911	
$C/r\exp(-mr)$	7.086	0.912	$m = (1.25^{+52}_{-54}) \times 10^{-6}$
$C/r\exp(-m^2r^2)$	7.090	0.911	$m^2 = (2.4^{+5951.2}_{-5784}) \times 10^{-10}$
C/r^2	31400	28.13	
$C/r^2\exp(-m^2r^2)$	7550	18.26	$m^2 = -3.3 \times 10^{-5}$
C/r^4	159500	248.9	
$C/r^4\exp(-m^4r^4)$	161000	10.0	$m = 0.0$

by the twist of the boundary conditions. The best fit functions C/r, $C/r\exp(-mr)$ with very small (actually, zero) m are signaling an increase of the mean magnetic field strength penetrating the plaquette perpendicular to the field direction. As a result, the flux though the whole $(X-Y)$ plain should increase. The only natural explanation is the spontaneous generation of the field inside the volume of the lattice.

As a general conclusion we note that the presence of Abelian temperature dependent magnetic fields in high temperature phase of QCD and other gauge field theories has to be taken into consideration when various phenomena are investigated.

References

[1] P. Cea, L. Cosmai and M. D'Elia, JHEP **0712**, 097 (2007).
[2] A. O. Starinets, A. S. Vshivtsev and V. C. Zhukovsky, Phys. Lett. B **322**, 403 (1994).
[3] K. Enqvist and P. Olesen, Phys. Lett. B **329**, 195 (1994) [arXiv:hep-ph/9402295].
[4] V. Skalozub and M. Bordag, Nucl. Phys. B **576**, 430 (2000) [arXiv:hep-ph/9905302].
[5] V. V. Skalozub, Int. J. Mod. Phys. A **11**, 5643 (1996).
[6] V. I. Demchik and V. V. Skalozub, Phys. Atom. Nucl. **71**, 180 (2008).
[7] G. K. Savvidy, Phys. Lett. B **71**, 133 (1977).
[8] D. Ebert, V. C. Zhukovsky and A. S. Vshivtsev, Int. J. Mod. Phys. A **13**, 1723 (1998).
[9] V.V. Skalozub and A.V. Strelchenko, Eur. Phys. J. C **33**, 105 (2004).
[10] M. Bordag and V. Skalozub, Phys. Rev. D **75**, 125003 (2007) [arXiv:hep-th/0611256].
[11] V. Demchik and A. Strelchenko, arXiv:0903.3053 [hep-lat].
[12] V. Demchik, Comp. Phys. Comm. **182**, 692 (2011), doi: 10.1016/j.cpc.2010.12.008; arXiv:1003.1898 [hep-lat].
[13] V. Demchik and V. Skalozub, arXiv:hep-lat/0601035.
[14] T. A. DeGrand and D. Toussaint, Phys. Rev. D **25** (1982) 526. Phys. Rev. D **25** (1982) 526.
[15] M. Creutz, Phys. Rev. D **36** (1987) 515.

Proceedings of the International School-seminar
"New Physics and Quantum Chromodynamics at External Conditions", pp. 81 – 84,
3-6 May 2011, Dnipropetrovsk, Ukraine

GENERALIZATION OF THE GROSS-PITAEVSKII EQUATION FOR BOSE GAS IN THE PRESENCE OF QUASI-PARTICLES

N. N. Bannikova [a], A. I. Sokolovsky [b]

Dnipropetrovsk National University, Dnipropetrovsk, Ukraine

The Gross-Pitaevskii equation has been generalized for the case of presence of the Bogolyubov quasi-particles at hydrodynamic stage of their evolution. Hydrodynamic equations for quasi-particle subsystem are constructed by the Chapman-Enskog method. The obtained equations can be considered as a new form of hydrodynamic equations of superfluid Bose gas. In the Landau-Khalatnikov hydrodynamics the total density of the system is used instead of amplitude of the condensate wave function.

1 Introduction

The problem of justification and generalization of the Gross-Pitaevskii equation is widely discussed in the literature (see, for example, [1, 2]). In the present paper it is studied on the basis of the Bogolyubov reduced description method which allows investigating domain of applicability of the theory and building corrections to it. Key issue of our consideration is definition of condensate wave function $\psi(x,t)$ as an average value of the Bose field operator $\psi(x)$ with statistical operator of the system $\rho(t)$

$$\psi(x,t) = \mathrm{Sp}\rho(t)\psi(x) = \eta(x,t)e^{i\varphi(x,t)} \qquad (\eta(x,t) \geq 0, \quad 0 \leq \varphi(x,t) < 2\pi). \tag{1}$$

This definition leaves aside the questions: is the condensate as a subsystem of a Bose gas in a pure state and is this state stable. However, this definition is a fruitful basis for various generalizations of the Gross-Pitaevskii equation. Hamilton operator of the system takes into account short range repulsive interaction between particles $\Phi(r)$. Our consideration is based on set of equations obtained in paper [3] in which nonequilibrium states Bose gas in the presence of condensate are described by amplitude $\eta(x,t)$ of the condensate wave function, local velocity of the condensate $\upsilon_n(x,t) = m^{-1}\partial\varphi(x,t)/\partial x_n$ (m is mass a particle; in this paper $\hbar = 1$), the Wigner distribution function for the Bogolyubov quasi-particles $f_p(x,t)$ in reference system of the condensate rest. Gradients of parameters $\xi_\mu(x,t)$: $f_p(x,t)$, $\eta(x,t)$, $\upsilon_n(x,t)$ are assumed to be small (small parameter g) and therefore states of the system are weak non-uniform. Interaction between particles $\Phi(r)$ is also considered as small one. For summation of contributions of the perturbation theory, which leads to the Bogolyubov quasi-particles spectrum in the leading approximation, estimations $\Phi(r) \sim \lambda^2$, $\eta \sim \lambda^{-1}$ are used (small parameter λ). Equations of the mentioned paper one can consider as a generalization of Gross-Pitaevskii equation for case of presence of quasi-particles at kinetic stage of their evolution. The purpose of the present work is a generalization of the Gross-Pitaevskii equation for case of presence of quasi-particles at hydrodynamic stage of their evolution.

2 Basic equations of the theory

Set of equations obtained in paper [3] has structure

$$\frac{\partial\eta}{\partial t} = -\upsilon_n\frac{\partial\eta}{\partial x_n} - \frac{\eta}{2}\frac{\partial\upsilon_n}{\partial x_n} + L \equiv L_\eta, \qquad \frac{\partial\varphi}{\partial t} = -m\left(\frac{\upsilon^2}{2} + h\right),$$

$$\frac{\partial f_p}{\partial t} = -\frac{\partial f_p}{\partial x_l}\frac{\partial(\varepsilon_p + p_n\upsilon_n)}{\partial p_l} + \frac{\partial f_p}{\partial p_l}\frac{\partial(\varepsilon_p + p_n\upsilon_n)}{\partial x_l} + L_p, \qquad \frac{\partial\upsilon_n}{\partial t} = -\upsilon_l\frac{\partial\upsilon_l}{\partial x_n} - \frac{\partial h}{\partial x_n} \equiv L_{\upsilon_n} \tag{2}$$

where ε_p is spectrum of the Bogolyubov quasi-particles

$$\varepsilon_p = (\alpha_p^2 - \beta_p^2)^{1/2}, \qquad \alpha_p \equiv \varepsilon_p^o + \beta_p, \qquad \varepsilon_p^o \equiv \frac{p^2}{2m}, \qquad \beta_p \equiv \nu_p\eta^2, \qquad \nu_p \equiv \int d^3x\Phi(|x|)e^{ipx}. \tag{3}$$

Right hand side part of this equations were calculated in [3] with accuracy shown below

$$h = h_0 + h^{(0,2)} + O(g^0\lambda^4, g^1\lambda^2, g^2\lambda^1), \qquad h_0 \equiv -\frac{\Delta\eta}{2m^2\eta} + \frac{1}{m}\int d^3x'\Phi\left(|x'|\right)\eta\left(x + x'\right)^2;$$

e-mail: [a]alexsokolovsky@mail.ru, [b]bnndnu@mail.ru

$$L = L^{(0,3)} + L^{(1,1)} + O(g^0\lambda^5, g^1\lambda^2, g^2\lambda^1); \qquad L_p = L_p^{(0,2)} + L_p^{(0,4)} + O(g^0\lambda^5, g^1\lambda^2, g^2\lambda^1), \tag{4}$$

where $L^{(0,3)}, L^{(1,1)}, h^{(0,2)}, L_p^{(0,2)}, L_p^{(0,4)}$ are known functions of parameters $\xi_\mu(x)$, which are given by bulky expressions and omitted here ($A^{(m,n)}$ is contribution to A of the order $g^m\lambda^n$; $L_p^{(0,2)}, L_p^{(0,4)}$ are collision integrals for quasi-particles). The forth equation in (2) is a consequence of the second one. The second equation was given above because it with the first one are equivalent to the Gross-Pitaevskii equation if we restrict ourselves by approximation

$$L = 0, \qquad h = h_0^{(0,0)} + h_0^{(2,0)} \tag{5}$$

The problem of this paper is to construct hydrodynamic equations for quasi-particle subsystem of the Bose gas interacting with the condensate subsystem. The hydrodynamic equations are a consequence of energy and momentum conservation laws for quasi-particles and in the local reference system of the condensate rest according to the third equation in (2) have the form

$$\frac{\partial \varepsilon^o}{\partial t} = -\frac{\partial q_n^o}{\partial x_n} - \frac{\partial \varepsilon^o \upsilon_n}{\partial x_n} - t_{ln}^o \frac{\partial \upsilon_l}{\partial x_n} - a\left(L - \frac{\eta}{2}\frac{\partial \upsilon_n}{\partial x_n}\right) \equiv L_0,$$

$$\frac{\partial \pi_l^o}{\partial t} = -\frac{\partial t_{ln}^o}{\partial x_n} - \frac{\partial \pi_l^o \upsilon_n}{\partial x_n} - \pi_n^o \frac{\partial \upsilon_n}{\partial x_l} + a\frac{\partial \eta}{\partial x_l} \equiv L_l. \tag{6}$$

Here ε^o, π_n^o are densities of energy and momentum, q_n^o, t_{ln}^o are flux densities of energy and momentum in the mentioned reference system, a is thermodynamic force which condensate acts on quasi-particle subsystem with. These values are given by formulas

$$\varepsilon^o = \int d\tau_p \varepsilon_p f_p, \qquad \pi_l^o = \int d\tau_p p_l f_p, \qquad q_n^o = \int d\tau_p \varepsilon_p \frac{\partial \varepsilon_p}{\partial p_n} f_p, \qquad t_{ln}^o = \int d\tau_p p_l \frac{\partial \varepsilon_p}{\partial p_n} f_p,$$

$$a = -\int d\tau_p \frac{\partial \varepsilon_p}{\partial \eta} f_p \qquad (d\tau_p \equiv \frac{d^3p}{(2\pi)^3}). \tag{7}$$

In order to close equations (6) we use the Bogolyubov functional hypothesis on which the Chapman-Enskog method is based [4]. According it distribution function of quasi-particles $f_p(x,t)$ at times of their hydrodynamic evolution ($t \gg \tau_o$) is a functional of parameters $\zeta_\alpha(x,t) : \varepsilon^o(x,t), \pi_n^o(x,t), \eta(x,t), \upsilon_n(x,t)$

$$f_p(x,t) \xrightarrow[t \gg \tau_0]{} f_p(x, \zeta(t)). \tag{8}$$

In hydrodynamics of quasi-particles instead of densities $\varepsilon^o(x,t)$,$\pi_n^o(x,t)$ one can use their local temperature $T(x,t)$ and drift velocity $\omega_n(x,t)$ in the reference system of the condensate rest which are defined by relations

$$\varepsilon^o(x) = \int d\tau_p \varepsilon_p(\eta(x)) f_p(x,\zeta) = \int d\tau_p \varepsilon_p(\eta(x)) n_p(\chi(x)),$$

$$\pi_n^o(x) = \int d\tau_p p_n f_p(x,\zeta) = \int d\tau_p p_n n_p(\chi(x)). \tag{9}$$

Here

$$n_p(\chi) = [e^{\frac{\varepsilon_p(\eta) - p_n\omega_n}{T}} - 1]^{-1} \tag{10}$$

is the Planck distribution (in this paper $k_B = 1$); $\omega_n(x,t) \equiv u_n(x,t) - \upsilon_n(x,t)$; $u_n(x,t)$ is local velocity of quasi-particle subsystem in the lab reference system; $\chi_\alpha(x)$ denotes parameters: $T(x), \omega_n(x), \eta(x), \upsilon_n(x)$. According to (2), (8) functional $f_p(x,\zeta)$ satisfies equation

$$\sum_\alpha \int d^3x' \frac{\delta f_p}{\delta \zeta_\alpha(x')} L_\alpha(x') = -\frac{\partial f_p}{\partial x_l}\frac{\partial(\varepsilon_p + p_n\upsilon_n)}{\partial p_l} + \frac{\partial f_p}{\partial p_l}\frac{\partial(\varepsilon_p + p_n\upsilon_n)}{\partial x_l} + L_p \tag{11}$$

($L_\alpha : L_0, L_n, L_\eta, L_{\upsilon_n}$) with additional conditions (9).

3 Hydrodynamic equations for quasi-particles

Distribution function of quasi-particles $f_p(x,\zeta)$ at the reduced description is calculated from equation (11) in perturbation theory in g and λ taking into account relations (9). As a result it has been obtained in the form

$$f_p = n_p + f_p^{(1,-2)} + O(g^0\lambda^4, g^1\lambda^{-1}),$$

$$f_p^{(1,-2)} = n_p(1+n_p)\{A_n(p)\frac{\partial T}{\partial x_n} + B_{nl}(p)\frac{\partial u_n}{\partial x_l} + C(p)\frac{\partial \omega_n \eta^2}{\partial x_n}\} \tag{12}$$

where functions $A_n(p), B_{nl}(p), C(p)$ are solution of integral equations

$$a_n(p) = \int d^3p' K(p,p') A_n(p'), \qquad b_{nl}(p) = \int d^3p' K(p,p') B_{nl}(p'), \qquad c(p) = \int d^3p' K(p,p') C(p') \tag{13}$$

($a_n(p), b_{nl}(p), c(p)$ are known functions) with additional conditions

$$\overline{A_n(p) p_l} = 0, \qquad \overline{B_{nl}(p)\varepsilon_p} = 0, \qquad \overline{C(p)\varepsilon_p} = 0 \tag{14}$$

where for arbitrary function $F(p)$ notation

$$\overline{F(p)} \equiv \int d\tau_p n_p (1+n_p) F(p)$$

is introduced. These conditions are a consequence of definition of the temperature T and drift velocity ω_n (9). Kernel $K(p,p')$ of integral equations (13) is defined by linearized collision integral

$$M(p,p') \equiv \left.\frac{\delta L_p^{(0,2)}}{\delta \mathrm{f}_{p'}}\right|_{f=n}, \qquad M(p,p') n_{p'}(1+n_{p'}) = -n_p(1+n_p) K(p,p'). \tag{15}$$

Solution of equations (13) will be discussed in another paper.

Main contribution in gradients to fluxes can be calculated using approach of our paper [5]

$$q_n^{o[0,0]} = \int d\tau_p \varepsilon_p \frac{\partial \varepsilon_p}{\partial p_n} n_p = (\varepsilon^o - \omega)\omega_n, \qquad t_{ln}^{o[0,0]} = \int d\tau_p p_l \frac{\partial \varepsilon_p}{\partial p_n} n_p = -\omega\delta_{ln} + \omega_n \pi_l^o \tag{16}$$

where ω is thermodynamic potential of quasi-particles defined by the formula

$$\omega = T \int d\tau_p \ln(1 - e^{\frac{p_s\omega_s - \varepsilon_p}{T}}). \tag{17}$$

Entropy density of their subsystem s is given by definition

$$s = s(n), \qquad s(f) \equiv \int d\tau_p \{(1+f_p)\ln(1+f_p) - f_p \ln f_p\} \tag{18}$$

which leads to thermodynamic relations

$$sT = \varepsilon^o - \omega - \pi_n^o \omega_n, \qquad d\omega = -sdT - \pi_n^o d\omega_n - a_0 d\eta. \tag{19}$$

Distribution function (12) gives equations

$$\frac{\partial \eta}{\partial t} = -u_n \frac{\partial \eta}{\partial x_n} - \frac{\eta}{2}\frac{\partial u_n}{\partial x_n} + \frac{1}{2\eta}\frac{\partial \omega_n \eta^2}{\partial x_n} + L^{[1,1]} + O(g^1\lambda^2, g^2\lambda^{-1}),$$

$$\frac{\partial \varphi}{\partial t} = -\frac{m\upsilon^2}{2} - m(h_0 + h^{[0,2]} + h^{[1,0]}) + O(g^0\lambda^4, g^1\lambda^1), \tag{20}$$

which generalize the Gross-Pitaevskii equation, and connected with them hydrodynamic equations for quasi-particles

$$\frac{\partial \varepsilon^o}{\partial t} = -\frac{\partial \varepsilon^o u_n}{\partial x_n} + (\omega + \frac{1}{2}a_0\eta)\frac{\partial u_n}{\partial x_n} - s\omega_n \frac{\partial T}{\partial x_n} - \frac{a_0}{2\eta}\frac{\partial \omega_n \eta^2}{\partial x_n} - \frac{\partial q_n^{o[1,-2]}}{\partial x_n} - t_{ln}^{o[1,-2]}\frac{\partial \upsilon_l}{\partial x_n} + a^{[1,-1]}\frac{\eta}{2}\frac{\partial \upsilon_n}{\partial x_n} + O(g^1\lambda^1, g^2\lambda^{-1}),$$

$$\frac{\partial \pi_l^o}{\partial t} = -\frac{\partial \pi_l^o u_n}{\partial x_n} - s\frac{\partial T}{\partial x_l} - \pi_n^o \frac{\partial u_n}{\partial x_l} - \frac{\partial t_{ln}^{o[1,-2]}}{\partial x_n} + a^{[1,-1]}\frac{\partial \eta}{\partial x_l} + O(g^1\lambda^0, g^2\lambda^{-1}),$$

$$\frac{\partial \upsilon_n}{\partial t} = -\upsilon_l \frac{\partial \upsilon_l}{\partial x_n} - \frac{\partial}{\partial x_n}(h_0 + h^{[0,2]} + h^{[1,0]}) + O(g^1\lambda^4, g^2\lambda^1). \tag{21}$$

In contrast to standard Chapman-Enskog method we took into account approximate nature of the equation set (2) ($A^{[m,n]}$ is contribution to A of the order $g^m\lambda^n$ connected with expansion of distribution function $f_p(x,\zeta)$ in series of the perturbation theory; $a^{[0.0]} \equiv a_0$). Equations (21) contain also dissipative values which have the structure

$$q_n^{o[1,-2]} = -\kappa_{nl}\frac{\partial T}{\partial x_l} - \alpha_{n,lm}\frac{\partial u_l}{\partial x_m} - \lambda_n \frac{\partial \omega_l \eta^2}{\partial x_l}, \quad t_{nl}^{o[1,-2]} = -\beta_{nl,m}\frac{\partial T}{\partial x_m} - \eta_{nl,ms}\frac{\partial u_m}{\partial x_s} - \mu_{nl}\frac{\partial \omega_s \eta^2}{\partial x_s},$$

$$h^{[1,0]} = -\chi_n \frac{\partial T}{\partial x_n} - \varphi_{nl} \frac{\partial u_n}{\partial x_l} - \psi \frac{\partial \omega_n \eta^2}{\partial x_n}, \quad a^{[1,-1]} = -\sigma_n \frac{\partial T}{\partial x_n} - \nu_{nl} \frac{\partial u_n}{\partial x_l} - \gamma \frac{\partial \omega_n \eta^2}{\partial x_n}. \tag{22}$$

Here κ_{nl} is heat conductivity and $\eta_{nl,ms}$ is viscosity of quasi-particle subsystem. For calculation of these kinetic coefficients we obtained the following expressions

$$\kappa_{nl} = -\overline{\varepsilon_p \frac{\partial \varepsilon_p}{\partial p_n} A_l(p)}, \qquad \alpha_{n,lm} = -\overline{\varepsilon_p \frac{\partial \varepsilon_p}{\partial p_n} B_{lm}(p)}, \qquad \lambda_n = -\overline{\varepsilon_p \frac{\partial \varepsilon_p}{\partial p_n} C(p)};$$

$$\beta_{ln,m} = -\overline{p_l \frac{\partial \varepsilon_p}{\partial p_n} A_m(p)}, \qquad \eta_{ln,ms} = -\overline{p_l \frac{\partial \varepsilon_p}{\partial p_n} B_{ms}(p)}, \qquad \mu_{ln} = -\overline{p_l \frac{\partial \varepsilon_p}{\partial p_n} C(p)};$$

$$\chi_n = -\frac{1}{m}\overline{(\frac{1}{2\eta}\frac{\partial \varepsilon_p}{\partial \eta} + \nu_0 \frac{\alpha_p}{\varepsilon_p}) A_n(p)}, \qquad \varphi_{nl} = -\frac{1}{m}\overline{(\frac{1}{2\eta}\frac{\partial \varepsilon_p}{\partial \eta} + \nu_0 \frac{\alpha_p}{\varepsilon_p}) B_{nl}(p)}, \qquad \psi = -\frac{1}{m}\overline{(\frac{1}{2\eta}\frac{\partial \varepsilon_p}{\partial \eta} + \nu_0 \frac{\alpha_p}{\varepsilon_p}) C(p)};$$

$$\sigma_n = \overline{\frac{\partial \varepsilon_p}{\partial \eta} A_n(p)}, \qquad \nu_{nl} = \overline{\frac{\partial \varepsilon_p}{\partial \eta} B_{nl}(p)}, \qquad \gamma = \overline{\frac{\partial \varepsilon_p}{\partial \eta} C(p)}. \tag{23}$$

These relations allow to investigate dependence of kinetic coefficients of quasi-particle subsystem on temperature. The result will be presented in another paper. This investigation can be simplified in the small drift velocity approximation. In this limit non-zero kinetic coefficients are scalar functions.

Additional information about properties of dissipative fluxes and kinetic coefficients can be obtained from evolution equation for entropy. This equation follows from relations (19) and has the form

$$\frac{\partial s}{\partial t} = -\frac{\partial s_n}{\partial x_n} + R \tag{24}$$

where s_n is flux and R is production of the entropy. In the considered approximation these values can be written as

$$s_n = s u_n + \frac{\varphi_n^{[1,-2]}}{T} + O(g^0\lambda^2, g^1\lambda^1),$$

$$R = -\varphi_n^{[1,-2]} \frac{1}{T^2}\frac{\partial T}{\partial x_n} - \tau_{ln}^{[1,-2]} \frac{1}{T}\frac{\partial u_l}{\partial x_n} - a^{[1,-1]} \frac{1}{2\eta T}\frac{\partial \eta^2 \omega_n}{\partial x_n} + O(g^2\lambda^1) \tag{25}$$

where

$$\varphi_n^{[1,-2]} \equiv q_n^{o[1,-2]} - \omega_l t_{ln}^{o[1,-2]}, \qquad \tau_{ln}^{[1,-2]} \equiv t_{ln}^{o[1,-2]} - \frac{\eta}{2} a^{[1,-1]} \delta_{ln}. \tag{26}$$

According to the Onsager principle this result allows to establish symmetry of kinetic coefficients (23) and to prove inequality $R \geq 0$.

4 Conclusions

The reduced description method allows to justify domain of applicability of the Gross-Pitaevskii equation and to find various corrections to it. The obtained in the paper equations can be applied to investigation of possibility of quasi-particles creation at evolution of the condensate and to problem of stability of equilibrium quasi-particle subsystem.

Acknowledgements. This work was supported in part by the State Foundation of Fundamental Research of Ukraine under project 25.2/102.

References

[1] L.P. Pitaevskii, Bose-Einstein condensates in a laser radiation field, Physics Uspekhi **49**, 333 (2006).

[2] E.H. Lieb, R. Seiringer, J. Ingvason, Bosons in a trap: A rigorous derivation of the Gross-Pitaevskii energy functional, Phys. Rev. A.**61**, 043602 (2000).

[3] S.V. Peletminsky, A.I. Sokolovsky and V.S. Shchelokov, Kinetics of a spatially inhomogeneous Bose gas in the presence of a condensate, Theoretical and Mathematical Physics **30**, No.1, 35 (1977).

[4] A.I. Akhiezer, S.V. Peletminsky, *Methods of Statistical Physics*, (London, Pergamon Press, 1981).

[5] S.V. Peletminsky, A.I. Sokolovsky and V.S. Shchelokov, Hydrodynamics of a superfluid bose liquid with allowance for dissipative processes in a model with weak interaction, Theoretical and Mathematical Physics **34**, No.1, 51 (1978).

Proceedings of the International School-seminar
"New Physics and Quantum Chromodynamics at External Conditions", pp. 85 – 88,
3-6 May 2011, Dnipropetrovsk, Ukraine

MONTE-CARLO STUDY OF FINITE-TEMPERATURE PHASE TRANSITIONS IN $(2+1)D$ $Z(5)$ LGT

O. A. Borisenko[a], V. O. Chelnokov[b], I. E. Surzhikov[c]

Bogolyubov Institute for Theoretical Physics, Kiev, Ukraine

We perform numerical study of finite-temperature phase transitions in $(2+1)d$ $Z(5)$ lattice gauge theory (LGT) with isotropic couplings, simulating both original gauge model and dual spin model. Critical points of these models are obtained. Critical indices are calculated in the vicinity of these points.

1 Introduction

Berezinsky-Kosterlitz-Thouless (BKT) phase transition, which is most widely known as the phase transition occuring in two-dimensional XY spin model, is actually exhibited by a large variety of two-dimensional spin models and three-dimensional gauge models. It can be shown analitically, that despite being discrete $Z(N)$ spin models have, for $N > 4$, an intermediate quasiordered self-dual phase, which is separated from ordered and disordered phases by two phase transitions of BKT type [1]. When N tends to infinity the critical coupling for the transition between ordered and quasi-ordered phase goes to infinity so in the limit $N \to \infty$ we obtain XY model phase structure.

Swetitsky-Yaffe conjecture [2] is known to connect critical properties of three-dimensional lattice gauge theories with corresponding properties of two-dimensional spin models if they share the same global symmetry of the action. According to it, the phase transitions in $3d$ $Z(N)$ models for $N > 4$ should be of BKT type and have the critical indices equal to those of corresponding $2d$ $Z(N)$ spin models.

The fact that BKT transition has infinite order makes it hard to study its properties using analytical methods. For $2d$ XY model a renormalization group providing critical indices of the phase transition was developed, but even in $2d$ $Z(N)$ spin model this approach was shown in [1] to lead to an involved system of differential equations, which are too hard to be solved.

These problems lead one to try obtaining critical indices of BKT transitions using numerical simulations. Here the infinite order of transitions also make them harder to investigate, because of the need to account for logarithmic by the size of lattice corrections. This makes one to perform simulations on very large lattices to obtain correct results.

We are studying the finite-temperature phase transitions in $3d$ $Z(5)$ LGT, since it is the lowest value of N for which the model undergoes two infinite-order transitions. In this work we consider isotropic couplings $\beta_s = \beta_t$. A detailed numerical study of strong-coupling limit $\beta_s = 0$ is available in I. Surzhikov's contribution. We expect our $3d$ gauge theory to undergo two phase transitions of infinite order with critical indices $\nu^{(1)} = 1/2,\ \eta^{(1)} = 1/4$, $\nu^{(2)} = 1/2,\ \eta^{(2)} = 4/25$ – critical indices of $2d$ $Z(5)$ model.

The partition function for the model can be written as

$$Z(\Lambda,\beta) \;=\; \left[\prod_{l\in\Lambda}\frac{1}{N}\sum_{s(l)=0}^{N-1}\right]\exp\left[\sum_{p\in\Lambda}\beta\cos\left(\frac{2\pi}{N}\sum_{l\in p}s(l)\right)\right]\;. \tag{1}$$

In our case $N = 5$, simulations are made on lattice Λ with dimensions $L \times L \times N_T$, where $N_T = 2$.

Simulations are made using two techniques. First we are simulating the theory using a straightforward heat-bath algorithm. Since this algorithm is very time-consuming and so does not allow one to perform calculations on large enough lattices, we also simulate a dual $3d$ $Z(5)$ spin model, defined as follows:

$$Z(\Lambda,\beta) \;=\; \left[\prod_{x\in\Lambda}\frac{1}{N}\sum_{s(x)=0}^{N-1}\right]\exp\left[\sum_{l\in\Lambda}\sum_{k=0}^{N-1}\beta_k\cos\frac{2\pi k\left(s(x)-s(x+e_n)\right)}{N}\right]\;, \tag{2}$$

where β_k are found from duality transformations of original gauge theory, i.e. β_k are solutions for the following system of equations:

e-mail: [a]oleg@bitp.kiev.ua, [b]yyyaduren@rambler.ru, [c]i_van_go@inbox.ru

$$\exp\left[\sum_{p=0}^{N-1}\beta_p\cos\frac{2\pi pk}{N}\right]=\sum_{p=0}^{N-1}\exp\left[\beta\cos\frac{2\pi p}{N}\right]\cos\frac{2\pi pk}{N}\ . \tag{3}$$

Simulations of the dual model are made using cluster algorithm similar to given in [3] which allows to simulate large lattices using reasonable time.

In the simulations we measure the following observables:

- complex magnetization $M_L=|M_L|e^{i\psi}$

$$M_L\ =\ \sum_{x\in\Lambda}\exp\left(\frac{2\pi i}{N}r_x\right) \tag{4}$$

- population S_L

$$S_L\ =\ \frac{N}{N-1}\left(\frac{\max_{i=0,N-1}n_i}{L^2}-\frac{1}{N}\right)\ , \tag{5}$$

  where n_i is number of r_x equal to i

- rotated magnetization $M_R=|M_L|e^{5i\psi}$
- susceptibilities of M_L, S_L and M_R: $\chi_L^{(M)}$, $\chi_L^{(S)}$ and $\chi_L^{(M_R)}$

$$\chi_L^{(\cdot)}\ =\ L^2\left(\left\langle\cdot^2\right\rangle-\left\langle\cdot\right\rangle^2\right) \tag{6}$$

- magnetization angle $m_\psi=\cos(5\psi)$
- Binder cumulants $U_L^{(M)}$, $B_4^{(M_R)}$ and $B_4^{(m_\psi)}$

$$U_L^{(M)}\ =\ 1-\frac{\left\langle|M_L|^4\right\rangle}{3\left\langle|M_L|^2\right\rangle^2}\ , \tag{7}$$

$$B_4^{(M_R)}\ =\ \frac{\left\langle|M_R-\langle M_R\rangle|^4\right\rangle}{\left\langle|M_R-\langle M_R\rangle|^2\right\rangle^2}\ , \tag{8}$$

$$B_4^{(m_\psi)}\ =\ \frac{\left\langle(m_\psi-\langle m_\psi\rangle)^4\right\rangle}{\left\langle(m_\psi-\langle m_\psi\rangle)^2\right\rangle^2}\ . \tag{9}$$

In gauge simulations r_x is taken to be a Polyakov loop spanning through the x space coordinate along the timelike direction – x is $2d$ coordinate. In dual spin simulation r_x is a spin in site x, so x is $3d$ coordinate.

2 Simulation results

Simulating gauge model we find β_{pc} values for different values of L from maxima of $\chi_L^{(M)}$ and $\chi_L^{(S)}$ (see Fig. 1 and 2). The results obtained are summarized in Table 1.

Finding the best overlap of $U_L^{(M)}$ Binder cumulant data for various L plotted versus $(\beta-\beta_c)(\log L)^{1/\nu}$ with ν fixed to $1/2$ provides us with $\beta_c^{(1)}=1.6084$ (see Fig. 3)

Because simulating original gauge theory on larger lattices takes too much time, we are simulating the dual model. Though one can not be sure that we may obtain critical points of the original model, simulating dual (because of the different nature of the observables considered in these models), we may suppose that critical behavior of dual model spins (if it exists) must correspond to some phase transition in the original model, and since there are only two of them we will obtain correct critical points if any. Also we may check the data obtained for consistency with data obtained from simulations of the original model.

β_{pc} values obtained from dual model are summarized in Table 2. One should note that while in gauge model $\beta_{pc}^{(1)}$ is obtained from the maximum of $\chi_L^{(M)}$ and $\beta_{pc}^{(2)}$ – from $\chi_L^{(S)}$, in dual model it is the other way round (since strong couplings of original model correspond to the weak couplings of the dual and vice versa).

Fitting the values of Table 2 using scaling

$$\beta_{pc}\ =\ \beta_c-\frac{A}{(\ln L+B)^{\frac{1}{\nu}}}\ , \tag{10}$$

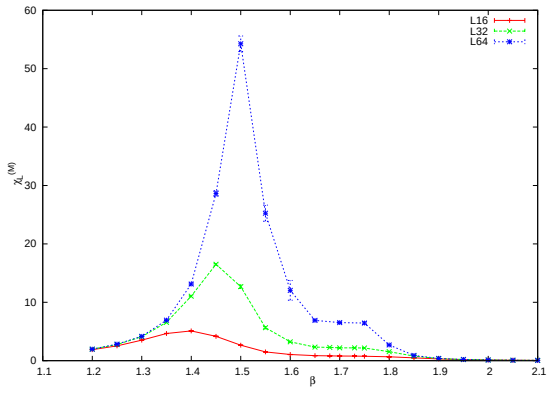

Figure 1. $\chi_L^{(M)}$ plot for different values of L.

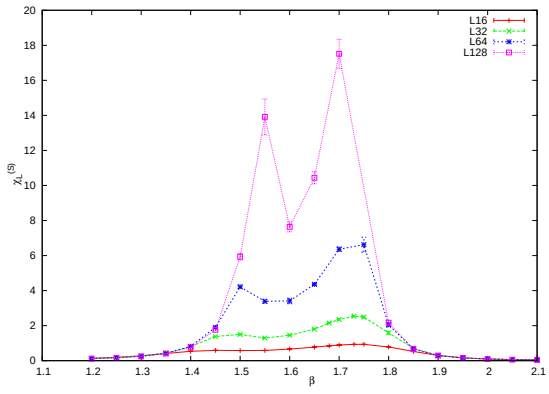

Figure 2. $\chi_L^{(S)}$ plot for different values of L.

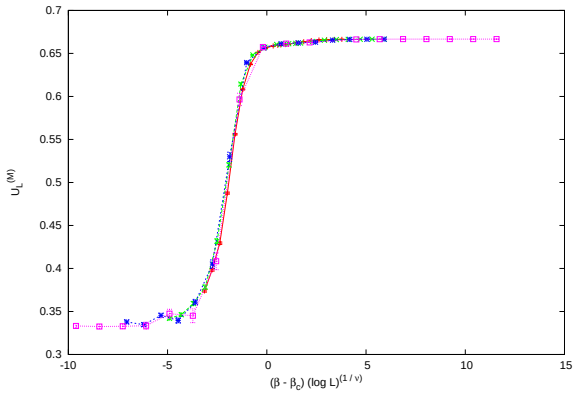

Figure 3. Binder cumulant $U_L^{(M)}$ overlap plot with $\beta_c^{(1)} = 1.6084$

with ν set to $1/2$ gives us following values of β_c:

$$\beta_c^{(1)} = 1.6172 \ ,$$
$$\beta_c^{(2)} = 1.7034 \ .$$

We see that these values are consistent with data obtained from simulations of original gauge model. Setting these values for β_c provides good fits for Binder cumulants for both dual and original models.

Finally we calculate critical indices for both original and dual models. Critical indices are obtained by fitting M_L, $\chi_L^{(M)}$ and M_R, $\chi_L^{(M_R)}$ for various L at $\beta = \beta_c^{(1)}$, $\beta_c^{(2)}$ respectively, using following scalings:

$$\begin{aligned} |M_L| &= AL^{-\beta/\nu}, \quad \chi_L^{(M)} = AL^{\gamma/\nu} \ , \\ |M_R| &= AL^{-\beta/\nu}, \quad \chi_L^{(M_R)} = AL^{\gamma/\nu} \ . \end{aligned} \tag{11}$$

Next, knowing γ/ν and β/ν we check the hyperscaling relation $2\beta/\nu + \gamma/\nu = 2$, and find $\eta = 2 - \gamma/\nu$.

The values obtained are given in Table 3, L_{min} is the minimal size of the lattices included into fit.

From these tables we see that gauge simulations suggest $\eta^{(1)} = 1/3$, $\eta^{(2)} = 0.16$, while dual simulations give $\eta^{(1)} = 0.16$, $\eta^{(2)} = 1/4$. These values are not of course final because maximum size of used lattices is not too large – $L = 384$ for all tables except for $\eta^{(1)}_{gauge}$ where maximum lattice has size $L = 768$.

3 Conclusions

Our simulation have shown that $(2+1)d$ $Z(5)$ model with isotropic couplings has two finite-temperature phase transitions of infinite order. Coupling values for these transitions are approximately $\beta_c^{(1)} = 1.6172$, $\beta_c^{(2)} = 1.7034$. We have also found that one can extract these critical couplings from both original gauge model simulation – using Polyakov loops as observables and dual spin model simulations, taking spins as observables. Initial results of finding critical indices for these transitions are given. They support that the second transition belongs to the universality class of $2d$ $Z(5)$ spin model, but for the first transition index η obtained is much larger than predicted by the Svetitsky-Yaffe conjecture (1/3 instead of 1/2), while ν index is still 1/2. This

Table 1. β_{pc} values calculated using gauge simulation for different lattice sizes

L	$\beta_{pc}^{(1)}$	$\beta_{pc}^{(2)}$
16	1.380 ± 0.006	1.760 ± 0.007
32	1.457 ± 0.007	1.753 ± 0.008
64	1.502 ± 0.003	1.727 ± 0.004

Table 2. β_{pc} calculated using dual model simulation for different lattice sizes

L	$\beta_{pc}^{(1)}$	${\beta_{pc}}^{(2)}$
16	1.560 ± 0.002	1.923 ± 0.004
32	1.568 ± 0.003	1.860 ± 0.003
64	1.578 ± 0.002	1.811 ± 0.002
128	1.582 ± 0.002	1.7758 ± 0.0014
192	1.597 ± 0.002	1.7667 ± 0.0007
256	1.5989 ± 0.0018	1.7576 ± 0.0011
384	1.5994 ± 0.0007	1.7478 ± 0.0003
512	1.6007 ± 0.0010	1.7434 ± 0.0005

Table 3. Critical indices η of the original gauge model and dual spin for the first and second transitions ($\beta_c^{(1)} = 1.6172,\ \beta_c^{(2)} = 1.7034$), calculated for different starting lattice sizes.

$L_{\min}$	$\eta_{gauge}^{(1)}$	$\eta_{gauge}^{(2)}$	$\eta_{dual}^{(1)}$	$\eta_{dual}^{(2)}$
16	0.39 ± 0.03	0.17 ± 0.02	0.18 ± 0.02	0.28 ± 0.05
32	0.33 ± 0.03	0.18 ± 0.03	0.20 ± 0.04	0.24 ± 0.05
64	0.38 ± 0.06	0.27 ± 0.05	0.18 ± 0.08	0.41 ± 0.06
128	0.32 ± 0.14	0.45 ± 0.05	0.1 ± 0.2	0.29 ± 0.07

may mean either that our estimate of $\beta_c^{(1)}$ is wrong, or that the Svetitsky-Yaffe conjecture does not hold in our case. The latter case is supported by similar results, found for $3d$ $U(1)$ LGT in [4]. Dual simulations give "swapped" values for η, which is quite predicted – $2d$ $Z(N)$ models have the same behavior, which is easy to understand considering that they are self-dual. However the meaning of dual model critical indices in terms of original gauge model is still unclear.

The simulations described above are to be carried out on larger lattices to get more precise values for critical points and critical indices. Another way of finding η index is considered – finding effective η from the Polyakov loop correlation function decay. Since one can write Polyakov loop correlation of the original model in terms of dual model variables, this method can be used to find original gauge model critical indices from dual model simulations. If the Svetitsky-Yaffe conjecture really does not hold in our case, it is worth studying the effect of β_s/β_t ratio on $\eta^{(1)}$ – since in strong coupling case ($\beta_s/\beta_t = 0$) $\eta^{(1)} = 0.25$ like in $2d$ $Z(N)$ spin model.

References

[1] S. Elitzur, R. B. Pearson, J. Shigemitsu, Phys. Rev. D **19** 3698 (1979).
[2] B. Svetitsky, L. Yaffe, Nucl. Phys B **210** 423 (1982).
[3] U. Wolff, Phys. Rev. Lett. **62** 361 (1989)
[4] O. Borisenko, R. Fiorre, M. Gravina, A. Papa, PoS **LATTICE2010** 274 (2010)

Proceedings of the International School-seminar
"New Physics and Quantum Chromodynamics at External Conditions", pp. 89 – 92,
3-6 May 2011, Dnipropetrovsk, Ukraine

BKT PHASE TRANSITION IN THREE-DIMENSIONAL Z(N) GAUGE THEORY

O. A. Borisenko[a], I. E. Surzhikov[b], V. O. Chelnokov[c]

Bogolyubov Institute for Theoretical Physics, Kiev, Ukraine

We perform numerical study of phase transitions in $(2+1)d$ $Z(5)$ lattice gauge theory in the strong coupling limit simulating effective two-dimensional spin model. Critical points of this model are obtained. Critical indices are calculated in the vicinity of these points.

1 Introduction

The Berezinskii-Kosterlitz-Thouless (BKT) phase transition is known to take place in a variety of two-dimensional ($2d$) systems: certain spin models, two-dimensional Coulomb gas, sine-Gordon model, Solid-on-Solid model, etc. The most elaborated case is the two-dimensional XY model [1, 2, 3]. There are several indications that this type of phase transition is not a rare phenomenon in gauge models at finite temperature - one can argue that in some three-dimensional lattice gauge models the deconfinement phase transition is of BKT type as well.

Some details of the critical behavior of $2d$ $Z(N)$ spin models are well known – see the review in Ref. [4]. The $Z(N)$ spin model in the Villain formulation has been studied analytically in Refs. [5, 6, 7, 8, 9]. It was shown that the model has at least two phase transitions when $N \geq 5$. The intermediate phase is a massless phase with power-like decay of the correlation function. The critical index η has been estimated both from the renormalization group (RG) approach of the Kosterlitz-Thouless type and from the weak-coupling series for susceptibility. It turns out that $\eta(\beta_c^{(1)}) = 1/4$ at the transition point from the strong coupling (high-temperature) phase to the massless phase, *i.e.* the behavior is similar to that of the XY model. At the transition point $\beta_c^{(2)}$ from the massless phase to the ordered low-temperature phase one has $\eta(\beta_c^{(2)}) = 4/N^2$. A rigorous proof that the BKT phase transition does take place, and so that the massless phase exists, has been constructed in Ref. [10] for both Villain and standard formulations (with one non-vanishing coupling β_1). Monte-Carlo simulations of the standard version with $N = 6, 8, 12$ were performed in Ref. [11]. Results for the critical index η agree well with the analytical predictions obtained from the Villain formulation of the model.

Swetitsky-Yaffe conjecture is known to connect critical properties of three-dimensional lattice gauge theory ($3d$ LGT) with corresponding properties of $2d$ spin models if they share the same global symmetry of the action. According to it, the phase transitions in $3d$ $Z(N)$ models for $N > 4$ should be of BKT type and have the critical indices equal to those of corresponding $2d$ $Z(N)$ spin models.

The fact that BKT transition has infinite order makes it hard to study its properties using analytical methods. For $2d$ XY model a renormalization group providing critical indices of the phase transition was developed, but even in $2d$ $Z(N)$ spin model this approach was shown in [5] to lead to an involved system of differential equations, which are too hard to be solved. To study this phase transition we need numerical simulations.

We are studying the phase transitions in $3d$ $Z(5)$ LGT at the finite temperature, since it is the lowest value of N for which the model undergoes two infinite-order transitions. We are simulating $2d$ $Z(5)$ spin model with modified action, which is shown to be equivalent to $3d$ $Z(5)$ LGT in the strong-coupling limit ($\beta_s = 0$).

The action for the model (in general $Z(N)$ case) is written as follows

$$S = \sum_{l\in\Lambda}\sum_{k=1}^{N-1} \beta_k \cos\left(\frac{2\pi k}{N}\left(r_x - r_{x+e_n}\right)\right). \tag{1}$$

In our case $N = 5$, simulations are made on lattice Λ with dimensions $L \times L \times N_T$, where $N_T = 2$.

Modified coupling constants β_i are derived from $\beta = \beta_t$ coupling constant of the $Z(N)$ LGT using following equations:

$$B_k = \sum_{p=0}^{N-1} \exp\left(\beta\cos\left(\frac{2\pi p}{N}\right)\right), A_k = \left(\frac{B_k}{B_0}\right)^{N_t}, Q_k = \sum_{p=0}^{N-1} A_p \cos\left(\frac{2\pi pk}{N}\right), \beta_k = \frac{1}{5}\sum_{p=0}^{N-1} \ln(Q_p)\cos\left(\frac{2\pi pk}{N}\right). \tag{2}$$

e-mail: [a]oleg@bitp.kiev.ua, [b]i_van_go@inbox.ru, [c]yyyaduren@rambler.ru

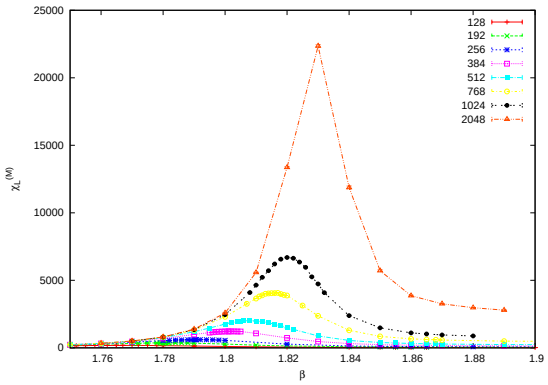

Figure 1. Dependence of magnetization susceptibility χ_M on β

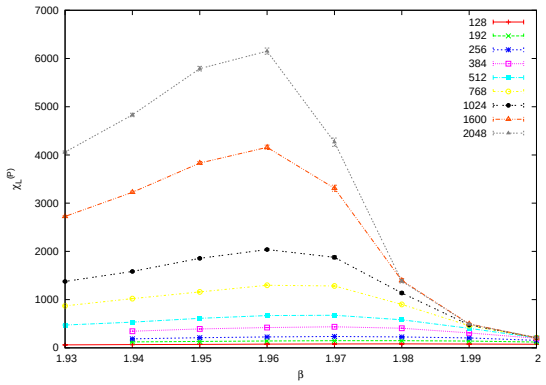

Figure 2. Dependence of population suspectibility χ_P on β

These equations can be obtained in few steps

- Fourier expansion of the original Boltzmann weight.
- Integration over spatial gauge fields. This leads to an effective $2d$ model for the Polyakov loops.
- Exponentiating and re-expansion in a new Fourier series.

To study these transitions we used a cluster algorithm described in [12]. The model is studied on a square $L \times L$ lattice Λ with periodic boundary conditions. Simulations were made for $N_t = 2$ but can easily be conducted for other values of N_t (it appears only in definition of the couplings (2)).

We expect that in our model there are two infinite-order phase transitions, which have critical indices $\nu = 1/2,\ \eta = 1/4$ (first transition) and $\nu = 1/2,\ \eta = 4/N^2$ (second transition).

In the simulations we measure the following observables

- complex magnetization $M_L = |M_L| e^{i\psi}$

$$M_L \ = \ \sum_{x \in \Lambda} \exp\left(\frac{2\pi i}{N} r_x\right) \tag{3}$$

- population S_L

$$S_L \ = \ \frac{N}{N-1}\left(\frac{\max_{i=0,N-1} n_i}{L^2} - \frac{1}{N}\right), \tag{4}$$

  where n_i is number of r_x equal to i.

- rotated magnetization $M_R = |M_L| e^{5i\psi}$
- susceptibilities of M_L, S_L and M_R: $\chi_L^{(M)}$, $\chi_L^{(S)}$, $\chi_L^{(M_R)}$

$$\chi_{\cdot} \ = \ L^2\left(\langle \cdot^2 \rangle - \langle \cdot \rangle^2\right) \tag{5}$$

- Binder cumulants $U_L^{(M)}$ and $B_4^{(M_R)}$

$$U_L^{(M)} = 1 - \frac{\left\langle |M_L|^4 \right\rangle}{3\left\langle |M_L|^2 \right\rangle^2}, B_4^{(M_R)} = \frac{\left\langle |M_R - \langle M_R \rangle|^4 \right\rangle}{\left\langle |M_R - \langle M_R \rangle|^2 \right\rangle^2}, \tag{6}$$

2 Simulation results

On Figure 1 one can see a clear peak of magnetization susceptibility for various lattice sizes. It showed us the location of the first phase transition.

Finding the best overlapping of the binder cumulants U_L for various values of L (see Figure 3) gives us another estimate

$$\beta_c \ = \ 1.8692$$

Fitting $|M_L|$ at $\beta_c^{(1)}$ (see Table 1)with formula

$$|M_L| \ = \ AL^{-\beta/\nu} \tag{7}$$

gives us

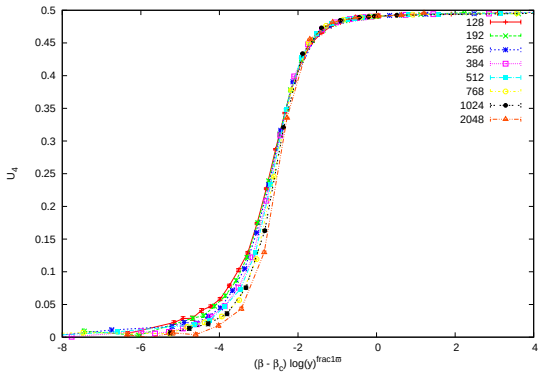

Figure 3. Binder cumulant U_L plotted versus $(\beta - \beta_c^{(1)})(\log(L))^{\frac{1}{\nu}}$.

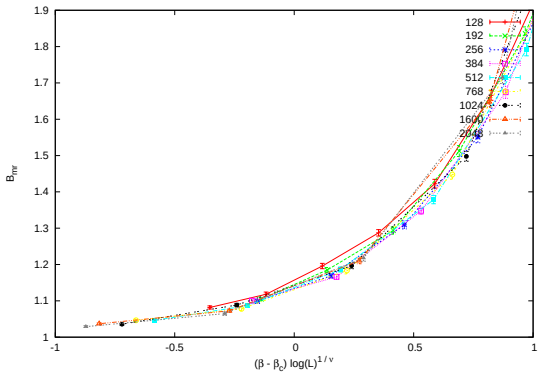

Figure 4. Binder cumulant B_{mr} plotted versus $(\beta - \beta_c^{(2)})(\log(L))^{\frac{1}{\nu}}$.

Table 1. Values of M_L and χ_{M_L} at $\beta = 1.8692$ for various lattice sizes.

L	M_L	Δ_{M_L}	χ_{M_L}	$\Delta_{\chi_{M_L}}$
128	0.5643	0.0002	26.1	0.2
192	0.5373	0.0002	53.4	0.4
256	0.5192	0.0002	87.2	0.8
384	0.4942	0.0002	175	1
512	0.4775	0.0002	285	2
768	0.4549	0.0002	592	5
1024	0.4393	0.0001	961	7
1600	0.4159	0.0001	2148	19
2048	0.4039	0.0001	3250	26

Table 2. Values of M_R and χ_{M_R} at $\beta_c^{(2)} = 1.945$ for various lattice sizes.

L	M_R	Δ_{M_R}	χ_{M_R}	$\Delta_{\chi_{M_R}}$
16	0.30	0.01	65.34	0.07
32	0.25	0.01	238.2	0.1
64	0.21	0.01	862.9	0.2
128	0.19	0.01	3112.5	0.3
192	0.17	0.01	6606.8	0.5
256	0.16	0.01	11256.7	0.6
384	0.16	0.01	23661.2	0.8
512	0.15	0.01	40671	1

$$\beta_c^{(1)} = 1.8692 \quad \beta/\nu = 0.120635 \quad \Delta_{\beta/\nu} = 0.000137$$

Fitting χ_L at $\beta_c^{(1)}$ with formula

$$\chi_L = AL^{\gamma/\nu} \tag{8}$$

gives us

$$\beta_c^{(1)} = 1.8692 \quad \gamma/\nu = 1.739745 \quad \Delta_{\gamma/\nu} = 0.003188 \quad \eta = 2 - \gamma/\nu = 0.260255$$

On Figure 2 one can see a clear peak of population suspectibility for various lattice sizes. It showed us the location of the second phase transition.

Fitting binder cumulant $B_4^{(M_R)}$ (Figure 4) for the second transition we get

$$\beta_c^{(2)} = 1.945$$

For this value of $\beta_c^{(2)}$ we extract critical index η from M_R and χ_{M_R} data given in Table 2. The result obtained is shown in Table 3, where $L_{\min}$ is a minimal size of the lattice, which we used for fitting.

3 Conclusions

In this paper we have presented a wealth of numerical data aimed at shedding light on the phase structure of the three-dimensional $Z(N)$ gauge theory at the finite temperature. In the strong coupling limit we find two phase transitions. We have determined the critical points $\beta_c^{(1)}$ and $\beta_c^{(2)}$. For these values we get critical index η, which coincide with critical indices of $2d$ $Z(5)$ spin model. So $(2+1)d$ $Z(5)$ LGT belongs to the universality class of the $2d$ $Z(5)$ spin model.

Table 3. Critical index η for second transition ($\beta_c^{(2)} = 1.945$), calculated for different starting lattice sizes

$L_{\min}$	β/ν	γ/ν	$d = 2\beta/\nu + \gamma/\nu$	$\eta = 2 - \gamma/\nu$
16	0.20 ± 0.01	1.853 ± 0.004	2.26 ± 0.02	0.147 ± 0.004
32	0.18 ± 0.01	1.853 ± 0.004	2.22 ± 0.02	0.147 ± 0.004
64	0.17 ± 0.01	1.853 ± 0.005	2.19 ± 0.03	0.147 ± 0.005
128	0.15 ± 0.02	1.853 ± 0.006	2.15 ± 0.04	0.147 ± 0.006
192	0.12 ± 0.01	1.854 ± 0.009	2.10 ± 0.03	0.146 ± 0.009
256	0.13 ± 0.01	1.86 ± 0.01	2.1 ± 0.2	0.14 ± 0.01

References

[1] V. Berezinskii, Sov. Phys. JETP **32** (1971) 493.
[2] J. Kosterlitz, D. Thouless, J. Phys. C **6** (1973) 1181.
[3] J. Kosterlitz, J. Phys. C **7** (1974) 1046.
[4] F. Y. Wu, Rev. Mod. Phys. **54** (1982) 235.
[5] S. Elitzur, R. B. Pearson, J. Shigemitsu, Phys. Rev. D **19** (1979) 3698.
[6] M. B. Einhorn, R. Savit, *A physical picture for the phase transitions in $Z(N)$-symmetric models*, Preprint UM HE 79-25.
[7] C. J. Hamer, J. B. Kogut, Phys. Rev. B **22** (1980) 3378.
[8] B. Nienhuis, J. Statist. Phys. **34** (1984) 731.
[9] L. P. Kadanoff, J. Phys. A **11** (1978) 1399.
[10] J. Fröhlich, T. Spencer, Commun. Math. Phys. **81** (1981) 527.
[11] Y. Tomita, Y. Okabe, Phys. Rev. B **65** (2002) 184405.
[12] O. Borisenko, G. Cortese, R. Fiore, M. Gravina and A. Papa, Phys. Rev. E **83** (2011) 041120 [arXiv:1011.5806v2 [hep-lat]].

Proceedings of the International School-seminar
"New Physics and Quantum Chromodynamics at External Conditions", pp. 93 – 96,
3-6 May 2011, Dnipropetrovsk, Ukraine

LOWER BOUND ON THE MAGNETIC FIELD STRENGTH IN THE HOT UNIVERSE

E. Elizalde[a], V. Skalozub[b]

[a] Institute for Space Science, ICE-CSIC and IEEC
[b] Dnipropetrovsk National University, Dnipropetrovsk, Ukraine

The lower bound on the long range magnetic field strength $B \sim 10^{14}$ G at the electroweak phase transition temperature T_c^{ew} is derived with accounting for the present day intergalactic magnetic field value $B \sim 10^{-15}$ G. The estimate is based on two features of nonabelian gauge fields at high temperature - the spontaneously vacuum magnetization and the zero magnetic mass value for the created Abelian magnetic field. Applications to cosmology are discussed.

1 Introduction

Recent observation of intergalaxy magnetic fields of the order $B \sim 10^{-15}G$ [1, 2] gives a support to nowadays notions on the origin of magnetic fields in the early universe and galaxies (see, for instance, [3]). The most important features of them are quantum and classical dynamics of fields and matter. On the other hand, it stimulates new ideas to make an incite on the dynamical mechanisms for generation of strong magnetic fields at high temperatures.

As it was discovered recently, in non-Abelian gauge theories at high temperature a spontaneous vacuum magnetization happens. This has been determined either by analytic quantum field theory methods [5], [7], [6] or in the lattice simulations [9]. This phenomenon is analogous to the spontaneous creation of Abelian chromomagnetic field $B = const$ discovered at zero temperature $T = 0$ by Savvidy [11]. However, in contrast to the zero temperature case when the magnetized state is unstable because of the tachyon mode $p_0^2 = p_{||}^2 - gB$ presenting in the charged gluon spectrum,

$$p_0^2 = p_{||}^2 + (2n+1)gB,\ n = -1, 0, 1, ..., \tag{1}$$

where $p_{||}$ is a momentum component along the field, B is field strength, g is gauge coupling constant, at finite temperature $T \neq 0$ the spectrum stabilization happens. The stabilization is ensured by two dynamical parameters generated at high temperature due to vacuum polarization: a charged gluon magnetic mass [6] and the A_0-condensate which is proportional to the Polyakov loop [12]. In this way a possibility of spontaneous creation of strong temperature-dependent and stable magnetic fields of the order $gB \sim g^4T^2$ is realized.

Important property of such type temperature dependent magnetic fields is the zero value of their magnetic mass, $m_{magn.} = 0$, as it also was found in one-loop approximation in analytic calculations [14] and in lattice simulations [10]. The mass parameter describes the inverse space scales of the transverse field components, similarly to the Debye mass m_D related to the inverse space scale for the electric (Coulomb) component. The absence of screening mass means that the spontaneously generated Abelian chromomagnetic fields are long range ones at high temperature, as usual $U(1)$ magnetic field. Hence, it is reasonable to believe that in the hot universe at each stage of evolution spontaneously created strong long range magnetic fields of different types had been present. Being unscreened, they influenced various processes and phase transitions.

The way of dependence on temperature for these fields differs from the familiar behavior proper to $U(1)$ magnetic fields. Remind that in the latter case the spontaneous vacuum magnetization absence. The magnetic (hypermagnetic, in fact) field, created by some specific mechanism, is implemented in a hot plasma and decreased according to the low $B \sim T^2$ which is the consequence of the magnetic flux conservation (see, for instance, [3]. However, because of the vacuum polarization resulting in the spontaneously created magnetic field, the magnetic flux conservation does not hold. Instead, at each temperature a specific magnetic flux is generated. This fact has to be taken into consideration when cooling of the hot nonAbelian plasma is investigated. This concerns also the $SU(2)_{ew}$ component of electromagnetic field.

2 Qualitative picture of phenomena

Our main assumption is that the intergalactic magnetic field had been spontaneously created at high temperature. We discuss the procedure to relate the present day value of the intergalactic magnetic field with the fields

e-mail: [a]elizalde@ieec.uab.es, [b]skalozubv@daad-alumni.de

generated in the restored phase of the electroweak theory.

First of all, we note that the spontaneous vacuum magnetization is strongly dependent on the scalar field value responsible for the spontaneous symmetry breaking at low temperature. It was investigated at zero temperature by Goroku [4]. For finite temperature, it is considered below. In both cases the main observation is that the magnetization takes place for small scalar field $\phi \neq 0$, only. For the values of ϕ corresponding to any first order phase transition the magnetization does not happen. This means that after the electroweak phase transition the vacuum polarization ceases to generate spontaneously the magnetic field, the magnetic flux conservation holds and the familiar temperature dependence of the type $B \sim T^2$ is restored.

Another aspect of the electroweak phase transition is the compose structure of the electromagnetic field A_μ in the standard model. The potentials read

$$A_\mu = (g' A^3_\mu + g b_\mu)/\sqrt{g^2 + g'^2}, \quad Z_\mu = (g A^3_\mu - g' b_\mu)/\sqrt{g^2 + g'^2}, \tag{2}$$

where Z_μ is the Z-boson potential, A^3_μ, b_μ are the Yang-Mills gauge filed third projection in the weak isospin space and the potential of the hypercharge gauge fields, g and g' are $SU(2)$ and $U(1)_Y$ couplings, correspondingly. After the phase transition, the Z-boson esquires mass and the field is screened at distances $r \geq 1/m_z$. Since the hypermagnetic field is Abelian and not spontaneously generated, only the component $A_\mu = \sin\theta_w A^3_\mu$ generated spontaneously at high temperature remains. Here θ_w is the Weinberg angle, $\tan\theta_w = g'/g$. This is just the component responsible for the intergalactic magnetic field, in the scenario investigated.

In the restored phase, the field $b_\mu = 0$, the complete weak-isospin chromomagnetic field $A^{(3)}_\mu$ is unscreened and nonzero. This is because the magnetic mass of this field in zero [10]. So, the field is long range one. It provides the coherence length is to be sufficiently large. After the phase transition, the part of the field is screened by the Z-boson mass. The electromagnetic field in the restored phase is given by the expression

$$B = \sin\theta_w(T) B^{(3)}(T), \tag{3}$$

where $B^{(3)}(T)$ is the field strength generated spontaneously.

To relate the present day intergalactic magnetic field with the field existed before the electroweak phase transition we take into consideration the fact that after the phase transition the spontaneous vacuum magnetization does not happen. We can write therefore for the electroweak transition temperature T_{ew}:

$$B(T_{ew})/B_0 = T^2_{ew}/T^2_0 = \sin\theta_w(T_{ew}) B^{(3)}(T_{ew})/B_0. \tag{4}$$

Here B_0 is the present day intergalactic magnetic field strength $B_0 \sim 10^{-15} G$. The l.h.s. relates the value $B(T_{ew})$ with B_0. The r.h.s. gives a possibility to express the weak isospin magnetic field in the restored phase through B_0 knowing the temperature dependence of the Weinberg angle $\theta_w(T)$. This relation is important because the r.h.s. contains an arbitrary temperature normalization parameter τ. The relation (4) can be used to fix it. After that the field strength values at various temperatures can be calculated assuming that it is spontaneously generated. In particular, the total weak isospin field strength is given by the sum $\cos\theta_w(T_{ew}) B^{(3)}(T_{ew}) + B(T_{ew})$.

Important aspect of this scenario is that the unknown till now theory extending the standard model is not very important for estimating the field strength B at temperatures close to T_{ew}. This is because other gauge fields belonging to the extended model are screened at higher temperatures corresponding to the spontaneous symmetry breaking and decoupled. At high temperatures when corresponding symmetry is restored these fields existed. In such a way the value of the field strength at the Planck era has been estimated by Pollock [8]. Hence we conclude that our estimate give a low bound on the magnetic field strength at high temperature.

3 Effective potential at high temperature

As we noted above the spontaneous vacuum magnetization and the absence of the magnetic mass for the Abelian magnetic fields are nonperturbation affects determined, in particular, in lattice simulations [9], [10]. The main conclusions of these investigations are - the stable magnetized vacuum does exist at high temperature and the magnetic mass of the created field is zero. As concerns the actual value of the field strength, is is close to the one calculated within the consistent effective potential accounting for the one-loop plus daisy diagrams. So, in the present investigation we restrict ourselves to this approximation. This is mainly because to present analytic calculations clarifying our results. The complete effective potential is given in the review arXiv:hep-th/9912071 v1 8 Dec 1999.

Of paramount importance for the discussed phenomenon is the part of the effective potential describing the contribution of W bosons

$$L^T_2 = \frac{h}{\pi^2\beta^2} \sum_{n=1}^{\infty} \Big[\frac{(\phi^2 - h)^{1/2}\beta}{n} K_1(n\beta(\phi^2 - h)^{1/2}) - \frac{(\phi^2 + h)^{1/2}\beta}{n} K_1(n\beta(\phi^2 + h)^{1/2}) \Big]. \tag{5}$$

Here we introduced the dimensionless notations: $h = eB/M^2_w$, $\phi = \phi_c/\phi_0, \beta = 1/T$, $K_1(z)$ is the MacDoland functon. This part will be used below in actual calculations.

4 Magnetic field strength at T_{ew}

Now let us show that the spontaneous vacuum magnetization does not happen at finite temperature and not small values of the scalar field condensate $\phi \neq 0$. To do that we note that the magnetization is generated due to the gauge field contribution given by eq. (5). So, we consider the limit of $\frac{gB}{T^2} \ll 1$ and $\phi^2 > h$. For this case we use the asymptotic expansion of $K_1(z)$:

$$K_1(z) \sim \sqrt{\frac{\pi}{2z}} E^{-z}\big(1 + \frac{3}{8z} - \frac{15}{128z^2} + \cdots\big), \tag{6}$$

where $z = n\beta(\phi^2 \pm h)^{1/2}$. We consider the limit $\beta \to \infty, \frac{T}{\phi} \ll 1$. For this case the leading term is given by the first term of the temperature sum. We also can substitute $(\phi^2 \pm h)^{1/2} = \phi(1 \pm \frac{h}{2\phi^2})$. In this limit the tree level Lagrangian and (5) read

$$L = -\frac{h^2}{2} + \frac{h^2}{\pi^{3/2}} \frac{T^{1/2}}{\phi^{1/2}}\big(1 - \frac{T}{2\phi}\big) e^{-\frac{\phi}{T}}. \tag{7}$$

The second term is exponentially small and the stationary equation $\frac{\partial L}{\partial h} = 0$ has trivial solution $h = 0$. This estimate can be verified easily in numeric calculation for the total effective potential. Hence we conclude that after symmetry breaking the spontaneous vacuum magnetization does not hold, as it was found at zero temperature [4].

Next we calculate the magnetic field created in the restored phase of the standard model. This part of calculations is completely the same as in Ref. [13] and we present in brief.

The high temperature limit of the one-loop effective potential coming from W-bosons is ($\tilde{B} \equiv B^{(3)}$)

$$V_w^{(1)}(\tilde{B}, T) = \frac{\tilde{B}^2}{2} + \frac{11}{48}\frac{g^2}{\pi^2}\log\frac{T^2}{\tau^2} - \frac{1}{3}\frac{(g\tilde{B})^{3/2}T}{\pi} - i\frac{(g\tilde{B})^{3/2}T}{2\pi} + O(g^2\tilde{B}^2), \tag{8}$$

where τ is a temperature normalization point, and the first term presents the tree-level energy density. The imaginary part is generated because of the unstable mode in the spectrum (1). It is canceled by the term standing in the contribution of the daisy diagrams [6]

$$V_{unstable} = (g\tilde{B}T[\Pi(\tilde{B}, T, n = -1) - g\tilde{B}]^{1/2} + i(g\tilde{B})^{3/2}T)/2\pi. \tag{9}$$

Here $\Pi(\tilde{B}, T, n = -1)$ is the mean value in the ground state $n = -1$ of the spectrum (1) for the charged gluon polarization tensor. If this value is sufficiently large, the spectrum stabilization due to radiation correction happens.

To estimate the magnetic field strength in the restored phase at the electroweak phase transition temperatures the total effective potential adduced in the previous section must be used and the parameters entering eq.(4) calculated. This can be done numerically. To explain the procedure we consider here a part of this potential accounting for the one-loop W-boson contributions. The high temperature expansion from charged vector fields is given in eq.(8). The high temperature expansion for charged scalars reads [7]

$$V_{sc}^{(1)}(\tilde{B}, T) = -\frac{1}{96}\frac{g^2}{\pi^2}\log\frac{T^2}{\tau^2} + \frac{1}{12}\frac{(g\tilde{B})^{3/2}T}{\pi} + O(g^2\tilde{B}^2). \tag{10}$$

This part of the potential presents the contribution of longitudinal vector components. This representation is convenient for the case of extended models including other gauge and scalar fields. Depending on the specific case, one can take into consideration the parts (8), (10), correspondingly. In the standard model, the contribution of Eq. (10) has to be taken with a factor 2, due to two charged scalar fields entering the scalar doublet of the model. Assuming stability of the vacuum state, we calculate the value of chromomagnetic weak isospin field spontaneously generated at high temperature from eqs.(8), (10):

$$\tilde{B}(T) = \frac{1}{16}\frac{g^3}{\pi^2}\frac{T^2}{(1 + \frac{5}{12}\frac{g^2}{\pi^2}\log\frac{T}{\tau})^2}. \tag{11}$$

This expression we relate with the intergalactic magnetic field B_0.

Let us introduce the standard parameters and definitions, $g^2/(4\pi) = \alpha_s, \alpha = \alpha_s \sin\theta_w^2, (g')^2/(4\pi) = \alpha_Y$ and $\tan^2\theta_w(T) = \alpha_Y(T)/\alpha_s(T)$, where α is the fine structure constant. In present investigation , for a rough estimate, we substitute the zero temperature number: $\sin^2\theta_w(T) = \sin^2\theta_w(0) = 0.23$.

For the given temperature of the electroweak phase transition, T_{ew}, the magnetic field is

$$B(T_{ew}) = B_0\, T_{ew}^2/T_0^2 = \sin\theta_w(T_{ew})\tilde{B}(T_{ew}). \tag{12}$$

Assuming $T_{ew} = 100$ GeV $= 10^{11}$ eV and $T_0 = 2.7$ K $= 2.3267 \cdot 10^{-4}$ eV, we obtain

$$B(T_{ew}) \sim 1.85\ 10^{14}\ \text{G}. \tag{13}$$

This value can be considered as a lower bound on the magnetic field strength at the electroweak phase transition temperature.

Hence, for the value of $X = \log \frac{T_{ew}}{\tau}$, we have the equation

$$B_0 = \frac{1}{2} \frac{\alpha^{3/2}}{\pi^{1/2} \sin^2 \theta_w} \frac{T_0^2}{(1 + \frac{5\alpha}{3\pi \sin^2 \theta_w} X)^2}. \tag{14}$$

Since all the values are known, $\log \tau$ can be estimated. After that the field strengths at different stronger temperatures can be found.

To guess the value of the parameter τ we take the field strength $B_0 \sim 10^{-9}$ G, usually used in cosmology (see, for example, [8]). In this case, from Eq. (14) we obtain $\tau \sim 300$ eV. For the lower bound value $B \sim 10^{-15}$ G this parameter is much smaller.

5 Discussion

Let us summarize the main results obtained.

First we note that in the scenario investigated the main point is the spontaneous vacuum magnetization at high temperature that prevents the magnetic flux conservation during cooling of the universe. The vacuum polarization is responsible for the field strength value $B(T)$ at each temperature and serves as the source of it. Hence it is reasonable to believe that actual content of extended model is not essential at sufficiently low temperatures when a decoupling of heavy gauge fields happened. This point is new as compared to the familiar picture based on the scenario with magnetic flux conservation which does not account for vacuum magnetization.

The value of the present day intergalactic magnetic field is related with the field strengths at high temperatures in the restored phase. Because of the zero magnetic mass for Abelian magnetic fields there are no problem with generation of the fields having large coherence length. This old problem is solved in our scenario. Knowing a particular content of extended model it is possible to estimate the field strengths at any temperature (in particular, at the Planck era). This can be done for different schemes of the spontaneous symmetry breaking (restoration) with taking into account the fact that after decoupling the magnetic fields are screened.

Our estimate shows that at the electroweak phase transition temperature the magnetic field of the order $B(T_{ew}) \sim 10^{14}$ G existed.

References

[1] S. Ando, A. Kusenko, Astrophys. J. Lett., **722**, L39 (2010).
[2] A. Neronov, E. Vovk, Science, **328**, 73 (2010).
[3] A. Kandus, K.E. Kunze, C.G. Tsagas, arXiv: 1007.3891 v2 [astro-ph. CO] 3 Mar 2011.
[4] K. Goroku Progr.Theor.Phys., **68**, No. 4, 1340 (1982).
[5] A. O. Starinets, A. S. Vshivtsev and V. C. Zhukovsky, Phys. Lett. B **322**, 403 (1994).
[6] V. Skalozub and M. Bordag, Nucl. Phys. B **576**, 430 (2000).
[7] V. V. Skalozub, Int. J. Mod. Phys. A **11**, 5643 (1996).
[8] M.D. Pollock, Int. J. Mod. Phys D **12** 1289 (2003).
[9] V. I. Demchik and V. V. Skalozub, Phys. Atom. Nucl. **71**, 180 (2008).
[10] S. Antropov, M. Bordag, V. Demchik and V. V. Skalozub, arXiv:1011.314/v1 [hep-ph] 13 Nov 2010.
[11] G. K. Savvidy, Phys. Lett. B **71**, 133 (1977).
[12] D. Ebert, V. C. Zhukovsky and A. S. Vshivtsev, Int. J. Mod. Phys. A **13**, 1723 (1998).
[13] V. Skalozub and V. Demchik, arXiv:hep-th/991207 v 1 8 Dec 1999.
[14] M. Bordag and V. Skalozub, Phys. Rev. D **75**, 125003 (2007).

Proceedings of the International School-seminar
"New Physics and Quantum Chromodynamics at External Conditions", pp. 97 – 99,
3-6 May 2011, Dnipropetrovsk, Ukraine

MODEL-INDEPENDENT ESTIMATES FOR THE Z' PRODUCTION CROSS SECTION AT HADRON COLLIDERS

A. V. Gulov[a], A. A. Kozhushko[b]

Dnipropetrovsk National University, Dnipropetrovsk, Ukraine

The model-independent constraints on the Abelian Z' couplings from the LEP data are applied to estimate the Z' production cross section in experiments at the Tevatron and LHC. The results are compared with model-dependent predictions for the LHC. The paper explains several technical details of the cross section calculation and is complementary to the authors' paper presented in the plenary talks section.

1 Introduction

The recently published results of the model-dependent Z' boson [1, 2, 3, 4] searches in the $p\bar{p} \to l\bar{l}$ process (the Drell-Yan process) report no deviations from the SM [5, 6, 7]. The comparison of the experiment data and the model predictions indicates that Z' is heavier than 770 GeV. The same analysis of the data collected by the LHC collaborations is to be carried out in the nearest future. Also, the recently performed analysis of the LEP data [8, 9] imposed model-independent bounds on the combinations of Z' mass and its couplings to the SM fermions. By using these bounds one can constrain the Z' production cross section in proton-(anti)proton collisions and its decay width. These characteristics fully describe the Z' contribution to the Drell-Yan process cross section in case of the narrow Z' resonance. In this way it is possible to obtain the LEP estimations for the Z' manifestation at modern hadron colliders and compare these estimations with the existing experimental data and model-dependent predictions.

In this paper we present the model-independent Z' production cross section estimations at the Tevatron and the LHC. We also use some of the results presented in [10] to estimate the $pp \to Z' \to l\bar{l}$ cross section at $\sqrt{S} = 7$ TeV and 14 TeV and compare them to the model-dependent results obtained in [11].

This paper is dedicated to some technical aspects of cross section calculations and is complementary to [10].

2 Z' production cross-section

In modern experiments Z' bosons are expected to be produced in proton-antiproton collisions $p\bar{p} \to Z'$ (Tevatron) or proton-proton collisions $pp \to Z'$ (LHC). At the parton level both the processes are described by the annihilation of a quark-antiquark pair, $q\bar{q} \to Z'$ (Fig. 1). The Z' production cross-section is the result of integration of the partonic cross-section $\sigma_{q\bar{q}\to Z'}$ with the parton distribution functions:

$$\begin{aligned}\sigma_{AB} &= \sum_{q,\bar{q}} \int_0^1 dx_q \int_0^1 dx_{\bar{q}}\, f_{q,A}(x_q, Q^2) f_{\bar{q},B}(x_{\bar{q}}, Q^2) \\ &\quad \times \sigma_{q\bar{q}\to Z'}(m_{Z'}, x_q k_A, x_{\bar{q}} k_B),\end{aligned} \tag{1}$$

where A, B mark the interacting hadrons (p or $\bar{p}$) with the four-momenta k_A, k_B; $f_{q,A}$ is the parton distribution function for the parton q in the hadron A with the momentum fraction x_q ($0 \le x_q \le 1$) at the energy scale Q^2. In our case $Q^2 = m^2_{Z'}$. We use the parton distribution functions provided by the MSTW PDF package [12].

The production cross-section is determined by quadratic combinations of the Z' couplings to quarks,

$$\begin{aligned}\sigma_{AB} &= \bar{a}^2 \sigma_{\bar{a}^2} + \bar{a}\bar{v}_u \sigma_{\bar{a}\bar{v}_u} + \bar{v}_u^2 \sigma_{\bar{v}_u^2} + \bar{a}\bar{v}_c \sigma_{\bar{a}\bar{v}_c} \\ &\quad + \bar{v}_c^2 \sigma_{\bar{v}_c^2} + \bar{a}\bar{v}_t \sigma_{\bar{a}\bar{v}_t} + \bar{v}_t^2 \sigma_{\bar{v}_t^2}.\end{aligned} \tag{2}$$

Here the relations between the Z' couplings to the SM fermions $\bar{a}_f$, $\bar{v}_f$ (see [10] for the parameterization and the relations) are taken into account. The factors σ depend on $m_{Z'}$, the process type (proton-proton or proton-antiproton collision), and the beam energy. The factors $\sigma_{\bar{a}\bar{v}_c}$, $\sigma_{\bar{v}_c^2}$, $\sigma_{\bar{a}\bar{v}_t}$ and $\sigma_{\bar{v}_t^2}$ are small compared to $\sigma_{\bar{a}^2}$, $\sigma_{\bar{a}\bar{v}_u}$ and $\sigma_{\bar{v}_u^2}$ and their contributions to the cross-section can be neglected.

e-mail: [a]alexey.gulov@gmail.com, [b]a.kozhushko@yandex.ru

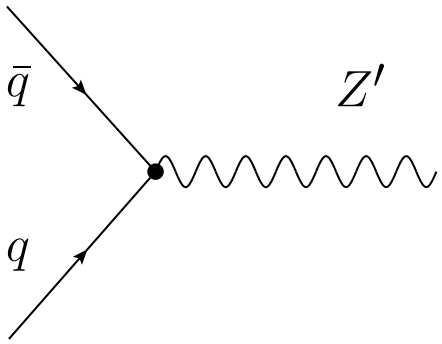

Figure 1. Z' production at the parton level.

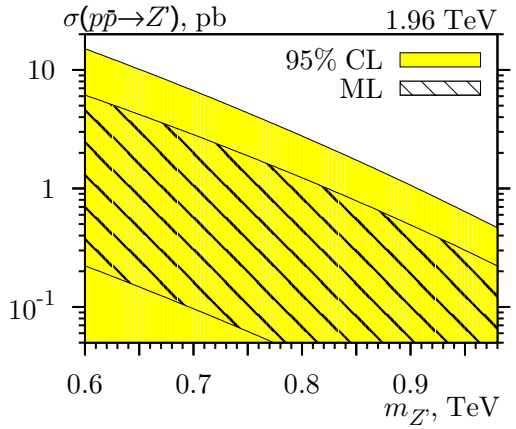

Figure 2. Z' production cross-section vs. $m_{Z'}$ in $p\bar{p}$ collisions at $\sqrt{S} = 1.96$ TeV. The filled area corresponds to the 95% CL estimate, and the hatched area is for the ML estimate.

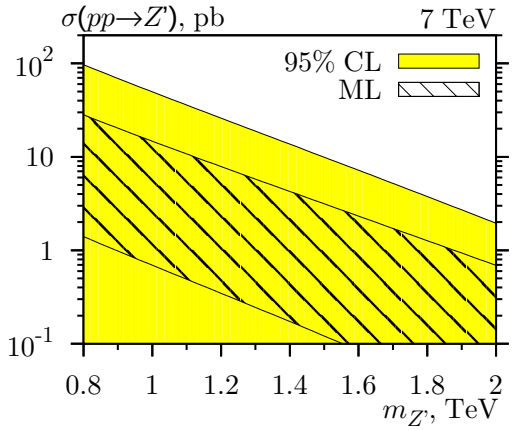

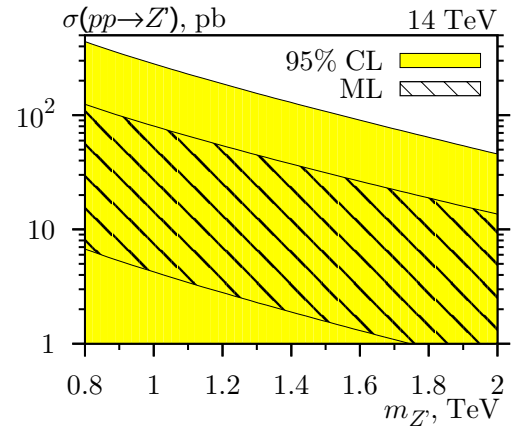

Figure 3. Z' production cross-section vs. $m_{Z'}$ in pp collisions at $\sqrt{S} = 7$ TeV and $\sqrt{S} = 14$ TeV. The filled area corresponds to the 95% CL estimate, and the hatched area is for the ML estimate.

We take into account the 90% CL uncertainties of the parton distribution functions provided by the MSTW PDF package. Finally, the production cross-section reads:

$$\begin{aligned} \sigma &= \bar{a}^2\sigma_{\bar{a}^2} + \bar{a}\bar{v}_u\sigma_{\bar{a}\bar{v}_u} + \bar{v}_u^2\sigma_{\bar{v}_u^2} \pm \Delta\sigma^{\rm pdf}, \\ \Delta\sigma^{\rm pdf} &= \bar{a}^2\Delta\sigma^{\rm pdf}_{\bar{a}^2} + \bar{a}\bar{v}_u\Delta\sigma^{\rm pdf}_{\bar{a}\bar{v}_u} + \bar{v}_u^2\Delta\sigma^{\rm pdf}_{\bar{v}_u^2}. \end{aligned} \tag{3}$$

The estimates for the Z' production cross-section in proton-antiproton collisions at the Tevatron and in proton-proton collisions at the LHC are shown in Figs. 2 and 3, respectively. The estimation schemes, the 95% CL estimation and the maximum likelihood estimation, are the same that were used in [10]. In the LHC case the $\sqrt{S}$ value is taken to be 7 TeV and 14 TeV, corresponding to the current and expected energies. The Z' mass is chosen to be from 600 to 980 GeV for the Tevatron process and from 800 to 2000 GeV for the LHC processes. At these masses it is possible to perform direct searches, and the boson production rate is not suppressed by the parton density effects.

3 Discussion

It is argued in [10], that for the maximum-likelihood estimation the Narrow Width Approximation (NWA) is applicable. By using this approach one can easily obtain the estimations for the Z' contribution to the Drell-Yan process cross section at the Tevatron and the LHC as $\sigma(pp\,(p\bar{p}) \to Z') \times BR(Z' \to l\bar{l})$. The branching ratio can be obtained from the decay width estimations presented in [10].

In Fig. 4 the ML estimations for the LHC processes are presented. We consider the e^+e^- and $\mu^+\mu^-$ decay channels as the most popular ones.

In the LHC case, the cross-section values are plotted for the Z' mass up to 2 TeV. For higher mass values

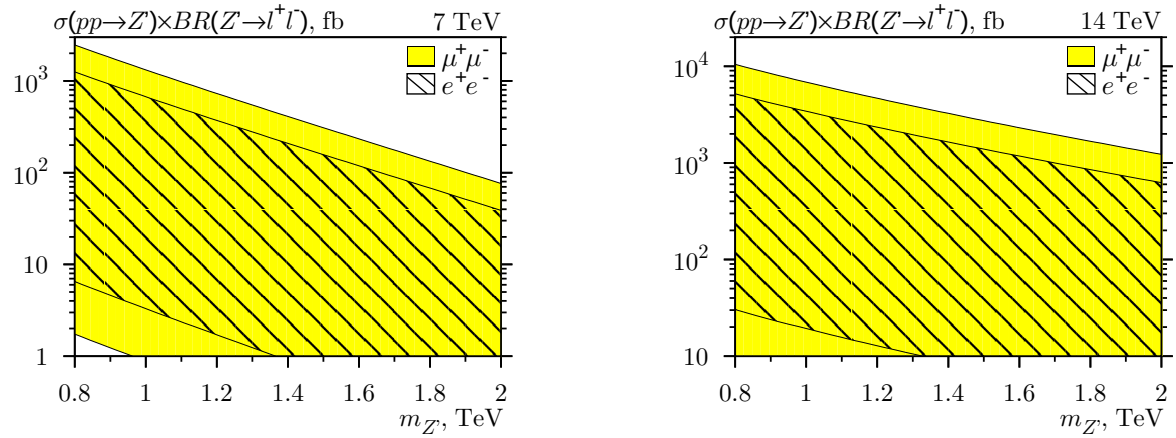

Figure 4. Z' production cross-section times the Z' branching ratio for electron-positron (hatched area) and muon-antimuon (filled area) channels vs. $m_{Z'}$ in pp collisions at $\sqrt{S} = 7$ TeV and $\sqrt{S} = 14$ TeV.

the validity of the NWA is not guaranteed even for the ML estimate. The comparison to the Tevatron data and estimations are carried out in [10].

Let us compare our predictions for the LHC to the ones presented in [11]. In Fig. 3 of Ref. [11] the number of $pp \to Z' \to l^+l^-$ events for 100 fb^{-1} of integrated luminosity at $\sqrt{S} = 14$ TeV versus $m_{Z'}$ is plotted. The ML number of $pp \to Z' \to e^+e^-$ or $\mu^+\mu^-$ events for this luminosity can be obtained by multiplying the cross-section values in the left plot in Fig. 4 by 10^5. It can be seen that all the model-dependent predictions from Ref. [11] are covered by the e^+e^- ML domain.

In Table 2 of Ref. [11] the model-dependent estimates for $\sigma(pp \to Z' \to l^+l^-) \times \Gamma_{Z'}$ are presented. $m_{Z'}$ is set to 1.5 TeV. The ML estimate for this observable is easy to calculate using Fig. 4 as $\sigma(pp \to Z') \times \tilde{\Gamma}^{l^+l^-} \times (m_{Z'}/1\ \text{TeV})^3$. We obtain 94 ± 92 pb $\cdot$ GeV and 210.7 ± 210.1 pb $\cdot$ GeV for e^+e^- and $\mu^+\mu^-$ decay channels, respectively. One can see that the predictions for the Z'_ψ and Z'_η models (487 ± 5 fb $\cdot$ GeV and 630 ± 20 fb $\cdot$ GeV) lie outside the ML interval for the dielectron channel case, and the Z'_ψ prediction is not covered by the dimuon channel estimate. This is because $m_{Z'} = 1.5$ TeV appears to be quite heavy to provide exact value of the axial-vector coupling from the LEP data as it is assumed in the ML scheme. Of course, the model-dependent results are covered by the 95% CL intervals and cannot be excluded by the LEP data.

The obtained results together with the LEP bounds are used for estimating Z' parameters at the Tevatron and the LHC. These estimations can be found in [10].

References

[1] A. Leike, Phys. Rep. **317**, 143 (1999).
[2] P. Langacker, Rev. Mod. Phys. **81**, 1199-1228 (2008) [arXiv:0801.1345 [hep-ph]].
[3] T. Rizzo, [hep-ph/0610104].
[4] J. Erler, P. Langacker, S. Munir and E. R. Pena, JHEP **08**, 017 (2009).
[5] CDF Collaboration, T. Aaltonen et al., Phys. Rev. Lett. **102**, 031801 (2009) [arXiv:0810.2059].
[6] CDF Collaboration, T. Aaltonen et al., Phys. Rev. Lett. **102**, 091805 (2009) [arXiv:0811.0053].
[7] D0 Collaboration, V. Abazov, et al., Phys. Lett. B **695**, 88 (2011) [arXiv:1008.2023].
[8] A. V. Gulov and V. V. Skalozub, [arXiv:0905.2596v2 [hep-ph]].
[9] A. V. Gulov and V. V. Skalozub, Int. J. Mod. Phys. A **25**, 5787-5815 (2010).
[10] A. V. Gulov and A. A. Kozhushko, Int. J. Mod. Phys. A **26**, 4083-4100 (2011) [arXiv:1105.3025v1]; see also the section for plenary talks of the current proceedings.
[11] M. Dittmar, A. Djouadi and A.-S. Nicollerat, Phys. Lett. B **583**, 111 (2004) [arXiv:hep-ph/0307020v1].
[12] A.D. Martin, W.J. Stirling, R.S. Thorne and G. Watt, Eur. Phys. J. C **63**, 189 (2009); *ibid.* **64**, 653 (2009); *ibid.* **70**, 51 (2010); [arXiv:0901.0002v3 [hep-ph]]; [arXiv:0905.3531v2 [hep-ph]]; [arXiv:1007.2624v2 [hep-ph]]; http://projects.hepforge.org/mstwpdf/.

Proceedings of the International School-seminar
"New Physics and Quantum Chromodynamics at External Conditions", pp. 100 – 104,
3-6 May 2011, Dnipropetrovsk, Ukraine

SPIN DETERMINATION AND MODEL IDENTIFICATION OF Z′ BOSONS AT THE LHC

A. V. Gulov[1,a], A. A. Pankov[2,b], V. V. Skalozub[1,c], A. V. Tsytrinov[2,d]

[1] The Abdus Salam ICTP Affiliated Centre at the Technical University of Gomel, Gomel, Belarus
[2] Dnipropetrovsk National University, Dnipropetrovsk, Ukraine

Heavy resonances arising in the dilepton channel may be the first new physics to be observed at the proton-proton CERN LHC. If a new resonance is discovered at the LHC as a peak or bump in the dilepton invariant mass distribution, the characterization of its spin and couplings will proceed via measuring production rates and angular distributions of the decay products. The discovery potential and diagnostic abilities of the LHC for new heavy neutral Z' gauge bosons are studied. We discuss the discrimination of the spin-1 of Z' representative models ($Z'_{\rm SSM}$, Z'_{ψ}, Z'_{η}, Z'_{χ}, $Z'_{\rm LR}$, $Z'_{\rm ALR}$ within the class of Abelian Z') against the Randall-Sundrum graviton resonance (spin-2) and a spin-0 resonance (sneutrino). We find that the spin of a heavy Z' gauge boson within the class of Abelian can be established up to $M_{Z'} \simeq 6.5$ TeV while its discovery reach extends up to 8 TeV, for an integrated luminosity of 100 fb^{-1}. We also examine the distinguishability of the considered Z' models from one another, once the spin-1 has been established. We find that one might be able to distinguish among these Z' models at 95% C.L. up to $M_{Z'} \simeq 2$ TeV.

1 Introduction

New heavy resonances are predicted by numerous New Physics (NP) scenarios, candidate solutions of conceptual problems of the standard model (SM). In particular, this is the case of models of gravity with extra spatial dimensions, grand-unified theories (GUT), and supersymmetric (SUSY) theories with R-parity breaking ($\not{R}_p$). These new heavy resonances, with mass $M \gg M_Z$, may be either produced or exchanged in reactions among SM particles at the high energy collider LHC. A particularly interesting process to be studied in this regard at the LHC is the Drell-Yan (DY) dilepton production ($l = e, \mu$)

$$p + p \to l^+ l^- + X, \tag{1}$$

where exchanges of the new particles can occur and manifest themselves as peaks in the (l^+l^-) invariant mass M. Once the heavy resonance is discovered at some $M = M_R$, further analysis is needed to identify the theoretical framework for NP to which it belongs. Correspondingly, for any NP model, one defines as *identification* reach the upper limit for the resonance mass range where it can be identified as the source of the resonance, against the other, potentially competitor scenarios, that can give a peak with the same mass and same number of events under the peak. This should be compared to the *discovery* reach, which specifies the (naturally more extended) mass range where the peak in the cross section pertaining to the model can just be observed experimentally. Clearly, the determination of the spin of the resonance represents an important aspect of the selection among different classes of non-standard interactions giving rise to the observed peak. Tests of the spin-2 of the Randall-Sundrum [1] graviton excitation (RS) exchange in the process (1) at LHC, against the spin-1 hypothesis, have been recently performed, e.g., in Refs. [2] on the basis of the lepton differential polar angle distribution. The identification of the spin-1 Z's has been discussed in [3]. The above-mentioned differential angular analysis in the polar angle has been applied to the search for spin-2, spin-1 and spin-0 exchanges in the experimental studies of process (1) at the Fermilab Tevatron proton-antiproton collider [4].

In Ref. [5], the discrimination reach at the LHC on the spin-2 RS graviton resonance or, more precisely, the simultaneous rejection of *both* the spin-1 and spin-0 hypotheses for the peak, has been assessed by using as basic observable an angular-integrated center-edge asymmetry, $A_{\rm CE}$, instead of the 'absolute' lepton differential angular distribution. The potential advantages of the asymmetry $A_{\rm CE}$ to discriminate the spin-2 graviton resonance against the spin-1 hypothesis were discussed in Refs. [6, 7, 9].

Here, along the lines of Ref. [8] but in the reverse direction, we apply the same basic observable $A_{\rm CE}$, to the spin-1 identification of a peak observed in the dilepton mass distribution of process (1) at the LHC, against the spin-2 and spin-0 alternative hypotheses.

The existence of heavy neutral Z' vector bosons are a feature of many extensions of the SM. They arise in extended gauge theories including grand unified theories, superstring theories, and Left-Right symmetric

e-mail: [a]gulov@ff.dsu.dp.ua, [b]pankov@ictp.it, [c]skalozubv@daad-alumni.de, [d]tsytrin@gstu.by

models and in other models such as the BESS model and models of composite gauge bosons. For explicit NP realizations, for the spin-1 Z' models we refer to Refs. [10, 11]; for the alternative spin-2 and spin-0 hypotheses we refer for the RS graviton resonance to [1] and for the SUSY $\not{R}_p$ sneutrino exchange to [12], respectively.

The search reach at a collider for new gauge bosons is somewhat model dependent due to the rather large variations in their couplings to the SM fermions which are present in extended gauge theories currently on the market. This implies that any overview of the subject is necessarily incomplete. Hence, we will be forced to limit ourselves to a few representative models. To be specific we consider the so-called $Z'_{\rm SSM}$, Z'_{E_6}, $Z'_{\rm LR}$, $Z'_{\rm ALR}$ models and also the generic class of the Abelian Z' models [13, 14, 15]. Particular attention has recently been devoted to the phenomenological properties and the search reaches on such scenarios, and in some sense we may consider these Z' models as representative of this NP sector. In this note we study the discovery potential of the experiments that will be performed over the next decade at the LHC. In addition to the discovery reach we also examine the diagnostic power of the LHC for heavy gauge boson physics.

It turns out that $A_{\rm CE}$ should provide a robust spin diagnostic for the spin-1 case also. Moreover, we examine the possibility, once the spin-1 for the discovered peak is established, of differentiating the various representative Z' models from one another. For this purpose, we must use the total dilepton production cross section or, equivalently, the rate of events of reaction (1) under the peak. Identification of Z' models have been discussed recently in, e.g. [3] with different sets of observables, namely, forward-backward asymmetry $A_{\rm FB}$ on and off the Z' resonance, Z' rapidity distribution, cross section times total width, $\sigma \times \Gamma_{Z'}$. It was found that, on the basis of $A_{\rm FB}$ only, pairs of Z' models become indistinguishable at a given level of significance, starting from relatively low values of $M_{Z'}$ of the order of 1–2 TeV, even at $\mathcal{L}_{\rm int}$ much higher than 100 fb^{-1}. These ambiguities can be reduced by the combined analysis of the observables mentioned above, and at $\mathcal{L}_{\rm int} = 100$ fb^{-1}, some models could be discriminated up to Z' mass of the order of 2–2.5 TeV. As we will note below, on the basis of a simple χ^2 criterion, the precise determination of the total cross section itself might provide a somewhat stronger discrimination potential, in the sense that all models could be pairwise distinguished from one another up to Z' masses of about 2 TeV.

2 Observables and considered NP models

The parton model cross section for inclusive production of a dilepton with invariant mass M can be written as

$$\frac{{\rm d}\sigma(R_{ll})}{{\rm d}M\,{\rm d}y\,{\rm d}z} = K\frac{2M}{s}\sum_{ij} f_i(\xi_1, M) f_j(\xi_2, M)\frac{{\rm d}\hat{\sigma}}{{\rm d}z}(i+j \to l^+ + l^-). \tag{2}$$

Here, s is the proton-proton center-of-mass energy squared; $z = \cos\theta_{\rm c.m.}$ with $\theta_{\rm c.m.}$ the lepton-quark angle in the dilepton center-of-mass frame; y is the dilepton rapidity; $f_{i,j}(\xi_{1,2}, M)$ are parton distribution functions in the protons P_1 and P_2, respectively, with $\xi_{1,2} = (M/\sqrt{s})\exp(\pm y)$ the parton fractional momenta; finally, ${\rm d}\hat{\sigma}_{ij}$ are the partonic differential cross sections. In (2), the factor K accounts for next-to-leading order QCD contributions. For simplicity, and to make our procedure more transparent, we will use as an approximation a global flat value $K = 1.3$.

Since we are interested in a (narrow) peak production and subsequent decay into the DY pair, $pp \to R \to l^+l^-$, we consider the lepton differential angular distribution, integrated over an interval of M around M_R:

$$\frac{{\rm d}\sigma(R_{ll})}{{\rm d}z} = \int_{M_R-\Delta M/2}^{M_R+\Delta M/2} {\rm d}M \int_{-Y}^{Y} \frac{{\rm d}\sigma}{{\rm d}M\,{\rm d}y\,{\rm d}z}\,{\rm d}y. \tag{3}$$

The number of events under the peak, that determines the statistics, is therefore given by:

$$\sigma(R_{ll}) \equiv \sigma(pp \to R)\cdot {\rm BR}({\rm R} \to {\rm l^+ l^-}) = \int_{-{\rm z_{cut}}}^{\rm z_{cut}} {\rm dz} \int_{\rm M_R-\Delta M/2}^{\rm M_R+\Delta M/2} {\rm dM} \int_{-\rm Y}^{\rm Y} {\rm dy} \frac{{\rm d}\sigma}{{\rm dM\,dy\,dz}}. \tag{4}$$

For the full final phase space, $z_{\rm cut} = 1$ and $Y = \log(\sqrt{s}/M)$. Concerning the size of the bin ΔM, it should include a number (at least one) of peak widths to enhance the probability to pick up the resonance. In our analysis, we adopt the parametrization of ΔM vs. M exploited in Ref. [8] and, denoting by N_B and N_S the number of 'background' and 'signal' events in the bin, the criterion $N_S = 5\sqrt{N_B}$ or 10 events, whichever is larger, as the minimum signal for the peak discovery.

To evaluate the statistics, we shall use in Eqs. (3) and (4) the CTEQ6.5 parton distributions [16], and impose cuts relevant to the LHC detectors, namely: pseudorapidity $|\eta| < 2.5$ for both leptons assumed massless (this leads to a boost-dependent cut on z [7]); lepton transverse momentum $p_\perp > 20\,{\rm GeV}$. Moreover, the reconstruction efficiency is taken to be 90% for both electrons and muons.

2.1 Z' models

The list of Z' models that will be considered in our analysis is the following:

(i) The three possible $U(1)$ Z' scenarios originating from the exceptional group E_6 spontaneous breaking. They are defined in terms of a mixing angle β. The specific values $\beta = 0$, $\beta = \pi/2$ and $\beta = \arctan -\sqrt{5/3}$, correspond to different E_6 breaking patterns and define the popular scenarios Z'_χ, Z'_ψ and Z'_η, respectively.

(ii) The left-right models, originating from the breaking of an $SO(10)$ grand-unification symmetry, and where the corresponding $Z'_{\rm LR}$ couples to a combination of right-handed and $B-L$ neutral currents (B and L denote lepton and baryon currents), specified by a real parameter $\alpha_{\rm LR}$ bounded by $\sqrt{2/3} \lesssim \alpha_{\rm LR} \lesssim \sqrt{2}$. We fix $\alpha_{\rm LR} = \sqrt{2}$, which corresponds to a pure L-R symmetric model.

(iii) The $Z'_{\rm ALR}$ predicted by the 'alternative' left-right scenario.

(iv) The so-called sequential $Z'_{\rm SSM}$, where the couplings to fermions are the same as those of the SM Z.

(v) The Abelian Z' boson. The Z'-boson can be introduced in a phenomenological way by specifying its effective low-energy couplings to the known SM particles [13, 14]. Considering the Z' effects at energies much below the Z' mass, it is enough to parametrize the tree-level Z' interactions of renormalizable types, only. The low energy Z' couplings to a fermion f are parameterized by two couplings, the axial-vector and vector fermion coupling. It was shown in Ref. [15], for any renormalizable theory beyond the SM these parameters content some relations which follow from the renorlalization group equations and the decoupling theorem. In case of the Z' boson this is reflected in correlations between a'_f and v'_f. These correlations are model-independent in a sense that they do not depend on an particular underlying model. The detailed discussion of these issues and the derivation of the RG relations are presented in Ref. [15].

Current Z' mass limits, from the Fermilab Tevatron collider, are in the range $800 - 1000$ GeV, depending on the model [17].

2.2 RS graviton excitation

We consider the simplest scenario in the class of models based on one compactified warped extra dimension and two branes, proposed in the context of the SM gauge-hierarchy problem in [1]. The model predicts a tower of narrow Kaluza–Klein (KK), spin-2, graviton excitations $G^{(n)}$ ($n \geq 1$) with the peculiar mass spectrum $M^{(n)} = M^{(1)} x_n / x_1$ (x_i are the zeros of the Bessel function, $J_1(x_i) = 0$). Their masses and couplings to the SM particles are proportional to Λ_π and $1/\Lambda_\pi$, respectively, with Λ_π the gravity effective mass scale on the SM brane. For Λ_π of the TeV order, such RS graviton resonances can be exchanged in the process (1) and mimic Z' exchange. The independent parameters of the model can be chosen as the dimensionless ratio $c = k/\overline{M}_{\rm Pl}$ (with k the 5-dimensional curvature and $\overline{M}_{\rm Pl} = 1/\sqrt{8\pi G_{\rm N}}$ the reduced Planck mass), and the mass M_G of the lowest KK resonance $G^{(1)}$. Accordingly, $\Lambda_\pi = M_G / c x_1$.

There are two partonic subprocesses, $q\bar{q} \to \gamma, Z, G \to l^+ l^-$ and $gg \to G \to l^+ l^-$, needed to describe hadronic production of lepton pair within KK models. The theoretically 'natural' ranges for the RS model parameters are $0.01 \leq c \leq 0.1$ and $\Lambda_\pi < 10\,{\rm TeV}$. Current lower bounds at 95% C.L. from the Fermilab Tevatron collider are: $M_G > 300$ GeV for $c = 0.01$ and $M_G > 900$ GeV for $c = 0.1$ [17].

2.3 Sneutrino exchange

Sneutrino ($\tilde{\nu}$) exchange can occur in SUSY with R-parity breaking, and represents a possible, spin-0, interpretation of a peak in the dilepton invariant mass distribution of the process (1). The cross section for the relevant partonic process, $q\bar{q} \to \tilde{\nu} \to l^+ l^-$, is flat in z and expressed in terms of two Yukawa couplings, λ and λ', are the R-parity-violating sneutrino couplings to $l^+ l^-$ and $d\bar{d}$, respectively. Actually, in the narrow-width approximation, the partonic cross section turns out to depend on the product $X = (\lambda')^2 B_l$, with B_l the sneutrino leptonic branching ratio. Current limits on X are rather loose, and we may consider for this parameter the range $10^{-5} \leq X \leq 10^{-1}$. For $10^{-4} \leq X \leq 10^{-2}$, the range is $M_{\tilde{\nu}} \gtrsim 280 - 800$ GeV [17].

3 Model signature spaces

In Fig. 1, we show the predicted number of resonance (signal) events N_S in the Drell-Yan process (1) at LHC, *vs.* M_R, where $R = Z', G, \tilde{\nu}$ denotes the three alternative possibilities outlined in the previous subsections. The assumed integrated luminosity is $\mathcal{L}_{\rm int} = 100\ {\rm fb}^{-1}$, the cuts in phase space relevant to the foreseen detector acceptance specified above have been imposed, and the channels $l = e, \mu$ have been combined. Also, the minimum signal for resonance discovery above the 'background' at 5σ is represented by the long-dashed line. For any model, one can define a corresponding *signature space* as the region, in the (M_R, N_S) plot of Fig. 1, that can be 'populated' by the model by varying its parameters in the domains mentioned above. Clearly, in

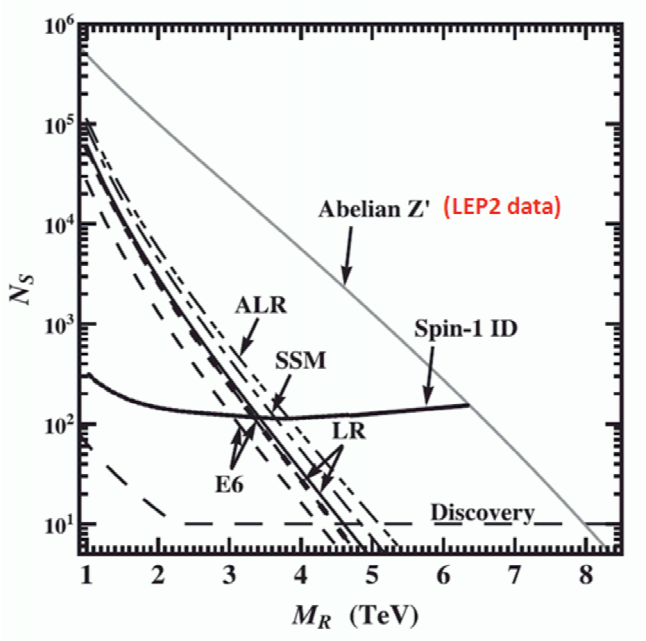

Figure 1. Expected number of resonance events at the LHC with $\mathcal{L}_{\rm int} = 100$ fb^{-1} for the process $pp \to R \to l^+l^- + X$, $(l = e, \mu)$. Event rates for various popular Z' models and the maximum possible resonant even rates for Abelian Z'-bosons are shown. The minimum number of signal events needed to detect the resonance (5σ-level) above the background and the minimum number of events to exclude the spin-2 and spin-0 hypotheses at 95% C.L. are shown ("Spin-1 ID"). The area above the line "Abelian Z'" is excluded by the LEP2 data.

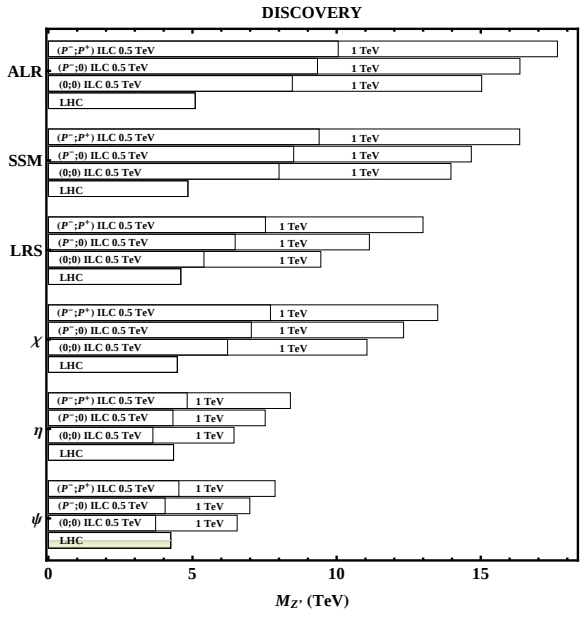

Figure 2. Discovery reaches on Z' models obtained from combined analysis of the unpolarized and polarized processes $e^+ + e^- \to f + \bar{f}$, $f = e, \mu, \tau, c, b$. (95% C.L.) at the ILC with $\sqrt{s} = 0.5$ TeV (1 TeV) and $\mathcal{L}_{\rm int} = 500$ fb^{-1} (1000 fb^{-1}), compared to the results expected from Drell-Yan processes at the LHC at the 5-σ level. Three options of polarization are considered at the ILC: unpolarized beams, $P^- = P^+ = 0$; polarized electron beam, $|P^-| = 0.8$; both beams polarized, $|P^-| = 0.8$ and $|P^+| = 0.6$.

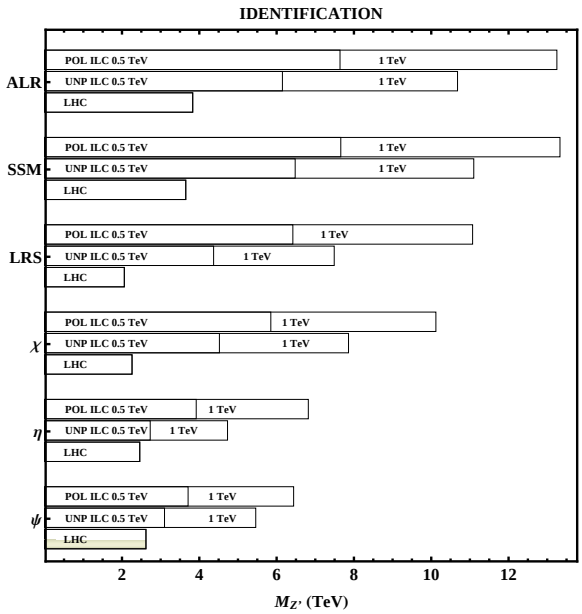

Figure 3. Comparison of the Z'-model distinction bounds on $M_{Z'}$ obtained from combined analysis of the unpolarized and polarized processes $e^+ + e^- \to f + \bar{f}$ at the ILC with $\sqrt{s} = 0.5$ TeV (1 TeV) and $\mathcal{L}_{\rm int} = 500$ fb^{-1} (1000 fb^{-1}), compared to the results expected from Drell-Yan processes at the LHC at 95% C.L. Two options of polarization are considered: unpolarized beams $P^- = P^+ = 0$ and both beams are polarized, $|P^-| = 0.8$ and $|P^+| = 0.6$.

regions where the signature spaces overlap, the values of M_R are such that it is not possible to distinguish a model as the source of the peak against the others, because the number of signal events under the peak can be the same. Further analyses are needed in these cases to perform the identification of the peak source with center-edge asymmetry. From Fig. 1 one finds that the spin of a heavy Z' gauge boson within the class of Abelian one can be established up to $M_{Z'} \simeq 6.5$ TeV while its discovery reach extends up to 8 TeV, at the LHC with the integrated luminosity of 100 fb^{-1}.

Fig. 2 and Fig. 3 show the comparison of discovery and identification reaches (or distinction bounds) on the Z'-models considered in Fig. 1, obtained from the process $pp \to l^+l^- + X$ at the LHC with c.m. energy 14 TeV and time-integrated luminosity 100 fb^{-1}. For comparison, the discovery and identification reaches obtained in Ref. [9] for the International Linear Collider (ILC) are also shown in Figs. 2 and 3. The figure speaks for itself, and in particular clearly exhibits the roles of the ILC parameters. One might be able to distinguish among the considered Z' models at 95% C.L. up to $M_{Z'} \simeq 3.1$ TeV (4.0 TeV) for unpolarized (polarized) beams at the ILC (0.5 TeV) and 5.3 TeV (7.0 TeV) at the ILC (1 TeV), respectively.

In the LHC discovery range, the cleaner ILC environment, together with the availability of beam polarization, allow for an identification of the particular Z' version realized. Actually, this ILC identification range extends considerably beyond the LHC discovery range. Specifically, the ILC with polarized beams at $\sqrt{s} = 0.5$ TeV and 1 TeV allows to identify all considered Z' bosons if $M_{Z'} \lesssim (6-7) \cdot \sqrt{s}$, substantially improving the LHC reach.

Acknowledgements. This research has been partially supported by the Abdus Salam ICTP under the TRIL and Junior Associate programmes and the Belarusian Republican Foundation for Fundamental Research.

References

[1] L. Randall and R. Sundrum, Phys. Rev. Lett. **83** (1999) 3370 [arXiv:hep-ph/9905221]; *ibid.* Phys. Rev. Lett. **83** (1999) 4690 [arXiv:hep-th/9906064].

[2] R. Cousins, J. Mumford, J. Tucker and V. Valuev, JHEP **0511**, 046 (2005).

[3] F. Petriello and S. Quackenbush, Phys. Rev. D **77**, 115004 (2008) [arXiv:0801.4389 [hep-ph]].

[4] A. Abulencia *et al.* [CDF Collaboration], Phys. Rev. Lett. **95**, 252001 (2005) [arXiv:hep-ex/0507104].

[5] P. Osland, A. A. Pankov, N. Paver and A. V. Tsytrinov, Phys. Rev. D **78**, 035008 (2008) [arXiv:hep-ph/0805.2734].

[6] P. Osland, A. A. Pankov and N. Paver, Phys. Rev. D **68**, 015007 (2003) [arXiv:hep-ph/0304123].

[7] E. W. Dvergsnes, P. Osland, A. A. Pankov and N. Paver, Phys. Rev. D **69**, 115001 (2004) [arXiv:hep-ph/0401199].

[8] P. Osland, A. A. Pankov, A. V. Tsytrinov and N. Paver, Phys. Rev. D **79**, 115021 (2009) [arXiv:0904.4857 [hep-ph]].

[9] P. Osland, A. A. Pankov and A. V. Tsytrinov, Eur. Phys. J. C **67** (2010) 191 [arXiv:0912.2806 [hep-ph]].

[10] For reviews and original references see, e.g., P. Langacker, arXiv:0801.1345 [hep-ph]; T. G. Rizzo, arXiv:hep-ph/0610104;
A. Leike, Phys. Rept. **317**, 143 (1999) [arXiv:hep-ph/9805494];
J. L. Hewett and T. G. Rizzo, Phys. Rept. **183**, 193 (1989).

[11] For recent constraints from electroweak data, see J. Erler, P. Langacker, S. Munir and E. R. Pena, arXiv:0906.2435 [hep-ph].

[12] J. Kalinowski, R. Ruckl, H. Spiesberger and P. M. Zerwas, Phys. Lett. B **406** (1997) 314 [arXiv:hep-ph/9703436]; *ibid.* Phys. Lett. B **414** (1997) 297 [arXiv:hep-ph/9708272];
T. G. Rizzo, Phys. Rev. D **59** (1999) 113004 [arXiv:hep-ph/9811440];
For a review see, *e.g.*: R. Barbier *et al.*, Phys. Rept. **420**, 1 (2005) [arXiv:hep-ph/0406039].

[13] A. Gulov and V. Skalozub, Int. J. Mod. Phys. A **25**, 5787 (2010) [arXiv:1009.2320 [hep-ph]].

[14] A. V. Gulov and V. V. Skalozub, Phys. Rev. D **70**, 115010 (2004) [arXiv:hep-ph/0408076].

[15] A. Gulov and V. Skalozub, Eur. Phys. J. C **17**, 685 (2000).

[16] J. Pumplin, D. R. Stump, J. Huston, H. L. Lai, P. Nadolsky and W. K. Tung, JHEP **0207**, 012 (2002) [arXiv:hep-ph/0201195].

[17] T. Aaltonen *et al.* [CDF Collaboration], Phys. Rev. Lett. **99**, 171802 (2007) [arXiv:0707.2524 [hep-ex]]; Phys. Rev. Lett. **102**, 091805 (2009) [arXiv:0811.0053 [hep-ex]]; R. J. Hooper [D0 Collaboration], Int. J. Mod. Phys. A **20**, 3277 (2005).

Proceedings of the International School-seminar
"New Physics and Quantum Chromodynamics at External Conditions", pp. 105 – 108,
3-6 May 2011, Dnipropetrovsk, Ukraine

TIME-DELAY IN QUANTUM RESONANT SYSTEMS

N. A. Ivanov[a], V. V. Skalozub[b]

Dnipropetrovsk National University, Dnipropetrovsk, Ukraine

Using developed recently modified saddle-points method the tunneling of the wave pulse having rectangular form through a quantum system with resonance levels is investigated. The analytic expressions describing the form of the transmitted pulse are obtained. It is shown that the form of outgoing pulse is represented as the standard error functions (erfc) superposition. The numeric solution results are compared with the analytically derived ones. The comparison shows a good agreement of both calculations. Tunneling of the wide wave-packages the Gaussian and the rectangular form is investigated in detail. The time-delay for the wave package tunneling through the quantum dot are obtained.

1 Introduction

In this work we consider the wave package tunneling through the open mesoscopic systems. Mesoscopic physic is a section of condensed matter physic which study systems with scales between macro and microscopic. In 2D transport microscopic is a scale which not exceeds mean current carriers free path of. The macroscopic is scale when in cause of inelastic collisions get lost a quantum coherence. This mean that particle interference become impossible. The open mesoscopic systems are a quantum systems which can make the energy and matter exchange with external ambience. The microcircuit miniaturization is the most actual direction of modern electronics development. Quantum dots, double-well diodes, quantum tunneling transistors are examples of objects which are now used for this purpose. The common feature of those systems is existence of potential wells with discreet energy levels. At the same time it supposes resonance conductivities of those systems. Thereby the problem of time-delay determination (for pulse tunneling) is put in the forefront [1]. Should say that it is commonly believed that this problem has not general solution. For it decision used different methods based on evolution operator, T-matrix approach and numerical calculations. To characterize the problem commonly should say that was not developed unit approach to describe quantum systems with broad and narrow resonance levels. For it decision used different methods based on evolution operator, T-matrix approach and numerical calculations. That's why for every quantum system was selected its own description method. This problem decision gives possibility to find out such parameters of the pulse or quantum system with which the speed of tunneling becomes maximal. That on the same level gives an opportunity for miniaturization and increasing a productivity of microcircuit with quantum elements. This problem solution should be started with finding a wave package argument of outgoing which is received from the quantum system. The using approach based on the S-matrix (scattering matrix) formalism and modified saddle point method [3]. That approach is completely formalized decision of the wave package tunneling problem. The developing approach gives a possibility to define form and time-delay for free-form wave packages tunneling through the quantum system with resonance levels. The describing tunneling parameters should be realized in the incident pulse terms. So the time delay of Gaussian-form wave-package and step-form wave-package tunneling thought the quantum dot are counted. The time delay dependencies from system and pulse parameters are illustrated.

2 Method

The incident and outgoing pulse are bound by next expression:

$$\Psi_a^{out} = \frac{1}{2\pi}\sum_b \int_{-\infty}^{\infty} \Psi_b^{in} S_{b,a} dk, \tag{1}$$

which integrated by all k-space. Characterized parameters the outgoing pulse wave function become x-coordinate variable, t-time variable,k- and k_0 - pulse and center of incident wave package localization in the momentum space. The k_j - are positions S-matrix poles. We consider the incident pulse width a in the real space and all calculations will be realized in the terms of unperturbed pulse. Use the next dimensionless variables:

$$q' = \frac{x}{a};\ \tau = \frac{t}{t_a};\ z = a(k-k_0);\ l_j = ak_j;\ \rho_j = a\frac{\Gamma_j}{2};\ l_0 = ak_0. \tag{2}$$

e-mail: [a]na_ivanov@dsu.dp.ua, [b]skalozubv@daad-alumni.de

Moreover we shell use next parameterization to simplify future expressions:

$$\beta = \frac{1+i\tau}{2},\ q_{0j} = l_0 - l_j + i\rho_j,\ q = q' - l_0\tau, \tag{3}$$

Here the coordinate variable become - q, time - τ, $t_a = \frac{ma^2}{\hbar}$, l_j and l_0 localization poles and center of wave package respectively, and ρ_j - width of j-th resonance level. This terms process presentation give us enough parameters to describe the wave package tunneling through a quantum system with resonance levels. Obtain next

$$\Psi(q>0,\tau) = \frac{1}{a\sqrt{2\pi}} e^{il_0(q-\frac{1}{2}l_0\tau)} \int_{-\infty}^{\infty} dz \Psi_0(z) S(z+l_0) e^{\left[izq' - \beta z^2 + \frac{1}{2}z^2\right]}, \tag{4}$$

$$S(z+l_0) = \sum_j \left[a_j \frac{i\rho_j}{l - l_j + i\rho_j} + b_j \right]. \tag{5}$$

Use the Saddle-point method to get tunneling problem solution. The parameter which allow this method is τ. Time through which we observe the outgoing wave package should be more than t_a. This is the necessary condition for the resonance existing. For resonant part we obtained equation:

$$\Psi(q>0,\tau) = \sum_j \frac{1}{a\sqrt{2\pi}} e^{il_0(q-\frac{1}{2}l_0\tau)} \left[\int_{-\infty}^{\infty} dz f_j^{res}(z) e^{g_j^{res}(z)} \right], \tag{6}$$

where

$$\begin{aligned} g_j^{res}(z) &= isq' - (\beta + \frac{1}{2})z^2 - ln(z - q_{0j}) + ln(\Psi_0(z)), \\ f_j^{res}(z) &= i\rho_j a_j, \end{aligned}$$

Calculation of the saddle point is defined from the stationary conditions:

$$\frac{dg(z)}{dz} = 0, \quad Img(z) = const, \quad Reg(z) < Reg(z_k). \tag{7}$$

where z_k is the k-th saddle point. Resulting resonance wave function amplitude part near the stationary points become

$$\Psi(q>0,\tau) \sim \frac{1}{a} e^{il_0(q-\frac{1}{2}l_0\tau)} \times (\sum_{jk} e^{g_j^{res}(x_k^s)} \sqrt{-\frac{1}{e^{g_j^{res\prime\prime}(x_k^s)}}} f_j^{res}(x_k^s) +$$

This formula gives the asymptotical presentation free form wave package tunneling though resonance quantum system.

3 Tunneling the Gaussian and square-form packages through the quantum dot

Use the developed method to study square-form wave package tunneling through the quantum dot with one resonance level. Package describe like difference between two step-function

$$\Psi(x) = \Theta(x) - \Theta(x-a), \tag{8}$$

where a is the package width. Using well known Fourier-transform for Θ-function in dimensionless variables, obtained

$$\begin{aligned} \Psi(q>0,\tau) &= \frac{1}{a\sqrt{2\pi}} e^{il_0(q-\frac{1}{2}l_0\tau)} \int_{-\infty}^{\infty} dz (\frac{a}{iz} + \pi\delta(\frac{z}{a}) - \\ &- e^{-iz}(\frac{a}{iz} + \pi\delta(\frac{s}{a}))) e^{izq' - (\beta - \frac{1}{2})z^2}. \end{aligned} \tag{9}$$

For outgoing wave package considering two saddle (7) points existing get:

$$\Psi_{j_T sp}^{res}(q,\tau) = i\rho_j a_j \left[e^{g^{res}(z_1)} \sqrt{-\frac{1}{g^{res\prime\prime}(z_1)}} + e^{g^{res}(z_2)} \sqrt{-\frac{1}{g^{res\prime\prime}(z_2)}} \right], \tag{10}$$

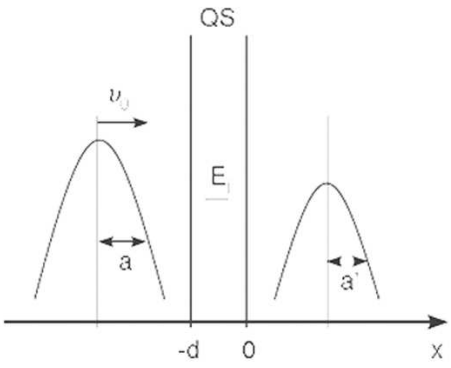

Figure 1. Tunneling free-form wave packet through the quantum system with resonance levels E_j

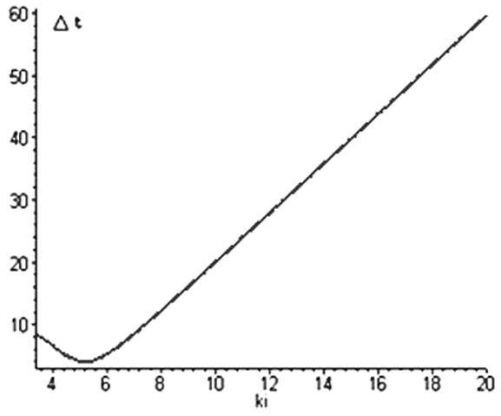

Figure 2. Time-delay for transmission Gaussian pulse with $t_a = 1, t = 100, x = 300, a = 1, k_0 = 1, \gamma = 1$.

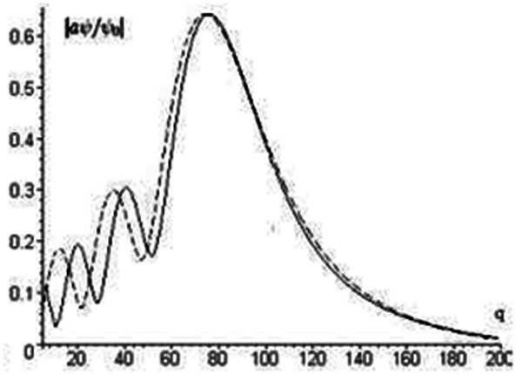

Figure 3. The package formed by transmission Gaussian pulse with $\tau = 100, a = 1, l_0 = 1, l_1 = 1, \rho_1 = 0.02$.

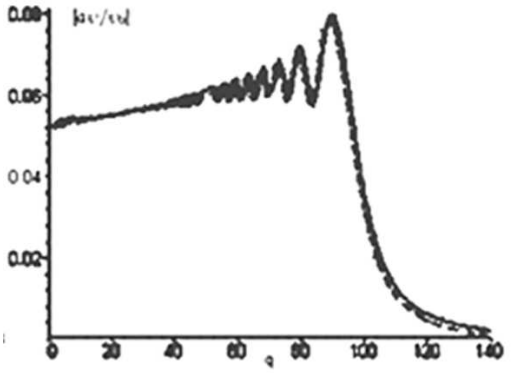

Figure 4. The package formed by transmission step-form pulse with $\tau = 100, a = 1, l_0 = 1, l_1 = 1, \rho_1 = 0.007$.

For the Gaussian-form incident wave package tunneling through such quantum system like in case with square-form package we get:

$$\Psi(z) = \Psi_0 e^{-\frac{z^2}{2}}, \tag{11}$$

where Ψ_0 - amplitude, $\Psi(z)$- form of incident wave package. In this way the exponential argument became:

$$g(z) = izq' - \beta z^2 - ln(z - q_0). \tag{12}$$

From which get the saddle point

$$z1 = \frac{1}{2}\left(q_0 + \frac{iq'}{2\beta}\left[(q_0 - \frac{iq'}{2\beta})^2 - \frac{1}{2}\right]^{1/2}\right) \tag{13}$$

For $\tau \to \infty$ with accurate to the second order obtained:

$$\Psi^r es = (q,\tau) = \frac{i\rho_j a_j}{\sqrt{2\pi}} e^{-\frac{(q-l_0\tau)^2}{2+2\tau^2} + iArg(\Psi)} \frac{(1+\tau^2)^{1/4}}{[(q+\rho_i - l_i\tau)^2 + (\rho_i\tau + l_i - l_0)^2]^{1/2}} \tag{14}$$

where the argument

$$Arg(\Psi) = \frac{1}{2} arctg(\tau) + \frac{(q-l_0\tau)^2\tau}{2+2\tau^2} - arctg\left[\frac{\rho_i\tau + l_i - l_0}{q + rho_i - l_i\tau}\right]. \tag{15}$$

To find time-delay

$$\triangle t = \frac{dArg(\Psi)}{dE}. \tag{16}$$

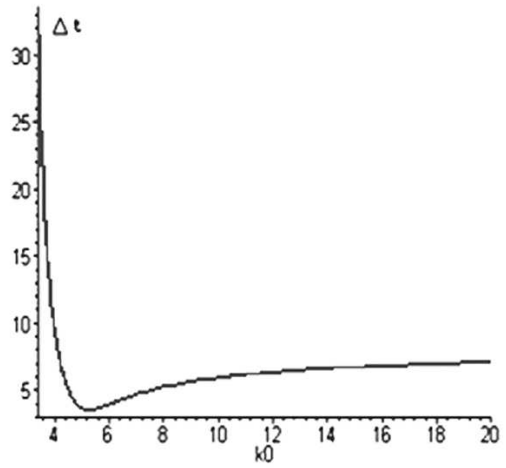

Figure 5. Time-delay for transmission Gaussian pulse with $t_a = 1, t = 100, x = 300, a = 1, k_i = 1, \gamma = 1$.

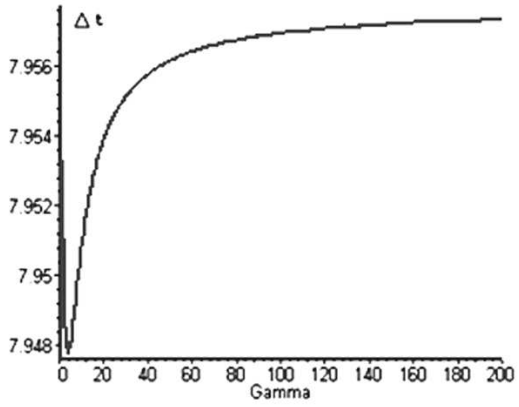

Figure 6. Time-delay for transmission Gaussian pulse with $t_a = 1, t = 100, x = 300, a = 1, k_0 = 1, k_i = 1$.

4 Results

Dependency the time-delay of wave package Gaussian forms passing through quantum system with resonance level was researched. The time-delay dependencies from parameter of system and initial pulse were shown in graphs. Internal particularities of open mesoscopic systems complicated the calculation of time-delay but using the developed method greatly simplifies this process. This approach gives a possibility to define form and time-delay for free-form wave packages tunneling through the quantum system with resonance levels. The graphs shows: Fig. 1 - schematic wave packet tunneling through the quantum system with resonance level E_j, Fig. 2, Fig. 5 and Fig. 6 - Gaussian form wave packet time-delay dependency from k_i, k_0 and Γ respectively, Fig. 3 and Fig. 4 - outgoing wave packet for incoming Gaussian and step-form wave packets (dotted line shows direct integration way and simple line shows Saddle point method solution).

References

[1] M. Razavy, *Quantum Theory of Tunneling*, (World Scientific, 2003).
[2] A.I. Baz', Y.B. Zel'dovich, A.M. Perelomov, *Scattering, reactions and decays in non relativistic quantum mechanics*, (Nauka, Moscow, 1971).
[3] U. Wulf, V.V. Skalozub and A. Zaharov, Phys. Rev. **B** 77, 045318 (2004).
[4] L. Brillouin, *Wave propagation and Group Velocity* (Academic Press, New York, 1960).
[5] L.E. Ballentine, *Quantum Mechanics: A Modern Development*, (World Scientific Publishing Co, Pte. Ltd, 1998).
[6] U. Wulf and V.V. Skalozub , Phys. Rev. **B** 72, 165331 (2005).
[7] M.A. Lavrent'ev, B.V. Shabat, *Methods of Function Theory of a Complex Variable*, (Nauka, Moscow, 1973).

Proceedings of the International School-seminar
"New Physics and Quantum Chromodynamics at External Conditions", pp. 109 – 112,
3-6 May 2011, Dnipropetrovsk, Ukraine

THE CRITICAL EXPONENTS OF THE QCD (TRI)CRITICAL ENDPOINT WITHIN EXACTLY SOLVABLE MODELS

A. I. Ivanytskyi[a], K. A. Bugaev[b]

Bogolyubov Institute for Theoretical Physics, Kiev, Ukraine

The critical indices α', β, γ' and δ of the Quark Gluon Bags with Surface Tension Model with the tricritical and critical endpoint are calculated as functions of the usual parameters of this model and two newly introduced parameters (indices). The critical indices are compared with that ones of other models. The universality class of the present model with respect to values of the model parameters is discussed. The scaling relations for the found critical exponents are verified and it is demonstrated that for the standard definition of the index α' some of them are not fulfilled in general case. Although it is shown that the specially defined index α'_s recovers the scaling relations, another possibility, an existence of the non-Fisher universality classes, is also discussed.

1 Introduction

Investigation of the properties of strongly interacting matter equation of state has become a focal point of modern nuclear physics of high energies. The low energy scan programs performed nowadays at CERN SPS and BNL RHIC are aimed at the discovery of the (tri)critical endpoint of the quantum chromodynamics (QCD) phase diagram. Despite many theoretical efforts neither an exact location nor the properties of the QCD (tri)critical endpoint are well known [1]. Therefore, the thorough theoretical investigation of the QCD endpoint properties are required in order to clarify whether this endpoint is critical or tricritical.

This work is devoted to calculation of the critical exponents of the QCD endpoint of both critical (CEP) and tricritical (triCEP) types. Unfortunately, such a task cannot be solved within the QCD itself. Moreover, even the possibilities of the lattice QCD are nowadays very limited in this respect. Then, unavoidably, one has to use some models of the (tri)CEP. The most popular models of this kind are the quark-meson model [2, 3] and the extended Nambu–Jona-Lazinio model [4]. Despite a great popularity both of these models contain a significant weakness, they are mean-field ones and hence there is no reason to expect that their critical exponents could differ from that ones of the Van der Waals model equation of state [5]. Therefore, to study the properties of non-classical endpoints one has to investigate the non-mean-field models.

The gas of bags model [6] is an example of such a non-mean-field model. Despite a significant success of this model in describing of the deconfinement phase transition, it can not generate the (tri)CEP in a natural way. The problem was solved in the Quark Gluon Bags with Surface Tension Model (QGBSTM) [7, 8]. This exactly solvable model accounts for the surface effects which play a decisive role in the critical phenomena and employes the same mechanism of the (tri)CEP generation which is typical for the liquid-gas phase transition (PT) and which is also used in the Fisher droplet model (FDM) [9] and in the statistical multifragmentation model (SMM) [10, 11]: the endpoint of the 1-st order PT appears due to vanishing of the surface tension coefficient at this point which leads to the indistinguishability between the liquid and gas phases. However, the surface tension coefficient in the QGBSTM has the region of negative values, which is a principally different feature of this model compared to the FDM, SMM and all other statistical models of the liquid-gas PT. Note that just this feature provides an existence of the cross-over at small values of the baryonic chemical potential μ in the QGBSTM with triCEP [7] and with CEP [11], and also it generates an additional PT in the model with triCEP at large values of μ. Therefore, it is very important and interesting to study the critical indices of such a novel statistical model as the QGBSTM, to determine its class of universality and to examine how the latter is related to that ones of the FDM and SMM.

The paper is organized as follows. A description of the QGBSTM is given in Section 2. In Section 3 the critical exponents of the CEP and triCEP are calculated. This section is also devoted to the analysis of scaling relations between the found critical exponents. Conclusions are given in Section 4.

2 Quark Gluon Bags with Surface Tension Model

An exact solution of the QGBSTM was found in [7]. The relevant degrees of freedom in this model are the quark gluon plasma (QGP) bags and hadrons. The attraction between them is accounted like in the original statistical

e-mail: [a]a_iv_@ukr.net, [b]bugaev@th.physik.uni-frankfurt.de

bootstrap model [12] via many sorts of the constituents, while the repulsion between them is introduced a la Van der Waals equation of state [6, 7]. An essential element of the QGBSTM is the T and μ dependence of its surface tension coefficient $T\Sigma(T,\mu)$ (here $\Sigma(T,\mu)$ is the reduced surface tension coefficient). Let us denote the nil line of the reduced surface tension coefficient in the $T-\mu$ plane as $T_\Sigma(\mu)$, i.e. $\Sigma(T_\Sigma,\mu)=0$. Note that for a given μ the surface tension is negative (positive) for T above (below) $T_\Sigma(\mu)$ line. Here it is appropriate to say a few words about the negative values of Σ which is a distinctive feature of QGBSTM compared to other models. There is nothing wrong or unphysical with the negative values of surface tension coefficient, since $T\Sigma\, v^\kappa$ is the surface free energy of the bag of mean volume v and, hence, as any free energy, it contains the energy part e_{surf} and the entropy part s_{surf} multiplied by temperature T [9]. Therefore, at low temperatures the energy part dominates and surface free energy is positive, whereas at high temperatures the number of bag configurations with large surface drastically increases and it exceeds the Boltzmann suppression and, hence, the surface free energy becomes negative since $s_{surf} > \frac{e_{surf}}{T}$. Such a behavior of the surface free energy can be derived within the exactly solvable model of surface deformations known as Hills and Dales Model [13].

In the grand canonical ensemble the pressure of QGP and hadronic phase are, respectively, given by

$$p_Q(T,\mu) = Ts_Q(T,\mu), \tag{1}$$

$$p_H(T,\mu) = Ts_H(T,\mu) = T\left[F_H(s_H,T,\mu) + u(T,\mu)I_\tau(\Delta s,\Sigma)\right], \tag{2}$$

$$F_H(s_H,T,\mu) = \sum_{j=1}^{n} g_j e^{\frac{b_j\mu}{T}-v_j s_H}\phi(T,m_j) \quad \text{and} \quad I_\tau(\Delta s,\Sigma) = \int\limits_{V_0}^{\infty}\frac{dv}{v^\tau}e^{-\Delta s v-\Sigma v^\kappa}, \tag{3}$$

where $\Delta s \equiv s_H(T,\mu) - s_Q(T,\mu)$. The particle density of a hadron of mass m_j, baryonic charge b_j, eigenvolume v_j and degeneracy g_j is denoted as $\phi_j(T,m_j) \equiv \frac{1}{2\pi^2}\int\limits_0^\infty p^2 dp\, e^{-\frac{(p^2+m_j^2)^{1/2}}{T}}$. Here, as in [7], it is assumed that the functions $u(T,\mu)$ and $s_Q(T,\mu)$, which are the parameters of the present model, and their first and second derivatives with respect to T and μ are finite everywhere at the $T-\mu$ plane. In the continuous part of the spectrum of bags denoted as $uI_\tau(\Delta s,\Sigma)$ the surface of a QGP bag of volume v is parameterized by the term v^κ. Usually one chooses $\kappa=\frac{2}{3}$ in 3-dimensional case (or $\kappa=\frac{d-1}{d}$ for the dimension d), but in what follows it is regarded as free parameter of the range $0<\kappa<1$.

The system pressure, that corresponds to a dominant phase, is given by the largest value between p_Q and p_H for each set of T and μ. As usual, the deconfinement PT occurs when pressure of QGP gets equal to that one of the hadron gas, which is nothing else as the Gibbs criterion. The sketch of $T-\mu$ phase diagram with triCEP is shown in the left panel of Fig. 1. Suppose that the necessary conditions for the deconfinement PT outlined in [7] are satisfied and its transition temperature is given by the function $T_c(\mu)$ for $\mu \geq \mu_{cep}$. The necessary condition of the triCEP occurrence is that at the nil line of the surface tension coefficient there exists the surface tension induced PT of 2-nd (or higher order) [7] for $\mu \geq \mu_{cep}$ and $T_c(\mu) \leq T_\Sigma(\mu)$ for these μ values. The both of these inequalities become equalities only at triCEP. Moreover, at triCEP the phase coexistence curve $T_c(\mu)$ is a tangent (not intersecting!) line to the nil line of the surface tension coefficient $T_\Sigma(\mu)$. For $\mu < \mu_{cep}$ the deconfinement PT degenerates into a cross-over since in this region $\Sigma < 0$ [7] and, hence, the system pressure is defined by a solution of Eq. (2). It is necessary to stress here that QGP exists as real quark gluon liquid (QGLiquid) with the pressure (1) only for $T_c(\mu) \leq T \leq T_\Sigma(\mu)$ and $\mu \geq \mu_{cep}$, outside this region the system is defined by Eq. (2). Now let us discuss phase diagram with CEP (see the right panel in Fig. 1). The only difference with the case of triCEP is that $T_c(\mu)$ and $T_\Sigma(\mu)$ lines coincide exactly for $\mu \geq \mu_{cep}$. Therefore, QGLiquid exists only at the PT line.

An actual parameterization of the reduced surface tension coefficient $\Sigma(T,\mu)$ is taken from [7, 14]:

$$\Sigma(T,\mu) = \frac{\sigma_0}{T}\cdot\left|\frac{T_\Sigma(\mu)-T}{T_\Sigma(\mu)}\right|^\zeta \text{sign}\left(T_\Sigma(\mu)-T\right) \quad \text{for triCEP}, \tag{4}$$

$$\Sigma^\pm(T,\mu) = \mp\frac{\sigma_0}{T}\cdot\left(T_{cep}-T+\frac{dT_c}{d\mu}(\mu_{cep}-\mu)\right)^{\xi^\pm}\left|\frac{T_\Sigma(\mu)-T}{T_\Sigma(\mu)}\right|^{\zeta^\pm} \quad \text{for CEP}. \tag{5}$$

In what follows the coefficient σ_0 is assumed to be a positive constant, i.e. $\sigma_0 = \text{const} > 0$, but it is easy to show that the obtained results hold, if $\sigma_0 > 0$ is a smooth function of T and μ.

In the vicinity of (tri)CEP the behavior of both the deconfinement PT curve and the nil surface tension coefficient line in the $\mu - T$ plane is parameterized via a single parameter $\xi^T > 0$:

$$T_{cep} - T_\Sigma(\mu) \sim (\mu-\mu_{cep})^{\xi^T} \quad \text{and} \quad T_{cep} - T_c(\mu) \sim (\mu-\mu_{cep})^{\xi^T}, \tag{6}$$

since, as discussed above, $T_c(\mu)$ and $T_\Sigma(\mu)$ lines are tangent to each other at the endpoint in the model with triCEP and coincide in the model with CEP. This is a new index which was not considered both in the FDM

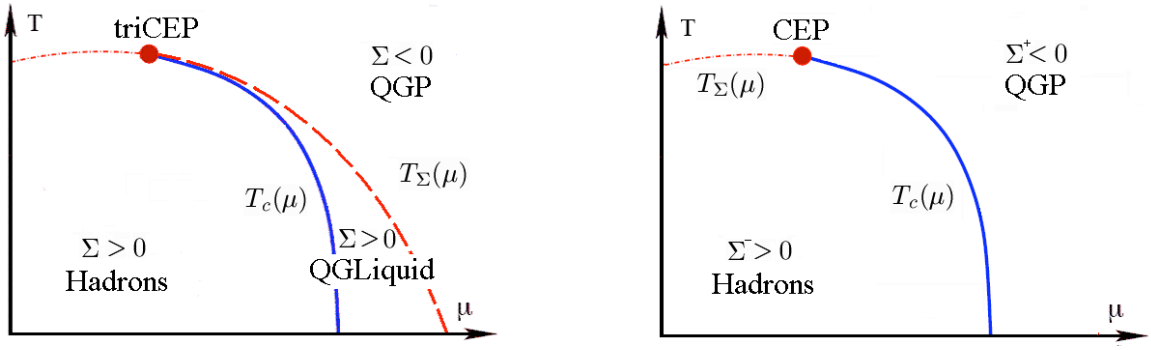

Figure 1. A schematic phase diagrams with triCEP (left panel) and CEP (right panel) in the $\mu - T$ plane. The dashed curve indicates the nil line of the surface tension coefficient $T_\Sigma(\mu)$, below (above) which Σ is positive (negative). The deconfinement PT line $T_c(\mu)$ is shown by the full curve for $\mu > \mu_{cep}$. At the phase diagram with CEP $T_c(\mu)$ and $T_\Sigma(\mu)$ lines coincide exactly for $\mu > \mu_{cep}$. A cross-over (the short dashed curve) takes place along the line $T_\Sigma(\mu)$ for $\mu \leq \mu_{cep}$. The cross-over and PT regions are separated by (tri)CEP (filled circle).

and SMM and as we show below, it is responsible for a new universality class compared to other exactly solvable models.

Since the entropy density and the baryonic density are, respectively, defined as T and μ partial derivatives of the corresponding pressure, then using (1) and (2) the Clapeyron-Clausius equation $\frac{d\mu_c}{dT} = -\frac{S_H - S_Q}{\rho_H - \rho_Q}\Big|_{T=T_c}$ for the model with triCEP can be explicitly rewritten as

$$\frac{d\mu_c}{dT} = -\frac{A_T - \frac{\partial\Sigma}{\partial T} u I_{\tau-\kappa}(0,\Sigma)}{A_\mu - \frac{\partial\Sigma}{\partial \mu} u I_{\tau-\kappa}(0,\Sigma)}\Bigg|_{T=T_c}, \tag{7}$$

where the following notation is used $A_i \equiv \frac{\partial F_H}{\partial i} + \frac{\partial u}{\partial i} I_\tau + \frac{\partial s_Q}{\partial i}\left(\frac{\partial F_H}{\partial s} - 1\right)$ for $i \in \{T, \mu\}$. Note that for the model with CEP the term $\frac{\partial\Sigma}{\partial i} u I_{\tau-\kappa}(0,\Sigma)$ does not appear in (7). Let us parameterize the behavior of the numerator and denominator in (7) at the (tri)CEP vicinity as

$$A_T\big|_{T=T_c} \sim (T_{cep} - T_c(\mu))^{\chi + \frac{1}{\xi^T} - 1} \quad \text{and} \quad A_\mu\big|_{T=T_c} \sim (T_{cep} - T_c(\mu))^{\chi}, \tag{8}$$

where $\chi \geq \max(0, 1 - \frac{1}{\xi^T})$ denotes another new index. The latter inequality follows from the fact that the integral I_τ and functions F_H, u, s_Q together with their derivatives are finite for any finite values of T and μ. An introduction of the index χ is quite general and could be done for any model with the PT of the liquid-gas type, since it unavoidably appears from the Clapeyron-Clausius equation, which is a direct consequence of the Gibbs criterion for phase equilibrium. To our best knowledge, this index was never used for the calculation of critical exponents.

3 Critical exponents of the QGBSTM

The standard set of critical exponents α', β and γ [5, 15] describes the T-dependence of the system near (tri)CEP:

$$\begin{aligned} C_\rho &\sim |t|^{-\alpha'} && \text{for } t \leq 0 \text{ and } \rho = \rho_{cep}, \\ \Delta\rho \sim |t|^{\beta} \quad \text{and} \quad \Delta K_T &\sim |t|^{-\gamma'} && \text{for } t \leq 0, \end{aligned} \tag{9}$$

where $\Delta\rho \equiv (\rho_Q - \rho_H)_{T=T_c}$ defines the order parameter, $C_\rho \equiv \frac{T}{\rho}(\frac{\partial S}{\partial T})_\rho$ denotes the specific heat at the critical density and $\Delta K_T \equiv (K_T^H - K_T^Q)_{T=T_c}$ is the discontinuity in the isothermal compressibility $K_T \equiv \frac{1}{\rho}(\frac{\partial \rho}{\partial p})_T$ across the PT line, the variable t is the reduced temperature $t \equiv \frac{T - T_{cep}}{T_{cep}}$. The critical isotherm shape is given by the index δ [15, 5] (hereafter the tilde indicates that $T = T_{cep}$):

$$p_{cep} - \widetilde{p} \sim (\rho_{cep} - \widetilde{\rho})^\delta \text{ for } \quad t = 0. \tag{10}$$

In this work we want to present the results of our calculations which are exhaustively explained in [16]. Not going into details here we give the standard set of critical exponents (see Table 1) and discuss the related physics issues. Since in some aspects the QGBSTM is similar to the FDM and SMM it is interesting to compare its critical exponents with that ones of the FDM [9] and SMM [17]. The QGBSTM with CEP generates quite unique set of the critical exponents which are independent of τ. Therefore, this model belongs to different

Table 1. Critical exponents of QGBSTM. For the model with CEP the notation $\beta^{\pm} \equiv \zeta^{\pm} + \xi^{\pm} \frac{1}{\xi^T}$ is introduced. The index α'_s describes the specific heat difference $\Delta C = (C_{\rho_H} - C_{\rho_Q})_{T=T_c} \sim |t|^{-\alpha'_s}$ for two phases [15].

	Model with triCEP		Model with CEP
	$\chi = 0$	$\chi > 0$	
α'	$2 - 2\min(1, \frac{1}{\xi^T})$		$2 - 2\min(1, \frac{1}{\xi^T})$
β	$\frac{\zeta}{\kappa}(2-\tau) + \min\left[\chi, \frac{\zeta}{\kappa}\min(\kappa, \tau-1) - \frac{1}{\xi^T}\right]$		$\min(\beta^+, \beta^-)$
γ'	$\frac{\zeta}{\kappa} - 2\beta$		$\frac{1}{\xi^T} - \beta$
δ	$\min^{-1}\left[\frac{\xi^T\zeta}{\max(\tau-1,\kappa)} - 1, \frac{2-\tau}{\tau-1}\right]$	$\left(\frac{\xi^T\zeta}{\max(\tau-1,\kappa)} - 1\right)^{-1}$	$\frac{1}{\xi^T\beta^+}$
α'_s	$2 - \min(2, \frac{1}{\xi^T}) - \beta$		$2 - \min(2, \frac{1}{\xi^T}) - \beta$

universality class, than that one of the SMM and FDM. As it is seen from Table 1, QGBSTM with triCEP has two regimes switched by parameter χ. Since the FDM and SMM implicitly treat the parameter $\chi = 0$, then it is most natural to compare their critical exponents with the QGBSTM results just for this case. In the QGBSTM with triCEP there is a regime, when its index $\delta|_{\chi=0} = \frac{\tau-1}{2-\tau}$ matches the SMM result [17]. Moreover, it is easy to see that in this regime all other indices the QGBSTM and SMM coincide for $\xi^T \leq 1$. The spectrum of values of the QGBSTM critical indices is more rich than the corresponding spectra of the FDM and SMM since this model contains two new indices ξ^T and χ.

The explicit expressions for the QGBSTM critical exponents allow us to examine scaling relations between them. For the model with triCEP Fisher inequality ($\alpha' + 2\beta + \gamma' \geq 2$) and Griffiths inequality ($\alpha' + \beta(1+\delta) \geq 2$) are not fulfilled in a general case, whereas the Liberman inequality ($\gamma' + \beta(1-\delta) \geq 0$) is always obeyed [16]. For the model with CEP the situation is similar. In order to 'save' the scaling inequalities it was suggested to replace the index α' by α'_s [15]. This hypothesis resolves the problem of scaling inequalities only for the triCEP model. Therefore, it is quite possible that the non-Fisher universality classes exist.

4 Conclusions

The critical indices of the QGBSTM are found in terms of the model parameters. Two parameters $\xi^T > 0$ and $\chi \geq \max(0, 1 - \frac{1}{\xi^T})$ are newly introduced and consequently the spectrum of the values of critical exponents of the present model is more rich compared to other models. It is shown there is a regime when QGBSTM with triCEP reproduces the critical exponents of the SMM with triCEP, whereas the critical exponents of the FDM are never reproduced by QGBSTM. Thus, for $\chi = 0$ QGBSTM and SMM fall into the same universality class.

The direct calculations show that for the standard definition of the critical index α' (found along the critical isochore) the Fisher and Griffiths scaling inequalities are not always fulfilled, whereas the Liberman inequality is obeyed for any values of the model parameters. According to Fisher hypothesis the scaling relations for the index α'_s are verified. The possibility of the non-Fisher universality classes existence is discussed.

References

[1] E. V. Shuryak, Prog. Part. Nucl. Phys. **62**, 48 (2009).
[2] O. Scavenius, A. Mocsy, I.N. Mishustin and D. H. Rischke, Phys. Rev. **C 64**, 045202 (2001).
[3] B.-J. Schaefer, J. M. Pawlowski and J. Wambach, Phys. Rev. **D 76**, 074023 (2007) and references therein.
[4] P. N. Meisinger and M. C. Ogilvie, Phys. Lett. **B 379**, 163 (1996); A. Mocsy, F. Sannino, and K. Tuominen, Phys. Rev. Lett. **92**, 182302 (2004);
[5] H. E. Stanley, *Introduction to phase transitions and critical phenomena*, (Clarendon Press, Oxford, 1971).
[6] M. I. Gorenstein, V. K. Petrov and G. M. Zinovjev, Phys. Lett. **B 106**, 327 (1981).
[7] K. A. Bugaev, Phys. Rev. C **76**, 014903 (2007); Phys. Atom. Nucl. **71**, 1615 (2008).
[8] K. A. Bugaev, Phys. Part. Nucl. **38**, 447 (2007).
[9] M. E. Fisher, Physics **3**, 255 (1967).
[10] J. P. Bondorf, A. S. Botvina, A. S. Iljinov, I. N. Mishustin, K. Sneppen, Phys. Rep. **257**, 131 (1995).
[11] K. A. Bugaev et al., Phys. Rev. **62** (2000); Phys. Lett. B **498**, 144 (2001).
[12] R. Hagedorn, Nuovo Cimento Suppl. **3**, 147 (1965).
[13] K. A. Bugaev, L. Phair and J. B. Elliott, Phys. Rev. E **72**, 047106 (2005); K. A. Bugaev and J. B. Elliott, Ukr. J. Phys. **52**, 301 (2007).
[14] K. A. Bugaev, V. K. Petrov and G. M. Zinovjev, arXiv:0904.4420 [hep-ph] (2009).
[15] M. E. Fisher and B. U. Felderhof, Ann. Phys. **58**, 217 (1970).
[16] A. I. Ivanytskyi, arXiv:1104.1900 [hep-ph] (2011).
[17] P. T. Reuter, K. A. Bugaev, Phys. Lett. B **517**, 233 (2001); Ukr. J. Phys. **52**, 489 (2007).

Proceedings of the International School-seminar
"New Physics and Quantum Chromodynamics at External Conditions", pp. 113 – 117,
3-6 May 2011, Dnipropetrovsk, Ukraine

ABOUT PHASE TRANSITION IN THREE-DIMENSIONAL QUANTUM ELECTRODYNAMICS AT $T \neq 0$

D. V. Kholod[a], M. Sh. Pevzner[b]

National Mining University, Dnipropetrovsk, Ukraine

Dynamic mass generation in 3D quantum electrodynamics (QED_3) is considered at $T \neq 0$. To solve the Schwinger-Dyson equation for the Matsubara electron Green's function, the ladder approximation is used and the corresponding photonic function is taken in the Landau gauge. In this case, the instanton approximation is used for the photonic function. It is established that the process of dynamical mass generation in QED_3 at $T \neq 0$ is accompanied by a phase transition. Formal analogy of transitions in the coupling constant is revealed at $T \neq 0$ in QED_3, at $T = 0$ in QED_4, and in graphene theory. Critical values of the coupling constant and temperature, calculated numerically based on an approximate analytical solution of the Schwinger-Dyson equation are of the same orders of magnitude.

1 Introduction

Three-dimensional quantum electrodynamics at $T \neq 0$ attracts more and more attention for some reasons. First, dynamical breaking of chiral symmetry that leads to mass generation for an initially massless particle is observed here [1]. Second, under certain conditions, confinement is present in QED_3, and due to comparative simplicity of the model, this phenomenon can be investigated in more detail than in quantum chromodynamics (QCD) [2, 3]. Moreover, definite analogy between QED_3 and graphene physics exists [4].

In the present work, dynamical breaking of the chiral symmetry is investigated in the QED_3 at $T \neq 0$ and the phase transition which accompanies this process and the subsequent restoration of the initial symmetry are studied. In this case, the Schwinger-Dyson equation for the Green's temperature function of a fermion in the ladder approximation with additional restrictions on the Green's photonic function is used in the Landau gauge and instanton approximation.

We proceed from the Schwinger-Dyson equation at $T \neq 0$ within the Matsubara formalism:

$$G^{(e)}(\mathbf{p}, p_{4n}) = \frac{1}{i\hat{p} + \Sigma_m(\mathbf{p}, p_{4n})}. \tag{1}$$

Here we assume that the bare fermion mass is equal to zero, $G^{(e)}(\mathbf{p}, p_{4n})$ is the total fermion propagator, $(i\hat{p})^{-l}$ is the propagator of the free massless fermion, $p_{4n} = (2n+1)\pi T$ are the Matsubara fermion frequencies, and $\Sigma_m(\mathbf{p}, p_{4n})$ is the Matsubara self energy integral of the fermion. This integral is determined by the relationship

$$\Sigma_m(\mathbf{p}, p_{4n}) = \frac{e_0^2}{(2\pi)^2} T \sum_s \int (d\mathbf{k}) \gamma_\mu G^{(e)}(\mathbf{k}, k_{4s}) \Gamma_\nu(\mathbf{p}, \mathbf{k}, p_{4n}, k_{4s}) G^{(\gamma)}_{\mu\nu}(\mathbf{p} - \mathbf{k}, p_{4n} - k_{4s}), \tag{2}$$

where e_0^2 is nonrenormalized coupling constant in QED_3, Γ_ν is the total vertex, and $G^{(\gamma)}_{\mu\nu}$ is the total photon propagator.

The self energy integral has the following structure [5, 6, 7]:

$$\Sigma(p) = i\hat{p}(F_1^{-1} - 1) + i(pu)\hat{u}F_1^{-1}F_2 + \frac{i}{2}(\hat{u}\hat{p} - \hat{p}\hat{u})F_3 + F_1^{-1}M, \tag{3}$$

where $\hat{p} = \gamma\mathbf{p} + \gamma_{4n}p_{4n}$; $(pu)\hat{u} = -\gamma_4 p_{4n}$ $(u = (0, 0, 0, i))$; F_1, F_2, F_3 and M are functions of invariant variables p^2 and (up). To conserve spatial parity, the relationship $F_3 = 0$ must be fulfilled [5]. Introduction of the vector $Q_\mu = q_\mu + (qu)u_\mu F_2$ allows us to write Eq. (1) in the form

$$G(q) = F_1(Q)(i\hat{Q} + M(Q))^{-1}. \tag{4}$$

The function M is called the mass function, and the function F_1 is the function which renormalizes the propagator.

e-mail: [a]holod_d@i.ua, [b]mark@omp.dp.ua

At zero temperature in the QED_3 with the Landau gauge in the ladder approximation, the relationships

$$F_1 = 1, F_2 = 0 \tag{5}$$

are true.

Generally speaking, at $T \neq 0$ these equalities are violated. However, for the sake of simplicity we assume below that Eq. (5) in the examined approximation is also valid at $T \neq 0$. This conceptually means that only first terms of expansion in series of the perturbation theory are taken for the functions F_1 and F_2. In principle, this approximation is enough to solve the problem on the presence or absence of the phase transition (see [8]).

As mentioned above, we consider the ladder approximation

$$\Gamma_\nu = \gamma_\nu, \;\; G^{(\gamma)}_{\mu\nu}(l) = \left(\delta_{\mu\nu} - \frac{l_\mu l_\nu}{l^2}\right)\frac{1}{l^2}. \tag{6}$$

Here $l^2 = \mathbf{l}^2 + l_4^2$, $\mathbf{l} = \mathbf{p} - \mathbf{k}$, $l_4 = p_{4n} - k_{4s}$ and $l_\mu = (\mathbf{l}, l_4)$. In this approximation, the Schwinger-Dyson equation for the mass function has the form

$$M(\mathbf{p}, p_{4n}) = \frac{2e_0^2}{(2\pi)^2} T \sum_{s=-\infty}^{+\infty} \int \frac{(d\mathbf{k})}{\mathbf{k}^2 + k_{4s}^2 + M^2(\mathbf{k}, k_{4s})} \frac{M(\mathbf{k}, k_{4s})}{(\mathbf{p}-\mathbf{k})^2 + (p_{4n} - k_{4s})^2}. \tag{7}$$

In addition, the instanton approximation, in which $p_{4s} - k_{4s} = 0$ can be set, is used. We also neglect the dependence of the mass function on k_{4s} on the right side of Eq. (7). It can be demonstrated that this is equivalent to the choice of a certain spectral density for the part of the Matsubara fermion Green's function even in γ-matrices [9, 10, 11].

Under above assumptions, the right side of Eq. (7) can be summed over s. After summation and integration of this equation over the angle, we obtain the following equation for the mass function:

$$M(p) = \frac{e_0^2}{2\pi} \int_0^{+\infty} k dk \frac{\tanh(\varepsilon/2T)}{\varepsilon} M(k) \left(\frac{\theta(p-k)}{p^2} \sum_{n=0}^{\infty} (k/p)^{2n} + \frac{\theta(k-p)}{k^2} \sum_{n=0}^{\infty} (p/k)^{2n} \right), \tag{8}$$

where $\varepsilon = \sqrt{M^2(k) + k^2}$. This equation is the key relationship of the present work. Obviously, it has zero solution with the chiral symmetry. In this regard, the problem of existence of nonzero solutions arises for this equation, which can lead to possible breaking of the chiral symmetry. To solve this problem is the purpose of the present work.

2 Approximate analytical solution

Since the process of symmetry breaking is essentially nonpertubative, to seek for nonzero solutions of Eq. (8), we must take advantage of the methods which are not based on the perturbation theory. At the same time, this equation is still too complicated to investigate it analytically. Therefore, it must be simplified. These simplifications are the following.

Only first terms of the series are considered in the integrand on the right side of Eq. (8):

$$M(p) = \frac{e_0^2}{2\pi} \int_0^{+\infty} k dk \frac{\tanh(\varepsilon/2T)}{\varepsilon} M(k) \left(\frac{\theta(p-k)}{p^2} + \frac{\theta(k-p)}{k^2} \right). \tag{9}$$

Moreover, we assume that $M \ll k \ll T$. The first restriction means that in the vicinity of the critical value of the parameter which describes the phase transition, the mass function is supposed to be very small that corresponds to the so-called bifurcation approximation, and the second restriction means that the temperature is a cutoff factor. Below we demonstrate that this leads to the formal analogy of the phase transition in the coupling constant in QED_4, graphene theory at $T = 0$ and the corresponding transition in QED_3 at $T \neq 0$.

Considering this, we set $\varepsilon \approx k$ and $\tanh(\varepsilon/2T) \approx \tanh(k/2T) \approx k/2T$. Then Eq. (9) assumes the form

$$M(p) = \frac{\lambda}{4\pi} \left(\frac{1}{p^2} \int_m^p k M(k) dk + \int_p^T \frac{1}{k} M(k) dk \right), \tag{10}$$

where $\lambda = e_0^2/T$. Moreover, the parameter of infrared cutoff m dependent on the temperature plays the role of the Euclidian dynamic fermion mass determined by the normalization condition $M(m) = m$.

Equation (10) is equivalent to the differential equation

$$p^2 M'' + 3pM' + \frac{\lambda}{2\pi} M = 0 \tag{11}$$

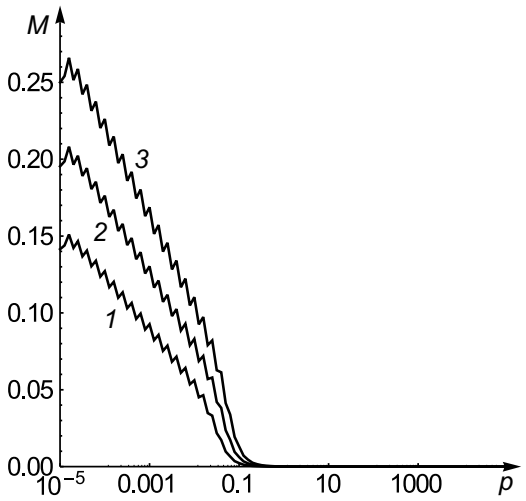

Figure 1. Dependence of the mass function on the momentum obtained by numerical solution of Eq. (8). $T = 0.01$ and $\alpha = 0.015$ (curve *1*), 0.02 (curve *2*), and 0.025 (curve *3*).

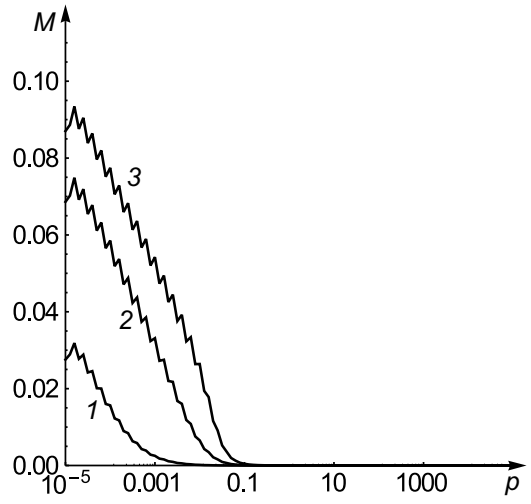

Figure 2. Dependence of the mass function on the momentum obtained by numerical solution of Eq. (8). $\alpha = 0.01$ and $T = 0.0175$ (curve *1*), 0.015 (curve *2*), and 0.01 (curve *3*).

with the boundary conditions

$$\left(p^2 M(p)\right)'\Big|_{p=T} = 0, \tag{12}$$

$$\left(p^3 M'(p)\right)\Big|_{p=m} = 0. \tag{13}$$

We note that the same equation can also be met in graphene physics [4].

The general solution of Eq. (11) has the form

$$M(p) = \frac{1}{p}\left(C_1 p^{\nu} + C_2 p^{-\nu}\right), \tag{14}$$

where $\nu = \sqrt{1 - \frac{\lambda}{2\pi}}$. Substituting Eq. (14) into Eqs. (12) and (13), we obtain the system of equations for the constants C_1 and C_2:

$$\begin{cases} (1+\nu)T^{\nu}C_1 + (1-\nu)T^{-\nu}C_2 = 0, \\ (1-\nu)m^{\nu+1}C_1 + (1+\nu)m^{1-\nu}C_2 = 0. \end{cases} \tag{15}$$

This system has nontrivial solutions when its determinant is equal to zero, that is, when

$$\begin{vmatrix} (1+\nu)T^{\nu} & (1-\nu)T^{-\nu} \\ (1-\nu)m^{\nu+1} & (1+\nu)m^{1-\nu} \end{vmatrix} = 0. \tag{16}$$

Considering that we work within the framework of the bifurcation approximation, the solution of Eq. (16) for the mass must satisfy the condition $m \ll T$. This relationship is fulfilled only if the coupling constant and temperature satisfy the condition $e_0^2/(2\pi T) > 1$. Then

$$m \approx 7.4T \cdot e^{-\pi n/|\nu|},\ n \in N, \tag{17}$$

where

$$|\nu| = \sqrt{\frac{e_0^2}{2\pi T} - 1}. \tag{18}$$

Thus, we observe the formal analogy with the phase transition in the charge in QED_4 and in graphene theory at $T = 0$ [4, 12, 13, 14] if we consider that the temperature here plays the role of the cutoff parameter and $e_0^2/(2\pi T)$ is the critical parameter.

We now distinguish the following cases: a) when the temperature T is fixed; then the mass generation must be considered as the phase transition in the coupling constant with the critical value $e_{0cr}^2 = 2\pi T$; b) when the coupling constant is fixed; then the mass generation occurs at the temperature satisfying the relation $T < e_0^2/(2\pi)$ with the critical value $T_{cr} = e_0^2/(2\pi)$.

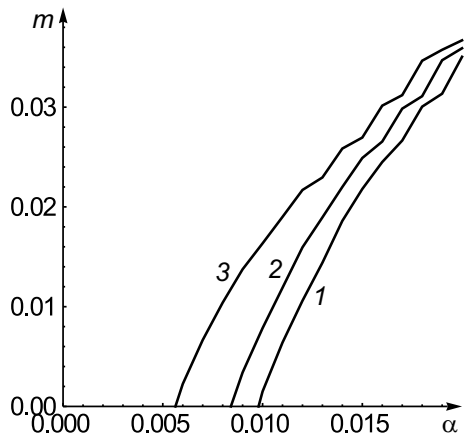

Figure 3. Dependence of m on α at fixed values of T calculated by numerical solution of Eq. (8).

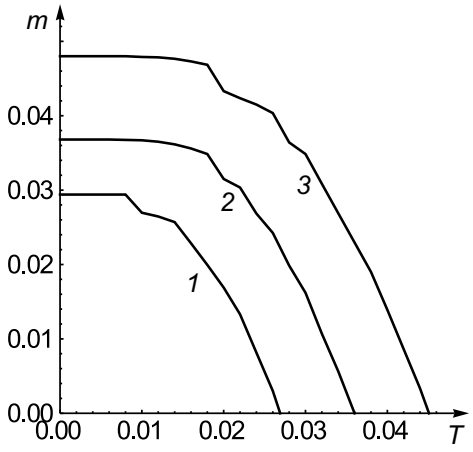

Figure 4. Dependence of m on T at fixed values of α calculated by numerical solution of Eq. (8).

3 Numerical solution

Below we present the results of solving this problem based on numerical solution of Eq. (8). The results of calculations for the indicated values $\alpha = e_0^2/(2\pi)$ and T are shown in Fig. 1, 2.

Thus, the results of numerical solution confirm our conclusion on dynamic breaking of the chiral symmetry. In numerical calculations, we considered the following cases: a) when the temperature T was fixed, b) when the coupling constant α was fixed.

In case *a*, we calculated the dependence of m derived from the relationship $M(p = m) = m$ on the coupling constant α. This dependence is shown in Fig. 3 at $T = 0.0175$ (curve *1*), 0.015 (curve *2*) and 0.01 (curve *3*). From Fig. 3 it can be seen that the mass is generated for this model only when the coupling constant α exceeds its critical values $\alpha_{cr1} = 0.00980$, $\alpha_{cr2} = 0.00841$ and $\alpha_{cr3} = 0.00563$.

In case *b*, the dependence of m on the temperature T was calculated. This dependence is shown in Fig. 4 for $\alpha = 0.015$ (curve *1*), 0.02 (curve *2*) and 0.025 (curve *3*). From Fig. 4 it can be seen that the mass is generated for our model only when the temperature T does not exceed its critical values $T_{cr1} = 0.0269$, $T_{cr2} = 0.0360$ and $T_{cr3} = 0.0451$.

Thus, the numerical study of Eq. (8) confirms our conclusion about the presence of the phase transition which accompanies the mass generation for the model examined based on the approximate analytical study performed in Section 2. In this case, the ratios of the critical values which describe this process have the following values. Case *a*: $(\alpha/T)_{cr1} = 0.560$, $(\alpha/T)_{cr2} = 0.561$, $(\alpha/T)_{cr3} = 0.563$; case *b*: $(\alpha/T)_{cr1} = 0.558$, $(\alpha/T)_{cr2} = 0.556$, $(\alpha/T)_{cr3} = 0.554$; from Eqs. (17) and (18) it follows that $(\alpha/T)_{cr} = 1$. Considering the roughness of the approximation used for analytical calculations and the fact that the results obtained coincide by the orders of magnitude with the results of numerical investigations, the coincidence level of these results can be considered satisfactory.

4 Conclusions

Here the dynamic mass generation in QED_3 has been considered for nonzero temperatures. While solving the Eq. (2) for the Matsubara electron Green's function, the approximations mentioned in introduction were used. Our investigations demonstrated the presence of the phase transition which accompanied the process of the dynamic mass generation in QED_3 at nonzero temperature. The formal analogy between the phase transition in the coupling constant in QED_4 and graphene physics was established at $T = 0$ on the one hand and in QED_3 at $T \neq 0$ on the other hand. Initial equation (8) was examined analytically with the use of some additional assumptions and then solved. In both cases, the orders of magnitude of the results obtained coincided. At the same time, our numerical investigation demonstrated that from all solutions of Eq. (17) corresponding to different n values, only one is realized, whereas the remaining ones are artifacts of the approximation.

We plan further to go beyond the limits of these approximations, in particular, beyond the limits of the instant approximation and consider the vacuum polarization and the contribution of radiative corrections to the vertex.

References

[1] V.P. Gysynin, A.W. Schreiber, A.W. Sizer and A.G. Williams, Phys. Rev. D **60**, 065007 (1999).
[2] P. Maris, Phys. Rev. D **52**, 6087 (1995).
[3] M.Sh. Pevzner, hep-ph/0210235.
[4] E.V. Gorbar, V.P. Gusynin, V.A. Miransky and J.A. Shovkovy, Phys. Rev. B **66**, 045108 (2002).
[5] A. Ayala and A. Bashir, Phys. Rev. D **67**, 076005 (2003).
[6] O.K. Kalashnikov, Pis'ma Zh. Eksp. Teor. Fiz., **41**, 447 (1985).
[7] O.K. Kalashnikov, Pis'ma Zh. Eksp. Teor. Fiz., **41**, 122 (1985).
[8] L.D. Landau and E.M. Lifshits, *Theoretical Physics. Vol. 9, Statistical Physics [in Russian]*, (Moscow, Nauka, 1978).
[9] V.L. Ginzburg and D.A. Kirzhnits, eds., *Problems in High-Temperature Superconductivity [in Russian]*, (Moscow, Nauka, 1977).
[10] M.Sh. Pevzner, *Nonperturbative Quantum Electrodynamics at $T \neq 0$*, (Kiev, Preprint/ITP-84-50E, 1991).
[11] M.Sh. Pevzner, Ukr. Fiz. Zh., **40**, 1042 (1995).
[12] T. Maskawa and H. Nakajima, Progr. Theor. Phys., **52**, 1326 (1974).
[13] R. Fukuda and T. Kugo, Nucl. Phys., B **117**, 250 (1976).
[14] P.I. Fomin, V.P. Gusynin, V.A. Miransky and Yu.A. Sitenko, Rev. Nuovo Cimento, **6**, 1 (1983).

Proceedings of the International School-seminar
"New Physics and Quantum Chromodynamics at External Conditions", pp. 118 – 121,
3-6 May 2011, Dnipropetrovsk, Ukraine

OBSERVABLE QUANTITIES IN KINETICS OF ELECTROMAGNETIC FIELD IN MEDIUM

S. F. Lyagushyn[a], A. I. Sokolovsky[b], Yu. M. Salyuk

Dnipropetrovsk National University, Dnipropetrovsk, Ukraine

The problem of parameters, which are necessary for nonequilibrium electromagnetic field description, is a key one for building the field kinetics whenever it is under discussion. This problem is investigated on the basis of the Bogolyubov reduced description method leading to the conclusion about the necessity of binary correlations in the minimal set of parameters taken into account in evolution equations. The corresponding theory can be built in terms of one-particle density matrices, Wigner distribution functions, and conventional simultaneous correlation functions of field operators. Rather different correlation functions are determined in measurements based on the coincidence scheme using quantum detectors and regarded as a basis for algebra of observables in quantum optics. Various approaches in theoretical and experimental research into field correlations are compared in the present paper.

1 Introduction

Quantum electromagnetic theory supposes using averages of operator dynamic variables for field state specification and experimental result analysis. A statistical operator gives the most general description of field states, but from the point of view of experiments only reduced description of electromagnetic fields is possible. The field kinetics embraces a number of physical theories such as electrodynamics of continuous media, radiation transfer theory, magnetic hydrodynamics, and quantum optics. In all the cases it is necessary to choose physical quantities providing an adequate picture of nonequilibrium processes after transfer to averages. In our previous investigations several approaches to the construction of kinetic equations have been outlined. Obviously, the choice depends on traditions and visibility of phenomenon description. All the methods can be connected due to relatively simple relations expressing their key quantities through one another. At the same time quantum optics introducing non-simultaneous correlation functions requires additional efforts for using the results obtained in the reduced description scheme.

2 Reduced description and necessary set of field parameters

The Bogolyubov reduced description method [1] can be a basis for the general consideration of the problem. Its starting point in this approach is a quantum Liouville equation for the statistical operator $\rho(t)$ of a system including electromagnetic field (subsystem f) and a medium (subsystem m)

$$\partial_t \rho(t) = -\frac{i}{\hbar}[\hat{H}, \rho(t)] \qquad (\hat{H} = \hat{H}_{\rm f} + \hat{H}_m). \tag{1}$$

The method is based on the functional hypothesis describing a structure of the operator $\rho(t)$ at long times

$$\rho(t) \xrightarrow[t \gg \tau_0]{} \rho(\gamma(t, \rho_0), \eta(t, \rho_0)) \qquad (\rho_0 \equiv \rho(t=0)) \tag{2}$$

where reduced description parameters of field $\gamma_\mu(t, \rho_0)$ and matter $\eta_a(t, \rho_0)$ are used. The complex of parameters $\gamma_\mu(t, \rho_0)$ is determined by the possibilities and traditions of experiments as well as by theoretical considerations. The development of the problem investigations has resulted in finding the main approximation for the statistical operator $\rho(\gamma, \eta)$, so called a quasi-equilibrium statistical operator $\rho_q(Z(\gamma), Z(\eta))$(though it describes states which are far from the equilibrium) defined by the relations

$$\rho_q(Z, Z_m) = \rho_{\rm f}(Z)\rho_m(Z_m);$$

$$\rho_{\rm f}(Z) = \exp\{\Phi(Z) - \sum_\mu Z_\mu \hat{\gamma}_\mu\}, \qquad {\rm Sp}_{\rm f}\rho_{\rm f}(Z) = 1, \quad {\rm Sp}_{\rm f}\rho_{\rm f}(Z(\gamma))\hat{\gamma}_\mu = \gamma_\mu;$$

$$\rho_m(X) = \exp\{\Omega(X) - \sum_a X_a \hat{\eta}_a\}; \qquad {\rm Sp}_m\rho_m(X) = 1, \qquad {\rm Sp}_m\rho_m(X(\eta))\hat{\eta}_a = \eta_a. \tag{3}$$

e-mail: [a]lyagush@dsu.dp.ua, [b]alexsokolovsky@mail.ru

Practically all the electrodynamics of continuous media operates with average values of electromagnetic field $E_n(x,t)$, $B_n(x,t)$ (hereafter we omit the dependence of reduced description parameters on an initial statistical operator ρ_0 of the system for simplicity). So corresponding operators $\hat{E}_n(x)$, $\hat{B}_n(x)$ are chosen as the operators $\hat{\gamma}_\mu$. In Coulomb gauge the following expressions can be used for them:

$$\hat{E}_n(x) = i\sum_{\alpha k}\frac{(2\pi\hbar\omega_k)^{1/2}}{V^{1/2}}e_{\alpha k n}(c_{\alpha k} - c^+_{\alpha,-k})e^{ikx},$$

$$\hat{B}_n(x) = i\sum_{\alpha k}\frac{(2\pi\hbar\omega_k)^{1/2}}{V^{1/2}}\varepsilon_{nlm}\tilde{k}_l e_{\alpha k m}(c_{\alpha k} + c^+_{\alpha,-k})e^{ikx} \tag{4}$$

with standard notations of quantum electrodynamics. Nevertheless in paper [2] it has been pointed out that for this choice of operators $\hat{\gamma}_\mu$ the statistical operator $\rho_{\rm f}(Z)$ does not exist because of containing a linear form on Bose field operators $c_{\alpha k}$, $c^+_{\alpha k}$ in the exponent. The situation can be corrected with the availability of a quadratic form of the operators in the exponent; hence the statistical operator has a structure

$$\rho_{\rm f}(Z) = \exp\{\Phi(Z) - \sum_{\alpha k,\alpha' k'} Z^{\alpha\alpha'}_{kk'} c^+_{\alpha k} c_{\alpha' k'} - (\sum_{\alpha k,\alpha' k'} \tilde{Z}^{\alpha\alpha'}_{kk'} c^+_{\alpha k} c^+_{\alpha' k'} + \sum_{\alpha k} Z^\alpha_k c^+_{\alpha k} + h.c.)\}. \tag{5}$$

In fact, it means that the minimal set of reduced description parameters of electromagnetic field contains its binary fluctuations (correlations) besides its average strength though the average field can be absent.

3 Various approaches to constructing the kinetic equations with binary correlation account

In order to describe binary fluctuations of the field, normal $n^{\alpha\alpha'}_{kk'}(t) = {\rm Sp}\rho(t)c^+_{\alpha k}c_{\alpha' k'}$ and anomalous $\tilde{n}^{\alpha\alpha'}_{kk'}(t) = {\rm Sp}\rho(t)c_{\alpha k}c_{\alpha' k'}$ one-particle density matrices can be used (a T-1 theory) as well as connected with them normal $\mathrm{f}^{\alpha\alpha'}_k(x,t) = {\rm Sp}\rho(t)\hat{\mathrm{f}}^{\alpha\alpha'}_k(x)$ and anomalous $\tilde{\mathrm{f}}^{\alpha\alpha'}_k(x,t) = {\rm Sp}\rho(t)\hat{\tilde{\mathrm{f}}}^{\alpha\alpha'}_k(x)$ Wigner distribution functions (WDF) (a T-2 theory) where

$$\hat{\mathrm{f}}^{\alpha\alpha'}_k(x) = \sum_q c^+_{\alpha,k-q/2}c_{\alpha',k+q/2}e^{iqx}, \quad \hat{\tilde{\mathrm{f}}}^{\alpha\alpha'}_k(x) = \sum_q c_{\alpha,k+q/2}c_{\alpha',-k+q/2}e^{iqx}. \tag{6}$$

The anomalous density matrix and WDF are absent in a state with the statistical operator $\rho_{\rm f}(Z)$ at $\tilde{Z}^{\alpha\alpha'}_{kk'} = 0$ and average electromagnetic field equals zero at $Z^\alpha_k = 0$. The terminology "normal-anomalous" is connected with the concept of spontaneous break of symmetry, at that from this point of view a nonzero average field value is also a consequence of some symmetry breakdown.

Electromagnetic field fluctuations can be described also with average values of field operators

$$\langle E^x_n E^{x'}_l\rangle_t = {\rm Sp}\rho(t)\hat{E}_n(x)\hat{E}_l(x'), \quad \langle B^x_n B^{x'}_l\rangle_t = {\rm Sp}\rho(t)\hat{B}_n(x)\hat{B}_l(x'),$$

$$\langle E^x_n B^{x'}_l\rangle_t = \frac{1}{2}{\rm Sp}\rho(t)\{\hat{E}_n(x), \hat{B}_l(x')\}, \tag{7}$$

or corresponding correlation functions $(E^x_n E^{x'}_l)_t$, $(B^x_n B^{x'}_l)_t$, $(E^x_n B^{x'}_l)_t$ (a T-3 theory). The unique relationship of such theories proceeds from the formulas (5) and their consequence

$$c_{\alpha k} = (8\pi\omega_k\hbar V)^{-1/2}\int d^3x\{\hat{Z}_n(x)/k - \hat{E}_n(x)\}e^{ikx} \qquad (\hat{Z}_n(x) \equiv {\rm rot}_n\hat{B}(x)). \tag{8}$$

T-2 and T-3 theories allow describing a spatial behavior of the electromagnetic field in medium. Temporal equations for one-particle density matrices and Wigner distribution functions are called kinetic equations for photons in medium.

In the paper [3] a theory of T-1 type has been built for electromagnetic field in equilibrium plasma medium. The corresponding kinetic equation has a form

$$\partial_t g^{\alpha\alpha'}_{kk'} = i(\tilde{\omega}_k - \tilde{\omega}_{k'})g^{\alpha\alpha'}_{kk'} - (\nu_k + \nu_{k'})(g^{\alpha\alpha'}_{kk'} - n_k\delta_{\alpha\alpha'}\delta_{kk'}),$$

$$\partial_t x_{\alpha k} = -(i\tilde{\omega}_k + \nu_k)x_{\alpha k} + (\nu_k + i\omega_k\chi_k)x^*_{\alpha,-k} \tag{9}$$

where

$$g^{\alpha\alpha'}_{kk'}(t) = n^{\alpha\alpha'}_{kk'}(t) - x^*_{\alpha k}(t)x_{\alpha' k'}(t), \quad x_{\alpha k}(t) = {\rm Sp}\rho(t)c_{\alpha k};$$

$$\tilde{\omega}_k = \omega_k(1 - 2\pi\chi_k), \quad \nu_k = 2\pi\sigma_k \tag{10}$$

($\tilde{\omega}_k$ is a photon spectrum in the medium, n_k is Planck distribution with a medium temperature). The second equation (11) is actually a Maxwell equation with account of a material equation, at that σ_k and χ_k are conductivity and magnetic susceptibility of the medium expressed via the Green function of currents. In terms of WDF in the case of weak nonuniformity of a system state such kinetic equation takes the form

$$\partial_t \mathrm{f}_k^{\alpha\alpha'} = -\frac{\partial\tilde{\omega}_k}{\partial k_n}\frac{\partial \mathrm{f}_k^{\alpha\alpha'}}{\partial x_n} + \frac{1}{4}\frac{\partial^2\nu_k}{\partial k_n \partial k_l}\frac{\partial^2 \mathrm{f}_k^{\alpha\alpha'}}{\partial x_n \partial x_l} - 2\nu_k(\mathrm{f}_k^{\alpha\alpha'} - n_k\delta_{kk'}\delta_{\alpha\alpha'}). \tag{11}$$

4 Kinetics of electromagnetic field interacting with nonequilibrium system of emitters

In our previous papers (see [4]) electrodynamics in a medium consisting of two-level emitters has been built. Such a theory emerges in the course of research into the Dicke superfluorescence [5] on the basis of the Bogolyubov reduced description method. A standard approach lies in the framework of a theory of T-3 type. Emitter subsystem is regarded as non-uniform and it is convenient to describe it with a density of emitter energy

$$\hat{\varepsilon}(x) = \hbar\omega\sum_a \hat{r}_{az}\delta(x - x_a) \tag{12}$$

Operators of the reduced description parameters of the system in the developed theory are $\hat{\varepsilon}(x)$, $\hat{\gamma}_\mu$

$$\hat{\gamma}_\mu: \qquad \hat{E}_n^t(x), \quad \hat{B}_n(x), \quad \frac{1}{2}\{\hat{E}_n^t(x), \hat{E}_l^t(x')\}, \quad \frac{1}{2}\{\hat{E}_n^t(x), \hat{B}_l(x')\}, \quad \frac{1}{2}\{\hat{B}_n(x), \hat{B}_l(x')\}.$$

Maxwell equations in terms of averages has the form

$$\partial_t E_n(x,t) = c\,\mathrm{rot}_n B(x,t) - 4\pi J_n(x, \varepsilon(t), \gamma(t)), \qquad \partial_t B_n(x,t) = -c\,\mathrm{rot}_n E(x,t) \tag{13}$$

with a material equation

$$J_n(x,\varepsilon,\gamma) = \int dx'\sigma(x-x',\varepsilon(x))E_n(x') + c\int dx'\chi(x-x',\varepsilon(x))Z_n(x') \qquad (Z_n(x,t) \equiv \mathrm{rot}_n B(x,t)) \tag{14}$$

where Fourier transforms of functions $\sigma(x,\varepsilon)$, $\chi(x,\varepsilon)$ are conductivity $\sigma_k(\varepsilon)$ and magnetic susceptibility $\chi_k(\varepsilon)$ of the system. Equations for field correlations acquire the form

$$\begin{aligned}
\partial_t(E_n^x E_l^{x'}) &= c\,\mathrm{rot}_n(B^x E_l^{x'}) + c\,\mathrm{rot}'_l(E_n^x B^{x'}) - 4\pi(J_n^x E_l^{x'}) - 4\pi(E_n^x J_l^{x'}),\\
\partial_t(E_n^x B_l^{x'}) &= c\,\mathrm{rot}_n(B^x B_l^{x'}) - c\,\mathrm{rot}'_l(E_n^x E^{x'}) - 4\pi(J_n^x B_l^{x'}),\\
\partial_t(B_n^x E_l^{x'}) &= -c\,\mathrm{rot}_n(E^x E_l^{x'}) + c\,\mathrm{rot}'_l(B_n^x B^{x'}) - 4\pi(B_n^x J_l^{x'}),\\
\partial_t(B_n^x B_l^{x'}) &= -c\,\mathrm{rot}_n(E^x B_l^{x'}) - c\,\mathrm{rot}'_l(B_n^x E^{x'}).
\end{aligned} \tag{15}$$

Current-field correlations are expressed via field correlations by material equations obeying the Onsager principle.

5 Power fluxes in medium and correlation functions

In the theory of energy transfer power fluxes in medium is a problem of interest. An operator of power flux is given by the formula

$$\hat{q}_n(x) = \frac{c}{8\pi}\varepsilon_{nlm}\{\hat{E}_l(x), \hat{B}_m(x)\}. \tag{16}$$

According to the reduced description method, in the theory taking into account only binary field correlations exact averages of binary field functions are determined by the quasi-equilibrium field distribution. Therefore the power flux is expressed exactly via one-particle density matrix or WDF. For example, if the average field is absent, we come to an exact formula

$$q_n(x) = \frac{1}{V}\sum_{kq,\alpha\alpha'} n^{\alpha\alpha'}_{k-q/2,k+q/2}\varphi_n^{\alpha\alpha'}(k,q)e^{iqx} = \frac{1}{V}\sum_{k,\alpha\alpha'}\varphi_n^{\alpha\alpha'}(k, -i\frac{\partial}{\partial x})\mathrm{f}_k^{\alpha\alpha'}(x) \tag{17}$$

where the notation is used

$$\varphi_n^{\alpha\alpha'}(k,q) = (\delta_{nl}\delta_{ms} - \delta_{ml}\delta_{ns})\frac{\hbar c^2}{2}(k_1k_2)^{1/2}\{\tilde{k}_{1l}e^*_{\alpha k_1 s}e_{\alpha' k_2 m} + \tilde{k}_{2l}e^*_{\alpha k_1 m}e_{\alpha k_2 s}\}_{k_1=k-q/2,\ k_2=k+q/2}. \tag{18}$$

In a weakly non-uniform state this formula leads in a well-known elementary result

$$q_n(x) = \frac{1}{V}\sum_{k\alpha}\omega_k\hbar c\tilde{k}_n \mathrm{f}_k^{\alpha\alpha}(x). \tag{19}$$

6 Field correlation properties in quantum optics

The most general approach of quantum optics to the statistical properties of light is based on the technique of photon counting and the concept of an ideal quantum detector. Its operation analysis by Glauber [6] has led to the conclusion that the rate of photon counting is proportional to the local value of the field correlation function of the first order (the polarization properties are neglected)

$$p(t) \sim G^{1,1}(x,t;x,t) = \langle \hat{E}^{(-)}(x,t)\hat{E}^{(+)}(x,t)\rangle \equiv \mathrm{Sp}\{\rho\hat{E}^{(-)}(x,t)\hat{E}^{(+)}(x,t)\} \tag{20}$$

The quantum-statistical averaging is executed with the statistical operator of field $\hat{\rho}$ and deals with positive-frequency and negative-frequency parts of the electric field operator (4) in the interaction picture:

$$\hat{E}_n(x,t) = \hat{E}_n^{(+)}(x,t) + \hat{E}_n^{(-)}(x,t) \tag{21}$$

where

$$\hat{E}_n^{(+)}(x,t) \equiv i\sum_{k\alpha}\frac{(2\pi\hbar\omega_k)^{1/2}}{V^{1/2}}e_{\alpha kn}c_{\alpha k}e^{i(kx-\omega_k t)}, \qquad \hat{E}_n^{(-)}(x,t) = \hat{E}_n^{(+)}(x,t)^{\dagger}. \tag{22}$$

In quantum optics properties of the electromagnetic field are discussed in terms of correlation functions of the form

$$G^{ss'}_{n_1\ldots n_s,l_1\ldots l_{s'}}(y_1\ldots y_s,y'_1\ldots y'_{s'}) \equiv \mathrm{Sp}\{\rho\hat{E}^{(-)}_{n_1}(y_1)\ldots\hat{E}^{(-)}_{n_s}(y_s)\hat{E}^{(+)}_{l_1}(y'_1)\ldots\hat{E}^{(+)}_{l_{s'}}(y'_{s'})\} \tag{23}$$

where $y \equiv (x,t)$ [7]. Experiments of the second order (for example, the Hunbury-Brown-Twiss scheme based on photon detection coincidence) determine correlation functions of the type

$$G^{(2,2)}_{nl,ms}(y_1,y_2,y_3,y_4) \equiv \mathrm{Sp}\{\rho\hat{E}^{(-)}_n(y_1)\hat{E}^{(-)}_l(y_2)\hat{E}^{(+)}_m(y_3)\hat{E}^{(+)}_s(y_4)\} \tag{24}$$

Note that correlation functions of the first order can be expressed through the one-particle density matrix $n^{\alpha\alpha'}_{kk'}$ exactly

$$G^{(1,1)}_{nl}(x_1,t_1;x_2,t_2) = \frac{2\pi\hbar c}{V}\sum_{k_1\alpha_1k_2\alpha_2}\sqrt{k_1k_2}e^{*}_{\alpha_1k_1n}e_{\alpha_2k_2l}n^{\alpha_1\alpha_2}_{k_1k_2}e^{i(\omega_{k_1}t_1-k_1x_1)}e^{-i(\omega_{k_2}t_2-k_2x_2)} \tag{25}$$

and those of the second order can be expressed through it only approximately. The most interesting quantum correlation effects (such as photon antibunching, squeezing, sub-Poissonian statistics) are described with correlation functions concerning different time moments [7].

7 Conclusions

Kinetic theory of electromagnetic field in media has choosing a set of parameters describing nonequilibrium states of the field as a starting point with necessity. The minimal set of such parameters includes binary correlations of field amplitudes. The corresponding mathematical apparatus uses different structures of averages: one-particle density matrices, Wigner distribution functions, and conventional simultaneous correlation functions of field operators. All approaches can be connected with each other due to the possibility of expressing the main correlation parameters in various forms. The reduced description method elucidates the construction of kinetic equations in electrodynamics of continuous media (plasma, complex of two-level emitters) and radiation transfer theory. Simultaneous correlation functions the method deals with are insufficient for the description of time-correlation properties investigated by quantum optics.

Acknowledgements. This work was supported in part by the State Foundation of Fundamental Research of Ukraine under project 25.2/102.

References

[1] A.I. Akhiezer, S.V. Peletminsky, *Methods of Statistical Physics*, (London, Pergamon Press, 1981).
[2] S.V. Peletminsky, V.I. Prikhod'ko, and V.S. Shcholokov, Theor. Math. Phys. **25**, 70 (1975) (in Russian).
[3] A.I. Sokolovsky, A.A. Stupka, Visnyk Kharkivskoho Universytetu, Series: Nuclei, particles, fields **3(25)**, 97 (2004) (in Ukrainian).
[4] S.F. Lyagushyn., A.I. Sokolovsky, Physics of Particles and Nuclei **41**, 1035 (2010).
[5] N.N. Bogolyubov (Jr.), A.S. Shumovsky, *Superradiance*, (Dubna, JINR, 1987), (in Russian).
[6] R.J.Glauber, Optical coherence and photon statistics, in *Quantum Optics and Electronics*, ed. C.DeWitt, A. Blandin, C. Cohen-Tannoudji,, (New York, 1964).
[7] M.O. Scully, M.S. Zubairy, *Quantum Optics*,(Cambridge University Press, 1997).

Proceedings of the International School-seminar
"New Physics and Quantum Chromodynamics at External Conditions", pp. 122 – 125,
3-6 May 2011, Dnipropetrovsk, Ukraine

EFFECTIVE THREE-PHOTON VERTEX IN A DENSE FERMIONIC MEDIUM

E. V. Reznikov[a] V. V. Skalozub[b],

Dnipropetrovsk National University, Dnipropetrovsk, Ukraine

The tensor of an effective three-photon vertex has been calculated in the one-loop approximation for a medium with non-zero chemical potential. The tensor properties at various photon wavelengths and frequencies have been analyzed. The case of photon scattering by a magnetic field has been studied in detail. Possible applications of the results obtained have been discussed.

1 Introduction

Physical vacuum is an object of quantum-mechanical origin. A lot of effects resulting from just this origin have been theoretically calculated and experimentally measured more than fifty years ago. First of all, it is the Casimir effect [1], which, being a macroscopic manifestation of quantum-mechanical processes in vacuum, is not only an important correction to the theories of Universe's and elementary particle structures, but also has practical applications. Quantum-mechanical effects in vacuum are responsible for processes that violate the superposition principle; in particular, these are light-by-light scattering, Delbrück scattering, and others [2, 3].

Interaction of an electromagnetic field through vacuum is described by means of Feynman diagrams with an even number of photon lines, the so-called two-photon vertices. The existence of unpaired vertices in vacuum is forbidden by the Furry theorem [4]. An introduction of even small number of particles into vacuum makes only quantitative, but not qualitative corrections to the process of photon–photon interaction. Such a situation takes place, as far as the chemical potential in the system is less than the particle rest energy, i.e. the medium formed by the particles can be considered rarefied.

However, the description of the behavior of photons and an electromagnetic field in a dense fermionic medium requires that Feynman diagrams with an odd number of external photon lines should be included as well. It is so, because, provided that the medium is dense, the C-parity becomes broken: and, in this connection, the conditions for the Furry theorem are not satisfied. As a result, unpaired photon vertices may exist. So, for the description of fields in a dense medium to be correct, the application of, e.g., the tensor of a three-photon vertex is necessary in principle, because it dominates as $\mu \to \infty$ and allows new, quite specific physical processes to run.

In works [5, 6, 7], the tensor of a three-photon vertex function was studied in the static-field approximation. The main results of those researches consist, first of all, in the substantiation of the essential non-conservation of vertex transversality, provided that the Feynman parametrization is used. The obtained characteristic features in the behavior of electromagnetic fields in the presence of a dense medium are also of importance. However, in this approximation, all effects stemming from the existence of a nonzero three-photon vertex can be observed only immediately from inside the medium itself. Namely, it is a very difficult task to observe the manifestations of the nonlinear behavior of an electromagnetic field as a result of quantum-mechanical effects in the medium in the static case in accessible experiments, because those manifestations are weak and indirect.

In this work, the three-photon vertex in a dense medium is studied. As a dense medium, a set of fermions is meant, for which the chemical potential μ is higher than the rest energy m. In particular, they may be electrons at moderate densities, baryons, and even quarks in the deconfinement phase. Not only static fields are studied, but also slowly changing ones, for which the inequality $\frac{k_4}{\sqrt{\mu^2-m^2}} < 1$, where k_4 is the photon frequency, is considered to be satisfied. This approximation is sufficient for many applications, because the high-frequency fields do not "feel" the medium, and the corresponding vertices are suppressed in the case of large k_4's. The attractiveness of this approximation as a research tool consists in that it describes the processes forbidden in the absence of a medium. The results of this work can be applied in the NICA and FAIR projects (where collisions between heavy nuclei are studied) to reliably and directly detect the very fact of the formation of a dense fermionic matter and to study the matter properties.

e-mail: [a]reznikovevgenii@mail.ru, [b]skalozubv@daad-alumni.de

2 Three-photon Vertex in the Static-field Case

In this section, we aim at calculating the nonzero components of the three-photon vertex tensor in a medium; they exist in the one-loop approximation for the state of rest at zero temperature. In a $(3+1)$-dimensional space, this case was examined in more details in work [6]. In case of static fields, the form of the vertex function becomes considerably simpler, with only the following tensor components remaining nonzero:

$$\Pi_{444} = \frac{ie^3}{2\pi^3}(4\sum_{i=1}^{3} J_2(k^{(i)}) + \sum_{n=1,n\neq l}^{3}\sum_{l=1}^{3} J_1(k^{(l)},k^{(n)})((k^{(l)})^2 + (k^{(n)})^2 + (k^{(l)},k^{(n)}) - 4m^2) - 4J_3(k^{(l)},k^{(n)})), \quad (1)$$

$$\Pi_{ij4} = \frac{ie^3}{2\pi^3}\left(\sum_{n=1,n\neq l}^{3}\sum_{l=1}^{3} J_1(k^{(l)},k^{(n)})(k_j^{(1)}k_i^{(3)} - (k^{(1)}k^{(3)})\delta_i j) - 4J_3(k^{(2)})\times\right.$$
$$\left.\times\left(\delta_{ij} + (k_j^{(1)}k_i^{(3)})\frac{(k^{(1)}k^{(3)}) - (k^{(1)})^2 - (k^{(3)})^2}{(k^{(1)}k^{(3)})^2}\right)\right). \quad (2)$$

Here, J_1, J_2, and J_3 are the functions of the external momenta $k^{(1)}$, $k^{(2)}$, and $k^{(3)}$, the chemical potential μ, and the mass m. The analytical integration for the functions J_1, J_2, and J_3 to a final result can be fulfilled only in the case where all the momenta are collinear. Otherwise, asymptotic approximations can be derived for J_1 and J_3. The symmetric components Π_{i4j} and Π_{4ij} are obtained by making the corresponding substitutions $k^{(1)} \to k^{(2)}$, $k^{(2)} \to k^{(3)}$, and $k^{(3)} \to k^{(1)}$ for the former, and $k^{(1)} \to k^{(3)}$, $k^{(3)} \to k^{(2)}$, and $k^{(2)} \to k^{(1)}$ for the latter.

Passing in formulas (1) and (2) to small momenta ($\frac{k^{(1)}}{a} \ll 1$ and $\frac{k^{(2)}}{a} \ll 1$), where $a = \sqrt{\mu^2 - m^2}$, we obtain the following asymptotic behavior for tensor components in the symmetric case $\frac{k^{(1)}}{k^{(2)}} \to 1$:

$$\Pi_{444} = \frac{e^3}{\pi^3}\theta(\mu^2 - m^2)\sqrt{\mu^2 - m^2}(6 + \sum_{n>1}^{3}\sum_{l=1`}^{2}\frac{\beta_{in} - \pi q_{in}}{\sin\beta_{in}}((2(1+\cos\beta_{12}))^{\frac{2-n}{2}} +$$
$$+(3-n)(1+\cos\beta_{12}) - \cos\beta_{in})) + O\left(\frac{k^{(1)}}{a}\right), \quad (3)$$

$$\Pi_{ij4} = \frac{e^3}{\pi^3}\theta(\mu^2 - m^2)\sqrt{\mu^2 - m^2}(\delta_{ij} + \cos\alpha_{3j}\cos\alpha_{1i}\cos\beta_{13} - \cos\alpha_{1i}\cos\alpha_{1j} -$$
$$-\cos\alpha_{3i}\cos\alpha_{3j}) + O\left(\frac{k^{(1)}}{a}\right), \quad (4)$$

where β_{in} is an angle between the vectors k^l and k^n, $\cos\alpha_{1i}$ is the direction cosine of the vector k^1, q_{in} are arbitrary integers that satisfy the equality $q_{12} + q_{13} + q_{23} = 2$, and $\theta(\mu^2 - m^2)$ is the Heaviside function.

For large momenta, $\left(\frac{k^{(1)}}{a}, \frac{k^{(2)}}{a}\right) \gg 1$, and in the symmetric limit, formulas (1) and (2) give the following result for tensor components:

$$\Pi_{444} = O\left(\frac{k^{(1)}}{a}\right), \Pi_{ij4} = O\left(\frac{k^{(1)}}{a}\right). \quad (5)$$

It testifies that, in the high-momentum and, accordingly, short-distance approximation, the medium becomes asymptotically transparent, and its influence on the field properties is insignificant. This takes place, because the vertex function is proportional to the chemical potential, the latter being a small parameter in the case of high momenta. However, for linear scales $r \geq (\mu^2 - m^2)^{-\frac{1}{2}}$, the substitution of $\Pi_{\mu\nu\gamma}$ by its asymptotic value does not violate the adequacy of description for the properties of an electromagnetic field with an arbitrary strength distribution. Under such conditions, the quantity $\sqrt{\mu^2 - m^2}/k$ is a large parameter, and there is no necessity to use the "adiabatic expansion".

3 Three-photon Vertex in the Case of Low-frequency Photons

In the case of low-frequency photons and, hence, low k_4-values, the determination of multipliers H_n demands that the linear approximation be used and the obtained expressions be expanded into power series of k_4. After carrying out the corresponding calculations, those multipliers can be expressed as follows:

$$\begin{aligned}
H_1 &\approx \frac{n_e(\varepsilon_0) - n_p(\varepsilon_0)}{2i\varepsilon_0[2\mathbf{pk}^{(1)} + (\mathbf{k}^{(1)})^2][-2\mathbf{pk}^{(2)} + (\mathbf{k}^{(2)})^2]};\\
H_2 &\approx (n_e(\varepsilon_1) - n_p(\varepsilon_1))(2i\varepsilon_1[2\mathbf{pk}^{(1)} - (\mathbf{k}^{(1)})^2][-2\mathbf{p}(\mathbf{k}^{(2)} + \mathbf{k}^{(1)}) + (\mathbf{k}^{(2)})^2 - (\mathbf{k}^{(1)})^2])^{-1};\\
H_3 &\approx (n_e(\varepsilon_2) - n_p(\varepsilon_2))(2i\varepsilon_2[2\mathbf{pk}^{(2)} - (\mathbf{k}^{(2)})^2](-2\mathbf{p}(\mathbf{k}^{(2)} + \mathbf{k}^{(1)}) + (\mathbf{k}^{(1)})^2 - (\mathbf{k}^{(2)})^2))^{-1}, \quad (6)
\end{aligned}$$

where $n_e(\varepsilon_n)$ and $n_p(\varepsilon_n)$ are the electron and positron, respectively, density functions, which look like $n_e(\varepsilon_n) = [1+\exp(\beta(\varepsilon_n-\mu)]^{-1}$, $n_p(\varepsilon_n) = [1+\exp(\beta(\varepsilon_n+\mu)]^{-1}$.

The H_n-multipliers generate three groups of terms for each vertex function component, each of the latter including k_4 raised to a certain power ranging from 0 to 4, and terms with k_4 raised to a power larger than one can be neglected. At the same time, the terms without k_4 comprise a static part of the components, which was calculated in work [6]. Then, all we need is to calculate those terms, which depend linearly on k_4:

$$\begin{aligned} F_{444} &\approx F_{444}^{stat} + Re\{H_1[\mathbf{pk}^{(2)}k_4^{(1)} + (\mathbf{pk}^{(1)} - \varepsilon_0^2)k_4^{(2)}] + H_2[(\varepsilon_0^2 + \mathbf{pk}^{(1)} + \varepsilon_1^2)k_4^{(2)} + (2\varepsilon_0^2 + \\ &+ \mathbf{pk}^{(2)} - \mathbf{k}^{(1)}\mathbf{k}^{(2)} + 2\varepsilon_1^2)k_4^{(1)}] - H_3[(\varepsilon_0^2 - \mathbf{pk}^{(2)} + \varepsilon_2^2)k_4^{(1)} + (2\varepsilon_0^2 - \mathbf{pk}^{(1)} - \mathbf{k}^{(1)}\mathbf{k}^{(2)} + 2\varepsilon_2^2)k_4^{(2)}]\}. \quad (7) \end{aligned}$$

The function F is coupled with Π by the relation $\Pi_{\mu\nu\gamma} = \frac{ie^3}{(2\pi)^3\beta}\int d^3pF_{\mu\nu\gamma}$. While calculating F_{ij4}, we should take into consideration that $i \neq 4$ and $j \neq 4$, so that $\delta_{i4} = \delta_{j4} = 0$. Moreover, we use the approximation, for which $k_4^{(a)}k_4^{(b)} = 0$. Therefore, we find

$$\begin{aligned} F_{ij4} &\approx F_{ij4}^{stat} + Re\{\varepsilon_0\delta_{ij}(H_2\varepsilon_1 k_4^{(1)} + H_3\varepsilon_2 k_4^{(2)}) + H_1[(\mathbf{pk}^{(2)}\delta_{ij} + 2p_ip_j - p_ik_j^{(2)} - p_jk_i^{(2)})k_4^{(1)} + \\ &+ (\mathbf{pk}^{(1)}\delta_{ij} + 2p_ip_j - p_ik_j^{(1)} - p_jk_i^{(1)})k_4^{(2)}] + H_2[((\mathbf{p}(2\mathbf{k}^{(1)} + \mathbf{k}^{(2)}) + (k^{(1)}))^2\delta_{ij} + 2p_ip_j + p_ik_j^{(2)} + \\ &+ p_jk_i^{(2)})k_4^{(1)} - ((\mathbf{p}\ \mathbf{k}^{(1)} + (\mathbf{k}^{(1)})^2\delta_{ij} + 2p_ip_j + p_ik_j^{(1)} + p_jk_i^{(1)})k_4^{(2)}] - H_3[((\mathbf{p}(2\mathbf{k}^{(2)} + \mathbf{k}^{(1)}) - (\mathbf{k}^{(2)}))^2\delta_{ij} - \\ &- 2p_ip_j + p_ik_j^{(1)} + p_jk_i^{(1)})k_4^{(2)} + ((-\mathbf{p}\ \mathbf{k}^{(2)} + (\mathbf{k}^{(2)})^2\delta_{ij} + 2p_ip_j - p_ik_j^{(2)} - p_jk_i^{(2)})k_4^{(1)}]\}. \quad (8) \end{aligned}$$

In a similar way, we make transformations for other tensor elements. Taking into account that $F_{i44}^{\rm stat} = F_{ijl}^{\rm stat} = 0$ in the static case, we obtain

$$\begin{aligned} F_{ijl} \approx Im\Bigg[& H_1\varepsilon_0\Bigg\{\begin{matrix}\{(k_l^{(2)}\delta_{ij}+k_j^{(2)}\delta_{il}- \\ -k_i^{(2)}\delta_{jl}-2p_j\delta_{il})\end{matrix}\Bigg\}k_4^{(1)} + \\ & + \Bigg\{\begin{matrix}(k_l^{(1)}\delta_{ij}-k_j^{(1)}\delta_{il}+ \\ +k_i^{(1)}\delta_{jl}+2p_i\delta_{jl})\end{matrix}\Bigg\}k_4^{(2)}\Bigg\} + H_2\varepsilon_1\Bigg\{\begin{matrix}\{(k_l^{(2)}\delta_{jl}-k_l^{(2)}\delta_{ij}-k_j^{(2)}\delta_{il}+(k_i^{(1)}+2p_i)\times \\ \times\delta_{jl}+(k_l^{(1)}+2p_l)\delta_{ij}-(k_j^{(1)}+2p_j)\delta_{il})\end{matrix}\Bigg\}\times \\ & \times k_4^{(1)} + \Bigg\{\begin{matrix}(k_l^{(1)}\delta_{ij}-k_j^{(1)}\delta_{il}+ \\ +k_i^{(1)}\delta_{jl}+2p_i\delta_{jl})\end{matrix}\Bigg\}k_4^{(2)}\Bigg\} + \\ & H_3\varepsilon_2\Bigg\{\begin{matrix}\{(k_j^{(1)}\delta_{il}-k_l^{(1)}\delta_{ij}-k_i^{(1)}\delta_{jl}+(k_j^{(1)}-2p_j)\times \\ \times\delta_{il}+(k_l^{(1)}-2p_l)\delta_{ij}-(k_i^{(1)}-2p_i)\delta_{jl})\end{matrix}\Bigg\}\times \\ & \times k_4^{(2)} + \Bigg\{\begin{matrix}(k_l^{(2)}\delta_{ij}+k_j^{(2)}\delta_{il}- \\ k_i^{(2)}\delta_{jl}-2p_i\delta_{jl})\end{matrix}\Bigg\}k_4^{(1)}\Bigg\}\Bigg], \end{aligned} \quad (9)$$

$$\begin{aligned} F_{i44} &\approx Im[H_2\varepsilon_1[((k_i^{(1)} + 2p_i) - k_i^{(2)})k_4^{(1)} + (k_i^{(1)} + 2p_i)k_4^{(2)}] + H_3\varepsilon_2[((k_i^{(2)} - 2p_i) - k_i^{(1)})k_4^{(2)}] \\ &+ (k_i^{(2)} - 2p_i)k_4^{(1)} - \varepsilon_0(H_2 + H_3)[(k_i^{(2)} - 2p_i)k_4^{(1)} + (k_i^{(1)} + 2p_i)k_4^{(2)}]]. \quad (10) \end{aligned}$$

The expressions derived for all tensor elements in the long-wave approximation compose a system that describes such photon–photon processes as the photon decay into two photons, the decay of an electric field into free photons, the generation of a magnetic field in the presence of the electric one, and the interaction between a free photon and a magnetic field. The expressions found for the tensor components testify that the processes of creation of real photons take place only in alternating fields, because the corresponding tensor components include only dynamic parts. Unlike the static case, dynamic processes can be observed "from outside" the medium. Therefore, they are suitable for studying the microscopic volumes in a dense medium.

4 Interaction Between Photons and a Magnetic Field in a Medium

On the basis of the results obtained, let us consider a case of the interaction between photons and a classical magnetic field in the presence of fermionic plasma. In this case, we have a state of the external field without energy transfer and with a definite fixed spatial momentum, which can be designated as $(k_l^{(1)} + k_l^{(2)})$, where $l \in 1, 3$. Then, the element of the scattering cross-section looks like

$$S = F_{ijl}k_i^{(1)}k_j^{(2)}(k_l^{(1)} + k_l^{(2)}) + F_{44l}k_4^{(1)}k_4^{(2)}(k_l^{(1)} + k_l^{(2)}) + F_{i4l}k_i^{(1)}k_4^{(2)}(k_l^{(1)} + k_l^{(2)}) + F_{4jl}k_4^{(1)}k_j^{(2)}(k_l^{(1)} + k_l^{(2)}). \quad (11)$$

According to the assumption that k_4 is small, the term $F_{44l}k_4^{(1)}k_4^{(2)}(k_l^{(1)} + k_l^{(2)})$ approximately equals zero, whereas the components with k_4 in the terms $F_{i4l}k_i^{(1)}k_4^{(2)}(k_l^{(1)} + k_l^{(2)})$ and $F_{4jl}k_4^{(1)}k_j^{(2)}(k_l^{(1)} + k_l^{(2)})$ – all of them are dynamic contributions – are also reduced. However, since they are written down as $(k_l^{(1)} + k_l^{(2)})$, the equality $k_4^{(1)} = -k_4^{(2)}$ must be satisfied, and we have a process of elastic photon scattering by a magnetic field. Then, the nonzero tensor elements look like $F_{i4l} = F_{i4l}^{\rm stat}$, $\quad F_{4jl} = F_{4jl}^{\rm stat}$,

$$\begin{aligned} F_{ijl} \approx Imk_4^{(1)}\{&H_1\varepsilon_0((k_l^{(2)} - k_l^{(1)})\delta_{ij} + (k_j^{(2)} + k_j^{(1)})\delta_{il} - (k_i^{(2)} + k_i^{(1)})\delta_{jl} - 2p_i\delta_{jl} - 2p_j\delta_{il}) + \\ &+H_2\varepsilon_1[k_i^{(2)}\delta_{jl} - k_l^{(2)}\delta_{ij} - k_j^{(2)}\delta_{il} + p_l\delta_{ij} - p_j\delta_{il}] + H_3\varepsilon_2[k_j^{(1)}\delta_{il} - k_l^{(1)}\delta_{ij} - k_i^{(1)}\delta_{jl} - p_l\delta_{ij} + p_i\delta_{jl}]\}. \quad (12) \end{aligned}$$

One can see that all dynamics of the process is contained in the element F_{ijl}, whereas the other nonzero tensor components describe only the statics. In addition, since we consider the process of free photon scattering by a magnetic field, the dispersion relations must be satisfied. Therefore, $\mathbf{k}^{(1)} = \mathbf{k}^{(2)} = k$, because $|k_4^{(1)}| = |k_4^{(2)}|$.

We can take advantage of this property by multiplying the tensor by the corresponding vectors k. Then, we immediately obtain an expression for the scattering cross-section; it contains only scalar products $(\mathbf{k}^{(1)}, \mathbf{k}^{(2)})$ that can be equalized to each other. The final expression for the effective scattering cross-section has the form

$$\begin{aligned} k_i^{(1)} k_j^{(2)} F_{ijl}(k_l^{(2)} + k_l^{(1)}) &\approx -Imk_4^{(1)}(\mathbf{k})^2\{2(1+\cos\gamma)(\cos\alpha+\cos\beta)\frac{n_e(\varepsilon_0)-n_p(\varepsilon_0)}{2i[2\mathbf{p}\cos\alpha+\mathbf{k}][-2\mathbf{p}\cos\beta+\mathbf{k}]}\mathbf{p} + \\ &+ (\mathbf{k}(1+\cos\gamma) + \frac{\mathbf{p}(\cos\alpha+\cos\beta)}{[-2\mathbf{p}(\cos\beta+\cos\alpha)]}(\frac{n_e(\varepsilon_1)-n_p(\varepsilon_1)}{2i[2\mathbf{p}\cos\alpha-\mathbf{k}]} + \frac{n_e(\varepsilon_2)-n_p(\varepsilon_2)}{2i[2\mathbf{p}\cos\beta-\mathbf{k}]})\}, \end{aligned} \quad (13)$$

where γ is the angle between the vectors $k^{(1)}$ and $k^{(2)}$, and α and β are the angles between the vector p and the corresponding k. As follows from the general form of expression (13), the cross-section of photon scattering by a magnetic field is proportional to the squared absolute value of the photon wave vector. The behavior of this dependence can be used, while studying this scattering process experimentally. Notice that, for instance, in the case of an external magnetic field without a medium, the scattering cross-section is proportional to k^4 [9, 10].

5 Discussion of Results

Thus, we have obtained the explicit expressions for the components of the three-photon vertex tensor in two approximations, the static-field and low-frequency ones, and a special case of the interaction between free photons and a magnetic field is analyzed. The static-case approximation demonstrates the essence of why the nonlinear behavior of fields emerges in a dense medium. At the same time, it forms a necessary basis for the description of various processes considered above. The low-frequency approximation describes a large number of nonlinear photon–photon interactions and allows dynamic processes to be studied. We consider the photon scattering by a magnetic field as the most interesting case. Therefore, it was examined in more details. As a result, we derived an exact expression for the scattering cross-section. The obtained dependence for the cross-section is a quadratic function of the absolute value of photon momentum. It can be used to experimentally check the presence (formation) of a dense medium.

The phenomena arising in media with broken C-parity are of great interest, first of all, because they are an experimental confirmation of theoretical principles used in quantum electrodynamics. However, physical phenomena of such an origin can also find practical applications even today, mainly, as a detector of the presence of dense fermionic substances and a tool of their research. Using the asymptotic relations that describe processes in the medium, the internal characteristics of such media—first of all, the chemical potential—can be measured.

The low-frequency approximation used in this work reveals new opportunities for taking the influence of a medium on the interaction between fields into consideration. This case can be reduced to a number of probable processes. In our opinion, the process of free photon scattering by a magnetic field is the most interesting. The scattering parameters depend only on the field characteristics and the chemical potential μ of a medium. Theoretically, this process allows one to measure μ by detecting scattered photons. The phenomenon of such a type can find application in the NICA and FAIR projects (where collisions between heavy nuclei are studied) both as a tool for the reliable detection of the very fact of the generation of a dense fermionic matter and to study the properties of this matter.

References

[1] M. Bordag, G.L. Klimchitskaya, U. Mohideen, and V.M. Mostepanenko, *Advances in the Casimir Effect* (Oxford Univ. Press, Oxford, 2009).

[2] R.L. Jaffe, Phys. Rev. D **72**, 021301 (2005).

[3] A.A. Grib, S.G. Mamayev, and V.M. Mostepanenko, *Vacuum Quantum-Mechanical Effects in Strong Fields* (Energoatomizdat, Moscow, 1988) (in Russian).

[4] W. Furry, Phys. Rev. **51**, 125 (1937).

[5] V.V. Skalozub and A.Yu. Tishchenko, Zh. Eksp. Teor. Fiz. **104**, 3921 (1993).

[6] A.I. Pas'ko and V.V. Skalozub, Ukr. Fiz. Zh. **41**, 1013 (1996).

[7] V. De la Insera V, E. Ferrer, and A.E. Shabad, Trudy Fiz. Inst. Akad. Nauk SSSR **169**, 183 (1986).

[8] V.O. Papanyan and V.I. Ritus, Zh. Eksp. Teor. Fiz. **65**, 1756 (1973).

[9] S.L. Adler, J.N. Bahcall, C.G. Callan, and M.N. Rosenbluth, Phys. Rev. Lett. **25**, 1061 (1970).

[10] A.V. Kuznetsov and N.V. Mikheev, *Electroweak Processes in an External Active Medium* (Yaroslavl State Univ., Yaroslavl, 2010) (in Russian).

Proceedings of the International School-seminar
"New Physics and Quantum Chromodynamics at External Conditions", pp. 126 – 129,
3-6 May 2011, Dnipropetrovsk, Ukraine

TWO LIQUID HYDRODYNAMICS OF PLASMA IN ISOTROPIC MAGNETIC FIELD

A. A. Stupka[a]

Oles' Honchar Dnipropetrovs'k National University, Dnipropetrovs'k, Ukraine

Two component conducting liquid in isotropic magnetic field is considered. Linearization and averaging taking into account fluctuating magnetic field in equations of two liquid magnetic hydrodynamics are performed. Hot electron and cold ion subsystems are considered. Dispersion equation for the system is analyzed. There is received new transversal Alfven-like acoustic wave velocity and is introduced new characteristic Larmor-like frequency in an isortopic magnetized plasma.

1 Introduction

In the two liquid hydrodynamics of plasma usually we suppose that constant magnetic field is characterized by the first moment (average magnetic induction) and has no fluctuations [1]. In isotropic systems the nonzero first moment is forbidden as vector value. But if a magnetic field has accidental nature then the second correlation moment [2], that arises in Euler equation, has nonzero value and essentially change the dynamics of a system. That gives the opportunity to obtain important physical information about isotropic conducting media by the study of the random phase approximation [3] for magnetic field. For example, even in one liquid approximation one can obtain new hydrodynamical modes [4].

2 Two liquid hydrodynamics of plasma

We will consider a two-liquid hydrodynamic model [1] with an isotropic magnetic field, which is characterized by a nonzero second moment. We will be limited to only cold ionic component. Opposite, we will consider hot electronic component, that we will take into account by means of pressure in Euler equation. We will take interest only by small oscillations, that allows linearization of equations near an equilibrium. Velocities of components have a small value after linearization, that is why only fluctuating part of the magnetic field enters in the Lorentz force. Temporal equations look like: Euler equation

$$\frac{d\mathbf{v}_i}{dt} = \frac{e_i}{m_i}(\mathbf{E} - [\mathbf{B}, \mathbf{v}_i]/c), \tag{1}$$

where we take into account, that $\mathbf{j}_a = e_a n_a \mathbf{v}_a$ - electric current density, $\rho_a = m_a n_a$ - mass density of a plasma component;

$$\frac{d\mathbf{v}_e}{dt} = -gradP_e/\rho_e + \frac{e_e}{m_e}(\mathbf{E} - [\mathbf{B}, \mathbf{v}_e]/c), \tag{2}$$

here the gradient of pressure must be calculated at adiabatic process, that allows to write down $\nabla P_e = \left(\frac{\partial P}{\partial n}\right)_s \nabla n_e$. Consequently for closing of the system we need continuity equation

$$\frac{\partial n_e}{\partial t} + n div \mathbf{v}_e = 0. \tag{3}$$

We differentiate equation (2) by time, put equation (3) in equation (2) and make Fourier-transformations

$$-\omega^2 v_{e\alpha} = -k_\alpha k_\beta u_e^2 v_{e\beta} + \frac{-i\omega e_e}{m_e}(E_\alpha + \varepsilon_{\alpha\beta\gamma} v_{e\beta} B_\gamma/c), \tag{4}$$

denotation

$$u_e^2 = \frac{1}{m_e}\left(\frac{\partial P}{\partial n}\right)_s \tag{5}$$

is here entered. Also we write out the standard Maxwell equations

e-mail: [a]antonstupka@mail.ru

$$\frac{\partial \mathbf{E}}{\partial t} = crot\mathbf{B} - 4\pi\mathbf{j}, \tag{6}$$

$$\frac{\partial \mathbf{B}}{\partial t} = -crot\mathbf{E}. \tag{7}$$

Magnetic induction appearing here in derivatives is determined by an electric current and does not have fluctuation nature.

We obtain from equations (6) and (7) after the Fourier transformations

$$-\omega^2 E_\alpha = -c^2k^2E_\alpha + k_\alpha k_\beta E_\beta + 4\pi i\omega(e_i n_i v_{i\alpha} + e_e n_e v_{e\alpha}). \tag{8}$$

As sound oscillations are accepted to describes by oscillations of a mass, we can get rid of electronic speed. We put $v_{e\alpha}$ from equation (8) in equation (4)

$$\left(-\omega^2\delta_{\alpha\beta} + k_\alpha k_\beta u_e^2 - \frac{-i\omega e_e}{m_e}\varepsilon_{\alpha\beta\gamma}B_\gamma/c\right)\frac{1}{4\pi i\omega e_e n_e} \times$$
$$\times\left(((-\omega^2 + c^2k^2)\delta_{\chi\beta} - k_\chi k_\beta)E_\chi - 4\pi i\omega e_i n_i v_{i\beta}\right) = \frac{-i\omega e_e}{m_e}E_\alpha. \tag{9}$$

Now we express from equation (1) strength of electric fields and put it after Fourier-transformations into equation (9)

$$\left(-\omega^2\delta_{\alpha\beta} + k_\alpha k_\beta u_e^2 + \frac{i\omega e_e}{m_e}\varepsilon_{\alpha\beta\gamma}B_\gamma/c\right)(-4\pi i\omega e_i n_i v_{i\beta}) = \left(\frac{4\pi\omega^2 e_e^2 n_e}{m_e}\delta_{\alpha\chi} -\right.$$
$$\left. - \left(-\omega^2\delta_{\alpha\delta} + k_\alpha k_\delta u_e^2 + \frac{i\omega e_e}{m_e}\varepsilon_{\alpha\delta\gamma}B_\gamma/c\right)\left((-\omega^2 + c^2k^2)\delta_{\chi\delta} - c^2k_\chi k_\delta\right)\right)\frac{m_i}{i\omega e_i}(\omega^2\delta_{\chi\varphi} - \frac{i\omega e_i}{m_i c}\varepsilon_{\chi\varphi\psi}B_\psi)v_{i\varphi}. \tag{10}$$

It is now possible to perform averaging on the random phase of fluctuating magnetic field [3].

$$\left(\left(-\omega^2\delta_{\alpha\varphi} + k_\alpha k_\varphi u_e^2\right)\omega^2\Omega_i^2 - \left(\omega^2\Omega_e^2\delta_{\alpha\chi} - \left(-\omega^2\delta_{\alpha\delta} + k_\alpha k_\delta u_e^2\right)\left((-\omega^2 + c^2k^2)\delta_{\chi\delta} - c^2k_\chi k_\delta\right)\right)\omega^2\delta_{\chi\varphi} +\right.$$
$$\left. +\omega^2\frac{e_e}{m_e c}\varepsilon_{\alpha\delta\gamma}\frac{e_i}{m_i c}\varepsilon_{\chi\varphi\psi}\langle B_\gamma B_\psi\rangle\left((-\omega^2 + c^2k^2)\delta_{\chi\delta} - c^2k_\chi k_\delta\right)\right)v_{i\varphi} = 0, \tag{11}$$

here the standard denotation for Langmuir frequency $\Omega_a^2 = 4\pi e_a^2 n_a/m_a$ is entered.

Equation (11) determines dispersion equation for our system because of arbitrariness of velocity. As stationary solutions do not interest us, we reduce on ω^2:

$$\left(-\omega^2\delta_{\alpha\varphi} + k_\alpha k_\varphi u_e^2\right)\Omega_i^2 - \left(\omega^2\Omega_e^2\delta_{\alpha\chi} - \left(-\omega^2\delta_{\alpha\delta} + k_\alpha k_\delta u_e^2\right)\right. \times$$
$$\left.\times\left((-\omega^2 + c^2k^2)\delta_{\chi\delta} - c^2k_\chi k_\delta\right)\right)\delta_{\chi\varphi} + \frac{e_e}{m_e c}\varepsilon_{\alpha\delta\gamma}\frac{e_i}{m_i c}\varepsilon_{\chi\varphi\psi}\langle B_\gamma B_\psi\rangle\left((-\omega^2 + c^2k^2)\delta_{\chi\delta} - c^2k_\chi k_\delta\right) = 0. \tag{12}$$

We receive biquadratic equation for frequency of small oscillations.

3 Isotropic correlation of the field

Because of isotropy we have a tensor structure $\langle B_\alpha B_\beta\rangle = \langle B^2\rangle\delta_{\alpha\beta}/3$. We consider relation of frequency and wave vector for longitudinal oscillations, that we multiply equation (12) on $k_\alpha k_\varphi/k^2$

$$\left(-\omega^2 + k^2u_e^2\right)\Omega_i^2 - \omega^2\Omega_e^2 - \left(-\omega^2 + k^2u_e^2\right)\omega^2 - 2\omega_i\omega_e\left(-\omega^2 + c^2k^2\right) = 0. \tag{13}$$

Here denotation for characteristic frequency of charged particles motion is introduced, that related to the isotropic magnetic field

$$\omega_a = \frac{e_a\sqrt{\langle B^2\rangle}}{\sqrt{3}m_a c}. \tag{14}$$

Apparently, this frequency is similar to the cyclotron one. Solution of equation (13) is

$$\omega_{12}^2 = \frac{1}{2}(\Omega_e^2 + \Omega_i^2 + k^2u_e^2 - 2\omega_i\omega_e \pm \sqrt{(\Omega_e^2 + \Omega_i^2 + k^2u_e^2 - 2\omega_i\omega_e)^2 - 4k^2(u_e^2\Omega_i^2 - 2c^2\omega_i\omega_e)}). \tag{15}$$

We consider limit cases of dispersion dependence. We assume that

$$\Omega_a^2 >> \omega_a^2 \tag{16}$$

Then the bigger solution corresponds to the electronic Langmuir waves,

$$\omega_1^2 = \Omega_e^2 + k^2 u_e^2. \tag{17}$$

The hydrodynamic approximation comes, when, as it is obvious from equation (15),

$$k << \Omega_e/u_e. \tag{18}$$

From here smaller value of frequency is:

$$\omega_2^2 = k^2 \frac{u_e^2\Omega_i^2 - 2c^2\omega_i\omega_e}{\Omega_e^2} = k^2 u_l^2 \tag{19}$$

If $\langle B^2\rangle = 0$, then equation (19) turns in spectrum of ionic-sound oscillations. Let ions have a charge Z, then because of electro-neutrality their density is $n_i = n_e/Z$ and it is possible to write down the identity

$$-\frac{\omega_i}{\omega_e} = \frac{\Omega_i^2}{\Omega_e^2}. \tag{20}$$

Then from (19) we obtain

$$u_l^2 = \frac{u_e^2\Omega_i^2}{\Omega_e^2} + \frac{2c^2\omega_i^2}{\Omega_i^2}. \tag{21}$$

As we can see, addition to velocity of ionic sound in a due form is similar to Alfvenic velocity.

In the limit of short waves with a condition reverse to (18) we receive, using again identity (20),

$$\omega_2^2 = \Omega_i^2\left(1 + \frac{2c^2\omega_e^2}{u_e^2\Omega_e^2}\right). \tag{22}$$

Lets pass to the transversal waves. It is necessary for this purpose to multiply dispersion equation (12) with combination $\delta_{\alpha\varphi} - k_\alpha k_\varphi/k^2$. We receive biquadratic equation

$$\omega^4 - \omega^2(\Omega_e^2 + \Omega_i^2 + c^2k^2 + \omega_i\omega_e) - \omega_i\omega_e c^2k^2 = 0, \tag{23}$$

and solution of which is

$$\omega_{12}^2 = \frac{1}{2}\left(\Omega_e^2 + \Omega_i^2 + k^2c^2 + \omega_i\omega_e \pm \sqrt{(\Omega_e^2 + \Omega_i^2 + k^2c^2 + \omega_i\omega_e)^2 + 4k^2c^2\omega_i\omega_e}\right). \tag{24}$$

Bigger frequency corresponds to the transversal plasma waves [5]

$$\omega_1^2 = \Omega_e^2 + k^2c^2. \tag{25}$$

For hydrodynamics it is required

$$k << \Omega_e/c, \tag{26}$$

that gives such sound mode

$$\omega_2^2 = k^2 \frac{-c^2\omega_i\omega_e}{\Omega_e^2} = k^2 u_t^2 \tag{27}$$

with velocity

$$u_t = \frac{c\omega_i}{\Omega_i} = \sqrt{\frac{\langle B^2\rangle}{12\pi n m_i}}. \tag{28}$$

In the reverse to condition (26) limit we obtain

$$\omega_2^2 = -\omega_i\omega_e, \tag{29}$$

such combination of frequencies (14) is similar to low-hybrid frequency of oscillations of magnetized plasma.

It is needed yet to specify the limit of applicability of quasi-hydrodynamic approach. It is possible to neglect by thermal motion of ions, in analogy to the case of ordinary magnetized plasma [1], when for wave vector is fulfill

$$k << \omega_i/u_i. \tag{30}$$

4 Conclusions

Magnetic field with random phase in isotropic plasma is considered. In equations of two-liquid magnetic hydrodynamics linearization and averaging with the account of the fluctuating magnetic field is performed. Received system equations of fluctuation magnetic two-liquid hydrodynamics can be applied for consideration of magnetized plasma.

Dispersion equations and frequencies of plane waves in such system are obtained. A new characteristic frequency of charged particles motion is introduced, that related to the isotropic magnetic field and determines the value of distribution velocity of transversal plane waves.

References

[1] V.L. Ginzburg and A.A. Ruhadze, *Volny v magnitoakyivnoy plazme* (in Russ.), (Moscow, Nauka, 1970)

[2] R.V. Fleishmann, *Stohasticheskaya teoriya izlucheniya* (in Russ.), (Moscow-Izhevsk, NIC regulyarnaya i stohasticheskaya dinamika, 2008).

[3] *Elektrodinamika plazmy* (in Russ.), Edited by A.I. Akhiezer (Nauka, Moscow, 1974, 720 p.). A.I. Akhiezer, I.A. Akhiezer, R.V. Polovin, A.G. Sitenko, and K.N. Stepanov, *Plasma Electrodynamics*, (Oxford, Pergamon, 1975).

[4] A.A. Stupka, Magnetohydrodynamics, **46**, 137 (2010).

[5] A.F. Aleksandrov, L.S. Bogdankevich and A.A. Rukhadze, *Osnovy elektrodinamiki plazmy* (in Russ.), (Moscow, Vysshaya shkola, 1988). A.F. Alexandrov, L.S. Bogdankevich, A.A. Rukhadze, *Principles of Plasma Electrodynamics*, (Springer Verlag, Heidelberg, 1984).

Proceedings of the International School-seminar
"New Physics and Quantum Chromodynamics at External Conditions", pp. 130 – 133,
3-6 May 2011, Dnipropetrovsk, Ukraine

DUAL REPRESENTATIONS OF $3D$ NON-ABELIAN GAUGE MODELS AND THEIR LOW-TEMPERATURE PROPERTIES

S. Voloshyn[a]

N.N.Bogolyubov Institute for Theoretical Physics, National Academy of Sciences of Ukraine, Kiev, Ukraine

Non-abelian $SU(N)$ lattice gauge theories can be formulated in terms of plaquette variables which correspond to continuum field-strength representation. Using this representation for the three dimensional models we derive exact dual formulation for the partition function and some observables like Wilson loop. Dual representation is then applied for the study of the low-temperature region of the model relevant for the construction of the continuum limit. In particular, we compute leading terms of the asymptotic expansion of the dual Boltzmann factor and derive an effective theory for dual potential and take its continuum limit.

1 Introduction

Dual transformations for lattice gauge models have a long history. In the context relevant to this paper we would like to mention duals of the abelian $U(1)$ model [1] which have been used to prove of confinement of static charges at all couplings in 3D gauge model [2]. In these cases the dual of the abelian models is a local theory for certain discrete variables. No similar representation was known so far for any non-abelian model. The conventional dual transformations [3], [4] for non-abelian gauge models also leads to a local dual theory for integers which label irreducible representations of local or global group but these transformations are not complete. First of all, the resulting dual variables are not independent but are subject to certain constraints known as triangular conditions, and as such they cannot really be associated with elements of a dual lattice. Secondly, although local dual formulation is expressed in terms of group invariants (for gauge models) like $6j$-symbols, etc., it involves also summation over auxiliary representations resulting from the multiplication of non-abelian matrices. Such formulation is so mathematically involved that hardly one can hope it can be useful for an analytical study of the model. It remains to see if the dual form can be useful for MC simulations: certain attempts in this direction revealed a number of problems which are still to be solved. But even worse is situation with analytical advances. At the moment it is not even clear how to construct the low-temperature (weak-coupling) expansion within dual approach (something that can be done relatively easily in the standard formulation). Derivation of the naive continuum limit proposed in [5] is far from being rigorous and arises a number of questions. But if correct, it proves the relation between naive continuum limit of $3D$ dual LGT's and quantum gravity. Unfortunately, even this does not help much in real analytical advance since no systematic low-temperature expansion was done. From recent result, we mention analytical approach in [6] and new attempt to use Monte-Carlo techniques to simulate dual $SU(2)$ LGT [7].

On the other hand, there exists so-called plaquette representation [8] and this representation can be formulated directly on the dual lattice. It the present paper we use plaquette representations for derivation of exact dual formulations of $3D$ $SU(N)$ LGT. The resulting dual formulations appear to be quite different from formulations mentioned above. In our opinion the most essential advantage of our dual formulations is that it is much more suitable for an analytical investigations of the model, especially in the low-temperature region. We refer for the detailed explanation of why it is so to our papers [9]. In the [10] we have already presented a plaquette approach to dual of $3D$ $SU(2)$ LGT and proposed approximate representation for the dual partition function at low temperatures. In previous paper [11] we used the plaquette representation to develop a new approach to the confinement problem in terms of the monopole configurations.

As is well known the dual formulations of abelian models have been extremely useful in clarifying all these important physical problems. Moreover, practically all rigorous mathematical results on the behaviour of abelian lattice models at low temperatures have been obtained within dual approaches. It is thus our second goal to develop a technique within dual formulation of non-abelian models which would allow to investigate them in the limit of bare weak coupling, i.e. in the low-temperature region.

2 Dual transformations in plaquette representations

LGT was formulated by K. Wilson in terms of group valued matrices on links of the lattice as fundamental degrees of freedom [12]. The plaquette representation was formulated on the lattice by G. Batrouni [8]. In

e-mail: [a]billy.sunburn@gmail.com

this representation the plaquette matrices play the role of the dynamical degrees of freedom and satisfy certain constraints expressed by Bianchi identities in every cube of the lattice. In paper [9] we have developed a slightly different form of plaquette formulation which we outline below. Crucial point is that plaquette variables by themselves can be considered as certain dual variables. Plaquette variables are subject to the Bianchi constraint which has nonlocal form for non-abelian models. Nevertheless, in this case one can obtain a dual representation for non-abelian models which is close to the corresponding abelian analog. In particular, dual variables are those associated with sites of dual lattice and, at least in certain cases the difficulties related to triangular constraints can be overcome. The essential advantage of this dual form is that it appears to be more suitable for an analytical study of both the high and low-temperature regions of non-abelian LGT.

As consequences we derive a different approach to duality transformations. It can be defined as a sequence of transformations consisting of the following steps:

1. Change of variables in the partition function $V(p) = U_\mu(x)U_\nu(x+e_\mu)U^\dagger_\mu(x+e_\nu)U^\dagger_\mu(x)$. Integration over original degrees of freedom. This integration generates a set of constraints on the plaquette matrices $V(p)$ known as the Bianchi identities.

2. Implementation of constraints into the partition function by making use of the invariant delta-function on the group. This step introduces new degrees of freedom which can be associated with cubes of the original lattice and which label the irreducible representations of the group G. At this step one can go over to the dual lattice so that the new variables belong to the elements of the dual lattice. Integration over plaquette variables.

3. Before integration over link variables one can decouple summations over matrix indices employing certain orthogonality relations for the CG coefficients (or for some other objects) of the group and multiplying the group matrices entering Bianchi identity in some specially ordered way. The result is that only independent dual variables remain in the theory and their interaction is confined to a subset of all cubes of the dual lattice.

We begin with the following partition function in the maximal axial gauge

$$Z = \int \prod_p dV_p \exp\left[\beta \sum_p \mathrm{ReTr} V_p\right] \prod_c J(V_c) \ , \tag{1}$$

where

$$J(V_c) = \sum_r d_r \chi_r(V_c) \ , \tag{2}$$

$$V_c = \left(\prod_{p\in A} V_p\right) C \left(\prod_{p\in B} V_p\right) C^\dagger \ , \ C = \prod_{p\in c} V_p \ . \tag{3}$$

Product over c runs over all cubes of $3D$ lattice. $J(V_c)$ is $SU(N)$ delta-function which introduces constraint on the plaquette matrices (the Bianchi identity). C is a connector of the non-abelian Bianchi identity. For details of this representation we refer the reader to our paper [9].

In what follows we write explicitly all formulae only for $SU(2)$ gauge group. Generalization to other groups is straightforward. Let x be a site dual to the cube of the original lattice and l be a link dual to the plaquette of the original lattice. Then it follows from (1) and from the expression for the Jacobian that in the case of the $SU(2)$ gauge group the partition function on the dual lattice can be written in the following form

$$Z = \sum_{r_x=0,\frac{1}{2},1,\ldots}^{\infty} \prod_x \left[(2r_x+1) \sum_{m_i(x)=-r_x}^{r_x}\right] \prod_l \Xi_0(l) \ . \tag{4}$$

The summation over r_x correspond to the summation over all irreducible representations of the $SU(2)$ group. The sums over magnetic numbers $m_i(x)$ correspond to the calculation of $SU(2)$ traces. The index i may run from 6 to $6+4L$ depending on the position of the original cube, L is the linear extent of the lattice. The link integral $\Xi_0(l) \equiv \Xi_0(J, \alpha_1, \alpha_2; r_{x+2}, m_2, n_2; r_i, k_i, k_{i+1}, p_i, p_{i+1}; \beta)$ is given by

$$\Xi_0(l) = \int dV e^{\beta \mathrm{Tr} V} \ V^{m_1 n_1}_{r_x} V^{\dagger\ m_2 n_2}_{r_{x+n}} \prod_{i=1}^{M(x)} \left(V^{k_i k_{i+1}}_{r_i} V^{\dagger\ p_i p_{i+1}}_{r_i}\right) \ , \tag{5}$$

where V^{mn}_r is a matrix element of r-th representation. The integer number $M(x) = L - z$ depends on the position of the plaquette on the lattice and indicates how many times a given plaquette (dual link) serves as connector in the Bianchi identities.

Similar form for the Wilson loop in the representation j reads

$$W_j(C) = \frac{1}{2j+1} \sum_{\{s_i\}=-j}^{j} \left\langle \prod_{l \in S^d(C)} \frac{\Xi_j^{s_i s_{i+1}}(l)}{\Xi_0(l)} \right\rangle , \tag{6}$$

where the link integral on $l \in S^d(C)$ is

$$\Xi_j^{s_i s_{i+1}}(l) = \int dV e^{\beta \mathrm{Tr} V} \; V_j^{s_i s_{i+1}} V_{r_x}^{m_1 n_1} V_{r_{x+n}}^{\dagger \; m_2 n_2} \prod_{i=1}^{N(x)} \left(V_{r_i}^{k_i k_{i+1}} V_{r_i}^{\dagger \; p_i p_{i+1}} \right) . \tag{7}$$

In general, $M(x) \neq N(x)$ for some x if Wilson loop also contains connectors. Here, $S^d(C)$ is some surface dual to the surface $S(C)$ which is bounded by the loop C and consisting of links dual to plaquettes of the original lattice.

Using the Clebsch-Gordan expansion one finds

$$\Xi_j^{s_i s_{i+1}}(l) = \sum_{J \alpha_1 \alpha_2} C^{J \alpha_1}_{r_x m_1 j s_1} C^{J \alpha_2}_{r_x n_1 j s_2} \; \Xi_0(l) . \tag{8}$$

This representation of the Wilson loop reduces the problem again to the calculation of the basic link integral $\Xi_0(l)$. Similar dual formulae can be obtained for a number of other observables like plaquette-plaquette correlation function, 't Hooft loop, etc. In paper [10] we calculated first terms of the asymptotic expansion of the link integral (5). If one proves a positivity of the dual Boltzmann weight (5) the theory could be useful for Monte-Carlo simulations.

3 Effective theory for $SU(2)$ LGT at large β and continuum limit

In this section we try to build the continuum limit of dual theory and discuss perspectives of further investigation of the developed theory. We start from the partition function that can be written on the dual lattice as [9]

$$Z = \int \prod_{l,k} d\omega_k(l) e^{-\frac{\beta}{4}(\omega^k(l))^2} \prod_x \frac{|W_x|}{\sin W_x} \sum_{m(x)=-\infty}^{\infty} \int \prod_k d\alpha^k(x) \exp \left[-i \sum_k \alpha^k(x) \frac{\omega^k(x)}{2} + 2\pi i m(x) \alpha(x) \right] , \tag{9}$$

where $\alpha(x) = (\sum_k (\alpha^k(x))^2)^{1/2}$, $W_x = \frac{1}{2}(\sum_k (\omega_k(x))^2)^{1/2}$ and similarly for W_l. $m(x)$ are arbitrary integers. Auxiliary fields $\alpha_k(x)$ have been introduced for integral representation of the Bianchi identity (see [9] for details). Near the continuum limit we take $\omega_\mu^k(x - e_\mu) \simeq \omega_\mu^k(x)$ so the Bianchi constraint reduces to

$$\omega^k(x) = \sum_{\mu=1}^{3} \left(\omega_\mu^k(x) - \omega_\mu^k(x - e_\mu) \right) - 2\epsilon^{kmn} \epsilon_{3\mu\nu} \left(\sum_{p=1}^{z-1} \omega_\mu^m(x, y, p) \right) \omega_\nu^n(x, y, z) + \mathcal{O}\left((\omega_\mu^k(x))^3 \right) . \tag{10}$$

Here, six links $l = (x, n)$ are attached to a site x and $\omega_k(l)$ are link variables dual to original plaquettes. It is known that in the continuum limit cubic and higher order terms do not contribute. Since we are not interested in nontrivial monopole configurations we put $m(x) = 0$ for all x. Also, $\frac{W_x}{\sin W_x}$ gives only exponentially small corrections which can be neglected.

Because $\alpha_k(x)$ is conjugate to the Bianchi identity, it is a natural candidate for the continuum dual potential. After making formal Gaussian integration over $\omega_k(l)$ we get an effective theory for $\alpha_k(x)$

$$\begin{aligned} e^{S_{eff}[\alpha_k(x)]} &= \int \prod_{l,k} d\omega_k(l) \exp \left[-\omega_k(l) M_{kk'}(ll') \omega_k(l') - \frac{i}{2} \sum_l \omega_k(l) \left(\alpha_k(x) - \alpha_k(x + e_n) \right) \right] \\ &= \left(\frac{2\pi}{\det M^{kk'}(ll')} \right)^{-\frac{3}{2}} \; e^{-(\alpha_k(x) - \alpha_k(x+e_n)) M^{-1}_{kk'}(ll') (\alpha_{k'}(x') - \alpha_{k'}(x+e_{n'}))} \end{aligned} \tag{11}$$

where matrix $M^{mn}(ll') \equiv M^{mn}(x, \mu; x', \nu)[\alpha_k(x)]$ has a form

$$M^{mn}(x, \mu; x', \nu)[\alpha_k(x)] = \frac{\beta}{4} \delta^{mn} \delta_{\mu\nu} \delta_{xx'} - \frac{i}{2} \epsilon^{kmn} \epsilon_{3\mu\nu} \left(\alpha^k(x) \sum_{p=1}^{z'-1} \delta_{x - pe_3, x'} + \alpha^k(x') \sum_{p=1}^{z-1} \delta_{x, x' - pe_3} \right) \tag{12}$$

This matrix has complicated structure due to the non-locality of the interaction in z direction. We therefore need some approximation to investigate the dual theory.

Making large-β expansion for the inverse matrix $M^{-1}_{mn}(ll')[\alpha_k(x)]$ and taking the continuum limit we obtain the following effective theory for the dual potentials

$$S_{eff}[\alpha_k(x)] = -\frac{1}{4\beta}\sum_{\mu,k}\int d^3x(\partial_\mu\alpha^k(x))^2 - \frac{i}{2\beta^2}\epsilon^{kmn}\epsilon_{3\mu\nu}\int d^3x\ \alpha^k(x)$$

$$\times\left(\int_{-\infty}^{z} dp\ \partial_\mu\alpha^m(x,y,p)\partial_\nu\ \alpha^n(x) + \partial_\mu\alpha^m(x)\int_{-\infty}^{z} dp\ \partial_\nu\alpha^n(x,y,p)\right) + \mathcal{O}\left(\frac{1}{\beta^3}\right)\ . \tag{13}$$

This theory is still quite non-local in z-direction and is too difficult for further investigation.

To investigate a non-perturbative context of the theory we consider another approximation for calculation of the Gaussian integral in (11), namely

$$\alpha^k(x,y,z) \to \langle\alpha^k\rangle(x,y) = \langle\alpha^k\rangle\ . \tag{14}$$

As a result one gets

$$S[\omega^k(l)] = -\frac{\beta}{4}\sum_{k,\mu,x}(\omega^k_\mu(x))^2 + i\epsilon^{nmk}\epsilon_{3\mu\nu}\sum_{x,y}\langle\alpha^k\rangle\left[\sum_{p=1}^{L}\omega^m_\mu(x,y,p)\right]\left[\sum_{p=1}^{L}\omega^n_\nu(x,y,p)\right]$$

$$-\frac{i}{2}\sum_{x,\mu=1,2}\omega^k_\mu(x)(\langle\alpha^k\rangle(x) - \langle\alpha^k\rangle(x+e_\mu)) \to \sum_z S^{2D}_{eff\ chiral}[\langle\alpha^k\rangle] \tag{15}$$

Without fluctuations the effective theory for dual potentials is reduced to a collection of independent effective dual theories for $2D$ chiral model [13]. Incorporating fluctuations like $\alpha^k(x,y,z) = \langle\alpha^k\rangle(x,y) + \xi(x,y,z)$ leads to an interaction between the $2D$ effective models. This result is in spirit of well known approach of [14] where authors used complete axial gauge (as we did). One could also link expectation value of the Wilson loop of $3D$ $SU(2)$ LGT and the correlation function of $2D$ $SU(2)$ principal chiral model. Then the area law for the Wilson loop (that expresses confinement of quarks) in $3D$ model is a consequence of the exponential fall off of the correlation function of $2D$ model.

4 Conclusion

In this article we proposed dual formulation of the non-abelian $SU(2)$ LGT. Our approach to the dual transformations is summarized in the beginning of the section 2. Main formulae of the present paper, Eqs.(4)-(8), give our versions of the dual formulation. One of advantages of this formulation is that in certain cases the difficulties related to triangular constraints can be overcome. As an application of our dual theory the low-temperature asymptotics of the dual Boltzmann weight (5) was computed. Also, we calculated the continuum limit of the dual representation Eqs. (11)-(13). We have shown within certain approximation the effective theory is the collection of independent, non-interacting $2D$ dual theories for principal chiral model in each slice with fixed z. If we include fluctuations the $2D$ theories on these slices become weakly interacting.

Acknowledgements. Authour thank O. Borisenko for stimulating discussions.

References

[1] T. Banks, J. Kogut, R. Myerson, Nucl.Phys. B **121**, 493 (1977).
[2] M. Göpfert, G. Mack, Commun.Math.Phys. **82** 545 (1982).
[3] R.Anishetty, S.Cheluvaraja, H.S.Sharatchandra and M.Mathur, Phys.Lett. B **314**, 387 (1993).
[4] I.Halliday, P.Suranyi, Phys.Lett. B **350**, 189 (1995).
[5] D. Diakonov, V. Petrov, J.Exp.Theor.Phys. **91**, 873-893 (2000).
[6] F. Conrady, Analytic derivation of dual gluons and monopoles from $SU(2)$ lattice Yang-Mills theory. II. Spin foam representation, 2006, [hep-th/0610237].
[7] J. Cherrington, J. Christensen, and I. Khavkine, Phys. Rev. **D** 76, 094503 (2007), [0705.2629].
[8] G. Batrouni, Nucl.Phys. B **208** 467 (1982).
[9] O. Borisenko, S. Voloshin, M. Faber, Field strength formulation, lattice Bianchi identities and perturbation theory for non-Abelian models, Nuclear Physics B **816** [FS], 399 (2009).
[10] O. Borisenko, V. Kushnir, S. Voloshin, Ukr. J. Phys. **48**, 300-308 (2003).
[11] O. Borisenko, S. Voloshyn, J. Boháčik, Monopoles in the plaquette formulation of the $3D$ $SU(2)$ lattice gauge model, arXiv:1106.0293v1, (to be published in Mod. Phys. Lett. A)
[12] K. G. Wilson, Phys.Rev. D **10** 2445 (1974).
[13] O.Borisenko, V.Kushnir, Nucl.Phys. B **730**, 103-126 (2005), [hep-lat/0412040].
[14] B. Durhuus, J. Frohlich, Commun. Math. Phys. **75**, 103-151 (1980).